INSTITUTE OF NUCLEAR PHYSICS,
POLISH ACADEMY OF SCIENCES, KRAKOW, POLAND

Prompt and non-prompt J/ψ production in Pb–Pb collisions at $\sqrt{s_{\mathrm{NN}}}$ = 5.02 TeV with ALICE experiment

Author
mgr. Himanshu SHARMA

Supervisor
dr. hab. Jacek OTWINOWSKI

Co-supervisor
dr. Sándor LÖKÖS

This dissertation is submitted for the degree of

Doctor of Philosophy

in

Physics

Krakow, 2023

Dedicated to my loving parents, my family, and my teachers

The Creation (Nasadiya Sukta)

Then even non-existence was not there, nor existence,
There was no air then, nor the space beyond it.
What covered it? Where was it? In whose keeping?
Was there then cosmic fluid, in depths unfathomed?

Then there was neither death nor immortality, nor was there then the torch of night and day.
The One breathed windlessly and self-sustaining, there was that One then, and there was no other.

At first there was only darkness wrapped in darkness.
All this was only unillumined water.
That One which came to be, enclosed in nothing,
Arose at last, born of the power of heat.

In the beginning desire descended on it. That was the primal seed, born of the mind.
The sages who have searched their hearts with wisdom, know that which is kin to that which is not.

And they have stretched their cord across the void,
And know what was above, and what below.
Seminal powers made fertile mighty forces.
Below was strength, and over it was impulse.

But, after all, who knows, and who can say, whence it all came, and how creation happened?
The gods themselves are later than creation, so who knows truly whence it has arisen?

Whence all creation had its origin,
The creator, whether he fashioned it or whether he did not,
The creator, who surveys it all from highest,
He knows — or maybe even he does not.

– Rigveda, 10:129

Acknowledgements

I am truly grateful to every individual who has extended their invaluable assistance and unwavering support throughout my journey in pursuing my Ph.D.. While there is an extensive list of individuals to acknowledge, I want to wholeheartedly express my deep appreciation to those who have played a significant role in the successful completion of this thesis.

First and foremost, I would like to express my heartfelt gratitude to my Ph.D. supervisor *Dr. hab. Jacek Otwinowski*, who graciously provided me with the opportunity to join the ALICE IFJ group and embark on an exciting journey of exploring charmonium production in the nuclear collisions. I am immensely grateful for his unwavering support throughout my Ph.D. studies. I deeply admire his remarkable patience and have strived to learn from his never panicking attitude and a calm personality. He is a compassionate, very humble and very responsible individual. I am incredibly grateful to have had someone like him as my Ph.D. supervisor. I am truly thankful to him for involving me in the FIT project during the second long shutdown of the LHC. It was a unique and enriching experience that allowed me to stay at CERN for an extended period, gaining insights into detector developments and conducting tests on the real ground. It significantly enhanced my understanding of the ALICE detector's geometry and data acquisition processes. Additionally, I acquired new skills while developing software for FIT quality control. Furthermore, I express my gratitude to Jacek for organizing group dinners. Although the Covid-19 period posed challenges, we managed to enjoy outings before and after that period. Lastly, I must mention the joy of engaging in the spontaneous discussions during our lunch breaks.

I express my deepest gratitude to *Dr. Sándor Lökös* for his thorough examination of the manuscript, offering detailed comments and insightful suggestions. His valuable feedback has greatly contributed to improving the quality of the text and enhancing the overall flow of information in this thesis. A million thanks to him and special gratitude for organising the social events. I enjoyed and learnt different things during those discussions. I extend my gratitude to *Dr. Jacek Biernat* for his teachings and discussions. I am grateful to the Management of International Ph.D. Studies at IFJ for showing the immeasurable support for whole duration of the Ph.D. studies.

I thank *Prof. Marek Kowalski* for his continuous support through my studies. I also want to express my appreciation for his entertaining anecdotes and memorable incidents shared during our social events.

I am deeply grateful to *Dr. Ionut Arsene*, without whom the conducted studies would not have been possible. He provided me with essential guidance and taught me the fundamentals of the DQ framework, as well as the necessary steps to execute the analysis. Meeting him at CERN and conferences was a pleasure, and throughout the course of these studies, we engaged in numerous fruitful discussions. His insightful knowledge has always been a source of great benefit to me. His guidance during the analysis was invaluable, and I thoroughly enjoyed collaborating with him.

I express my gratitude to *Dr. Fiorella Fionda* for her tremendous help and for responding to my emails in great detail, despite her responsibilities within the PWG. I am truly grateful for the knowledge and understanding I gained from her regarding the intricacies of non-prompt J/ψ measurements. Additionally, I would like to thank her for hosting me at INFN Cagliari, where I had the opportunity to meet her and learn the fundamentals of the analysis. It was a wonderful experience, and I greatly appreciate her guidance and support throughout.

I thank *Jon-Are, Alena, Xiaozhi, Minjung* for your great support and sharing the important information related to the analysis quite many times. I thank all the members of Jpsi2ee PAG and PWG conveners for their suggestions and inputs.

I extend my profound gratitude to *Dr. Arvind Khuntia*. Among the individuals listed, he is the only person I knew prior to embarking on my Ph.D. journey. He has served as a mentor, motivator, and a considerate flatmate, always willing to engage in discussions. Having someone like him, who constantly encourages me to strive for greater accomplishments, is truly a pleasure. I thoroughly enjoyed the time spent with him in Krakow.

I am deeply grateful to a very special person, *Karishma*, for bringing numerous *chromos* to this journey and for being there in every situation. Her presence has been invaluable, without her, the journey would have been really challenging. She has become a family in Krakow, and having her by my side has been an immense pleasure. I have cherished numerous delightful and amusing memories with both her and *Rajeev*. We had a fantastic time discovering the streets of Krakow together! It was filled with fun and memorable moments.

The experience of having office mates like *Sneha* and *Sebastian* was truly enjoyable. Both of them possessed a great sense of humor, making our time together even more delightful. There are numerous amusing and engaging conversations from that time stored in my memory. Additionally, collaborating with *Sebastian* during my stay at CERN was a valuable opportunity for learning. Engaging in discussions with *Arpan Das* on various random topics during weekends or during tea/coffee breaks was also a delightful experience. Having chats with *Adam Matya* in the corridors and office brought me a great joy and was a source of genuine delight.

I would like to express my sincere gratitude to *Dr. Andrea Rossi* and *Dr. Andrea Dainese* and my current research group at INFN Padova for their invaluable support in allowing me to continue my postdoctoral work and the preparation of this manuscript. Without their assistance, it would have been incredibly challenging to navigate through the these tasks.

In conclusion, I would like to extend my deep gratitude to all of my hardworking and passionate *ALICE collaborators* who tirelessly work on multiple fronts to explore the nature of our world and push the boundaries of human knowledge. Their commitment and contributions are instrumental in advancing our understanding and expanding the horizons of what we know.

Author's contributions

Conference presentations

- **MESON 2021, Krakow**, Beauty production in pp and Pb–Pb collisions with ALICE (*online*).
- **Epiphany 2022, Krakow**, Charmonium as a probe of hot quark matter in nuclear collisions in ALICE at the LHC (*online*).
- **ICHEP 2022, Bologna**, Inclusive, prompt, and non-prompt J/ψ production at midrapidity in Pb–Pb collisions at $\sqrt{s_{\rm NN}}$= 5.02 TeV with ALICE (*in-person*).
- **EMMI Workshop 2022, Krakow**, Prompt, non-prompt, and coherent J/ψ production in Pb–Pb collisions with ALICE (*in-person*).

Conference posters

- **Initial Stages 2021, Rehovot**, Measurements of non-prompt J/ψ-meson at midrapidity in Pb–Pb collisions with ALICE at the LHC (*online*).
- **PANIC 2021, Lisbon**, Non-prompt J/ψ measurements at midrapidity in pp, p-Pb & Pb–Pb collisions with ALICE (*online*).
- **Quark Matter 2022, Krakow**, Nuclear Modification factor of prompt and non-prompt J/ψ in Pb–Pb collisions at $\sqrt{s_{\rm NN}}$ = 5.02 TeV at midrapidity with ALICE (*online*).
- **LHCP 2022, Taipei**, Prompt and non-prompt J/ψ production at midrapidity in Pb–Pb collisions at $\sqrt{s_{\rm NN}}$ = 5.02 TeV with ALICE (*online*).

Publications

- Nuclear modification of prompt and non-prompt J/ψ in Pb–Pb collisions at $\sqrt{s_{\rm NN}}$= 5.02 TeV, Paper to be submitted to JHEP, *in collaboration review*.
- Non-prompt J/ψ measurements at midrapidity in pp, p–Pb and Pb–Pb collisions with ALICE (*Proceedings, PANIC 2021*), PoS(PANIC2021) 239.
- Charmonium as a probe of hot quark matter in nuclear collisions with ALICE at the LHC (*Proceedings, Epiphany 2022*), Acta Phys. Pol. B Proc. Suppl. 15, 3-A37 (2022).
- Prompt and non-prompt J/ψ production in Pb–Pb collisions at $\sqrt{s_{\rm NN}}$= 5.02 TeV at midrapidity with ALICE (*Proceedings, LHCP 2022*), PoS(LHCP2022) 339.

ALICE Upgrade

- Participated in the commissioning and development of data quality control framework for Fast Interaction Trigger detector during the Long Shutdown of the LHC (2018-2021).

Abstract

Charmonium production has been widely recognized as an excellent probe for investigating the properties of hot and dense nuclear matter formed in ultrarelativistic nuclear collisions at the Relativistic Heavy Ion Collider (RHIC) and the Large Hadron Collider (LHC) within the framework of Quantum Chromodynamics (QCD). The measurements of directly produced J/ψ and those originated from feed-down of heavy charmonium states, prompt J/ψ, provide a direct comparison with models that include J/ψ production through regeneration, the dominant production mechanism at low transverse momentum ($p_{\rm T}$) and in central collisions at the LHC. This is crucial to understand the J/ψ production via regeneration mechanism. The measurements of J/ψ originating from the weak decay of b-hadrons, non-prompt J/ψ, provide an estimate of beauty quark production in nuclear collisions. Such measurements are important to investigate the beauty quark energy loss in the nuclear medium. The ALICE experiment has unique tracking and particle identification capabilities down to very low momentum at midrapidity ($|y| < 0.9$), enabling the J/ψ reconstruction down to $p_{\rm T} \sim 0$ and separation of prompt and non-prompt J/ψ down to $p_{\rm T} \sim 1.5$ GeV/c in Pb–Pb collisions.

This study utilizes the complete datasets from Pb–Pb collisions at center of mass energy, $\sqrt{s_{\rm NN}}$= 5.02 TeV, collected by the ALICE experiment during the LHC Run 2 program. The analysis is performed by reconstructing J/ψ meson at midrapidity in the dielectron decay channel. To separate the prompt and non-prompt J/ψ contributions, non-prompt J/ψ fraction ($f_{\rm B}$) is extracted by simultaneous unbinned fits on invariant mass and pseudoproper decay length of dielectron candidates in different $p_{\rm T}$ intervals in the range $1.5 < p_{\rm T} < 10$ GeV/c. Additionally, the analysis is performed in different centrality intervals, namely, 0-10%, 10–30%, and 30-50%. The fits rely on the templates obtained from Monte-Carlo simulation and data collected in the experiment. The fractions obtained from the fits are corrected for the detector's acceptance and reconstruction efficiency. Similarly, non-prompt J/ψ fractions in pp collisions are obtained by interpolating available non-prompt J/ψ measurements at midrapidity in the same $p_{\rm T}$ intervals as in Pb–Pb collisions. The production yields of prompt and non-prompt J/ψ are determined by scaling inclusive J/ψ $R_{\rm AA}$ by the ratio of $f_{\rm B}$ in Pb–Pb to $f_{\rm B}$ in pp collisions in the same $p_{\rm T}$ and centrality intervals. Systematic uncertainties in $f_{\rm B}$ measurements in Pb–Pb collisions due to possible sources are estimated and propagated to the measurements of yields of prompt and non-prompt J/ψ.

The prompt and non-prompt J/ψ production is modified in nuclear collisions in comparison to binary nucleon-nucleon collisions at the same collision energy due to various nuclear effects. Such modifications can be quantified by measurements of nuclear modification factors ($R_{\rm AA}$). The nuclear modification factors of prompt and non-prompt J/ψ are measured as a function of $p_{\rm T}$ in Pb–Pb collisions at $\sqrt{s_{\rm NN}}$= 5.02 TeV across aforementioned centrality intervals. The systematic uncertainties obtained in the $f_{\rm B}$ measurements are propagated to the measurements of the $R_{\rm AA}$. The final results are compared with the previous measurements performed by the ALICE experiment at lower collision energy $\sqrt{s_{\rm NN}}$= 2.76 TeV. Notably, the presented new results are more precise in terms of $p_{\rm T}$ and centrality intervals compared to results at lower collision energy. The results are further compared with similar measurements at high $p_{\rm T}$ by the CMS and ATLAS experiments. The measurements presented in this study complement the existing results obtained at high $p_{\rm T}$ by extending the analysis to lower $p_{\rm T}$ values. The state-of-the-art theoretical model calculations that include several medium effects for charm and beauty quarks depending on $p_{\rm T}$ are adopted to compare with the production yields and $R_{\rm AA}$ of both prompt and non-prompt J/ψ. An extension to these studies is also presented, where the future plans of ALICE experiment for such measurements are briefly discussed.

Streszczenie

Produkcja czarmonium jest powszechnie uważana za znakomity próbnik w badaniu własności gorącej i gęstej materii jądrowej produkowanej w zderzeniach jądrowych przy pomocy Relativistic Heavy Ion Collider (RHIC) i Large Hadron Collider (LHC) w ramach chromodynamiki kwantowej (QCD). Pomiary produkcji J/ψ bezpośrednio w zderzeniach oraz z rozpadów cięższych stanów czarmonium, natychmiastowe J/ψ, pozwalają na porównanie do modeli produkcji J/ψ uwzględniających regenerację, która jest dominującym mechanizmem produkcji J/ψ przy małych pędach poprzecznych (p_{T}) w centralnych zderzeniach ciężkich jonów. Pomiary te mają kluczowe znaczenie w zrozumieniu mechanizmu produkcji J/ψ poprzez regenerację. Pomiar produkcji J/ψ pochodzącej z rozpadów słabych b-hadronów, opóźnione J/ψ, dostarczają informacji o produkcji kwarków pięknych w zderzeniach jądrowych. Takie pomiary są ważne w badaniu zjawiska straty energii kwarków pięknych w materii jądrowej. Eksperyment ALICE ma unikatowe możliwości pomiaru trajektorii cząstek i ich identyfikacji przy niskich pędach w centralnym zakresie pospieszności ($|y| < 0.9$), pozwalające na pomiar J/ψ przy pędach $p_{\mathrm{T}} \sim 0$ oraz separację produkcji natychmiastowych i opóźnionych J/ψ począwszy od $p_{\mathrm{T}} \sim 1.5$ GeV/c w zderzeniach Pb–Pb.

Badania przedstawione w tej rozprawie wykorzystują dane ze zderzeń Pb–Pb przy energii w centrum masy na parę nukleonów $\sqrt{s_{\mathrm{NN}}}$= 5 TeV, zebrane przez kolaborację ALICE podczas LHC Run 2. Analiza polega na rekonstrukcji J/ψ w centralnym obszarze pospieszności w dielektronowym kanale rozpadu. Aby odseparować natychmiastowe od opóźnionych J/ψ, frakcja opóźnionych J/ψ (f_{B}) jest wyznaczona wykorzystując dopasowanie funkcji jednocześnie do masy niezmienniczej i pseudowłaściwej długości rozpadu J/ψ, w różnych przedziałach p_{T} w zakresie $1.5 < p_{\mathrm{T}} < 10$ GeV/c. Dodatkowo, analiza jest przeprowadzona w różnych przedziałach centralności zderzeń Pb–Pb: 0-10%, 10-30% i 30-50%. To dopasowanie bazuje na szablonach otrzymanych z symulacji Monte-Carlo i danych eksperymentalnych. Frakcje otrzymane z dopasowania są poprawione na efekty związane z geometrią detektora i wydajnością rekonstrukcji. Frakcje opóźnionych J/ψ w zderzeniach pp wyznaczone są wykorzystując interpolację pomiędzy zmierzonymi wcześniej rozkładami opóźnionych J/ψ w centralnym przedziale pospieszności, w tych samych przedziałach pędowych jak w przypadku zderzeń Pb–Pb. Rozkłady produkowanych natychmiastowych i opóźnionych J/ψ, wyznaczone są poprzez przeskalowanie inkluzywnych rozkładów J/ψ R_{AA} przez stosunek f_{B} w zderzeniach Pb-Pb do f_{B} w zderzeniach pp, w tych samych przedziałach p_{T} i

centralności. Błędy systematyczne pomiarów f_{B} w zderzeniach Pb–Pb zostały wyznaczone biorąc pod uwagę wkłady z różnych źródeł i są uwzględnione w rozkładach natychmiastowych i opóźnionych J/ψ. Rozkłady produkcji natychmiastowych i opóźnionych J/ψ w zderzeniach jądrowych są zmodyfikowane w porównaniu do tych z binarnych zderzeń nukleon-nukleon przy tej samej energii zderzeń z powodu różnych efektów jądrowych. Takie modyfikacje można opisać ilościowo poprzez pomiar współczynników modyfikacji jądrowej (R_{AA}). Współczynniki modyfikacji jądrowej dla natychmiastowych i opóźnionych J/ψ są zmierzone w zderzeniach Pb–Pb przy energii $\sqrt{s_{\mathrm{NN}}}$= 5 TeV w funkcji p_T i przedziałach centralności wspomnianych powyżej. Błędy systematyczne wyznaczone dla f_{B} są uwzględnione w zmierzonych rozkładach R_{AA}.

Końcowe wyniki są porównane z poprzednimi pomiarami wykonanymi przez eksperyment ALICE przy niższej energii zderzeń $\sqrt{s_{\mathrm{NN}}}$= 2.76 TeV. Należy zauważyć, że otrzymane nowe wyniki są znacznie dokładniejsze od tych przy niższej energii biorąc pod uwagę ilość przedziałów pędowych i centralności. Otrzymane wyniki są również porównane do podobnych pomiarów przy wysokich pędach wykonanych przez eksperymenty CMS i ATLAS. Prezentowane wyniki uzupełniają te otrzymane przy wysokich pędach rozszerzając zakres pędowy w stronę niskich p_{T}. Wyniki najnowszych obliczeń teoretycznych opisujące produkcję J/ψ z uwzględnieniem różnych efektów w medium dla kwarków powabnych i pięknych w zależności od p_{T}, użyte są do porównania ze zmierzonymi rozkładami i R_{AA} dla natychmiastowych i opóźnionych J/ψ. Rozszerzenie tych badań jest również prezentowane, gdzie plany przyszłych pomiarów eksperymentu ALICE są w skrócie dyskutowane.

Contents

List of Figures

List of Tables

Chapter 1

Introduction

"A physical understanding is a completely unmathematical, imprecise, and inexact thing, but absolutely necessary for a physicist."

Feynman Lectures, Vol 2

Strong interaction, being one of the fundamental forces of nature, plays a vital role in the stability and structure of matter. The strong interaction is governed by a gauge theory called quantum chromodynamics (QCD), which describes the behavior of quarks and gluons and their interactions [1]. Understanding the effective interaction between sub-nuclear particles containing different quark compositions stands as a crucial challenge in contemporary nuclear physics, requiring a comprehensive grasp of fundamental principles. Despite significant advancements made in various aspects, there are still a number of persistent challenges that demand attention in order to advance the field further [2].

1.1 Quantum Chromodynamics

Quantum chromodynamics provides a theoretical description of the strong interaction, which are the fundamental interactions between quarks and gluons. There is a total of six quarks found in Nature as listed in Table 1.1. Hadrons are the composite particles of quarks and antiquarks that are bound together through the exchange of gluons. They can be further categorized into two distinct groups, namely mesons, and baryons, which are determined by their specific quark compositions.

The features of the QCD can be understood by probing the interaction strength between quarks as a function of separation between them. As the distance between quarks decreases, the coupling strength between them, denoted by α_s becomes weak according to Eq. 1.1. In the limit where the distance approaches zero, α_s reaches zero as well. This phenomenon in QCD is known as asymptotic freedom, where quarks, at short distances or large momentum scales,

Quark	Mass (MeV/c^2)	Electric charge (e)	Baryon number
Up (u)	$2.3 + 0.7 - 0.5$	$+2/3$	$1/3$
Down (d)	$4.8 + 0.5 - 0.3$	$-1/3$	$1/3$
Strange (s)	95 ± 5	$-1/3$	$1/3$
Charm (c)	1275 ± 25	$+2/3$	$1/3$
Bottom (b)	4180 ± 30	$-1/3$	$1/3$
Top (t)	173210 ± 510	$+2/3$	$1/3$

Table 1.1 Quarks with their mass, electric charge, and baryon number [3].

behave as if they were almost free. In contrast, the strength of their interaction intensifies with the increasing distance between quarks resulting in another important phenomenon called color confinement. The confinement prevents quarks from being separated and forces them to remain bound together, making their isolation impossible.

Asymptotic freedom enables the application of perturbative techniques to solve problems involving large momentum transfer or short distance processes. In such cases, the cross section for these processes can be expanded in terms of the α_s [4, 5]. Since the coupling strength is small therefore only a limited number of terms make significant contributions to the cross section. The asymptotic freedom is described by the running coupling constant $\alpha_s(Q^2)$, which decreases logarithmically with increasing energy scale Q^2:

$$\alpha_s(Q^2) = \frac{12\pi}{(11N_c - 2N_f)\ln(Q^2/\Lambda^2_{\mathrm{QCD}})}, \tag{1.1}$$

$N_c = 3$ represents the number of colors. The QCD scale parameter, denoted as Λ_{QCD}, sets the characteristic energy scale of strong interactions. It is characterized as the minimum momentum scale, ranges 100-300 MeV, below which the application of QCD becomes inappropriate. In Eq. 1.1, if N_f is less than 17, α_s gradually diminishes towards zero as Q rises towards infinity. This behavior indicates that QCD exhibits asymptotic freedom in such cases. Furthermore, Eq. 1.1 shows the coupling constant experiences a divergence towards infinity at low momentum scales (low Q) or large distances. This is the energy range where perturbative expansions in α_s lose their significance and reliability [6]. Consequently, energy scales below approximately 1 GeV are considered part of the non-perturbative regime, where the phenomenon of confinement becomes prominent [7]. The Fig. 1.1 demonstrates the behavior of α_s with energy scale for several QCD processes.

1.2 Phase Diagram of QCD Matter

The QCD phase diagram, as shown in Fig. 1.2 (left), is a representation of the various phases that nuclear matter can undergo based on the temperature (T) and baryon chemical potential (μ_{B}). According to the standard definition, the baryon chemical potential corresponds to the energy required to raise the baryon number by a single unit while keeping the

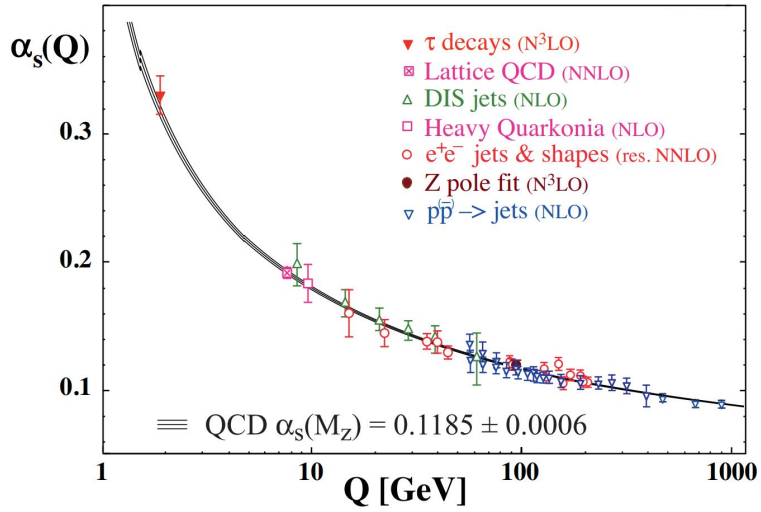

Figure 1.1 α_s as a function of energy scale Q for different processes with order of perturbation in brackets [3].

volume and entropy of the system constant, and it is directly linked to net baryon density of the system. In the horizontal axis of Fig. 1.2 (left), the value of μ_{B} grows from less dense to highly dense baryonic matter. The hadron colliders e.g. the Large Hadron Collider, produce an extremely hot phase of matter with zero low baryon density supposed to be present in the earlier stages of the universe [8–10]. The key aspects of the QCD phase diagram are briefly described below.

Hadronic phase

In the low T and low μ_{B} regime of the QCD phase diagram, the phase of nuclear matter is known as the hadronic phase. In this phase, quarks are confined within color-neutral hadrons, such as protons and neutrons. The strong interactions between quarks and gluons bind them together, forming stable bound states.

Quark–Gluon plasma phase

With increasing T and/or μ_{B} , the strong interactions between quarks weaken, and the nuclear matter undergoes a phase transition. A crossover transition from the hadrons to free partons has been observed at $T_c \simeq 155$ MeV, $\mu_{\mathrm{B}} = 0$ [11–13]. Such smooth transition allows the coexistence of both deconfined and confined hadronic matter. The deconfined phase of nuclear matter is known as the quark–gluon plasma (QGP). The deconfinement temperature T_c is marked by a notable rise in the energy density, ε, normalized to the fourth power of temperature as shown in Fig. 1.2 (right) [13], pressure and entropy densities are also shown. Such behavior is consistent with the Stefan-Boltzmann law, and the increased energy density suggests the emergence of numerous additional degrees of freedom during

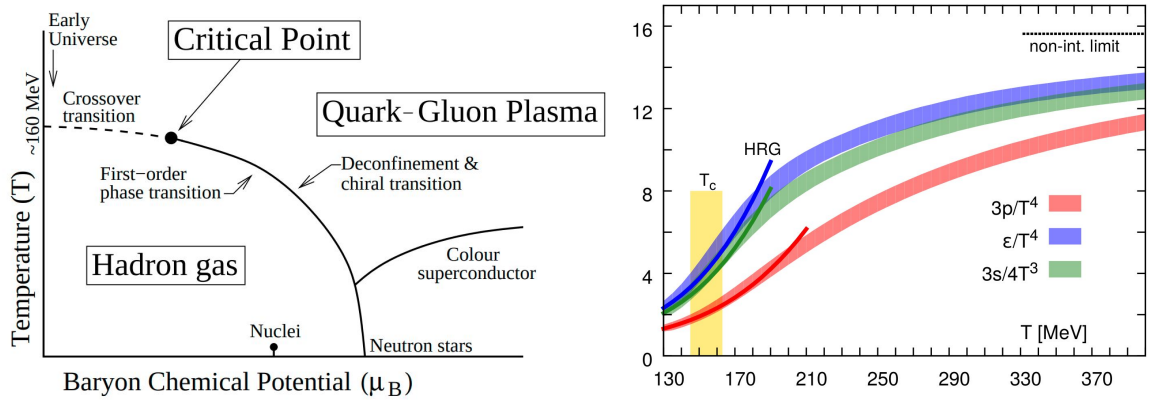

Figure 1.2 Left: Phase diagram of the QCD matter, taken from [24]. Right: Pressure, energy density, and entropy density normalized to the temperature from the Lattice QCD calculations [13].

the phase transition. The right panel in Fig. 1.2 suggests that the energy density increases with temperature and reaches closer and closer to the energy density corresponding to the non-interacting ideal gas as $T \to \infty$. It is consistent with the scenario at the large energy density; the interaction between the quarks becomes weaker, $i.e.$, asymptotic freedom. Below the ideal gas limit, the QGP behaves as a strongly interacting system of quarks and gluons and exhibits the properties of an almost perfect liquid [14, 15].

It is widely excepted that the QGP phase exists in the extremely high baryon density conditions. The core of massive stable neutron stars exhibits distinct features that indicate the presence of the deconfined phase in the matter [16].

Chiral Symmetry restoration

Spontaneous breaking of chiral symmetry is a notable aspect of strong interactions in the non-perturbative regime [17, 18]. This phenomenon contributes significantly to the mass of hadrons. Theoretical approaches, such as Lattice QCD [19, 20] and Effective Field Theories [21, 22], offer viable means to describe and analyze the non-perturbative regime of strong interactions. The QCD phase diagram also encompasses the restoration of chiral symmetry as an essential aspect. At high temperatures or densities, there are indications of the restoration of chiral symmetry [10, 13, 23].

Critical point

In Fig. 1.2 (left), as we move towards the higher values of μ_{B} starting from a particular non-zero μ_{B}, the nuclear matter undergoes a first-order phase transition from confined to deconfined nuclear matter. This transition causes an abrupt phase change, leading to a discontinuity in the thermodynamic variables. At the boundary between phases, distinct forms of matter are separated. Conversely, when μ_{B} is below this particular value, the

transition occurs smoothly through a crossover, as indicated by the dashed line in Fig. 1.2. This specific point in the phase diagram is the critical point, but its precise position is still unknown, and ongoing experimental research is dedicated to its discovery. A recent review discussing the current status of experimental searches for the critical point can be found in Ref. [25].

1.3 Ultrarelativistic nuclear collisions

To study the internal structure of nuclear matter and the strong interactions in extreme conditions, ultrarelativistic nuclear collisions serve as an efficient tool. By means of these collisions, it becomes possible to generate a phase of nuclear matter where quarks and gluons act as the fundamental degrees of freedom. The exploration of nuclear collision at very high energies is a deep and challenging topic. An illustration of the space-time evolution of ultrarelativistic nuclear collisions is shown in Fig. 1.3. Various stages of nuclear collisions are categorized at different time scales, according to [26]:

- At the time scale $\tau < 0$, two Lorentz-contracted disc shape nuclei with a diameter of 14 fm perpendicular to their motion and $14/\gamma$ fm along their motion approach each other, where γ is the Lorentz factor in the center of mass reference frame ranging 100-2500 for beam rapidity range 5.3-8.5 at the LHC [27]. Due to their relativistic motion, the nuclear matter possesses a large parton density inside the nuclei. At this point, the nuclear matter is consistent with a state of Color-Glass-Condensate [28].

- At the initial time point of $\tau = 0$, the nuclei come close, initiating the interactions between their constituent partons. Initially, there is a dominance of processes involving large momentum transfer ($Q^2 \gg 1$ GeV^2), which gives rise to the production of hard partons.

- The produced partons do not scatter away in the vacuum, but they start interacting with each other. These multiple interactions take the system to a local thermal equilibrium and produce a phase of matter consisting of quarks and gluons, the QGP. Thermal pressure in the system causes the fireball to undergo a collective expansion. The collective expansion of the fireball is modeled by fluid hydrodynamics, meaning that the QGP exhibits fluid-like behavior. The cooling of the fireball during the collective expansion causes a decrease in its energy density. Once the energy density drops to around 1 GeV/fm^3, the partons within the fireball hadronize to form color-neutral hadrons.

- Once the fireball undergoes hadronization, the resulting hadrons interact through rescattering processes. As the system evolves the inelastic interactions between hadrons stops after some time resulting no new particle production means the hadron yields are frozen, this stage is known as chemical freeze-out. Later, the elastic scatterings

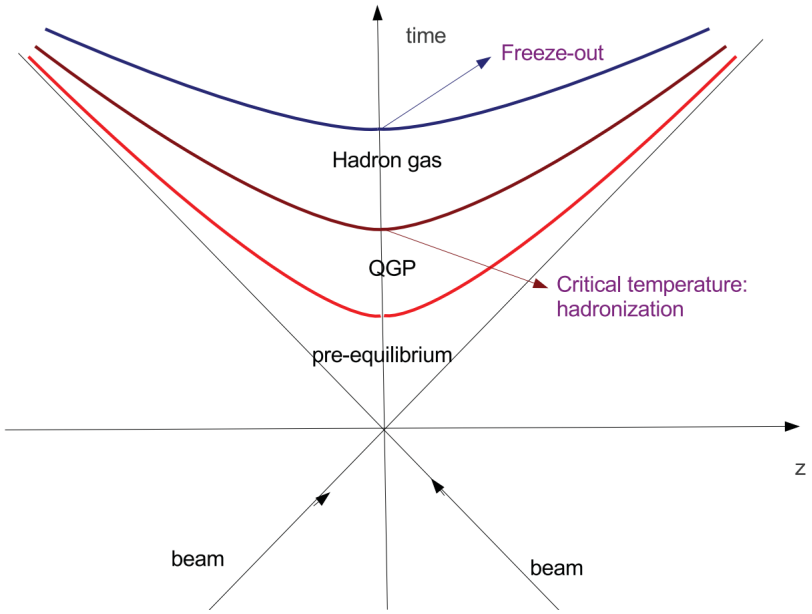

Figure 1.3 Space-time evolution of ultrarelativistic nuclear collisions, taken from [29].

between these hadrons also come to halt as system evolves further, known as kinetic freeze-out. After this stage the hadrons freely propagate to the detectors.

1.4 Experimental probes in the nuclear collisions

Different measurements in ultrarelativistic nuclear collisions allow us to obtain information about the different stages involved in nuclear collisions. Some of the key measurements are described in this section.

1.4.1 Charged particle multiplicity

Charged particle multiplicity is driven by the collision geometry; therefore, its measurement provides insight into initial parton densities and energy density produced in heavy ion collisions. Such measurements provide constraints on the underlying mechanisms of particle production in nuclear collisions. Collisions of nuclei can be categorized based on their centrality determined by the degree of overlap between the nuclei. Centrality is directly associated with the number of nucleons participating in the collision, $\langle N_{\rm part} \rangle$, and the later quantity can be determined by the Monte Carlo Glauber model [30]. The charged-particle pseudorapidity density normalized by the average number of participating nucleon pairs, $\frac{2}{\langle N_{\rm part} \rangle} \langle dN_{\rm ch}/d\eta \rangle$, is shown in Fig. 1.4 (left) as a function of $\langle N_{\rm part} \rangle$ in Pb–Pb collisions in comparison to pp and p–Pb collisions at $\sqrt{s_{\rm NN}} =$ 2.76 and 5.02 TeV, and the same is shown as a function of center-of-mass collision energy in the right panel. In the left panel of Fig. 1.4, the $\frac{2}{\langle N_{\rm part} \rangle} \langle dN_{\rm ch}/d\eta \rangle$ increases with the number of participating nucleons in the collisions. In

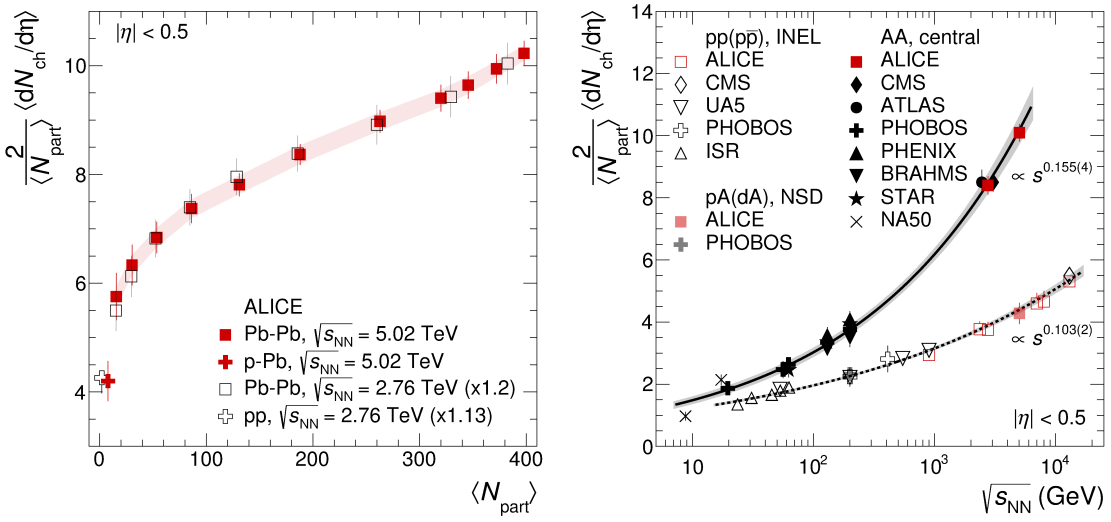

Figure 1.4 Left: $\frac{2}{\langle N_{\rm part}\rangle}\langle dN_{\rm ch}/d\eta\rangle$ as a function of $\langle N_{\rm part}\rangle$ in Pb–Pb collisions at $\sqrt{s_{\rm NN}}$= 5.02 TeV and 2.76 TeV in 0–80% centrality interval compared with results in pp and p–Pb collisions, Right: $\frac{2}{\langle N_{\rm part}\rangle}\langle dN_{\rm ch}/d\eta\rangle$ as a function of the center of mass energy in pp, pA and AA collisions [33].

comparison to the peripheral collisions, charged particle multiplicity is larger by a factor of 1.8 in most central collisions. The charged-particle multiplicity is influenced by the center of mass energy of the collision. It is consistently 1.2 times larger in Pb–Pb collisions at $\sqrt{s_{\rm NN}}$= 5.02 TeV than at $\sqrt{s_{\rm NN}}$= 2.76 TeV as a function of $\langle N_{\rm part}\rangle$. Moreover, the right panel of Fig. 1.4 indicates that the charged particle pseudorapidity density exhibits a positive correlation with the center of mass collision energy, both in Pb–Pb collisions and smaller collision systems. Interestingly, such dependence is characterized by the different power-law functions in pp/pA and AA collisions. The charged-particle pseudorapidity density measurements allow us to estimate the transverse energy density in the initial stages of the collisions. In 0–5% centrality interval, estimated transverse energy density is larger than 12.3 $\pm$ 1 GeV/fm^3 in Pb–Pb collisions at $\sqrt{s_{\rm NN}}$= 2.76 TeV, while assuming the system forms at 1 fm/c whereas, in the core, it reaches more than 21 $\pm$ 2 GeV/fm^3 [31]. It is also estimated that the transverse energy density in 0-5% central Pb–Pb collisions at $\sqrt{s_{\rm NN}}$= 2.76 TeV is approximately 2.3 times larger as compared to Au–Au collisions at $\sqrt{s_{\rm NN}}$= 200 GeV [32].

1.4.2 Collective flow

Measurements of anisotropic and radial flow offer an opportunity to study the dynamical properties of the QGP. Anisotropic flow measurements at RHIC [34–37] had confirmed that the QGP exhibits behavior that is consistent with a nearly perfect fluid. A quantitative analysis of transverse momentum ($p_{\rm T}$) spectra and azimuthal distributions of light hadrons yields a remarkably low value of shear viscosity to entropy density ratio, η/s, ranging from

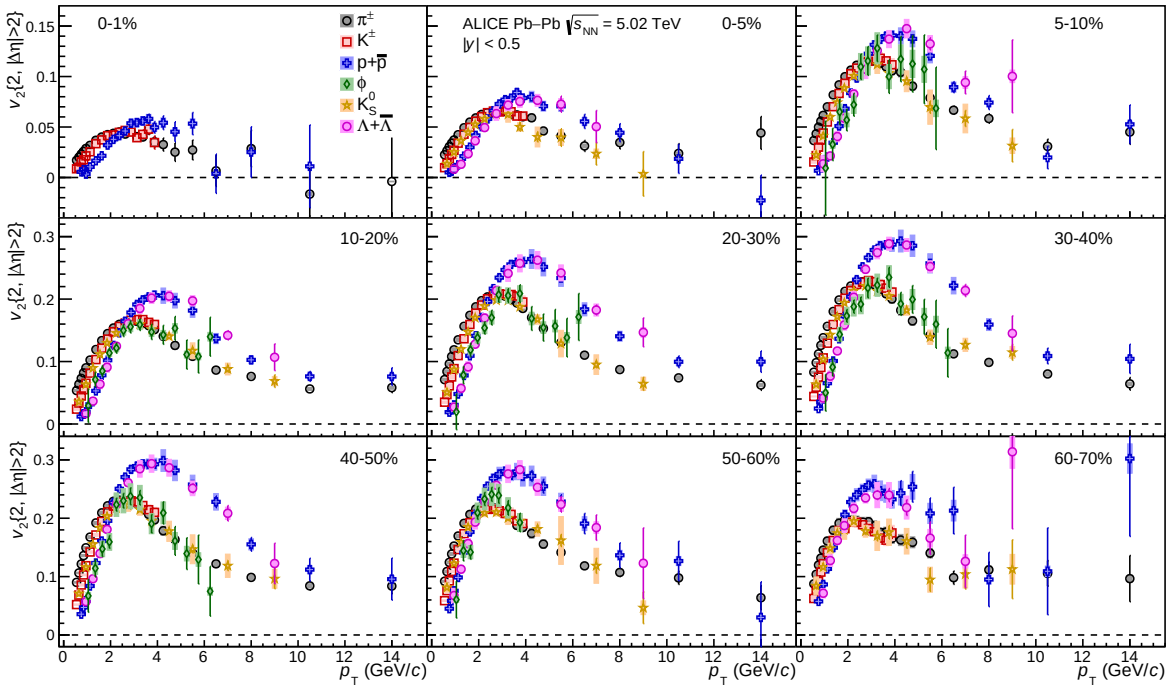

Figure 1.5 v_2 of $\pi^{\pm}, K^{\pm}, p+\bar{p}, \Lambda+\bar{\Lambda}, K^s_0$ and ϕ meson for various centrality classes in Pb–Pb collisions at $\sqrt{s_{\rm NN}}$= 5.02 TeV [41].

approximately 0.1 to 0.3 [38, 39]. The extracted values are very close to the lower bound, $1/4\pi$, predicted by the AdS/CFT theory [34–37, 40].

In the non-central Pb–Pb collisions, the nuclear overlap region is spherically asymmetric, leading to a spatial anisotropy in the nuclear matter distribution. The spatial anisotropy gives rise to a corresponding momentum anisotropy in the azimuthal plane. Fourier expansion of the produced particle azimuthal distribution with respect to the reaction plane quantifies the magnitude of azimuthal anisotropy and can be written as,

$$\frac{\mathrm{d}N}{\mathrm{d}\phi} \propto 1 + 2\sum_{\mathrm{n}=1}^{\infty} v_{\mathrm{n}}\cos[\mathrm{n}(\phi - \psi_{\mathrm{n}})]. \tag{1.2}$$

The reaction plane is defined by the impact parameter vector and beam direction, and ψ_n is the reaction plane angle in Eq. 1.2, v_n are n$^{\rm th}$ order harmonic coefficients, ϕ is the azimuthal angle of the track. The second-order harmonic coefficient v_2, known as elliptic flow, is the largest contribution to the asymmetry observed in non-central collisions. This contribution arises from the ellipsoidal geometry of the overlap region between the colliding nuclei, particularly in the plane perpendicular to the beam direction. The magnitude of v_2 is higher for non-central collisions than the most central ones, which indicates the production of a more spatially anisotropic system in non-central collisions than most central collisions.

The Fig. 1.5 demonstrates the ALICE results on $p_{\rm T}$-differential v_2 measurements for $\pi^{\pm}, K^{\pm}, p+\bar{p}, \Lambda+\bar{\Lambda}, K^s_0$ and ϕ meson in different centrality intervals. Low $p_{\rm T}$ hadrons

demonstrate the azimuthal anisotropy originating from the initial spatial anisotropy that translates into momentum anisotropies due to the pressure gradient. The pressure gradient is a consequence of the almond shape nuclear overlap region in the collision and the subsequent collective interactions among partons. It is described by the hydrodynamical evolution of the system, especially in p_{T} smaller than 2 GeV/c [15, 42]. It has been observed that hadrons with the same number of constituent quarks demonstrate the same magnitude of anisotropic flow at $2 < p_{\mathrm{T}} < 4$ GeV/c , which is consistent with the quark recombination or coalescence process [43–45].

This phenomenon occurs during the early stages of the collision, where collective flow develops. It indicates that the underlying degrees of freedom responsible for this flow are quarks rather than hadrons. [46]. While at higher $p_{\mathrm{T}} > 8$ GeV/c , other processes e.g. jet quenching (described in Sec. 1.4.4), start to contribute to azimuthal anisotropy and such measurements help to understand path-length dependence of energy loss in medium [47–49].

1.4.3 Heavy flavor production

Since the mass of heavy flavor quarks, beauty, and charm are larger than the Λ_{QCD} limit, therefore, their production cross sections can be determined within pQCD [50]. Also, their masses are sufficiently larger than the estimated temperature of QGP; therefore, thermal production of heavy quarks is rarely possible. The formation timescale for heavy quarks is approximated to $t \sim 1/m_Q \sim 0.1$ fm/c while the QGP lifetime is 1-10 fm/c. Heavy quarks are predominantly produced in the earlier stages of collision as a result of hard parton scatterings. It allows them to experience the evolution of the collision, including the interactions with the QGP medium, and lose their energies via different processes depending on momentum. Heavy quark thermalization time window spans beyond the QGP lifetime. Hence, they partially thermalize within the QGP medium [51, 52]. In the later stages, heavy quarks hadronize into different heavy-flavor hadrons, which can then be detected and reconstructed in the experiment. The induced modifications by the surrounding medium on the kinematic characteristics of heavy quarks are manifested in the kinematics of hadrons. Therefore, heavy flavor measurements offer an opportunity to quantify those heavy quark energy loss effects within the QGP. The nuclear modification factor (R_{AA}) can quantify such nuclear matter effects, defined as a ratio of particle production in A–A collisions to particle production in pp collisions scaled by binary nucleon-nucleon collisions,

$$R_{\mathrm{AA}}(y, p_{\mathrm{T}}) = \frac{1}{\langle T_{\mathrm{AA}} \rangle} \frac{\mathrm{d}^2 N_{\mathrm{AA}}/\mathrm{d}y\mathrm{d}p_{\mathrm{T}}}{\mathrm{d}^2 \sigma_{\mathrm{pp}}/\mathrm{d}y\mathrm{d}p_{\mathrm{T}}}, \tag{1.3}$$

where $\mathrm{d}^2\sigma_{\mathrm{pp}}/\mathrm{d}y\mathrm{d}p_{\mathrm{T}}$ is double differential cross section in pp, $\mathrm{d}^2 N_{\mathrm{AA}}/\mathrm{d}y\mathrm{d}p_{\mathrm{T}}$ is double-differential yield in Pb–Pb and $\langle T_{\mathrm{AA}} \rangle$ is the average nuclear overlap function proportional to binary nucleon–nucleon collisions. $\langle T_{\mathrm{AA}} \rangle$ is determined by MC Glauber model simulations as described in Sec. 3.6.

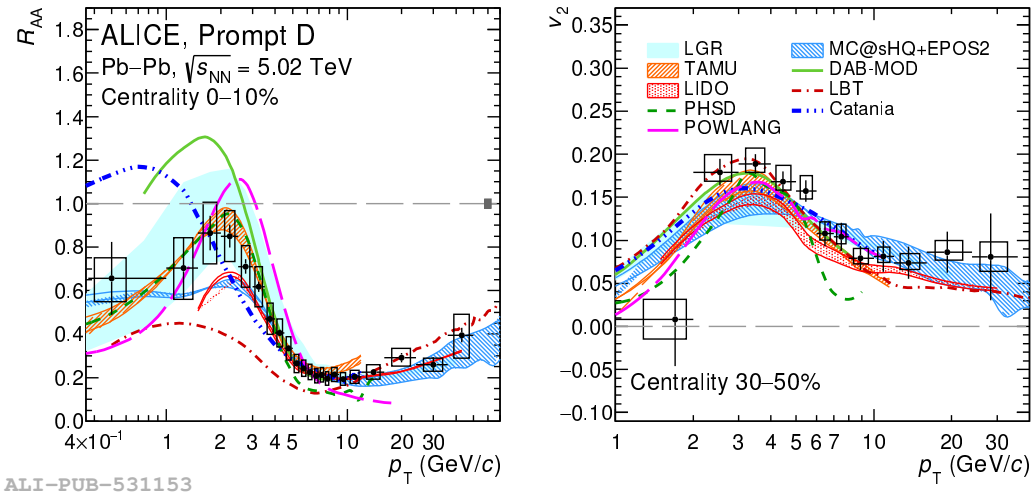

Figure 1.6 R_{AA} (left) [57] and v_2 (right) [53] of prompt D meson in 0–10% and 30–50% centrality intervals, respectively.

The measurements of nuclear modification factors allow probing the energy loss mechanism of heavy quarks within the medium via elastic or collisional mechanism dominant at low p_{T} and inelastic processes or radiative mechanism at high p_{T}.

Beauty and charm anisotropic flow measurements also help to access the mass-dependent energy loss of heavy quarks within the medium, which helps determine the transport coefficient of this medium. The Fig. 1.6 shows p_{T}-differential measurements for D-meson R_{AA} (left) and v_2 (right) in Pb–Pb collisions in 0–10% centrality interval, also compared to theoretical predictions including the charm quark transport mechanism in a hydrodynamically evolving hot medium [53]. The models incorporate charm quark hadronization via coalescence and fragmentation at high p_{T}.

In the momentum range $p_{\mathrm{T}} < 4$ GeV/c , R_{AA} is significantly larger compared to R_{AA} at high p_{T}. This observation manifests a larger suppression in prompt D production at high p_{T} where charm quarks experience radiative energy loss within the medium. At low p_{T}, heavy quarks are subjected to soft collisions with QGP constituents *i.e.* , which is characterized by Brownian motion within the medium [51, 52]. Heavy quarks may gain some collective flow due to such multiple interactions. Therefore, measurements of anisotropic flow at low p_{T} allow quantifying the degree of their participation in collective motion. While at p_{T} up to 10 GeV/c, such measurements can shed light on the hadronization of heavy flavor quarks via the recombination mechanism [54, 55]. Also, at higher p_{T} (> 10 GeV/c), flow measurements allow probing the path-dependent energy loss mechanism for heavy quarks.

A comprehensive review of heavy flavor production in ultrarelativistic nuclear collisions is provided in Ref. [56].

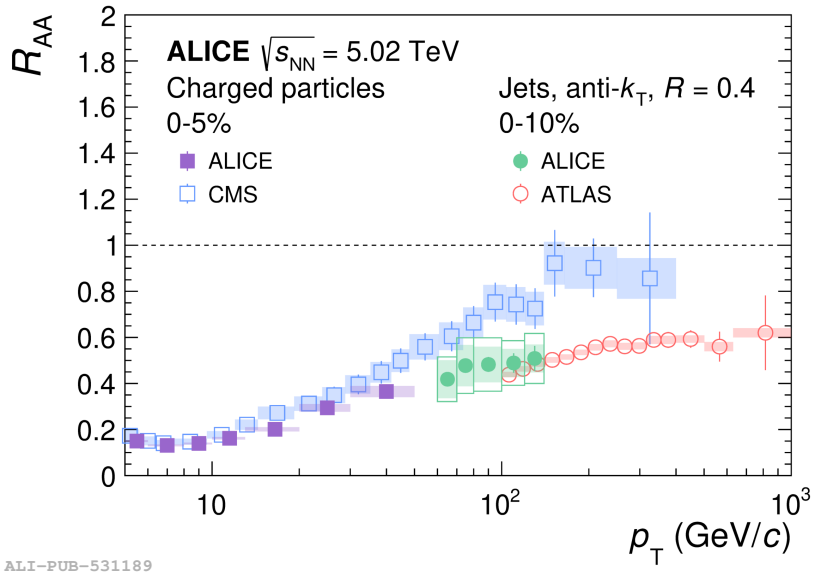

Figure 1.7 R_{AA} of jets and charged hadrons as a function of p_{T} in Pb–Pb collisions at $\sqrt{s_{\mathrm{NN}}}$= 5.02 TeV [62].

1.4.4 Jet production

Jets are produced as parton showers that emerge as a result of hard parton scatterings in high-energy collisions. The partons, generated within 1 fm/c after the collision, undergo showering and evolve into a cascade of particles. Partons with momenta up to a few GeV/c travel through the surrounding medium and lose their energy via gluon radiation [58]. This phenomenon, known as jet quenching, leads to modifications in the characteristics of the jet shower. These phenomena encompass high momentum transfers and are described within the framework of pQCD [59]. Experimentally, the parton energy loss within the QGP is quantified by nuclear modification factors. Also, jet substructure measurements suggest that partons near the jet axis possess larger momentum than those situated on larger angles. Numerous experimental measurements have quantified the jet quenching effects in nuclear collisions [60]. Despite extensive theoretical [61] and experimental [60] explorations, the interactions between the constituents of a jet and the surrounding medium remain incompletely comprehended. In Fig. 1.7, the R_{AA} is presented for inclusive jets along with charged hadrons in the central Pb–Pb collisions at $\sqrt{s_{\mathrm{NN}}}$= 5.02 TeV [62].

1.4.5 Direct photons production

Temperature plays an essential role in characterizing any thermodynamic system at a given time during its evolution. Direct photon measurements allow us to determine the temperature of the medium produced in the heavy-ion collisions. Throughout the evolution of the system, various sources produce electromagnetic radiation in the form of direct or virtual photons that decay into dilepton pairs and are not affected by the strong interaction in

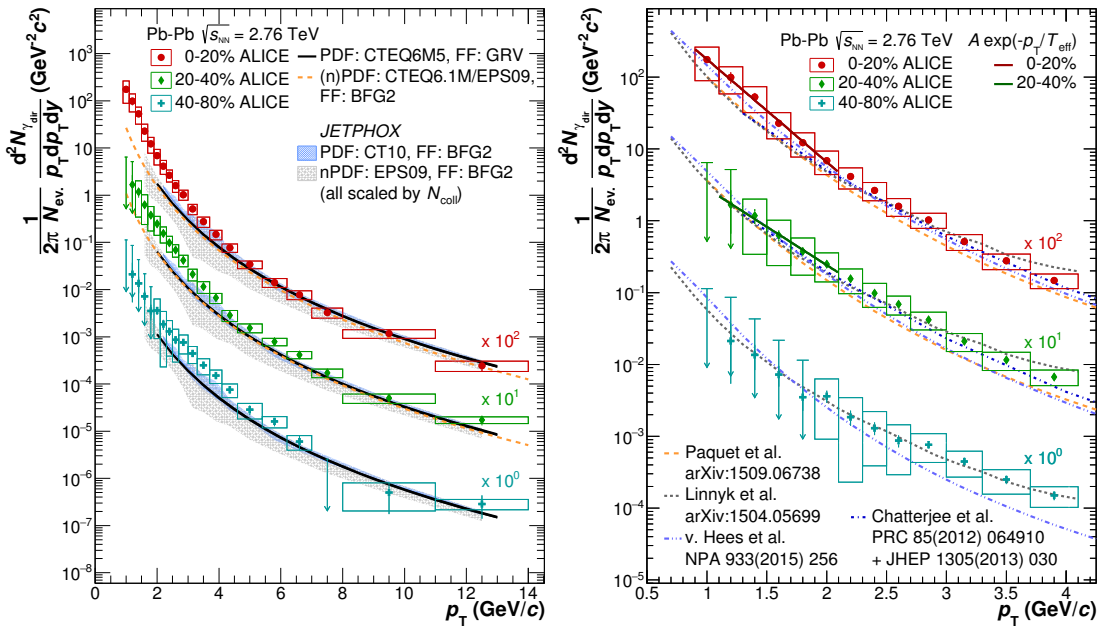

Figure 1.8 Left: p_{T}-differential direct photon spectra in Pb–Pb collisions at $\sqrt{s_{\mathrm{NN}}} = 2.76$ TeV in different centrality classes compared to predictions from different models, Right: parameterized p_{T}-differential spectra in low p_{T} region [66].

the created medium. Thermal photons are emitted by the medium produced in the collisions, which allows one to determine the temperature of the system; in contrast, prompt photons are produced during the hard parton scattering in the initial stage of collisions, carrying the information about the nuclear parton distribution functions [63]. Different processes dominate the direct photon transverse momentum spectrum and allow one to access the different stages of collisions. Thermal photons dominate the low transverse momentum region *i.e.* smaller than 4 GeV/c while prompt photons contribute in the region where p_{T} is larger than 5 GeV/c [64, 65]. In the ALICE measurements, shown in Fig. 1.8 (left), a significant surplus of direct photons at p_{T} smaller than 4 GeV/c as compared to the predicted values from pQCD photon calculations is observed, particularly in the most central and semicentral collisions. The medium temperature can be extracted by parameterizing this excess production of direct photons at low p_{T} by a function, $\propto \exp(-p_{\mathrm{T}}/T_{\mathrm{eff}})$, where T_{eff}, inverse slope parameter represents the average effective temperature of the medium. This parameterization is shown in Fig. 1.8 (right), and the extracted temperature from the inverse slope parameter is $T_{\mathrm{eff}} \simeq 297 \pm 43$ MeV in 0–20% centrality interval in Pb–Pb collisions [66].

Chapter 2

J/ψ production in hadronic collisions

"Reward of research is the joy of creation."

P.L. Bhatnagar

This chapter provides an overview of J/ψ production in the hadronic collisions. In the beginning, a brief history of J/ψ, e.g., discovery and charmonium spectrum, is given as a short introduction. It is followed by a discussion on inclusive J/ψ production in hadronic collisions where different contributions to J/ψ yield are addressed. In the later sections, a specific description of J/ψ production in different collision systems is discussed related to J/ψ production mechanism and recent measurements at the Large Hadron Collider. The last section provides a description of exclusive J/ψ production in ultraperipheral nuclear collisions.

2.1 Charmonium

Bound states of a heavy quark (c or b) and its anti-quark ($\bar{c}$ or $\bar{b}$) are known as charmonium and bottomonium, inclusively called quarkonium.

2.1.1 Discovery of J/ψ

In 1968, L.M. Lederman and his research group studied $p + \text{Nucleus} \rightarrow \mu^+ + \mu^-$ reaction in the Dimuon experiment at Brookhaven National Laboratory (BNL). They measured the cross section of dimuon events where a suspicious hump was observed in the invariant mass distribution, specifically around the value of 3.5 GeV/c^2. These results were published in 1970 [67]. They could not further resolve the structure with their limited experimental resolution. These results motivated experimental physicists to probe further in this direction. The observed hump in the dimuon mass spectrum is later named as *Lederman's shoulder*.

In November 1974, two independent research groups claimed to observe a heavy resonance in the dilepton invariant mass spectrum. This resonance was named "J" by the research

group led by Samuel Ting, working in Alternating Gradient Synchrotron (AGS) at BNL [68]. They studied invariant mass spectrum of e^+e^- pairs in $p + \text{Be} \rightarrow e^+ + e^- + \text{X}$ reaction at 30 GeV collision energy. The dielectron invariant mass spectrum is shown in the left panel of Fig. 2.1. Another group, led by B. Richter, measured the dilepton mass spectrum in $e^+e^- \rightarrow$ hadrons reaction at Stanford Positron Electron Asymmetric Ring (SPEAR) experiment at the Stanford Linear Accelerator Center (SLAC). They observed the same resonance and called it ψ [69] as shown in the right panel of Fig. 2.1. These discoveries added a new color to the incomplete picture of fundamental physics. Scholars named this important discovery as *November Revolution*, and the observed particle was named as J/ψ.

These discoveries raised questions about our understanding of nature. Especially the lifetime of J/ψ was the most puzzling problem. Heavy particle decays faster due to Heisenberg's uncertainty principle. However, the lifetime of J/ψ was exceptionally larger than its expected lifetime. The J/ψ is almost three times heavier than $\phi(s\bar{s})$, but still, it lives longer than ϕ. The scholars illustrated this by discovering an island where the average lifetime of humans is 70000 years instead of 70 years.

In this era, theorists had described the existence of three quarks (u, d, and s) in Nature, and efforts were going on towards a new theory with the next quark in the fleet, *i.e.* , the charm quark. The electroweak theory by Glashow, Weinberg, and Salam (GWS), was well-known for leptons and their interactions, but it fails for quarks. In 1964, Bjorken and Glashow hypothesized the fourth quark and added a new quantum number named *charm*, but there was no experimental evidence for charm hadrons by that time [70]. In 1970, Glashow-Iliopoulos-Maiani extended the GWS theory and proposed a model for weak interactions. They introduced a fourth quark field [71] along with three known quark fields. This model is known as *GIM mechanism*. It successfully explains the suppression of the neutral Kaon decay into muon pair. Later, based on GIM's assumption of the charm quark, J/ψ was recognized as a bound state of charm and anti-charm quark. In 1978, the Charmonium model was proposed, which assumes J/ψ state is similar to the positronium system [72]. It successfully described intrinsic properties of J/ψ , e.g., lifetime and spin. It also predicted other excited charmonium states later discovered in experiments.

2.1.2 Charmonium spectrum

Charmonium spectrum can be obtained by classifying charmonium states by their masses and their quantum properties, e.g., angular momentum, as shown in Fig. 2.2. Heavier charmonium states are placed higher on the vertical scale of mass, while on the horizontal scale, J^{PC} is the total angular momentum of the state with its charge (C) and parity (P). It is equivalent to a positronium system where para and ortho states are represented by η_c ($^1S_0$) and J/ψ ($^3S_1$), respectively. Like the positronium system, ortho state J/ψ decays into para state η_c by radiative decay. The heavier charmonium state $\psi(2s)$ decays into J/ψ by a radiative decay process as shown in Fig. 2.2.

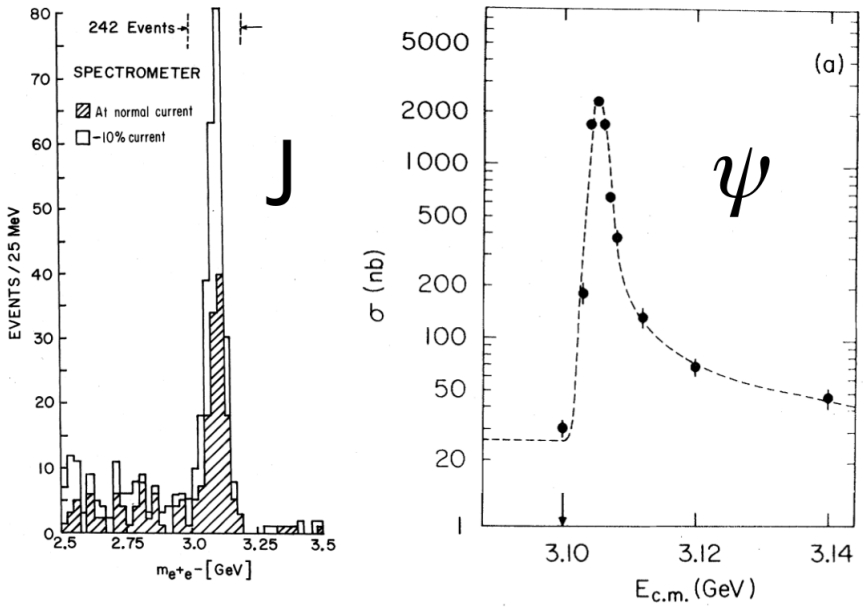

Figure 2.1 The invariant mass of J/ψ that was reconstructed using dilepton pairs as measured at AGS [68] and at SLAC [69].

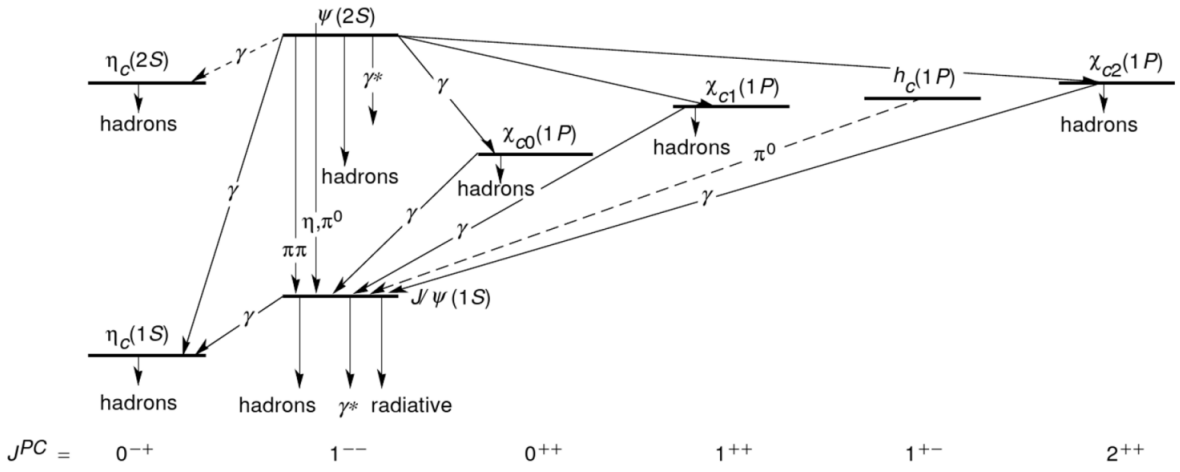

Figure 2.2 Illustration of charmonium states and their transitions [73].

The lifetimes of J/ψ (2270 fm/c) and η_c (15 fm/c) states are enormously different [74]. The J/ψ ($c\bar{c}$) meson and the $\phi(s\bar{s})$ meson share similarities in terms of their quark content. Hidden strange ϕ (1020 MeV/c^2) meson decays strongly into K^+ and K^-, open strange mesons. Such decay of J/ψ is forbidden due to decay kinematics as the mass of J/ψ is smaller than open charm meson pair, *i.e.* , D$\bar{\text{D}}$. Therefore, J/ψ can decay via a gluonic or a photonic interaction. In the first case, J/ψ can decay via strong interaction into three pions, as shown in the top of Fig. 2.3. This process is suppressed by the OZI (Okuba-Zweig-Iiluka) rule as the parton lines on the left side are not connected with those on the right side [75–77].

Therefore, J/ψ decays via electromagnetic interactions into dilepton pairs. Such constraints are responsible for a small decay width of 87 keV [78], consequently a larger lifetime of J/ψ. The branching fraction for J/$\psi \to \mu^+\mu^-$ is 5.93 $\pm$ 0.06%, and for J/$\psi \to e^+e^-$, 5.94 $\pm$ 0.06%. J/ψ is reconstructed through its decay daughters *i.e.* $\mu^+\mu^-$ and e^+e^-. Heavy charmonium states having larger mass than $D\bar{D}$ threshold decay into open charm hadrons, similar to ϕ, via strong interaction with a large decay width of 25 MeV as shown in the bottom of Fig. 2.3.

As discussed before, heavier charmonium states can decay into J/ψ. Therefore, there are more than one source of J/ψ production. J/ψ produced from different sources are reconstructed inclusively, and later these contributions can be separated in the offline physics analysis.

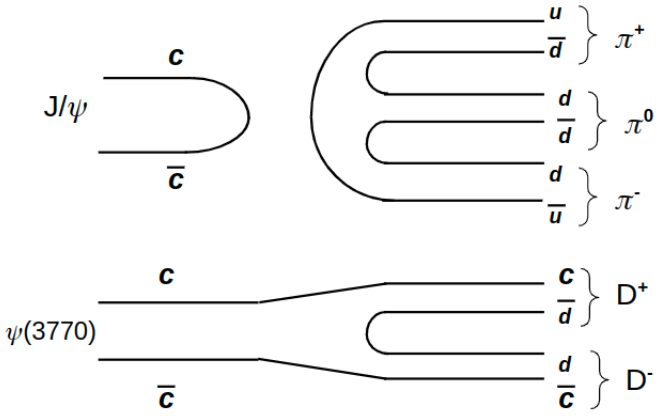

Figure 2.3 Illustration of J/ψ and $\psi(3770)$ decays via hadronic channel (strong interaction).

2.2 Inclusive J/ψ production

Inclusive production of J/ψ is referred to all J/ψ states produced in a final state irrespective of their production sources. Heavy quark-antiquark pairs, e.g., c$\bar{\text{c}}$, are produced in the hard parton-parton scatterings during the early stages of hadronic collisions. These quark-antiquark pairs evolve into charmonium states, e.g., J/ψ , known as direct production. Another production is via radiative decay of excited charmonium states, e.g., ψ(2s) and χ_c. The above mentioned two sources of J/ψ are known as prompt J/ψ production. The excited charmonium states have a significant contribution to prompt J/ψ production, e.g. χ_c contributes around 25% while $\psi(2s)$ contribution is estimated to be around 8%, as shown in the left of Fig. 2.4 [79, 80]. Prompt J/ψ production is dominated by gluon fusion and gluon fragmentation processes at LHC energies. Prompt J/ψ production mechanism is discussed by different theoretical models as described in Sec. 2.3 and Sec. 2.5.

An additional contribution to J/ψ production comes from weak decays of B hadrons (so-called feed down). B hadrons, containing at least one b or $\bar{\text{b}}$, e.g., B^0, B_s^0, $B^{\pm}$, decay into J/ψ as shown in Fig 2.4. The J/ψ produced via such processes is considered non-prompt J/ψ. Since the lifetime of B hadrons is relatively larger than prompt J/ψ, they travel a significantly

large distance (around $\sim 500\ \mu\mathrm{m}$) before decaying. Therefore, the B hadron decay vertex is displaced from the primary vertex. Consequently, a separation between prompt and non-prompt J/ψ is possible based on their characteristic decay length distributions. Non-prompt J/ψ production significantly contributes to the inclusive production depending on p_{T}. The non-prompt J/ψ contributes $\sim 10\%$ in the inclusive J/ψ production at low p_{T}, which rises up to 70% at high p_{T} in pp collisions. Non-prompt J/ψ fraction $f_{\mathrm{B}}(p_{\mathrm{T}})$ exhibits a weak dependence on the collision energies and rapidity [81].

Moreover, non-prompt J/ψ production is directly related to b-hadron production in the experiment. Therefore, measurement of non-prompt J/ψ allows access to the b quark production, which later fragments into a B-hadron. Production of non-prompt J/ψ can be described in three stages: production of b$\bar{\mathrm{b}}$ pair, fragmentation of b quark into B hadron, and decay of B hadron into J/ψ as described in the following equation,

$$\frac{d}{dp_{\mathrm{T}}}\sigma(\mathrm{b} \to \mathrm{B} \to \mathrm{J}/\psi) = \frac{d\sigma(\mathrm{b})}{dp_{\mathrm{T}}} \otimes f(\mathrm{b} \to \mathrm{B}) \otimes g(\mathrm{B} \to \mathrm{J}/\psi). \tag{2.1}$$

Beauty quarks are produced in hard scattering processes, and the cross section of such processes is perturbatively calculable. The FONLL calculations represent an approach to evaluate such perturbative cross sections [82]. The second stage is the fragmentation of produced b quark into B-hadron, a non-perturbative process determined by the experimental data. The determination of fragmentation function of b quark [83] is based on the experimental results at Tevatron [84–86]. The last part of Eq. 2.1 is extracted by the branching fraction of B hadrons into J/ψ.

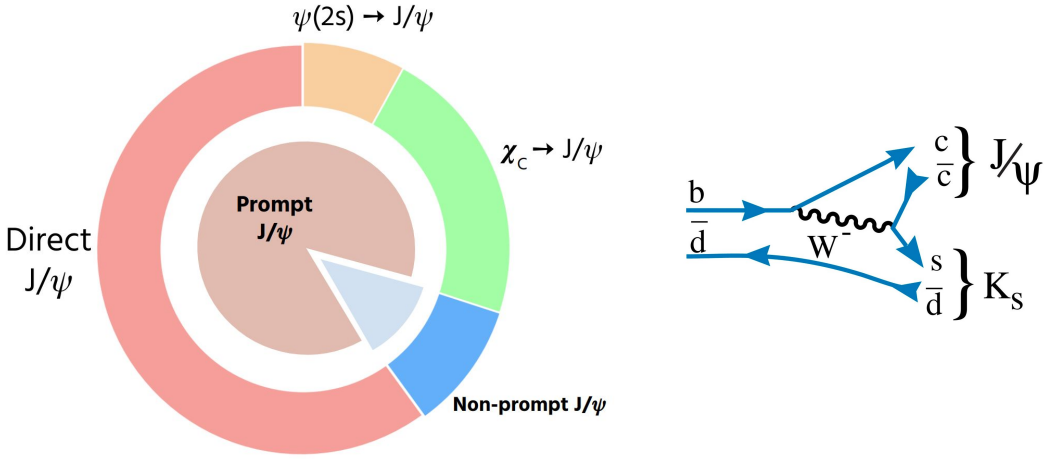

Figure 2.4 Various feed down contributions to inclusive J/ψ production (left). Feynman diagram representing weak decay of B hadron into J/ψ (right).

Since the discovery of J/ψ, it has been rigorously studied in several colliding systems at different collision energies. Despite of such efforts, J/ψ production is not entirely understood. To understand the J/ψ production, different observables, e.g., cross section, polarization, etc,

have been measured under different experimental conditions. Various theoretical approaches are adopted to describe J/ψ production mechanism in different hadronic collisions. These approaches and the recent measurements on J/ψ production in ultrarelativistic collisions are described in the following sections.

2.3 J/ψ production in pp collisions

Charm quark mass ($m_c \sim 1.3$ GeV/c^2) is larger than $\Lambda_{\rm QCD} \sim 200$ MeV/c [2], and they are produced in the scatterings of partons involving large momentum transfer (large Q^2). In this kinematic region, the strong coupling becomes weak, *i.e.*, the value of $\alpha_s \ll 1$. Therefore, the pQCD approach is applicable for describing such processes, allowing for the calculation of c$\bar{\rm c}$ production cross section. Later, with appropriate quantum properties, c and $\bar{\rm c}$ can combine to produce a charmonium state. The evolution of c and $\bar{\rm c}$ into a charmonium state is a soft process, *i.e.*, a process involving small momentum transfer (small Q^2), lies in the non-perturbative regime. Based on different assumptions, phenomenological models are proposed to describe the evolution of c$\bar{\rm c}$ pair into a charmonium state. Some of those are described below [87].

Color Singlet Model

Color Singlet Model (CSM) [88] is one the first models developed after J/ψ discovery. The underlying assumption is that the quantum properties of c and $\bar{\rm c}$, such as their spin angular momentum and color charge, remain unchanged throughout the entire transformation into a quarkonium state. The c$\bar{\rm c}$ pair is produced in a color-neutral or color-singlet state, the same as the final charmonium state. The CSM successfully describes charmonium production at relatively lower energies up to a few hundred GeV in hadronic and other collision systems [73, 87]. At the Tevatron energies, the CSM underestimates $\psi(2s)$ production cross section by larger than an order of magnitude, which is known as $\psi(2s)$ surplus puzzle [89].

Color Evaporation Model

In Color Evaporation Model (CEM) [90, 91] model, the production of c$\bar{\rm c}$ pairs occurs in the color octet state, and subsequently, these pairs emit a gluon to make a transition into a color neutral state. According to this model, a c$\bar{\rm c}$ pair can evolve into a given charmonium state only if the invariant mass of c$\bar{\rm c}$ is less than the mass of the lightest possible open charm hadron pair ($D\bar{D}$). In contrast to CSM, there is no restriction on the quantum properties of produced c$\bar{\rm c}$ pairs to form a charmonium state. Charm and anti-charm quark pairs having different quantum properties than the final charmonium state can still evolve into it by emission of soft gluon(s). The term *evaporation* corresponds to a process with zero momentum loss through which c$\bar{\rm c}$ pair neutralizes its color. Since CEM similarly treats open charm and charmonium, there is a large possibility that c and $\bar{\rm c}$ can hadronize into open charm hadrons. Only a small

fraction of the total produced c$\bar{\text{c}}$ evolve into charmonium states. In the collider experiments, prompt J/ψ p_{T} spectrum can be described by the CEM involving the leading order and next-to-leading order (NLO) contributions in cross sections [92]. ALICE has measured ratio $\psi(2s)$/J/ψ which increases with p_{T} [93]. CEM describes such behavior by constraining the invariant mass of c$\bar{\text{c}}$ to be larger than that of produced quarkonium state [94].

NRQCD Factorization model

Perturbative QCD can describe the processes involving large momentum transfer, $i.e.$, hard scattering processes such as heavy quark production. Therefore, separating hard and soft process contributions is necessary to apply the pQCD approach. Such factorization is done by the effective field theory framework of Nonrelativistic QCD (NRQCD) [95]. The NRQCD is an expansion of QCD in terms of the relative velocity of c$\bar{\text{c}}$ with respect to the charmonium state. The c$\bar{\text{c}}$ pair can be produced either in a color-singlet or color-octet state. In the NRQCD approach, the production cross section of J/ψ is described by two factors – production of c$\bar{\text{c}}$ at hard scales and hadronization of c$\bar{\text{c}}$ at soft scales, represented by the factorization formula described in the following way,

$$\sigma_{J/\psi} = \sum_{n} \sigma_{c\bar{c}[n]} \times \langle \mathcal{O}^{J/\psi}[n] \rangle. \tag{2.2}$$

In Eq. 2.2, the sum run over all states. The coefficients $\sigma_{c\bar{c}[n]}$ are partonic cross sections that describe the production of a c$\bar{\text{c}}$ pair in state n, calculated using perturbative QCD. The next coefficient, $\langle \mathcal{O}^{J/\psi}[n] \rangle$, are Long Distance Matrix Elements (LDMEs) represent the soft part of cross section, which is the hadronization of c$\bar{\text{c}}$ into J/ψ. The model assumes that LDMEs are independent of c$\bar{\text{c}}$ kinematics and do not change with colliding system. These elements can be extracted by global fits to available experimental data.

The NRQCD approach has been highly successful in explaining quarkonium production, but it is not immune to certain challenges and limitations. The NRQCD approach predicts large transverse polarization for quarkonium production at high p_{T}, which is inconsistent with experimental measurements.

2.3.1 Experimental measurements

In the experiments, J/ψ production is studied by the measurement of various physics observables e.g., differential production cross section and polarization. Measurements by different experiments can be compared after corrections of detector-specific effects e.g. acceptance and efficiency corrections. Such corrections are also necessary for comparing the model predictions with experimental measurements. Understanding J/ψ production in pp collision is essential because it serves as a reference or a baseline for J/ψ production in Pb–Pb collisions.

Polarization measurement is an important tool for understanding the particle production mechanism. J/ψ polarization can be affected by large magnetic fields in the initial stages

of collisions and a highly vortical medium. Polarization measurements are performed by analyzing the angular distribution $W(\theta, \phi)$ of J/ψ decay products in the rest frame of J/ψ [96] which is described by the following expression,

$$W(\theta, \phi) \propto \frac{1}{3 + \lambda_\theta} \left[1 + \lambda_\theta \cos^2\theta + \lambda_\phi \sin^2\theta \cos 2\phi + \lambda_{\theta\phi} \sin 2\theta \cos\phi\right], \tag{2.3}$$

θ and ϕ are polar and azimuthal angle in reference frames. Polarization is quantified by the $\lambda_\theta, \lambda_\phi, \lambda_{\theta\phi}$. Table 2.1 lists the polarization states based on the λ_θ parameter.

$\lambda_\theta = 0$	No polarization
$\lambda_\theta > 0$	Transverse polarization
$\lambda_\theta < 0$	Longitudinal polarization

Table 2.1 Suggested polarization of charmonium states based on λ_θ measurements.

Differential cross sections of prompt and non-prompt J/ψ are measured at several center-of-mass energies in pp collisions by ALICE [97, 98], CMS [99, 100], ATLAS [101, 102] and LHCb[103, 104] at the LHC. ALICE results are shown in Fig. 2.5 for prompt and non-prompt J/ψ cross section with respect to p_{T} at midrapidity at $\sqrt{s}$ = 13 TeV. Prompt J/ψ cross section is described by NRQCD and CEM model predictions within uncertainties. However, large uncertainties in these predictions restrict the discrimination among different models. Non-prompt J/ψ production cross section is described by FONLL prediction.

Prompt J/ψ polarization is measured by LHCb [105] and CMS [106] in pp collisions at $\sqrt{s}$ = 7 TeV. The LHCb measurements demonstrate small longitudinal polarization based on λ_θ parameter, shown in Fig. 2.6 (top), while measurements performed by CMS[106], CDF [107], PHENIX [108] and HERA-B [109] suggest no significant transverse or longitudinal polarization in J/ψ production. Various theoretical approaches completely fail to describe the J/ψ polarization measurements.

ALICE has measured inclusive J/ψ polarization in pp collisions at $\sqrt{s}$ = 7 TeV [110] and $\sqrt{s}$ = 8 TeV [111] at $2.5 < y < 4$, as shown in Fig. 2.6 (bottom), where J/ψ polarization is consistent with zero. The Color Singlet model and NRQCD model [112] cannot describe these polarization measurements.

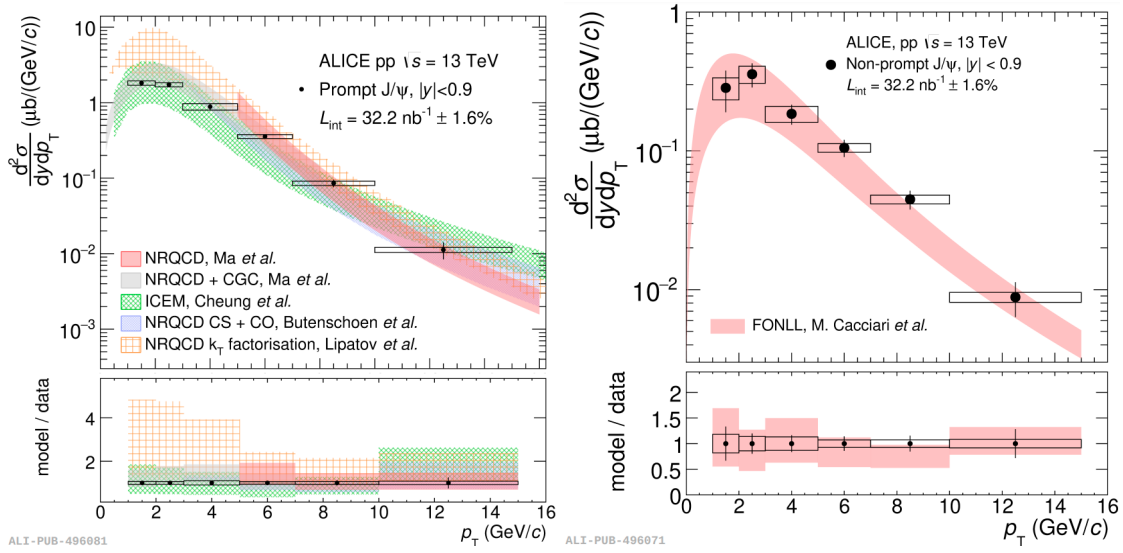

Figure 2.5 p_{T}-differential production cross sections of prompt (left) and non-prompt J/ψ (right) in pp collisions at 13 TeV by ALICE, compared to theoretical predictions [98].

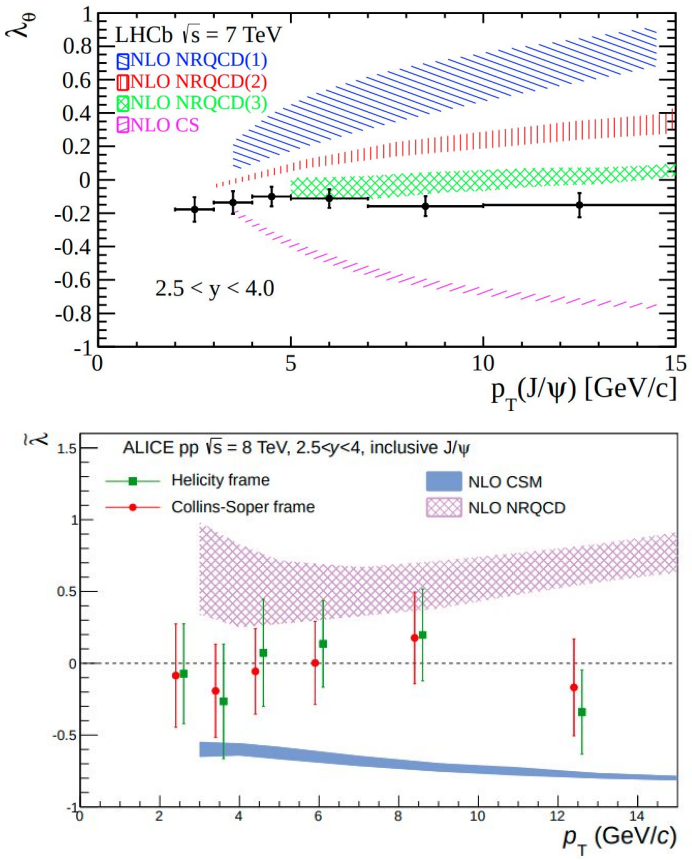

Figure 2.6 Top panel: Polarization parameter λ_θ for prompt J/ψ in pp collisions at $\sqrt{s} = 7$ TeV [105]. Bottom panel: frame invariant polarization parameter $\tilde{\lambda}$ for inclusive J/ψ at $\sqrt{s} =$ 8 TeV (bottom) [111].

2.4 J/ψ production in p–Pb collisions

J/ψ measurements in proton-proton collisions develop our understanding of J/ψ production mechanism in a vacuum. One can utilize this knowledge to understand the J/ψ production mechanism in larger collision systems, such as, Pb–Pb. There is evidence of modified J/ψ production in p–Pb collisions compared to pp collisions. These modifications are attributed to so-called Cold Nuclear Matter (CNM) effects. Measurements of such effects are essential to understand the J/ψ production on Pb–Pb collisions. Therefore, p–Pb collisions offer an opportunity to quantify CNM effects.

2.4.1 Cold nuclear matter effects

The effects responsible for modified J/ψ production in Pb–Pb collisions with respect to pp collisions can be classified as:

- Initial state effects: Effects before the collision or charmonium production, e.g., parton shadowing and parton energy loss in the nucleus.
- Final state effects: After collision or production, e.g. absorption of pre-resonant state by inelastic scatterings with nucleons and comovers.

Initial state effects

Nuclear parton distribution functions (nPDFs) cannot be obtained from the superposition of single parton distribution function [77, 113]. This effect is quantified by the ratio, which depends on the Bjorken-x and four-momentum transfer Q^2 in the interaction:

$$R_i^A(x, Q^2) = \frac{f_i^A(x, Q^2)}{A \cdot f_i(x, Q^2)}, \tag{2.4}$$

where $f_i(x, Q^2)$ and $f_i^A(x, Q^2)$ are parton distribution function in nucleons and nucleus, respectively and A is mass number of nucleus. In Fig. 2.7 (left), $R_g^A(x, Q^2)$ represents modifications in gluon PDF in Pb nucleus with respect to Bjorken-x for a range of Q^2 values. At the LHC, gluon-gluon interactions contribute to heavy quark production; therefore, modifications in the gluon PDF can directly influence heavy quark production. As seen in Fig. 2.7, gluon PDFs are significantly modified in smaller x regions, corresponding to LHC energies. Therefore, it is important to consider such effects in the measurements. At $x < 10^{-2}$, $R_i^A(x, Q^2)$ drops below 1 and for $10^{-2} < x < 10^{-1}$ it is larger than 1. These regions correspond to shadowing and anti-shadowing, respectively. Nuclear modifications of PDFs can be quantified by global parametrization on available experimental data. An example of such parametrization is shown in Fig. 2.7 (right).

At extremely low values of x, the density of gluons rises, eventually reaching a saturation point beyond which the number of gluons cannot increase any further, known as a state of

Color Glass Condensate (CGC). Consequently, gluon PDF is suppressed in a very small-x regime in nuclear PDFs. Such effects are described in the CGC effective theory [114].

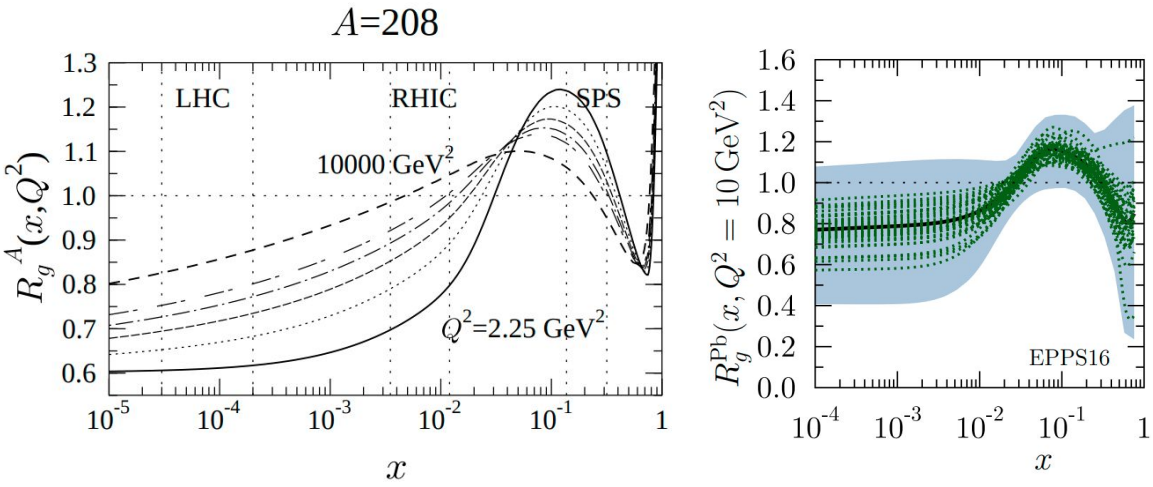

Figure 2.7 Evolution of gluon $R_i^A(x, Q^2)$ with x for Pb nucleus for different values of Q^2 [115] (left), and example of EPPS16 parametrization for gluon nuclear modification [116] (right).

Parton energy loss is another effect that can influence charmonium production. Partons travel inside their parent nucleus before scattering with partons from another nucleus, and during this journey, they lose a fraction of their total energy [117, 118].

Final state effects

Charm and anti-charm quark pairs are produced in the hard parton-parton scattering processes in the initial stages of collisions. The charmonium state is formed after the appearance of a pre-resonance state which emerges after $c\bar{c}$ pair production. This pre-resonance state can be destroyed in the hadronic nuclear matter due to multiple scatterings with nucleons. Such nuclear absorption processes results in a suppression in charmonium production which has a dominant contribution up to RHIC energies [119, 120]. At the LHC, nuclear overlap time is shorter than resonance formation, $i.e.$, nuclei pass each other before the pre-resonance state comes into existence [121]. Therefore, feeble absorption effects are observed at the LHC energies compared to RHIC.

Other suppression effects arise from light particles moving close to the pre-resonance state. In the parton scatterings, several light particles are produced, and scatterings of the pre-resonance state with these comovers can dissociate the pre-resonance state. This effect is stronger in regions where the particle density is large and for heavy charmonium due to their relatively low binding energy [118].

2.4.2 Experimental measurements

ALICE has measured inclusive J/ψ $R_{\rm AA}$ in p–Pb collisions at $\sqrt{s_{\rm NN}}$= 8.16 TeV at forward (p going direction at $+y_{\rm cms}$) and backward (Pb going direction at $-y_{\rm cms}$) rapidity with covering a $p_{\rm T}$ range up to 20 GeV/c [122]. It is observed that J/ψ production is largely suppressed at forward rapidity compared to backward rapidity, as shown in Fig. 2.8. Models with coherent energy losses [123] reproduce the data at both forward and backward rapidity. At forward rapidity, models including the shadowing effects [118, 124, 125] with nPDFs from nCTEQ [126] and EPPS16 [116] provides a good description of data and using nPDFs from EPS09 [127] also describe the data at a reasonable extent within uncertainties. In addition, CGC based models [128, 129] provides a fair description of data at forward rapidity.

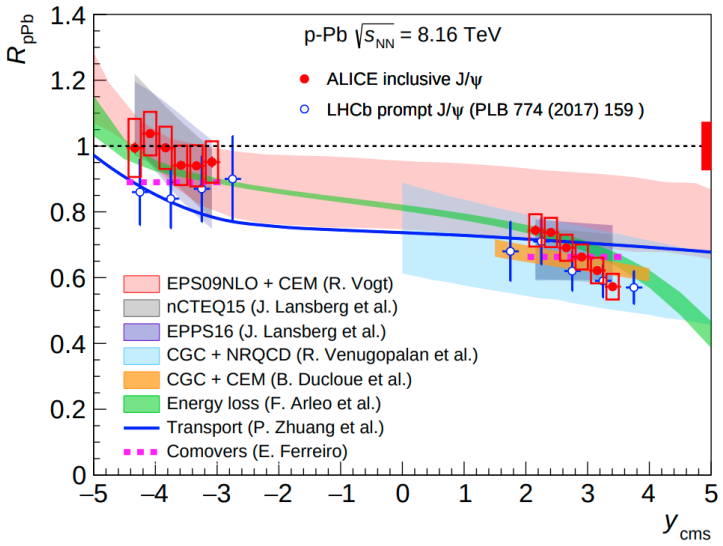

Figure 2.8 $R_{\rm pPb}$ of inclusive J/ψ at forward and backward rapidity at $\sqrt{s_{\rm NN}}$= 8.16 TeV by ALICE [122] in comparison with prompt J/ψ measurement by LHCb and models including various CNM effects.

The ALICE measured $R_{\rm pPb}$ of inclusive, prompt and non-prompt J/ψ at midrapidity and in p–Pb collisions at $\sqrt{s_{\rm NN}}$= 5.02 TeV [130]. Prompt J/ψ production is suppressed with respect to pp collisions at $p_{\rm T}$ smaller than 3 GeV/c while production of non-prompt J/ψ hints towards less suppression in comparison to prompt J/ψ , as shown in Fig. 2.9. Models including energy loss effects with nuclear shadowing [124, 131], describe the $R_{\rm pPb}$ of prompt J/ψ as shown in Fig. 2.9 whereas models based on FONLL calculation including nuclear shadowing [116, 132] describe non-prompt J/ψ $R_{\rm pPb}$ within uncertainties.

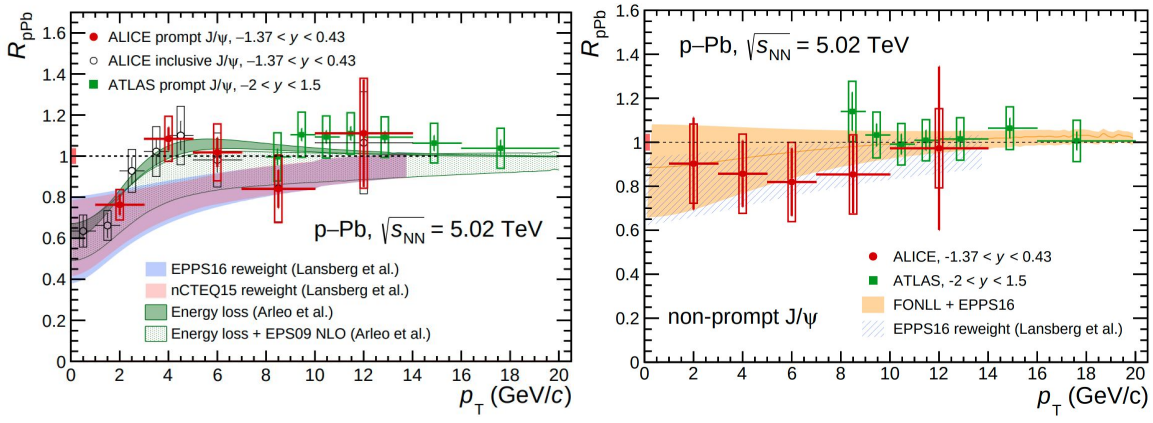

Figure 2.9 R_{pPb} of prompt and inclusive J/ψ at $\sqrt{s_{\mathrm{NN}}}$= 5.02 TeV (left) and non-prompt J/ψ (right) measured by ALICE [130] in comparison to ATLAS measurements and model predictions including various CNM effects.

CMS has measured the elliptic flow (v_2) of prompt J/ψ in high multiplicity events in p–Pb collisions at $\sqrt{s_{\mathrm{NN}}}$= 8.16 TeV at $0.2 < p_{\mathrm{T}} < 10$ GeV/c [133]. A positive v_2 is observed for prompt J/ψ as shown in the Fig. 2.10, suggesting significant collective behavior of charm quarks in high multiplicity events. The results are consistent with v_2 of prompt D^0 in p–Pb collisions [134]. These measurements can provide constraints for charm quark collectivity in smaller systems and help to understand the measurements in Pb–Pb collisions.

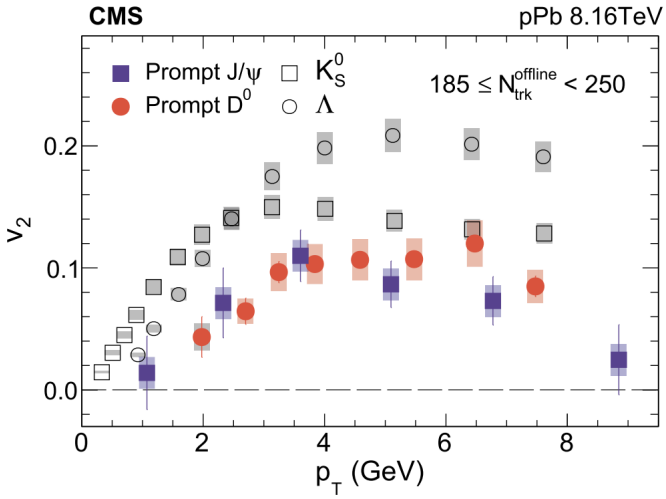

Figure 2.10 Prompt J/ψ v_2 as a function of p_{T} at forward rapidity in p–Pb collisions at $\sqrt{s_{\mathrm{NN}}}$= 8.16 TeV by CMS experiment [133].

2.5 J/ψ production in Pb–Pb collisions

In the vacuum, $i.e.$, at zero temperature, charmonium states are seen as a bound state of c and $\bar{\text{c}}$ quarks where their interaction is governed by Cornell potential [72], described in the following way,

$$V_{q\bar{q}} = -\frac{\alpha_{\text{eff}}}{r} + \sigma r, \tag{2.5}$$

where r is the separation between $q\bar{q}$ in the quarkonium state. The first term is Coulomb term for gluon exchange interaction in pQCD and $\alpha_{\text{eff}} = \frac{4}{3}\alpha_s(r) \approx 0.471$, α_s is strong coupling constant. The second term represents non-perturbative confinement where $\sigma \approx$ 0.19 GeV^2 corresponds to QCD string coupling. The large mass of charm quarks and small velocity allows us to treat charmonium with a non-relativistic approach. One can obtain the properties of charmonium states such as mass (M), radius (R), and formation time (τ) by solving the non-relativistic Schrödinger equation with Cornell potential. Indicative values of those obtained parameters using this approach are listed in Table 2.2.

	J/ψ	ψ	χ_c
M (GeV/c^2)	3.07	3.698	3.5
R(fm)	0.453	0.875	0.696
τ (fm/c)	0.89	1.5	2.0

Table 2.2 Charmonium properties obtained by the solution of non-relativistic Schrödinger equation [135].

The presence of hot nuclear matter can influence charmonium production. Such modifications are observed in the charmonium production in several experiments [136] due to hot nuclear matter effects. A brief description concerning the origin of these effects and their influence on charmonium production is described in the next section.

2.5.1 Hot nuclear matter effects

The potential as given by Eq. 2.5 is modified in the presence of an extremely hot medium ($T \gg 0$), which can be rewritten in terms of a temperature-dependent function as

$$V_{q\bar{q}}(r,T) = -\frac{\alpha_{\text{eff}}}{r} e^{-\mu_s(T)r} + \frac{\sigma}{\mu_s(T)}\left(1 - e^{-\mu_s(T)r}\right). \tag{2.6}$$

Eq. 2.6 introduces a temperature dependent screening mass term, $\mu(T)$. In comparison to Eq. 2.5, string tension gets weaker with increasing temperature. According to Matsui and Satz [137], there is a screening of color potential between c and $\bar{\text{c}}$ in presence of an extremely hot medium. The screening effects can be characterized in terms of Debye screening radius r_{D}, theoretically $r_{\text{D}} \to \infty$ in vacuum (at T=0). The $q\bar{q}$ pair in charmonium state having

a binding radius larger than that of r_{D} experience screening in their binding potential. In simple terms, c quark will no longer see $\bar{\mathrm{c}}$, and the existence of charmonium state is no longer possible and dissociates into c and $\bar{\mathrm{c}}$. Screening mass, $\mu(T)$, in Eq. 2.6 is inverse of r_{D}, and it increases with the temperature of the medium, *i.e.*, r_{D} decreases with temperature. Heavy charmonium states e.g. $\psi(2s)$ and χ_c have a larger binding radius in comparison to J/ψ according to Table 2.2, which makes them dissociate earlier than J/ψ. Thus charmonium states undergo a sequential suppression in nucleus–nucleus collisions where heavier states e.g. $\psi(2s)$ and χ_c melt before J/ψ. The dissociation temperature for different charmonium states depends on their binding radius. Due to the sequential melting of charmonium states, their production probability exhibits a step-like behavior with energy density as represented in Fig. 2.11.

In contrast to suppression, an enhancement in J/ψ production with respect to pp collisions was predicted at the LHC [138, 139]. The number density of produced heavy quark pairs increases with the energy density, e.g., the number of $\mathrm{c\bar{c}}$ is $\mathcal{O}(10)$ at RHIC and $\mathcal{O}(100)$ at LHC. At the LHC energies, the number density of produced $\mathrm{c\bar{c}}$ pairs is sufficiently large to bring them closer in the phase space and combine to form J/ψ at the phase boundary or within the medium. This is known as charmonium production by regeneration or recombination. These interactions are attributed to low energies in comparison to initial hard scatterings, therefore, the $\langle p_{\mathrm{T}} \rangle$ of recombined J/ψ shifts towards smaller values. An interplay between these two production mechanisms, charmonium suppression and regeneration, governs the charmonium production at LHC energies. ALICE has measured a significant contribution from J/ψ recombination at p_{T} smaller than 5 GeV/c, especially at forward rapidity in central Pb–Pb collisions [140].

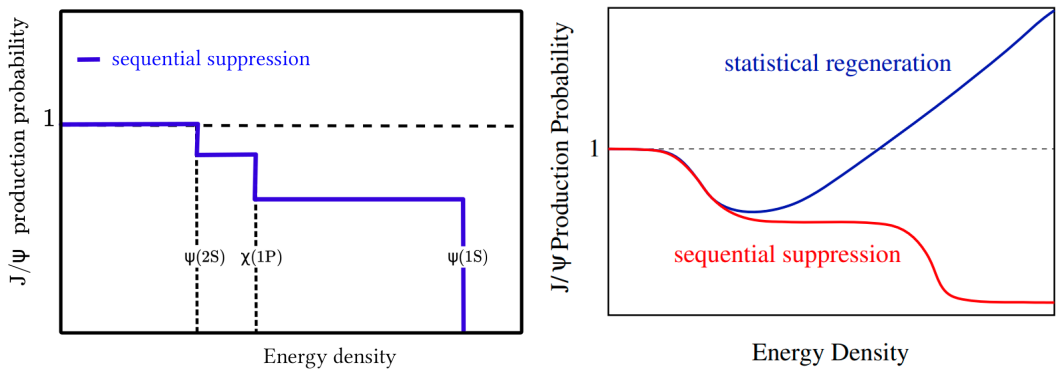

Figure 2.11 Sequential suppression of charmonium states with respect to the energy density of the produced medium (left), and in comparison to statistical regeneration (right), Fig. from [141].

Several theoretical models incorporating suppression and regeneration effects are proposed to understand the J/ψ production in Pb–Pb collisions at LHC energies. Some of them are briefly described in the following sections.

Statistical Hadronization Model

According to Statistical Hadronization Model (SHM), [138, 142–144], charm and anti-charm quarks are produced in the hard partonic scatterings and assumed to be thermalized in the deconfined nuclear medium. No charm quarks can be produced in the medium because their mass is larger than the temperature of the medium by an order of magnitude. Therefore their number is conserved during the evolution of the system. Charm and anti-charm quarks are hadronized at the phase boundary or chemical freeze-out according to their thermal weights. In SHM, the number of total c$\bar{\text{c}}$ produced in Pb–Pb collisions is represented by the following expression,

$$N_{c\bar{c}}^{direct} = \frac{1}{2} g_c V \left(\sum_i n_{D_i}^{thermal} + \sum_i n_{\Lambda_i}^{thermal} \right) + g_c^2 V \left(n_{\psi_i}^{thermal} \right) + ..., \tag{2.7}$$

where g_c is the charm fugacity factor or charm enhancement factor, V is the volume of fireball, and $n_{thermal}$ is charm quark yield predictions by thermal model. The SHM resolves the problems of thermal model predictions for charmonium production where J/ψ yield is underestimated for different centrality intervals, e.g., by a factor of two for central collisions. The number of directly produced c$\bar{\text{c}}$ deviates from the values obtained at chemical equilibrium. To overcome such problems, SHM introduces a charm quark enhancement factor (g_c) which gives a larger yield of J/ψ (and D) by a factor of g_c^2 (and g_c) in comparison to thermal model predictions. The model has two inputs: charm quark production cross section measured in pp collisions and thermal parameters obtained from the light hadrons analysis.

In this model, J/ψ production cross section is estimated in the Pb–Pb collisions using core-corona approach [143]. In the core part, QGP formation is assumed due to multiple parton scattering leading to thermalization. The corona behaves like a pp system having a density of $1/10^{\text{th}}$ of the density of the core part. They dominate J/ψ production cross section at low p_{T} (< 5 GeV/c) and high p_{T}, respectively. The SHM describes J/ψ production as measured by ALICE [145] at $\sqrt{s}$ = 5.02 TeV at low p_{T} but underestimates the production at high p_{T} [143].

Transport Models

In transport models [146–150], the number of produced c$\bar{\text{c}}$ is derived from charm production cross section in pp collisions. Charmonium production is governed by a relativistic Boltzmann transport equation with incorporating dissociation and regeneration contributions. Charmonium states are formed during the evolution of the system if the medium temperature is below the dissociation temperature for a given charmonium state. Charmonium dissociation occurs due to its scattering with a quark or gluon present in the medium, e.g., $\psi + q(\text{or } g) \rightarrow c + \bar{c} + q(\text{or } g)$ while by inverting the process one gets regeneration of charmonium. The possibility of charmonium formation at the phase boundary is not excluded. Different transport models assume a different degrees of charm quark thermal-

ization in the medium. Various cold nuclear matter effects, e.g., shadowing and nuclear absorption, are considered in the transport models.

2.5.2 Experimental measurements

ALICE has measured inclusive J/ψ $R_{\rm AA}$ at forward rapidity [151] and at midrapidity [152] in Pb–Pb collisions at $\sqrt{s_{\rm NN}}$= 5.02 TeV. J/ψ production is significantly suppressed in comparison to pp collisions at high $p_{\rm T}$ due to dissociation and charm quark energy loss in the medium as shown in Fig. 2.12. In contrast, J/ψ regeneration is an additional production mechanism that significantly contributes at low $p_{\rm T}$ at the LHC energies. ALICE measurements confirm the J/ψ production via regeneration mechanism at low $p_{\rm T}$. It is also observed that inclusive J/ψ $R_{\rm AA}$ does not show any significant rapidity dependence.

Prompt and non-prompt J/ψ $R_{\rm AA}$ has been measured in Pb–Pb collisions at $\sqrt{s_{\rm NN}}$= 2.76 TeV by ALICE [153] down to $p_{\rm T}$ = 1.5 GeV/c. Similar measurements by CMS [154] and ATLAS [155] at $\sqrt{s_{\rm NN}}$= 5.02 TeV show that J/ψ production is strongly suppressed in the most central collisions as demonstrated in Fig. 2.13.

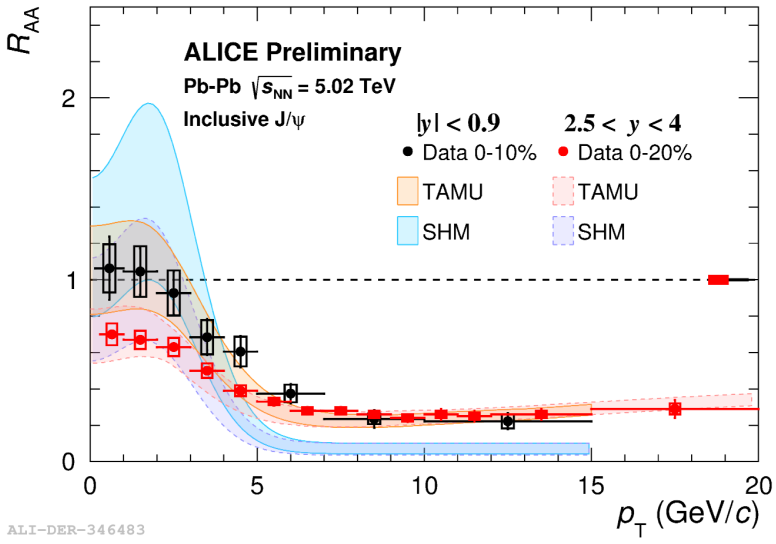

Figure 2.12 Inclusive J/ψ $R_{\rm AA}$ as a function of $p_{\rm T}$ in Pb–Pb collisions at $\sqrt{s_{\rm NN}}$= 5.02 TeV, compared with theoretical predictions by SHM and Transport model [152].

Elliptic flow (v_2) has been measured by PHENIX [156] and STAR [157] experiments at midrapidity in Au–Au and U–U collisions. PHENIX results for J/ψ v_2 are consistent with zero, while results from the STAR experiment suggested that there might be significant v_2 for J/ψ. These results inspired further investigations. At the LHC, ALICE has performed precise v_2 measurements for inclusive J/ψ [158], and D-meson [53] as shown in Fig. 2.14. The results support the idea of charm quark thermalization or a strong coupling of charm quarks with the medium.

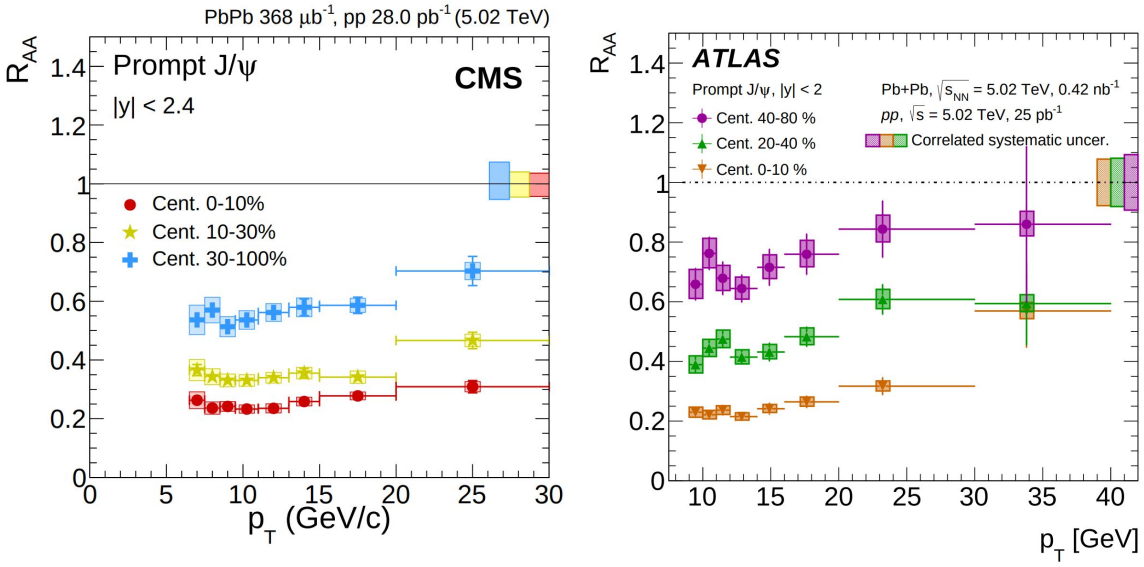

Figure 2.13 Prompt J/ψ R_{AA} as a function of p_{T} across different centrality ranges in Pb–Pb collisions at $\sqrt{s_{\mathrm{NN}}}$= 5.02 TeV by CMS [154] (left) and ATLAS (right) [155].

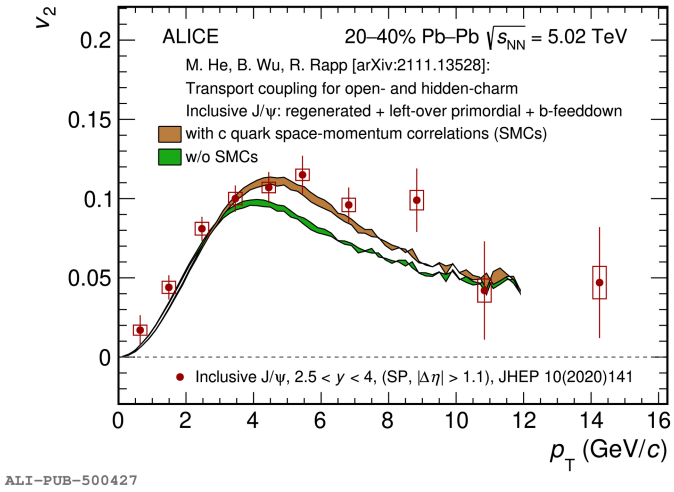

Figure 2.14 Elliptic flow (v_2) of inclusive J/ψ as a function of p_{T}, for $2.5 < y < 4$, in Pb–Pb collisions in 20-40% centrality interval at $\sqrt{s_{\mathrm{NN}}}$= 5.02 TeV [158] compared to theoretical calculations [159].

For the first time, ALICE measured J/ψ polarization in Pb–Pb collisions at $\sqrt{s_{\mathrm{NN}}}$= 5.02 TeV at $2.5 < y < 4$ [160] as demonstrated in Fig. 2.15. The measurements indicate a hint of longitudinal and transverse polarisation of J/ψ at low p_{T} in different reference frames and also show significant differences relative to prompt J/ψ polarization as measured by LHCb in pp collisions in similar kinematic regime [105].

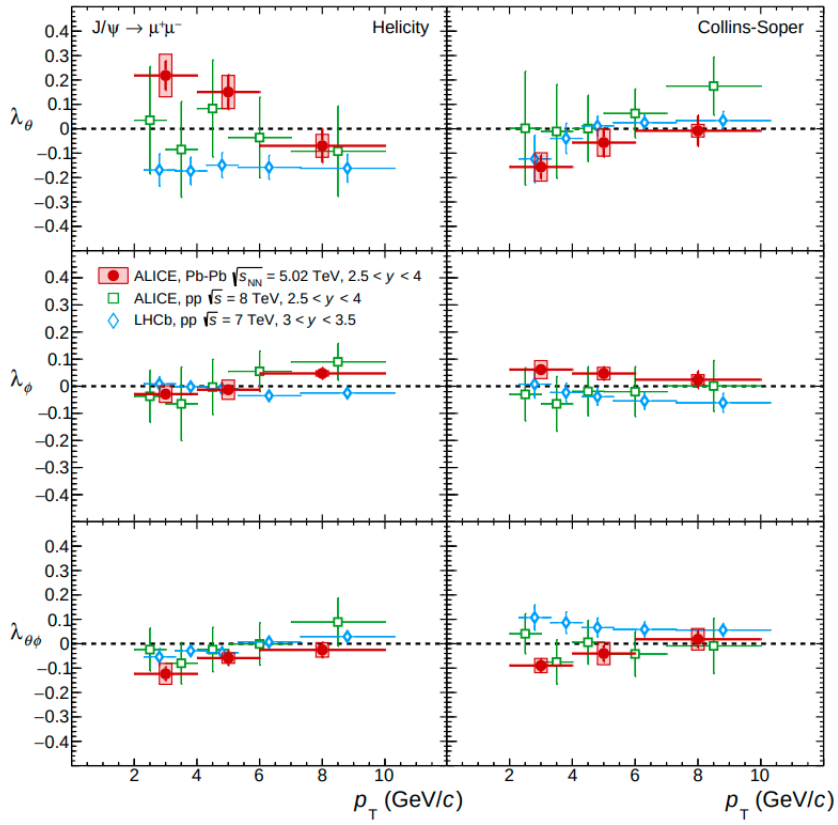

Figure 2.15 Inclusive J/ψ polarization parameters as a function of transverse momentum for Pb–Pb collisions at $\sqrt{s_{\rm NN}}$= 5.02 TeV, compared with results obtained in pp collisions by ALICE at $\sqrt{s}$ = 8 TeV and by LHCb for prompt J/ψ at $\sqrt{s}$ = 7 TeV [160].

2.6 J/ψ photoproduction in ultraperipheral Pb–Pb collisions

Inclusive J/ψ production is discussed in the previous sections where J/ψ is produced in the strong interactions with nuclear overlap. The exclusive production of J/ψ is governed by electromagnetic interactions where the nuclear overlap is absent. Such conditions in the collisions where the impact parameter (b) is larger than twice the radius (R) of colliding nuclei, $i.e.$, $b > 2R$, are known as ultraperipheral collisions (UPC). A quasi-real photon (having large Q^2) is emitted from the projectile nucleus interact with the target nucleus. This interaction can occur either coherently, involving the entire nucleus, or incoherently, limited to just one nucleon within the target nucleus. Either of the interactions lead to a vector meson production where the target nucleus remains intact in coherent interaction while it breaks up in case of incoherent interaction. Incoherently produced J/ψ tends to have larger transverse momentum, $\langle p_{\rm T} \rangle \sim$ 500 MeV/c in comparison to coherently produced J/ψ $\langle p_{\rm T} \rangle \sim$ 60 MeV/c as seen in Fig. 2.16. These measurements provide constraints on gluon distribution inside nuclei at smaller values of x in a range 10^{-5} - 10^{-2} where gluon shadowing effects are not precisely determined.

In UPC, the strong interactions are suppressed by the large impact parameters. J/ψ photoproduction is not limited to only UPC, but it is also observed in the non-central collisions where $b < 2R$. Such contributions are removed in (non) central collisions where J/ψ production from strong interactions is concerned.

Coherent J/ψ photoproduction cross section is sensitive to gluon PDFs in the nucleus at leading order. For this process, a relation for Bjorken-x with rapidity (y) can be written by

$$x = \frac{m_{\mathrm{J}/\psi}}{\sqrt{s_{\mathrm{NN}}}} \exp\left(\pm y\right), \tag{2.8}$$

where $\sqrt{s_{\mathrm{NN}}}$ represents the center of mass energy of Pb–Pb system and $m_{\mathrm{J}/\psi}$ refers to J/ψ mass.

ALICE has demonstrated broad interest in this subject and performed impressive measurements [161–163]. Furthermore, recent measurements by the LHC experiments provide new constraints for theoretical models and reduce the uncertainties in nuclear parton distribution functions [164].

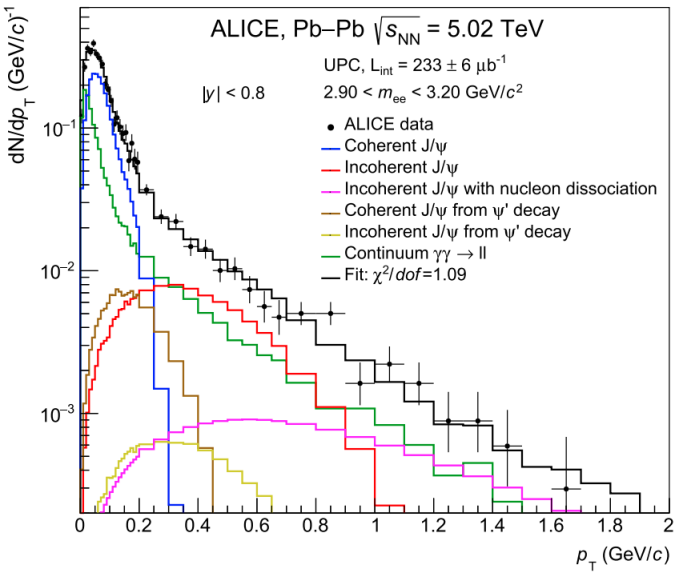

Figure 2.16 The p_{T} distribution of photoproduced J/ψ in ultraperipheral Pb–Pb collisions at $\sqrt{s_{\mathrm{NN}}}$= 5.02 TeV [165].

Chapter 3

A Large Ion Collider Experiment (ALICE)

"An experiment is a question which science poses to Nature and a measurement is the recording of Nature's answer"

Max Planck

This chapter describes the working principles of the ALICE detector, which are particularly important for the J/ψ measurements. The chapter begins by providing an overview of the Large Hadron Collider, followed by a detailed description of the internal geometry of the ALICE subdetectors. The subsequent sections delve into the procedures of track reconstruction, particle identification (PID), and centrality determination in Pb–Pb collisions.

3.1 The Large Hadron Collider (LHC)

LHC is the world's largest and most powerful hadron accelerator and collider located at *Conseil Européen pour la Recherche Nucléaire* (CERN) near Geneva, which started operation in September 2008 [166]. The accelerator is comprised of a superconducting ring with two beam pipes, spanning approximately 26.7 km in circumference. It is situated within an underground tunnel, ranging in depth from 45 m to 170 m. The LHC is designed to accelerate and collide protons with maximum achievable center of mass energy $\sqrt{s}$ = 14 TeV and Pb nuclei at $\sqrt{s_{\rm NN}}$= 5.52 TeV with corresponding luminosities $\mathcal{L}_{\rm pp} = 10^{34}$ cm^{-2} s^{-1} and $\mathcal{L}_{\rm Pb-Pb} = 10^{27}$ cm^{-2} s^{-1}.

Several stages are involved in particle acceleration, starting from a proton source to collisions at the LHC, as shown in Fig 3.1. Protons are accelerated up to 50 MeV in a linear accelerator LINAC2 and injected into a Booster as proton bunches. The Booster further accelerates the proton bunches until they reach the injection energy required for the Proton Synchrotron (PS), which is approximately 1.4 GeV. These bunches are injected into the PS

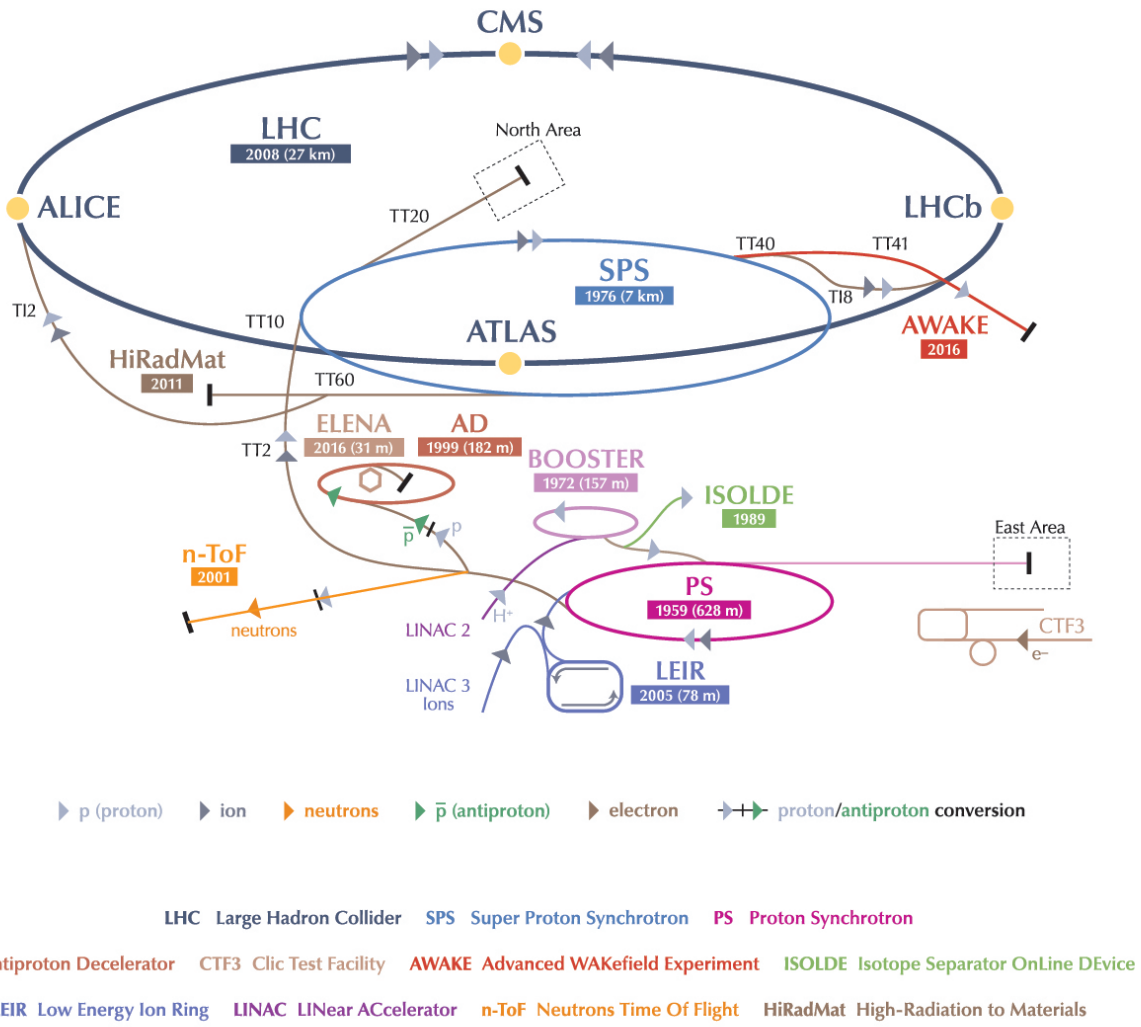

Figure 3.1 Schematic layout of the CERN accelerator complex.

once they reach desired energy level. Within the PS, the bunches undergo acceleration, reaching energies of up to 26 GeV in preparation for injection into the Super Proton Synchrotron (SPS). Additionally, bunches are split and arranged at a bunch spacing of 50 ns or 25 ns before injecting into SPS, where they are accelerated up to LHC injection energy *i.e.* 450 GeV. To initiate the Pb-ion beams in the LHC, a 2 cm long segment of pure lead, weighing 500 milligrams, is used. The Pb sample is subjected to a temperature of approximately 500°C, causing vaporization of a few atoms. Subsequently, an electrical current is applied to strip a few electrons from each atom. The ions are passed through LINAC3, a linear accelerator,

where they gain a small energy boost of 4.5 MeV per nucleon and undergo additional electron removal. The ions are injected into the Low Energy Ion Ring (LEIR), where they are accelerated up to 72 MeV per nucleon. These two initial stages involving LINAC3 and LIER are exclusive to ions. However, once ions exit they go through the same acceleration stages as the protons. The Pb-ion beams are accelerated by the SPS up to 177 GeV per nucleon before being injected into the LHC in two opposing directions.

The four main experimental facilities are placed at different beam interaction points – ALICE (A Large Ion Collider Experiment) [167] at Point 2, ATLAS(A Toroidal Lhc ApparatuS) [168] at Point 1, CMS (Compact Muon Solenoid) [169] at Point 5 and LHCb [170] at Point 8 as shown in Fig. 3.1.

CMS and ATLAS experiments are dedicated to studying Higgs boson and beyond standard model physics, e.g. supersymmetry, precision tests of QCD, and, electroweak interactions. They are designed to operate at the highest interaction rates delivered by the LHC to achieve these physics goals. Higgs boson was discovered in 2012 by the ATLAS and CMS collaborations [171, 172]. The LHCb experiment is designed to study the mechanisms that led to matter-antimatter asymmetry during the early stages of the Universe. It focuses on the measurements involving b quarks, with a particular emphasis on measuring CP violation parameters, exploring rare decays, and studying phenomena associated with mesons and baryons containing c and b quarks.

The ALICE is designed to study the deconfined state of nuclear matter, e.g., Quark–Gluon Plasma (QGP) which exists at extremely high temperatures and energy densities [167]. Such extreme conditions are achieved in high-energy collisions of Pb nuclei traveling at ultrarelativistic speeds at the LHC. ALICE recorded the first proton-proton collisions in November 2009 and Pb–Pb collisions in November 2010 [173, 174] during LHC Run 1. Table 3.1 presents a summary of recorded collisions and their corresponding integrated luminosity ($\mathcal{L}_{int}$) from the ALICE experiment across all LHC Run programs.

3.2 ALICE Detector

ALICE detector is a giant complex machine with dimensions of approximately 26 meters in length, 16 meters in width, and 16 meters in height with a weight of $\sim$ 10000 tons, as demonstrated in Fig. 3.2. The Fig. 3.3 illustrates a cross-sectional view of the central barrel of the ALICE detector. The ALICE geometry in a global coordinate system, a right-handed Cartesian system with the origin at the interaction point, is shown in Fig. 3.4 [175]. The z-axis extends along the beam direction, pointing towards ATLAS. In the transverse plane, x-axis points to the center of the accelerator ring, and y-axis points up, perpendicular to the ground. The pseudorapidity η is defined in terms of spherical polar coordinates (r, θ, ϕ), formulated as $\eta = -\ln\left(\tan\frac{\theta}{2}\right)$ where θ is direction of particle with respect to $+z$ direction in yz plane. In spherical coordinates, the transverse plane is defined by the $r\phi$ plane, where the direction of the particle is expressed in terms of ϕ.

System	Year	$\sqrt{s}$ (TeV)	$\mathcal{L}_{int}$
pp	2009-13	0.9	$\sim 200\ \mu\mathrm{b}^{-1}$
		2.76	$\sim 100\ \mathrm{nb}^{-1}$
		7	$\sim 1.5\ \mathrm{pb}^{-1}$
		8	$\sim 2.5\ \mathrm{pb}^{-1}$
	2015, 2017	5.02	$\sim 1.3\ \mathrm{pb}^{-1}$
	2015-2017	13	$\sim 25\ \mathrm{pb}^{-1}$
p–Pb	2013	5.02	$\sim 15\ \mathrm{nb}^{-1}$
	2016	5.02	$\sim 13\ \mathrm{nb}^{-1}$
	2016	8.16	$\sim 25\ \mathrm{nb}^{-1}$
Xe–Xe	2017	5.44	$\sim 0.3\ \mu\mathrm{b}^{-1}$
Pb–Pb	2010-11	2.76	$\sim 75\ \mu\mathrm{b}^{-1}$
	2015	5.02	$\sim 250\ \mu\mathrm{b}^{-1}$
	2018	5.02	$\sim 0.9\ \mathrm{nb}^{-1}$

Table 3.1 Data collected by the ALICE experiment for different collision systems during Run 1 (2009-13) and Run 2 (2015-18).

The ALICE is composed of Central barrel covering pseudorapidity interval $|\eta| < 0.9$, and Muon Spectrometer covering $2.5 < \eta < 4$. The central barrel part is encapsulated in a large solenoid L3 magnet, producing a uniform magnetic field up to 0.5 T along the z–axis. It allows one to determine particle momentum and identify positively and negatively charged particles.

Forward detectors, e.g., Muon spectrometer, T0, V0, Forward Multiplicity Detector, and Zero Degree Calorimeter are placed in different η regions at forward rapidity. The ZDC modules are placed at the farthest points along the beam axis on both sides of the ALICE. The ALICE Diffractive detector system helps in diffractive physics measurements at forward rapidity by increasing the acceptance of those events.

A complete description of the ALICE detector, along with the working principles of its subdetectors, can be found in Ref. [167]. A brief description of all the subdetectors is given below.

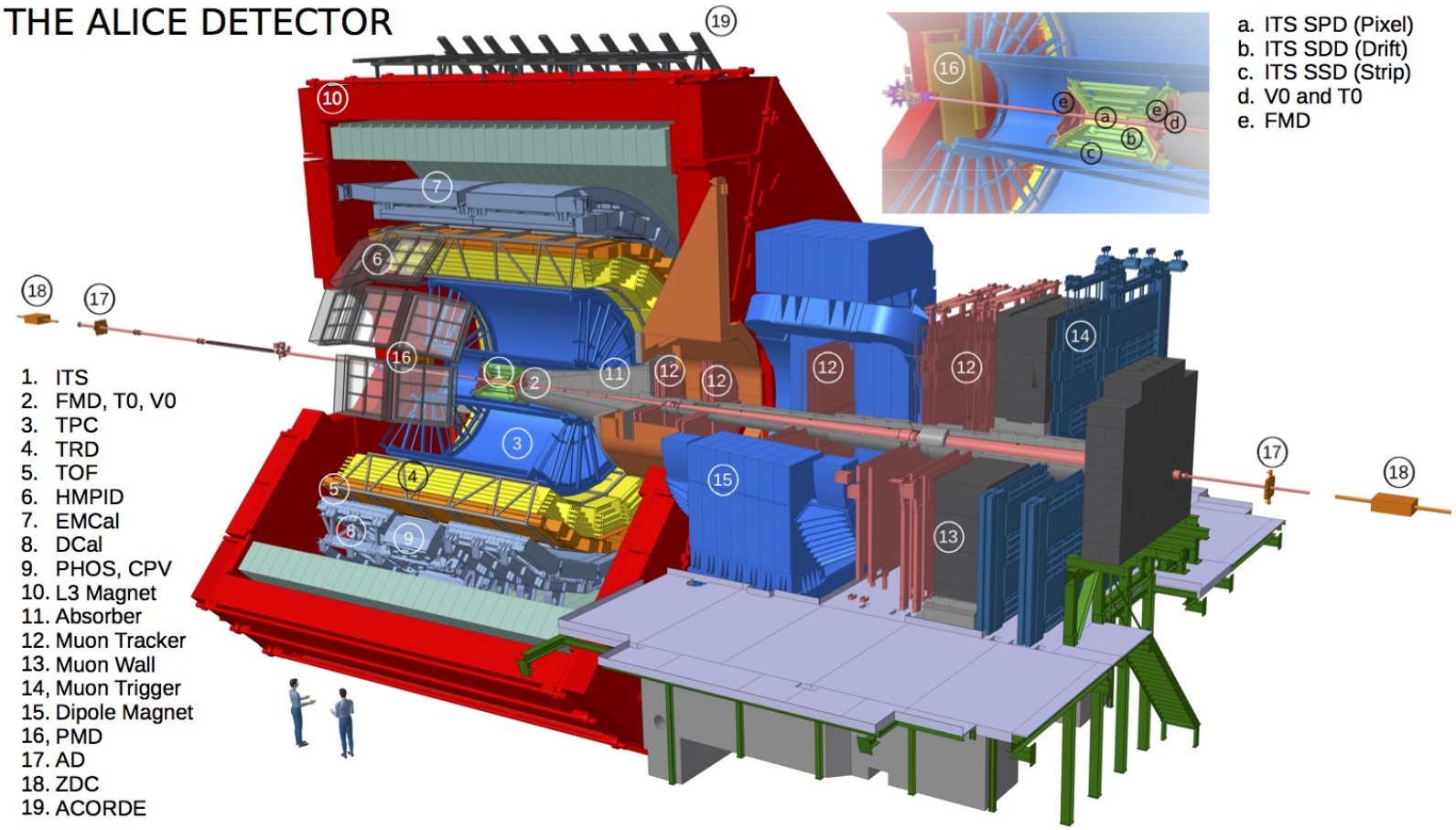

Figure 3.2 Illustration of the ALICE detector with its components labeled by the numbers, image credit to the ALICE Collaboration

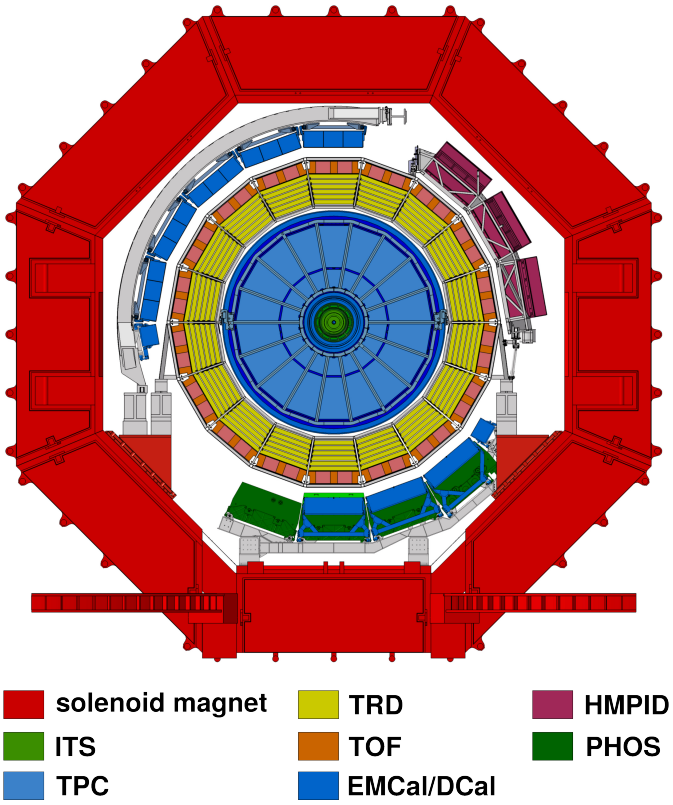

Figure 3.3 A schematic cross-section of the ALICE detector, taken perpendicular to the direction of the LHC beam [176].

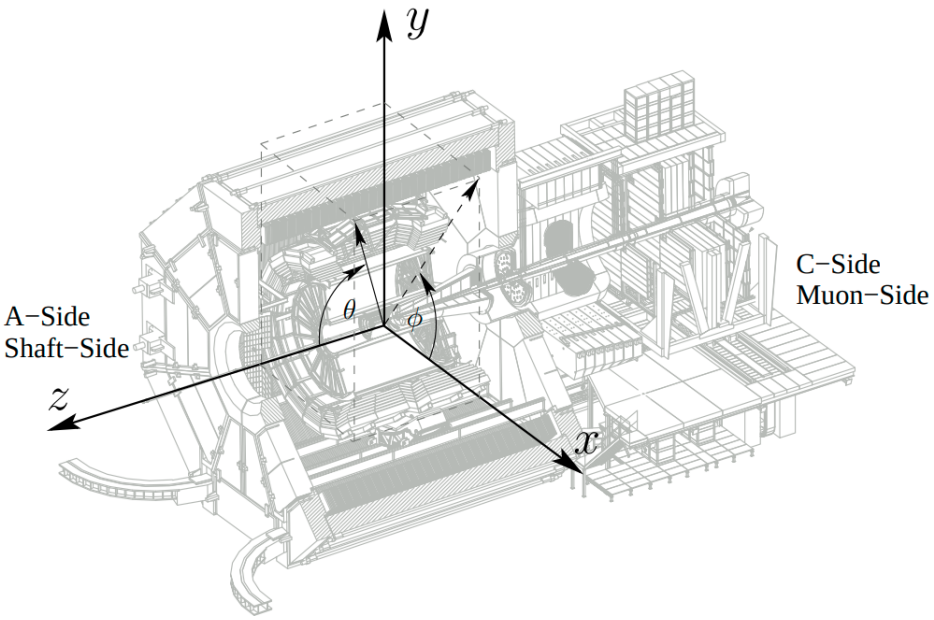

Figure 3.4 Global coordinate system of the ALICE experiment, figure taken from Ref. [175].

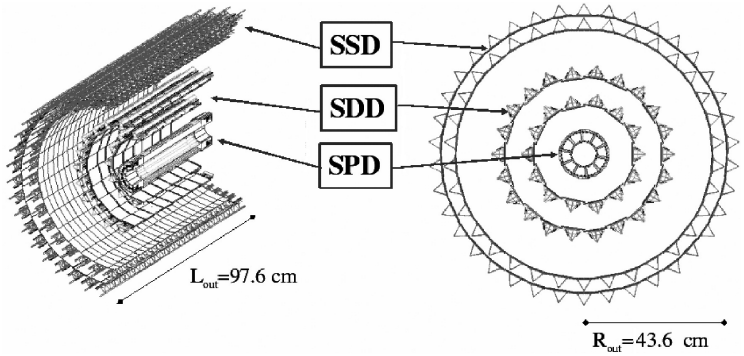

Figure 3.5 An illustration of the layered structure of ITS detector, taken from [177].

3.2.1 Central Barrel Detectors

Central barrel detectors are crucial in tracking and particle identification at midrapidity $|y| < 0.9$ in a wide p_{T} range, 0.1-100 GeV/c. This section describes central barrel detectors with full ϕ acceptance.

Inner Tracking System (ITS)

ITS is a six-layered, cylindrical silicon tracking detector with acceptance of $|\eta| < 0.9$ enclosing the interaction point. It is the closest detector from the interaction point, placed at a radial distance of 3.9 cm (innermost layer) and 43 cm (outermost layer) from the beam axis. The ITS consists of 3 subdetectors – Silicon Pixel Detector (SPD), Silicon Drift Detector (SDD), and Silicon Strip Detector (SSD), as shown in Fig. 3.5. The ITS is crucial in event vertex reconstruction and secondary vertices reconstruction, e.g. decay of beauty, charm, and strange hadrons. The SPD is based on hybrid silicon pixels. It provides low-level trigger inputs to the ALICE trigger system. With SDD and SSD signal response, charged particles are identified by measuring their specific energy loss per unit length ($\mathrm{d}E/\mathrm{d}x$). It is essential for the particles having momentum less than 200 MeV/c , which trajectories are highly curved in the magnetic field and cannot travel further to reach TPC.

Time Projection Chamber

TPC is the primary detector for charged particle tracking in a pseudorapidity interval $|\eta| < 0.9$. It is a cylindrical gaseous detector with an inner radius of 80 cm, an outer radius of 250 cm, and a total length of 500 cm in beam direction with an active volume of 90 m^3. The TPC is a tracking device with a small possibility of multiple scatterings and secondary particle production in its active volume, often called low material budget detector. A gas mixture of NO_2–CO_2–N_2 (90–10–5) is used in the active volume of the TPC. A central high voltage electrode perpendicular to the beam direction divides TPC into two equal volumes (A and C sides). It is kept at –100 kV to produce a homogeneous electric field of 400 V/cm parallel to the beam direction. TPC uses multiwire proportional chambers (MWPCs) with

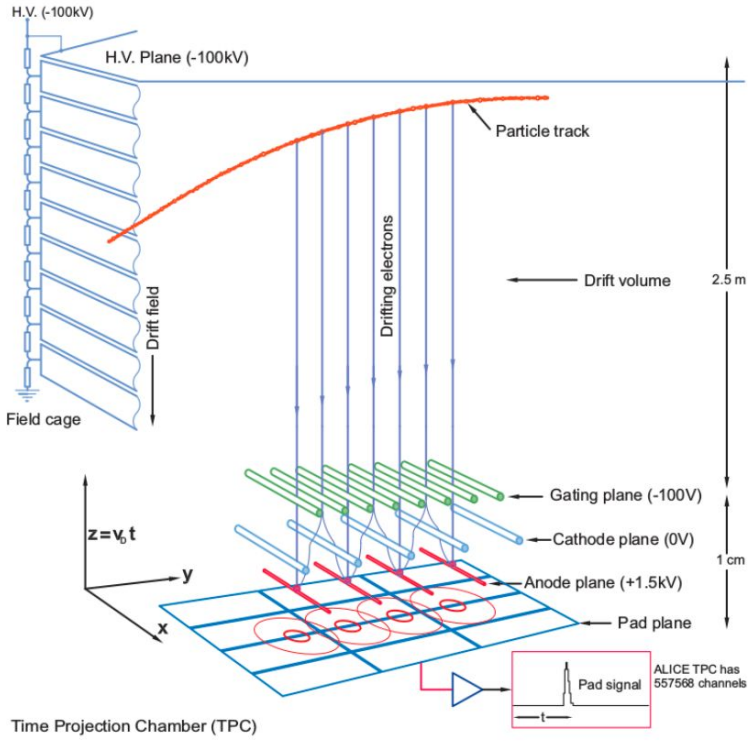

Figure 3.6 Illustration of particle track in TPC volume in XYZ-plane.

cathode pad readouts installed on both endplates, $i.e.$, A and C sides. In total, approximately 570000 pads are installed to achieve the required dE/dx and position resolution. Readout chambers on each side are segmented into 18 azimuthal sectors, each covering 20 degrees in azimuth, called 0-17 on the A-side and 18-35 on the C-side. Each sector is further radially separated into Inner Readout chambers (IROC) and Outer Readout chambers (OROC) with 159 pad rows to provide excellent tracking and particle identification performance. The setup is placed inside a uniform magnetic field of 0.5 T along the beam direction during operation. A 3D schematic representation of tracking a particle's trajectory in TPC is shown in Fig. 3.6 while a 2D projection in XY plane in TPC sector is depicted in Fig. 3.7.

A fast-moving charged particle ionizes the gas in TPC volume and produces ion–electron pairs in its path. These ions and electrons drift towards the central electrode and readout chambers at different drift velocities, as shown in Fig. 3.6. While entering the amplification region, these electrons do not have enough energy to induce a sufficiently large signal on readout pads. Therefore, an assembly of anode wires maintained at a positive voltage of +1.5 kV contributes to their kinetic energy, resulting in the generation of high-energy electrons that ionize the gas. This ionization process produces secondary electrons. Thus, the primary charge is amplified by a factor of several thousand at the anode plane, and this charge induces a signal on the readout pad. The induced signal on the pad is always proportional to the primary charge. A gating grid stops produced ions in the amplification region from entering the drift region, where they can cause space charge distortions of the electric field.

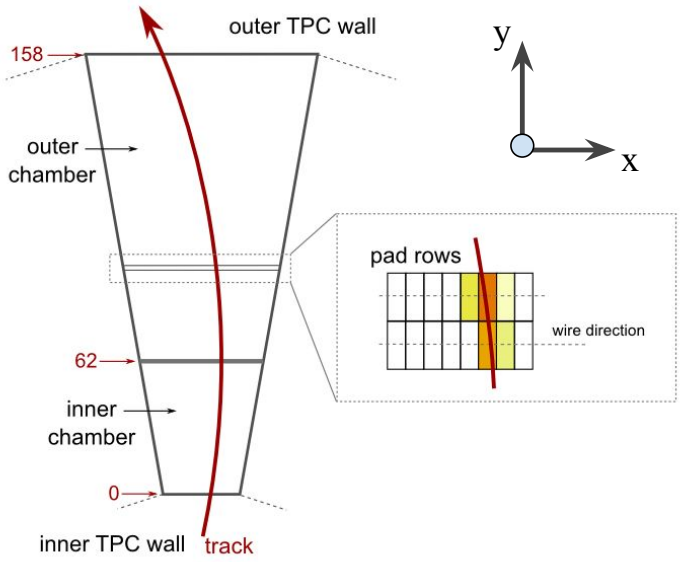

Figure 3.7 Illustration of particle track reconstruction in a TPC sector based on signal collected in pad rows.

TPC allows reconstructing the particle trajectories in three dimensions with good precision in such a high track density environment in Pb–Pb collisions.

For any trajectory, position in the XY plane is determined by signal distribution in the pads with a precision of 800-1100 μm. The z coordinate is determined with a precision of 1100-1250 μm by the trigger time and given drift velocity of the electron in the TPC gas.

Transition Radiation Detector

The TRD is a tracking detector consisting of 522 detector modules arranged into 18 sectors within the azimuthal plane. Furthermore, each sector is subdivided into 5 stacks along the longitudinal direction, with each stack containing 6 layers. It is located at 2.9–3.68 m radially outward from the interaction point after ITS and TPC. Each module consists of a radiator, multiwire proportional readout chamber, and front-end electronics. The readout chambers in the TRD utilize a mixture of Xe and CO_2 as the gas in the active volume. Each individual readout chamber within the TRD is comprised of a drift region that spans a length of 3 cm. When charged particles traverse the drift volume, they leave a trace of the ionization of the gas. The determination of a particle's momentum is done by the deflection angle of the track in the $r\phi$ plane. The time information is utilized to acquire measurements of the $r\phi$ coordinates. Using such information a local track segment is reconstructed in TRD, which helps in matching the TRD information with ITS and TPC tracks. The primary function of the TRD is to provide trigger input to the ALICE trigger system for high p_{T} electrons, charged particles, and jets while also performing electron identification. It improves the overall tracking performance at high p_{T} by increasing the global track length leading to better p_{T} resolution.

Time-Of-Flight detector (TOF)

TOF is located radially outward at 3.7 m from the interaction point after TRD with a pseudorapidity acceptance $|\eta| < 0.9$. It is based on Multiwire Resistive Plate Chambers and segmented into 18 azimuthal sectors to provide full azimuthal coverage. It offers charged particle identification, as described in Sec. 3.5, by measuring their time of flight. It is capable of performing time of flight measurements with a resolution better than 50 ps. This information is also helpful in separating pileup events. Also, TOF supplies trigger input to the ALICE trigger system for cosmic ray events and ultraperipheral collisions.

3.2.2 Forward Detectors

This section provides a detailed discussion of the ALICE subdetectors positioned at forward rapidity.

Muon Spectrometer

Muon spectrometer is employed to reconstruct muons at forward pseudorapidity with capability in a wide momentum range of down $p_{\mathrm{T}} = 0$. It consists of a hadron absorber for background rejection, an array of muon trackers, a dipole magnet to bend muon trajectories, and a muon trigger system, as demonstrated in Fig. 3.2. This arrangement allows the reconstruction of single muon and $\mu^+\mu^-$ pair down to very low p_{T} in the pseudorapidity interval $2.5 < \eta < 4$. It plays a crucial role in quarkonium studies at forward rapidity, where quarkonium states (J/ψ, $\psi(2s)$ and Υ states) are reconstructed via their dimuon decay channel with a good invariant mass resolution to separate among those states. It also provides trigger inputs for the events having at least one muon.

T0 detector

T0 detector [178] is designed with two arrays of Photomultiplier Tubes (PMTs) placed on opposite sides of the interaction point covering a pseudorapidity range –3.3 $< \eta <$ –2.9 and 4.5 $< \eta <$ 5. The primary objective of T0 is to deliver fast time signals crucial for the LM trigger system in ALICE (see Sec. 3.3). These signals serve multiple purposes, including waking up the electronics of TRD and providing a reference collision time to TOF. The T0 detector has a remarkable time resolution of less than 50 ps. It determines the precise location of the interaction point within predefined boundaries, ensuring an accuracy better than 1.5 cm.

V0 detector

V0 detector [178] consists of two scintillator arrays namely V0A and V0C placed at $z = 329$ and -87 cm from nominal interaction point (at $z = 0$) which cover pseudorapidity ranges 2.8 $< \eta <$ 5.1 and –3.7 $< \eta <$ –1.7, respectively. Each array consists of four concentric rings to

cover different pseudorapidity intervals. Detector geometry is further segmented into eight azimuthal sectors. Each array is equipped with 32 channels. A complete description of the V0 detector is available in Ref. [167]. The main functions of V0 are triggering, determination of charged-particle multiplicity and azimuthal distributions, LHC background rejection, and luminosity determination. In nucleus-nucleus collisions, centrality and event-plane determination are based on charged-particle multiplicity and azimuthal distributions. V0 performs the following measurements:

- Time measurement: V0 measures the time of particles' flight from the interaction point to the detector array. Based on time of flight, it is possible to discriminate between particles produced in collisions and background from beam-gas interactions. Such measurements are important for triggering collision events.
- Charge measurement: The charge collected in the V0 arrays is proportional to particle hits in the detector. Charged-particle multiplicity is determined based on the total charge collected in V0 channels, which is used for event centrality determination (described in the Sec. 3.6). V0 also provides centrality triggers based on charge measurements. The detailed detector simulations extract the relation between the total amount of charge collected by V0 rings and the number of produced primary charged particles in corresponding $\Delta\eta$.

Forward Multiplicity Detector

Consisting of silicon strip channels, the Forward Multiplicity Detector (FMD) is divided into five ring counters. These ring counters are categorized into two types: one with containing 20 sectors and the other containing 40 sectors in the azimuthal angle. The primary role of the FMD system is to provide accurate measurements of the charged particle multiplicity in the pseudorapidity range of $-3.4 < \eta < -1.7$ and $1.7 < \eta < 5.0$. The FMD information is helpful in the analysis of the multiplicity fluctuations per event and flow measurements.

Zero Degree Calorimeter

The Zero Degree Calorimeter (ZDC) [179] comprises two sets of calorimeters positioned symmetrically on either side of the interaction point at a distance of 112.5 meters and very close to the beam pipe. The main functions of the ZDC are event centrality determination, beam-gas background rejection and luminosity determination. It also provides information about diffractive events in pp collisions.

3.3 Trigger system in ALICE

A trigger system not only allows to separate the important events from the physics perspective but also guarantees an efficient usage of resources in the experiment. Central

Trigger Processor (CTP) [180] is the responsible unit for trigger management in the ALICE experiment, which is installed in the ALICE cavern. Some essential trigger requirements exist for the LHC Run 2 program, e.g., selecting events for different physics interests and optimizing for different running scenarios for pp, p–Pb, and Pb–Pb system. ALICE uses a 4-level trigger system due to the different readout speeds of different subdetectors. The CTP makes triggering decisions quickly in 100 ns based on trigger inputs sent by triggering detectors and sends trigger signals to readout detectors. The trigger system is described in the following points.

- In Run 2, the LM level was introduced to activate the TRD electronics by delivering a rough minimum bias-like trigger signal.
- The triggering detectors send L0 trigger input to the CTP, which sends the L0 trigger signal to readout detectors in response. Readout detectors receive L0 trigger signal in 1.2 μs after the interaction, and the digitization process gets started.
- For the next trigger signal, L1, the triggering detector further determines the quality of the same event by applying some criteria online. If the event passes this criterion, then L1 trigger input is sent to the CTP where it is checked and directed to the readout detectors. Readout detectors receive L1 trigger after 6.5 μs of L0 trigger. In case of no L1 trigger input, CTP does not send any further trigger signal to readout detectors, and in the absence of an L1 trigger, the event is not further processed.
- Triggering detectors further checks for more event properties and generate L2 trigger input to be sent to the CTP. Similarly, readout detectors receive L2 trigger after 100 μs of L0 trigger.

After following these steps, an event is fully collected by readout detectors and then sent to ALICE data acquisition for further reconstruction. Usually, triggering and readout detectors are grouped into classes and clusters, respectively, for efficient data-taking performance.

3.4 Tracking in the Central Barrel

In the central barrel, track and vertex reconstruction is based on information from several tracking detectors. The complete procedure is briefly described below:

- **Clusterization**: Reconstruction begins with cluster finding for all central barrel detectors, and the process is called Clusterization. In TPC, for example, a cluster is defined by consecutive five pads in the wire direction as shown in Fig. 3.7 and five bins in the time direction if it fulfills the standard criteria.
- **Vertex finding (based on SPD clusters)**: Tracklets are reconstructed from SPD clusters within its layers, and these SPD tracklets determine the initial primary vertex. It is a

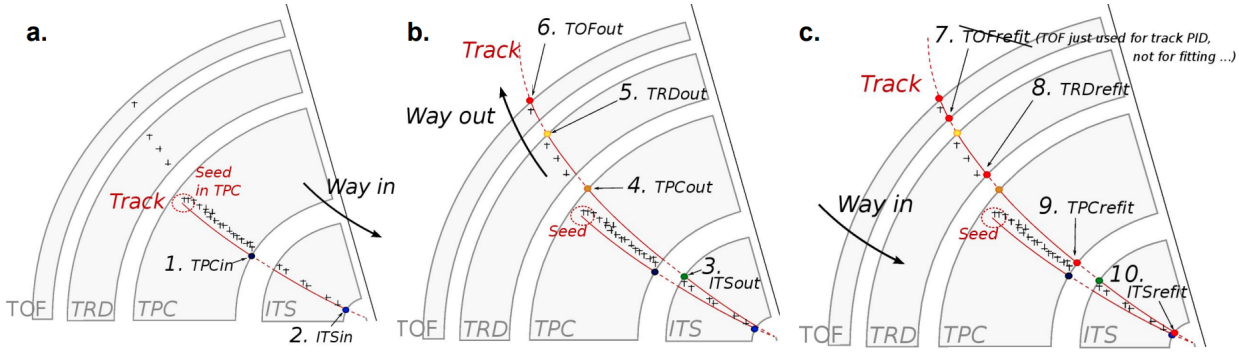

Figure 3.8 Illustration of track reconstruction steps in central barrel detectors: a) clusterization and TPC tracking and inward propagation to ITS, b) Starting from ITS, propagation of track towards TPC and matching with outer detectors, e.g., TRD and TOF, c) Final propagation of track from TOF clusters to ITS [182]

space point where most SPD tracklets converge, which serves as an initial primary vertex for further particle track reconstruction.

- **TPC track finding**: Track finding in the TPC starts with searching for seed clusters in the outermost two pad rows where track density is relatively lower than in the inner pad rows. It is to be noted that particle trajectories follow a helical path in the central barrel due to a solenoidal magnetic field in z-direction. To completely define a trajectory, it is parameterized by five track parameters: $y, z, 1/R, \gamma$ and $\tan\lambda$. These parameters are updated by the Kalman-filter algorithm [181] in each pad row with corresponding cluster parameters and errors. Thus, the following clusters in the next inner TPC pad rows are determined. The SPD-based primary vertex constraints track reconstruction in TPC.

- **TPC to ITS tracking**: TPC track is propagated to the outer layer of ITS by matching with SSD clusters and propagated to the inner layers of ITS. In this propagation from TPC to ITS, many potential track hypotheses appear, and the best one is found using the χ^2 value. The procedure is shown in Fig. 3.8(a). If some ITS clusters are not matched with any TPC track due to low momentum or dead zones in TPC segments, a standalone ITS tracking is applied to such ITS clusters. In the end, newly found tracks are projected towards a point at a distance to the closest approach (DCA) to the SPD-based primary vertex.

- **Inside–out tracking**: As shown in Fig. 3.8(b), tracking is started from the DCA point and propagated to the ITS layers and then to the outer layer of TPC using the Kalman-filter algorithm. Further, the track is propagated to the inner layer of TRD, which is matched with the TRD tracklets and propagated to the outer layers of TRD. Similarly, the track is extended to the TOF clusters and propagated further to match the clusters in HMPID and EMCal.

- **Final track and vertex reconstruction**: After full central barrel tracking, the track is further updated by refitting from the outer layers of TOF to the DCA point. In this step, track reconstruction is completed in the central barrel, and the final primary vertex is determined based on the global tracks as shown in Fig. 3.8(c).

Secondary vertices related to the decay of strange hadrons, e.g. K^0_s, Λ, $\bar{\Lambda}$, and photon conversions are reconstructed after primary vertex determination. A complete description is given in Ref. [183].

3.5 Particle Identification

After track reconstruction in the central barrel, it is required to tag the tracks according to the particle species. ALICE is known for its excellent particle identification capabilities, especially in the low momentum range in the central barrel region. In the central barrel, ITS, TPC, TRD, TOF, and HMPID play a crucial role in the identification of charged particles. These detectors offer different performances depending on the particle momentum. The overall particle identification (PID) performance is enhanced by combining the individual PID information from these detectors. The information from each detector is used to allocate a distinct set of probabilities, one for each particle type, to every track. These probabilities from several detectors for each track are normalized to one. Also, in the cases where a detector lacks identification capability for a specific track, it allocates equal probabilities to all possible particle types. If any detector clearly determines the type of track then sets the probability to unity for particular type and to 0 for other types. In the central barrel, particle identification relies on various techniques that differ across different detectors.

In the TPC and ITS, particle identification is done by measuring simultaneously the specific energy loss per unit length ($\mathrm{d}E/\mathrm{d}x$) and the momentum (p) of particles. The TPC provides particle identification in a wide momentum range from 150 MeV/c to few tens of GeV/c covering $|\eta| < 0.9$. In the TPC, the energy loss of particles as a function of their momenta is described by the Bethe-Bloch formula as illustrated in Fig. 3.9. The solid lines show parametrization the Bethe-Bloch formula, proposed for the first time by the ALEPH experiment [184]. It can be described as,

$$f(\beta\gamma) = \frac{P_1}{\beta^{P_4}} \left(P_2 - \beta^{P_4} - \ln \left[P_3 + \frac{1}{(\beta\gamma)^{P_5}} \right] \right), \tag{3.1}$$

where β is particle velocity, γ is Lorentz factor, and P_{1-5} are fit parameters. As shown in Fig. 3.9(left), at low momentum $p < 1$ GeV/c, particles can be identified individually while at high momentum the separation between different particle species is done on statistical basis via multi-Gaussian fits. A pure sample is selected on the criteria of n standard deviations ($n\sigma$) around theoretical value of $\mathrm{d}E/\mathrm{d}x$ for particle species. The $n\sigma$ value is calculated as

$$n\sigma = \frac{(\mathrm{d}E/\mathrm{d}x)^{\text{Measured}} - (\mathrm{d}E/\mathrm{d}x)^{\text{Expected}}}{\sigma}, \tag{3.2}$$

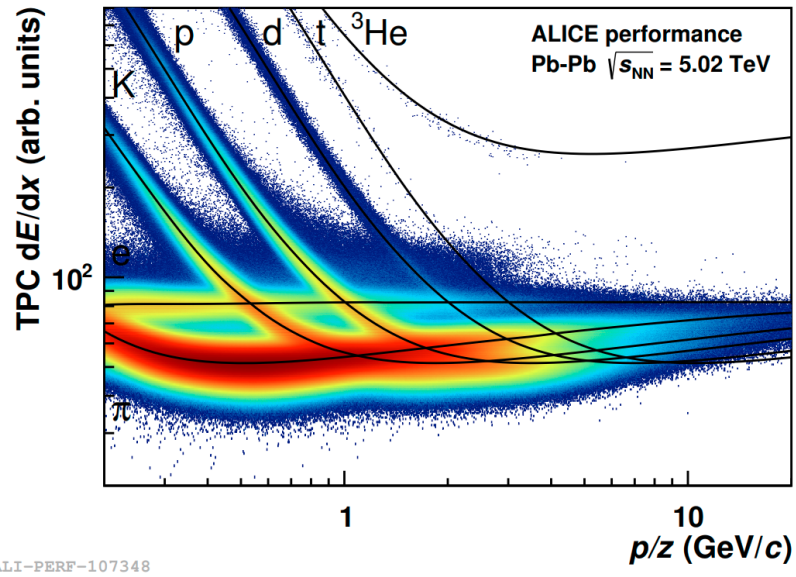

Figure 3.9 Specific energy loss per unit length as a function of momentum in TPC in Pb–Pb collisions at $\sqrt{s_{\rm NN}}$= 5.02 TeV. Solid lines represent fit results with ALEPH parametrization function as described by Eq. 3.1.

where σ is the dE/dx resolution, $(\mathrm{d}E/\mathrm{d}x)^{\rm Measured}$ is the measured and $(\mathrm{d}E/\mathrm{d}x)^{\rm Expected}$ is expected energy loss of particle at a given momentum in the TPC.

In the TPC, energy loss measurement of a particle is based on the collected charge in TPC clusters assigned to a track in each pad row. The clusters at the edges of TPC sectors along with overlapping clusters are excluded from this process to guarantee a good PID performance. In pp and Pb–Pb collisions, dE/dx is determined using different treatments of the collected charge in the clusters. In pp collisions, total cluster charge is used for dE/dx determination while in case of Pb–Pb collisions the maximum cluster charge is used to ensure the best separation power [1] in central Pb–Pb collisions.

As discussed in Sec. 3.2.1, in the ITS, SSD and SDD offers particle identification down to 100 MeV/c by measuring dE/dx. The ITS dE/dx measurement achieves a resolution approximately 10-12% up to 1 GeV/c, offering excellent separation capabilities for pions and kaons up to a momentum of 450 MeV/c and between protons and kaons up to around 1 GeV/c.

In the TOF, particle identification is based on the measurement of time of flight (t) of the particle, its momentum (p) and the global track length(l). The mass (m) of particle can be written as a function of these three quantities in a form of the following expression (considering speed of light, $c = 1$) [185],

$$m = p\sqrt{\frac{t^2}{l^2} - 1}. \tag{3.3}$$

[1]Separation power is the mean difference between dE/dx of two particle species at a given momentum in terms of multiples of their standard deviations.

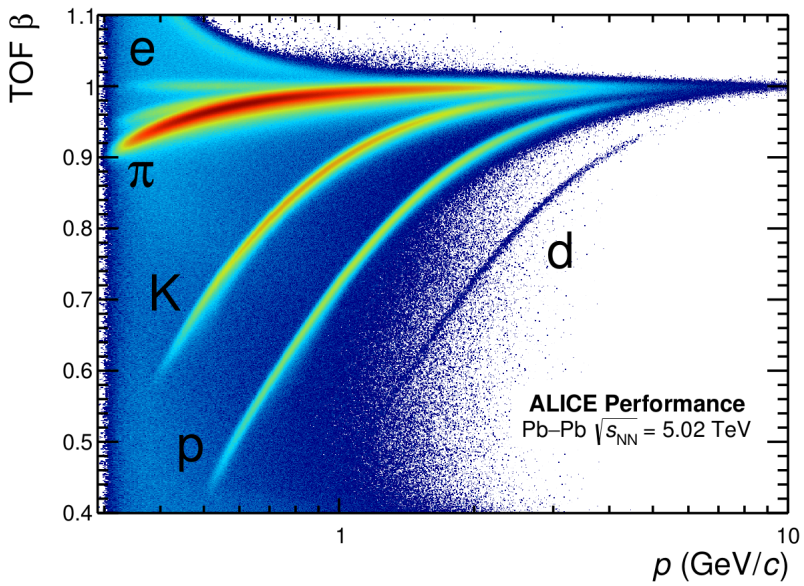

Figure 3.10 Velocity (β) as a function of momentum measured by TOF in Pb–Pb collisions at $\sqrt{s_{\rm NN}}$= 5.02 TeV.

The starting time of the particle's trajectory is provided by the T0 [186] and particle's arrival time is measured by TOF. The time of flight is calculated using this information while momentum is obtained from the the ITS and TPC. The particle identification is represented by the velocity (β) of particle as function of its momentum as shown in Fig. 3.10. The TOF offers particle identification in the intermediate momentum range (up to 4 GeV/c) at $|\eta| <$ 0.9. It offers 3σ separation between kaon-pion in a momentum range up to 2.5 GeV/c and kaon-proton up to 4 GeV/c.

3.6 Centrality Determination

Centrality is an event property that characterizes the nuclear overlap region of an event in nuclear collisions. The precise centrality determination is of utmost importance in nuclear collisions due to the centrality dependence exhibited by various physics observables. By precisely determining the centrality, we can better understand and interpret the experimental results, as different centrality ranges correspond to varying degrees of overlap and energy deposition in the collision system. Centrality is defined as a percentile of total hadronic cross section ($\sigma_{\rm AA}$) above a threshold multiplicity of charged particles ($N_{\rm ch}^{\rm th}$) as shown in the following expression,

$$c \approx \frac{1}{\sigma_{\rm AA}} \int_{N_{\rm ch}^{\rm th}}^{\infty} \frac{d\sigma_{\rm AA}}{dN'_{\rm ch}}\, dN'_{\rm ch}\,. \tag{3.4}$$

Centrality determination in nuclear collisions is often based on the measurement of charged-particle multiplicity within the event which is closely related to the amplitude of the V0 detector signal. Geometrical quantities such as impact parameter (b), number of

interacting nucleons ($N_{\rm part}$), and number of binary nucleon–nucleon collisions ($N_{\rm coll}$) are essential to characterize the event but they are not directly measurable in the experiment. A Monte Carlo Glauber model [30] is utilized to establish a correlation between the geometrical characteristics of an event and the corresponding charged-particle multiplicity. This model assumes that there are only two sources of particle production: hard and soft interactions, which are proportional to $N_{\rm coll}$ and $N_{\rm part}$, respectively. The particle multiplicity in each nucleon–nucleon collision is described by a Negative Binomial Distribution (NBD). Therefore, the charged particle multiplicity distribution in the nuclear collisions is described by the following relation,

$$p(n) = P_{\mu,k}(n) \cdot (f \times N_{\rm part} + (1-f) \times N_{\rm coll}) \,, \tag{3.5}$$

where $P_{\mu,k}(n)$ represents the probability of producing n particles in final state by a single source and f is free parameter to be determined in the parameterization of V0 signal amplitude.

The V0 amplitude distribution is parameterized by the NBD-MC-Glauber model represented by Eq. 3.5 as shown in Fig. 3.11. The events are classified into centrality percentiles by introducing sharp cuts on V0 multiplicity distribution as demonstrated in Fig. 3.11. The quantities such as $\langle N_{\rm part} \rangle$, $\langle N_{\rm coll} \rangle$ and nuclear overlap density $\langle T_{\rm AA} \rangle$ can be evaluated for each centrality class which are shown in Table 3.2 for $\sqrt{s_{\rm NN}}$= 5.02 TeV, taken from [187]. $T_{\rm AA}$ is ratio of $N_{\rm coll}$ and total inelastic hadronic cross section ($\sigma^{\rm inel}_{\rm AA}$) which represents effective nucleon luminosity in the collisions.

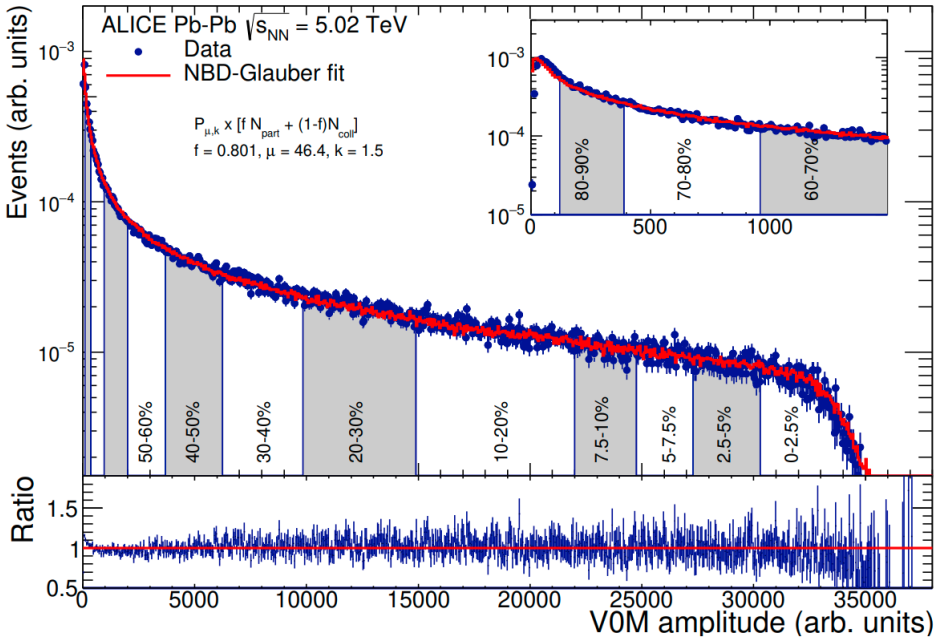

Figure 3.11 Illustration of events as a function of V0 amplitude parametrized by the Monte-Carlo Glauber model, and classified into centrality classes [187].

The V0 detector is the main detector for centrality determination because it offers the best resolution for the overall centrality range. In central events, the resolution for centrality determination is approximately 0.5%, while in peripheral Pb-Pb collisions, the resolution is around 2%. Other detectors such as TPC and ITS are also capable of centrality determination. However, only the V0 and ZDC detectors are considered to eliminate the biases in the centrality determination within the central barrel.

Centrality	$\langle T_{\mathrm{AA}} \rangle (\mathrm{mb}^{-1})$	$\langle N_{\mathrm{part}} \rangle$	$\langle N_{\mathrm{coll}} \rangle$
0-5%	26.08 ± 0.18	383.40 ± 0.57	1763.00 ± 19.40
0-10%	20.44 ± 0.17	357.30 ± 0.75	1572.00 ± 17.40
10-20%	14.4 ± 0.13	262.00 ± 1.15	973.40 ± 11.30
20-30%	8.77 ± 0.10	187.90 ± 1.34	592.70 ± 8.21
30-40%	5.09 ± 0.08	130.80 ± 1.33	343.80 ± 5.76
40-50%	2.75 ± 0.05	87.14 ± 0.93	185.70 ± 3.33
50-60%	1.35 ± 0.03	54.34 ± 0.80	91.41 ± 2.11
60-70%	0.60 ± 0.016	30.97 ± 0.57	40.50 ± 1.03
70-80%	0.24 ± 0.005	15.72 ± 0.24	16.12 ± 0.34
80-90%	0.08 ± 0.001	6.97 ± 0.07	5.67 ± 0.10

Table 3.2 Nuclear overlap function $\langle T_{\mathrm{AA}} \rangle$, $\langle N_{\mathrm{part}} \rangle$, and $\langle N_{\mathrm{coll}} \rangle$ with systematic uncertainties in Pb–Pb collisions for each centrality class, taken from [187].

Chapter 4

Measurement of non-prompt J/ψ fractions

"If we knew what it was we were doing, it would not be called research, would it?"

Albert Einstein

This chapter is dedicated to a detailed description of the extraction of non-prompt J/ψ fraction (f_{B}) in Pb–Pb collisions at $\sqrt{s_{\mathrm{NN}}}$= 5.02 TeV. In the opening section, an overview of the utilized data sample is presented, encompassing the criteria employed for the selection of J/ψ candidates. The subsequent section provides a detailed account of the extraction procedure for non-prompt J/ψ. In the following sections, a thorough description is given regarding the corrections to the non-prompt J/ψ fraction and the estimation of systematic uncertainties.

4.1 Data Sample

The analysis conducted in this study utilizes the complete available statistics obtained from Pb–Pb collisions at $\sqrt{s_{\mathrm{NN}}}$= 5.02 TeV collected by the ALICE experiment in 2015 and 2018. The datasets were collected with minimum bias (MB) triggered event, a coincidence of signals registered in the both scintillator arrays of the V0 detector, corresponding to an integrated luminosity approximately 24 $\mu\mathrm{b}^{-1}$. During data taking in 2018, the Pb–Pb dataset was enriched with central (0–10%) and semicentral (30–50%) events. This enrichment was made possible by utilizing the centrality triggers provided by the V0 detector. The integrated luminosity of the full data sample reaches approximately 105 $\mu\mathrm{b}^{-1}$ in 0–10% and 51 $\mu\mathrm{b}^{-1}$ in 30–50% centrality interval.

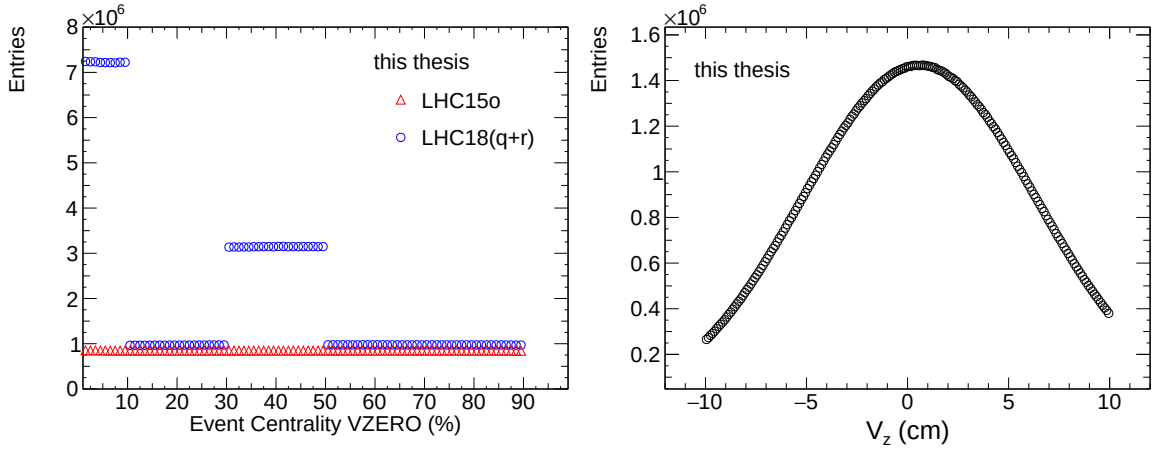

Figure 4.1 Distribution of event centrality (left) and z-position (right) of the events.

4.1.1 Event selection

In the analysis, both minimum bias events and the events selected by centrality triggers, as provided by the V0 detectors, are included. The event centrality determination is performed by parameterization of V0 amplitude as described in the Sec. 3.6. To account for the presence of electromagnetic background, peripheral events with a centrality exceeding 90% are excluded from the analysis. To ensure the optimal detector acceptance, the selected events must meet the criterion of primary vertex z position (V_z), falling within the range of $|V_z| < 10$ cm. This requirement is imposed to exclude events with V_z values outside this range, as they would experience a reduction in detector acceptance. The Fig. 4.1 demonstrates the distribution of event centrality (left) and V_z (right).

There can be more than one collision in a single bunch crossing, $i.e.$, in-bunch pileup, and also, collision(s) from different bunch crossings can be registered as a good event known as an out-of-bunch pileup event. Such events are removed from the analyzed data sample. A correlation between the number of TPC clusters and the total number of SSD and SDD clusters is used to identify the pileup events. The number of TPC clusters in an event can be significantly influenced by subsequent interactions occurring tens of microseconds related to the triggered event. However, the number of clusters in the SSD and SDD detectors remains unaffected. In cases where there is only one interaction or where the second interaction has a minimal impact, a narrow correlation is observed between the total number of SSD and SDD clusters and the number of TPC clusters. Events with a higher number of interactions generally exhibit a larger number of TPC clusters compared to events with only a single interaction. The Fig. 4.2 illustrates the correlation between the total number of SSD and SDD clusters and the number of TPC clusters, both before (left) and after (right) the removal of pileup events. The Table 4.1 provides the number of events in each centrality interval after passing trigger and event selection requirements.

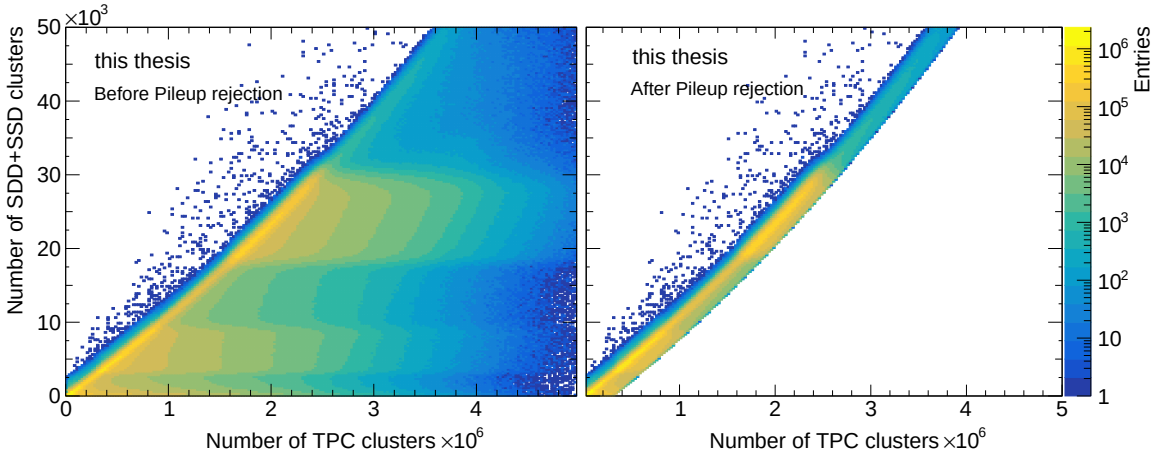

Figure 4.2 Total number of SSD and SDD clusters as a function number of TPC clusters. Before (left) and after (right) rejection of pileup events. Color palette represents the number of entries on z-axis.

Data period	Centrality	Triggers	N_{Events}
LHC18(q+r)	0–10%	MB + Central	72 M
	10–30%	MB	19 M
	30–50%	MB + Semicentral	62 M
LHC15o	0–10%	MB	8 M
	10–30%	MB	17 M
	30–50%	MB	17 M

Table 4.1 Number of events after passing event selection used in the analysis.

4.1.2 Track selection

To ensure the selection of good quality tracks and minimize background contamination, a set of track selection criteria is applied, as summarized in Table 4.2. The track selection criteria are classified into several groups, namely acceptance, tracking, and PID cuts. The acceptance selections is based on η and p_{T}. The tracks with p_{T} below 1 GeV/c are excluded from analyses which helps to suppress background from photon conversions or Dalitz decays. Only tracks with $|\eta|$ less than 0.9 are considered.

The selection criteria based on the TPC play a crucial role in ensuring optimal tracking and PID performance. The TPC track refit serves as a important quality criterion to eliminate tracks not properly reconstructed in the TPC. There are several background contributions from other sources, e.g., charged particles, such as pions and kaons, producing one neutral and one charged decay product in the TPC active volume. It is possible to identify them by looking for TPC trajectories that exhibit small-angle kinks. Such tracks are excluded from the analysis. Also, tracks with sparse space points or large continuous missing areas along their

trajectory are excluded from this analysis based on the number of clusters used for particle identification, crossed rows, and crossed rows over the number of clusters in the TPC. To exclude the tracks affected by TPC space charge distortions, an additional selection criterion is applied to the TPC χ^2 of the track fit per cluster. Due to a modification in parametrization of the uncertainties of the TPC clusters, this selection criterion differs for the 2015 and 2018 data sets.

Further track selection criteria, such as ITS refit and at least a hit in the SPD layer, helps in pile-up rejection and improve the momentum resolution. Also, electrons originating from photon conversions in the detector material are rejected if there is at least one SPD hit in the pixel layer. An evaluation of ITS-TPC matching efficiency is done at the track level through data and MC simulation. There is also a requirement for the distance of the closest approach (DCA) of tracks from their primary vertex to be constrained within 3 cm in the z direction and 1 cm in the xy plane. Such constraints on DCA_z helps to reduce out-of-bunch pileups events, whereas constraining DCA_{xy} helps to suppress background from secondary particles. These DCA constraints do not exclude non-prompt J/ψ candidates as the limits are sufficiently wide.

Selection Group	Description	Selection criteria
Acceptance	p_{T}	> 1 GeV/c
	$\lvert\eta\rvert$	< 0.9
Tracking	Impact parameter	$\lvert DCA_{xy}\rvert < 1$ cm
		$\lvert DCA_z\rvert < 3$ cm
(TPC related)	Number of TPC crossed rows	> 70
	TPC crossed rows/findable cluster	> 0.8
	Number of TPC clusters for PID	> 50
	TPC χ^2 per cluster	< 2.5 (for 2018 dataset)
	-	< 4.0 (for 2015 dataset)
	TPC refit	applied
	Kinks	rejected
(ITS related)	ITS refit	applied
	ITS χ^2 per cluster	< 36
	SPD layer hit	Any layer
Pre-filter cuts	p_{T}	> 900 MeV/c
	Mass	< 50 MeV/c^2

Table 4.2 Track selection criteria used in the analysis.

4.1.3 Electron Identification

After selecting good quality tracks based on detector response, it is very important to identify the tracks based on their specific energy loss in the TPC volume. An essential part is the identification of electrons. It requires a careful examination of the tracks left by the particles in the detector. The momentum of the track is determined by its curvature in the magnetic field. This information is then used to calculate the energy loss, $\mathrm{d}E/\mathrm{d}x$, as described in Sec. 3.5. In this analysis, the electron identification is based on the $\mathrm{d}E/\mathrm{d}x$ measurements in the TPC. Generally, electrons having momentum larger than 1 GeV/c have almost constant specific energy losses, as illustrated in Fig. 3.9. In contrast, heavier particles behave differently. Fig. 3.9 illustrates that the momentum threshold at which the $\mathrm{d}E/\mathrm{d}x$ signal of proton intersects with the $\mathrm{d}E/\mathrm{d}x$ signal of a typical electron is around 1 GeV/c. At higher momentum, the $\mathrm{d}E/\mathrm{d}x$ of pion approaches the $\mathrm{d}E/\mathrm{d}x$ of electron. Tracks with $\mathrm{d}E/\mathrm{d}x$ close to the pion and the proton hypotheses are excluded as electrons are rare compared to pions and protons. It decreases hadron contamination in the electron sample. Several detector effects during data taking have the potential to alter the PID responses of the TPC. To account for these effects, an offline calibration has been carried out on the TPC $\mathrm{d}E/\mathrm{d}x$ signals for electrons, pions, protons, and kaons which is described in Appendix A. After this calibration, a selection criteria has been applied to electron $\mathrm{d}E/\mathrm{d}x$ signal in terms of standard deviations of TPC $\mathrm{d}E/\mathrm{d}x$. The Fig. 4.3 demonstrates the $n\sigma$ distribution of $\mathrm{d}E/\mathrm{d}x$ for electrons in the TPC. It is shown as a function of the momentum of particles estimated at the inner wall of the TPC (p_{IN}). Only those tracks which are 4.5σ away from the pion and proton expectation are included in 0–10% and 10–30% centrality classes for p_{IN} below 5 GeV/c. The pions are the largest source of contamination in the electron sample therefore, a tight selection criteria is used. In 30–50% centrality interval, a 3.5σ exclusion cut is used irrespective of p_{IN}. Table 4.3 provides an overview of all particle identification criteria in terms of standard deviations of TPC $\mathrm{d}E/\mathrm{d}x$ for electrons.

Centrality	p_{IN} selection	PID cuts
0-10%, 10-30%	$p_{\mathrm{IN}} < 5$ GeV/c	$-2 < n\sigma(e) < 3$
		$n\sigma(\pi, p) > 4.5$
	$p_{\mathrm{IN}} > 5$ GeV/c	$-1 < n\sigma(e) < 3$,
30-50%		$-3 < n\sigma(e) < 3$
		$n\sigma(\pi, p) > 3.5$

Table 4.3 TPC PID selection criteria used in the analysis.

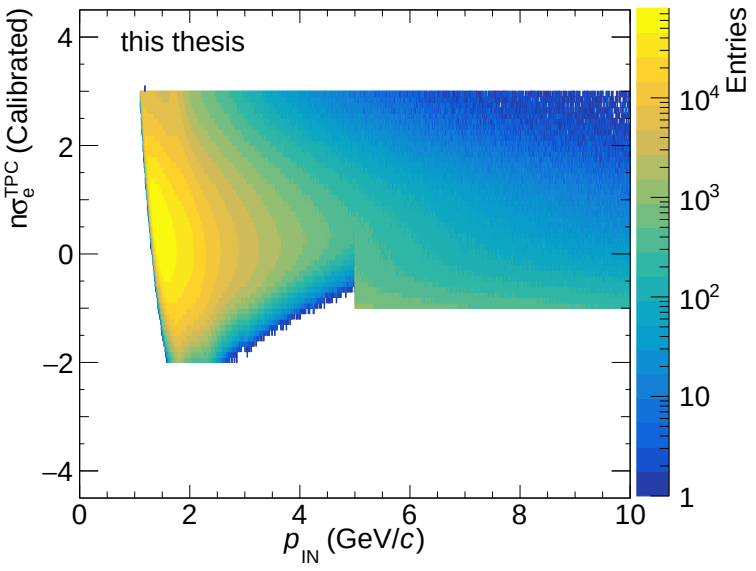

Figure 4.3 $n\sigma$ distribution of electron dE/dx in the TPC as a function of track momentum in the inner wall of the TPC, p_{IN}, after application of all selection criteria. Color palette represents the number of entries on z-axis.

4.1.4 Monte Carlo sample

A large fraction of the total J/ψ produced in the collisions could not be reconstructed due to detector acceptance and reconstruction efficiency limitations. To reconstruct J/ψ candidate, both of the dielectron daughters must be inside detector acceptance $|\eta| < 0.9$. All simulated particle tracks must pass the acceptance, tracking and PID selection criteria to ensure J/ψ signals are being reconstructed and the background is being suppressed. Detector acceptance and efficiency is determined using Monte Carlo simulation, keeping the same data-taking conditions.

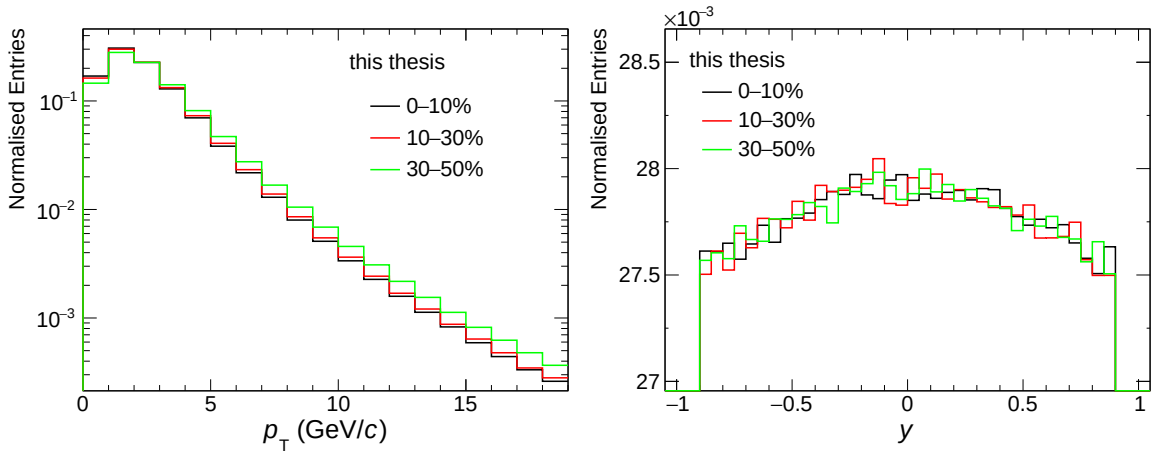

Figure 4.4 Normalized distribution of transverse momentum and rapidity of J/ψ produced by MC simulation.

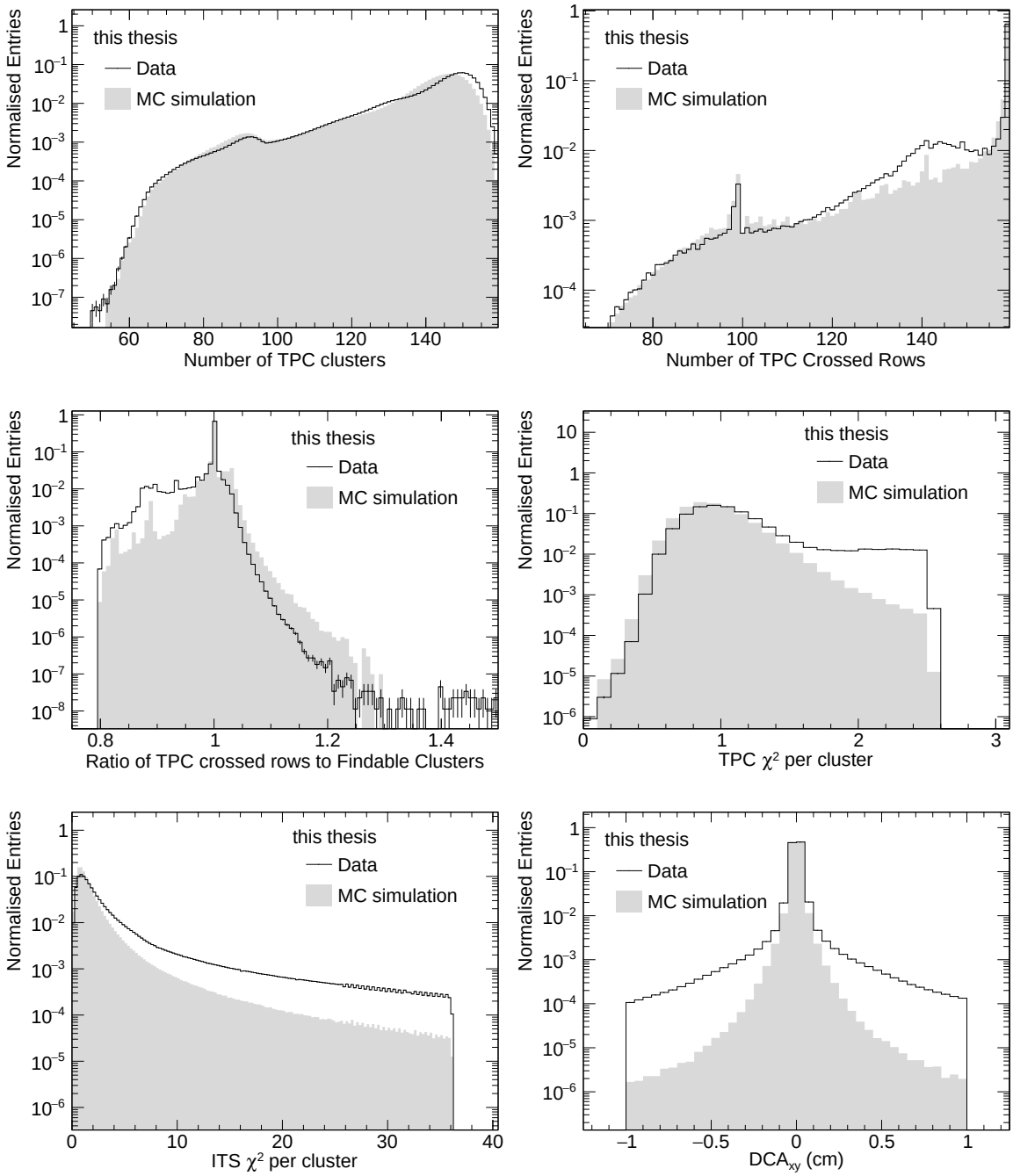

Figure 4.5 Normalized distribution of tracking variables for tracks selected for analysis in data and MC simulation.

Within the ALICE experiment, Pb–Pb collisions are simulated using the HIJING [188] Monte Carlo model developed to study ultrarelativistic nuclear collisions. In the LHC18r and LHC18q data sets, approximately 16M events were simulated. The simulation is divided into three parts: LHC20g5a, LHC20g5b, and LHC20g5c, corresponding to the different centrality classes: 0–10%, 10–30%, and 30–50%. Since J/ψ production cross section is small, they are injected into each HIJING Pb–Pb event from PYTHIA 6.4 [189] to increase the statistics. The kinematic distribution of J/ψ produced by MC simulations is shown in Fig. 4.4. In the MC simulation, a sample of prompt J/ψ is generated with a realistic p_{T} distribution from available inclusive J/ψ measurements in Pb–Pb collisions at midrapidity. For obtaining a non-prompt J/ψ sample, beauty hadrons are generated using PYTHIA 6.4 and then forced to decay into J/ψ. In the sample, around 70% of total injected J/ψ are prompt while the rest 30% are non-prompt. Following previous measurements [111, 160], it is assumed in this study that both prompt J/ψ and beauty hadrons are unpolarized. Each J/ψ is decayed via a dielectron channel by EvtGen [190] that simulates final state radiation using the PHOTOS [191] algorithm. The GEANT 3 [192] simulates particle propagation through the detector setup where detector performance, data-taking conditions, including dead detector zones, and other physics processes, are taken into account. A comparison of normalised track distributions from data and MC simulation are shown in Fig. 4.5.

4.1.5 Impact parameter tuning

The separation of prompt and non-prompt J/ψ candidates is based on their pseudo-proper decay length distribution (described in Sec. 4.2). The pure samples of prompt and non-prompt J/ψ are extracted from the MC simulations. A good pseudoproper decay length resolution is an important element for the analysis. It is essential to have a similar impact parameter resolution ($d_0(r\phi)$) for both, data and MC simulations. In the data, the impact parameter resolution is worse as compared to MC sample as a function of p_{T}. A tuning procedure is applied to MC sample to achieve a similar performance of impact parameter resolution as in the data. In this procedure, the impact parameter residuals are re-scaled on-the-fly with respect to their true kinematic values to achieve a similar impact parameter resolution performance in the data and MC sample [193]. As shown in Fig. 4.6, the discrepancy between data and MC sample rises up to 15% (left panel), while it is only 3% (right panel) after applying the tuning procedure.

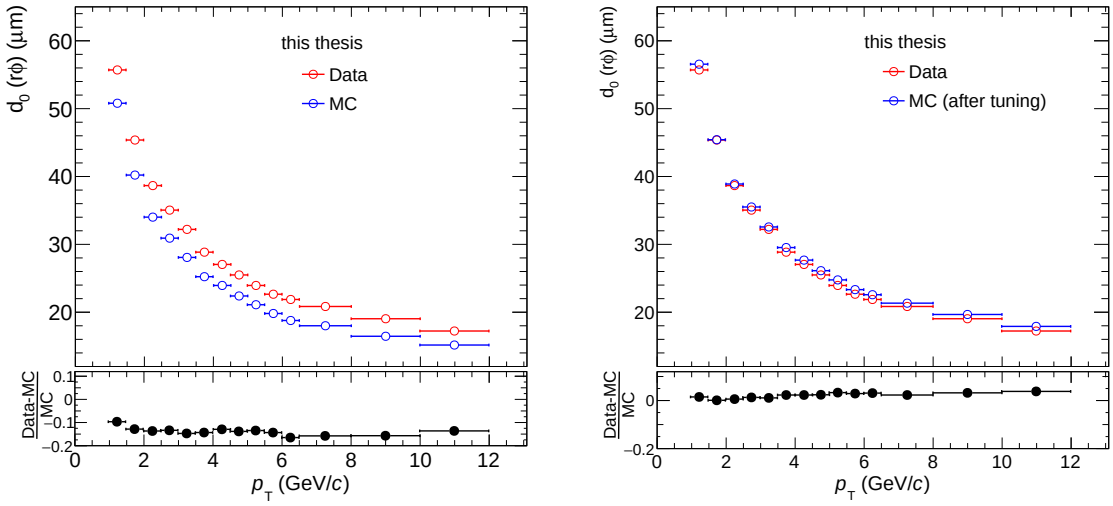

Figure 4.6 Impact parameter resolution of the tracks in real-data and MC sample before (left) and after (after) application of tuning procedure.

4.2 Extraction of Non-prompt J/ψ fraction

Non-prompt J/ψ is distinguished by its longer decay length ($\vec{L}$), which is quantified as the vector connecting the primary vertex to the reconstructed B-hadron decay vertex. The quantity for extraction of the non-prompt J/ψ component depends on the signed projection between $\vec{L}$ and p_{T} of J/ψ, as described in the following expression,

$$L_{xy} = \vec{L} \cdot \frac{\vec{p}_{\mathrm{T}}}{|p_{\mathrm{T}}|}. \tag{4.1}$$

As shown in Fig. 4.7, B-hadron travels L_{xy} distance before decaying into J/ψ in xy plane. Therefore, prompt and non-prompt J/ψ component are separated based on pseudoproper decay length (x), described by the following expression,

$$x = L_{xy} \cdot \frac{m_{\mathrm{J}/\psi}}{p_{\mathrm{T}}}, \tag{4.2}$$

where, $m_{\mathrm{J}/\psi}$ is the mass and p_{T} is transverse momentum of J/ψ.

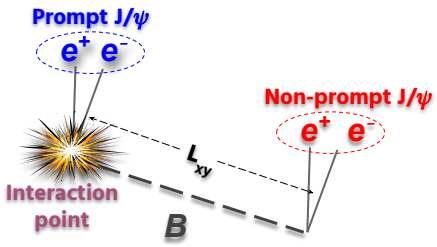

Figure 4.7 Illustration of prompt and non-prompt J/ψ decay in xy plane.

4.2.1 Unbinned likelihood fit method

Non-prompt J/ψ fraction is extracted by two-dimensional unbinned maximum likelihood fits on invariant mass and pseudoproper decay length of dielectron candidates. By comparing the signal components' distributions with the pseudoproper decay length, the non-prompt J/ψ fraction of the yield can be determined statistically. Statistical analysis allows discrimination between the prompt and non-prompt J/ψ components based on their decay length.

The experimentally measured invariant mass, m and x can be regarded as a randomly selected sample of two independent variables, statistically distributed as a function of an overall probability density function describing the differences between candidates. In this case, we can estimate the parameters related to m and x using the maximum likelihood principle if we can separate the m and x. If the total number of J/ψ candidates in a sample is N, the maximum likelihood estimation is represented by the following expression,

$$\ln L = \sum_{i=1}^{N} \ln F(m, x), \tag{4.3}$$

where function $F(m, x)$ is estimated for each set of m and x. The sum runs over all the J/ψ candidates, denoted by N, in a given mass interval. The function, $F(m, x)$, indicates the probability of seeing a signal or background candidate. It can be written as a combination of the product of probability density functions (PDFs) of the random variables m and x in the following way,

$$F(m, x) = f_{\text{Sig}} \cdot F_{\text{Sig}}(x) \cdot M_{\text{Sig}}(m) + (1 - f_{\text{Sig}}) \cdot F_{\text{Bkg}}(x) \cdot M_{\text{Bkg}}(m), \tag{4.4}$$

where

$$f_{\text{Sig}} = \frac{N_{\text{J}/\psi}}{N_{\text{J}/\psi} + N_{\text{Bkg}}}, \tag{4.5}$$

where $N_{\text{J}/\psi}$, N_{Bkg} are the signal and background yields obtained from the invariant mass distributions. The signal component $F_{\text{Sig}}(x)$ describes the pseudoproper decay length PDF for prompt and non-prompt J/ψ as described by the following expression,

$$F_{\text{Sig}}(x) = f_{\text{B}}^{'} \cdot F_{\text{B}}(x) + (1 - f_{\text{B}}^{'}) \cdot F_{\text{Prompt}}(x), \tag{4.6}$$

where $F_{\text{B}}(x)$ and $F_{\text{Prompt}}(x)$ represents non-prompt and prompt J/ψ pseudoproper decay length PDFs and $f_{\text{B}}^{'}$ is non-prompt J/ψ fraction, obtained from unbinned likelihood fitting procedure. It can be written in the following way,

$$f_{\text{B}}^{'} = \frac{N_{\text{B}\to\text{J}/\psi}}{N_{\text{B}\to\text{J}/\psi} + N_{\text{Prompt J}/\psi}}, \tag{4.7}$$

where $N_{\mathrm{B}\to \mathrm{J}/\psi}$ is the yield of non-prompt J/ψ and $N_{\mathrm{Prompt\,J}/\psi}$ is the yield of prompt J/ψ. The prompt J/ψ decays at the primary vertex. It is considered that their pseudoproper decay length distribution coincides with the pseudoproper decay length resolution function $R(x)$. The $R(x)$ measures how accurately x can be reconstructed in the experiment. All the x-dependent distributions must be convoluted with experimental resolution, $R(x)$. In Eq. 4.4, the terms $M_{\mathrm{Sig}}(m)$, $M_{\mathrm{Bkg}}(m)$ are the invariant mass signal and background PDFs while $F_{\mathrm{Bkg}}(x)$ is the background PDF for pseudoproper decay length.

Once the PDFs are known, the maximum likelihood approach can be used to provide the best estimate of unknown parameters. Based on simulations of samples, these estimators have been verified to be unbiased and consistent. Since we do not know the underlying models, we infer some information from the data. It is possible to parameterize functional shapes with an appropriate number of parameters and then extract the values of unknown parameters, *i.e.*, $f_{\mathrm{B}}^{'}$ and f_{Sig}. This approach can bring in some biases in the estimation of final parameters. It is important to consider these biases while evaluating systematic uncertainties.

The signal PDF components are extracted by parameterization of m and x distributions obtained from MC simulation, while background components are from the data. These components are fixed in the Eq. 4.4 leaving $f_{\mathrm{B}}^{'}$ and f_{Sig} free. This approach evaluates the statistical uncertainties of $f_{\mathrm{B}}^{'}$ and f_{Sig}, including their correlations. Furthermore, the fit results are also subject to systematic uncertainties as component PDFs are kept fixed.

The width of $R(x)$ depends on the p_{T} of J/ψ candidate and the number of hits by J/ψ decay daughters in the SPD layers. The J/ψ candidates can be divided into categories according the hits in the SPD layers, e.g., candidates with hits in the first layer of SPD by both decay daughters are named "first-first" or "FF" while with only one daughter in first layer are named "first-second" or "FS". These conventions are used in this thesis to refer such J/ψ candidates. The experimental resolution for x becomes worse while going from high to low p_{T} and FF to FS candidate type. Such behavior can be observed in the pseudoproper decay length distribution of prompt J/ψ in different p_{T} bins and FF or FS type candidates, extracted from the MC sample. It is the transverse impact parameter resolution, $d_0(xy)$ as described in Sec. 4.1.5, that determines the p_{T}-dependent behavior of $R(x)$. The pair decay vertex is precisely reconstructed depending on the hits in the inner layers of SPD.

4.2.2 Extraction of fitting templates

The PDFs in Eq. 4.4 and 4.6 are fixed functional forms, referred as templates, obtained by parameterizing m and x distributions from data and MC sample.

J/ψ invariant mass signal

The invariant mass distribution of J/ψ, obtained from the MC sample, is parameterized by the Crystal Ball function [194]. This parameterized shape is used as an invariant mass signal template in the unbinned likelihood fits. It accounts for radiative decay of J/ψ as well

as particle interaction with detector material that affects detector performance. It is likely that low invariant mass regions display asymmetric tails as a result of such effects, also known as the bremsstrahlung process. Therefore, the Crystal Ball function has been adapted to parameterize the dielectron signal distribution in order to describe these features, as shown in Fig. 4.8. It is composed of a Gaussian distribution having a mean m_0 and standard deviation σ, and a power-law function parameterized by n and α as described in Eq. 4.8. The mean m_0 represents the mean value of J/ψ invariant mass distribution, and σ is the resolution of the dielectron invariant mass distribution.

$$f(m;\alpha,n,m_0,\sigma,N) = N.\begin{cases}\exp(-\frac{(m-m_0)^2}{2\sigma^2}), & \text{for } \frac{m-m_0}{\sigma} > -\alpha \\ A\cdot(B-\frac{m-m_0}{\sigma})^{-n}, & \text{for } \frac{m-m_0}{\sigma} \leq -\alpha,\end{cases}$$

$$A = \left(\frac{n}{|\alpha|}\right)^n \cdot \exp\left(-\frac{|\alpha|^2}{2}\right), B = \frac{n}{|\alpha|} - |\alpha|. \tag{4.8}$$

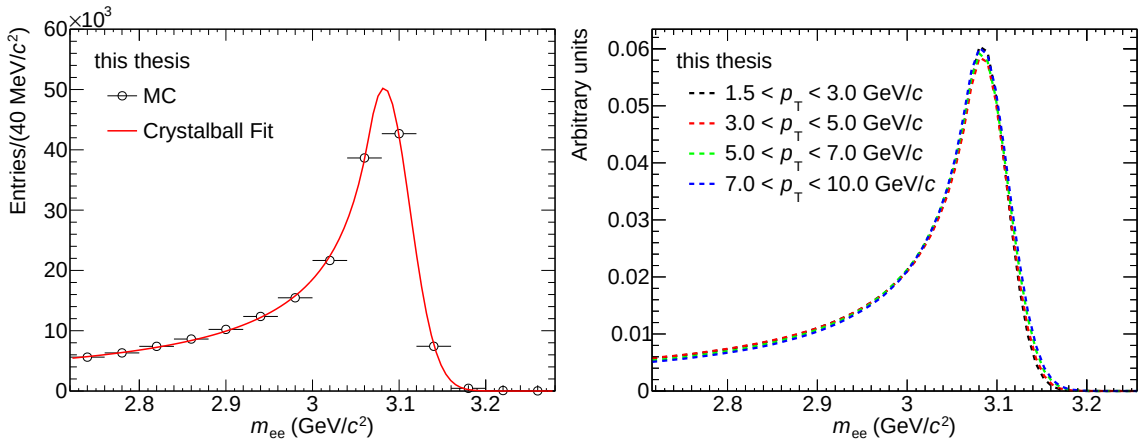

Figure 4.8 Invariant mass distribution of dielectrons from J/ψ parameterized by Crystal Ball function (left); invariant mass signal templates for different p_{T} ranges in Pb–Pb collisions in 0–10% centrality interval (right).

J/ψ invariant mass background

A data-driven approach is employed to obtain the invariant mass background PDFs. Generally, the method most suitable for reproducing uncorrelated invariant mass background is the Mixed-event technique [195]. It involves the pairing of leptons from different events having almost identical global properties. In this work, events are classified based on two global properties: event-plane angle divided into 9 bins in $[-\pi/2$ to $\pi/2]$ interval, and centrality divided into 23 bins in 0–90% interval. In order to determine the shape of the $M_{\mathrm{Bkg}}(m)$ PDF, binned fits were performed directly on the mixed event dielectron mass distributions. The dielectron spectrum is parameterized using a 3$^{\mathrm{rd}}$ order polynomial. The

Fig. 4.9 shows the fitting projections of mixed-event dielectron mass spectrum in different p_{T} bins in 0–10% centrality class.

The dielectron invariant mass spectra for unlike sign pairs have three contributions: signal pairs, combinatorial background, and residual or correlated background. The combinatorial background is fixed from mixed event pairs. After subtracting the combinatorial background from the unlike sign invariant mass distribution, the signal events reside with some background events known as correlated background. It is parameterized by a 2^{nd}order polynomial. Therefore, the dielectron invariant mass spectrum of signal pairs is parameterized by a function comprising with signal shape adopted from MC signal shape and a 2^{nd} order polynomial as shown in Fig. 4.10 for 0–10% centrality interval.

Mixed event and correlated backgrounds are added to obtain a total invariant mass background PDF used in the likelihood fits.

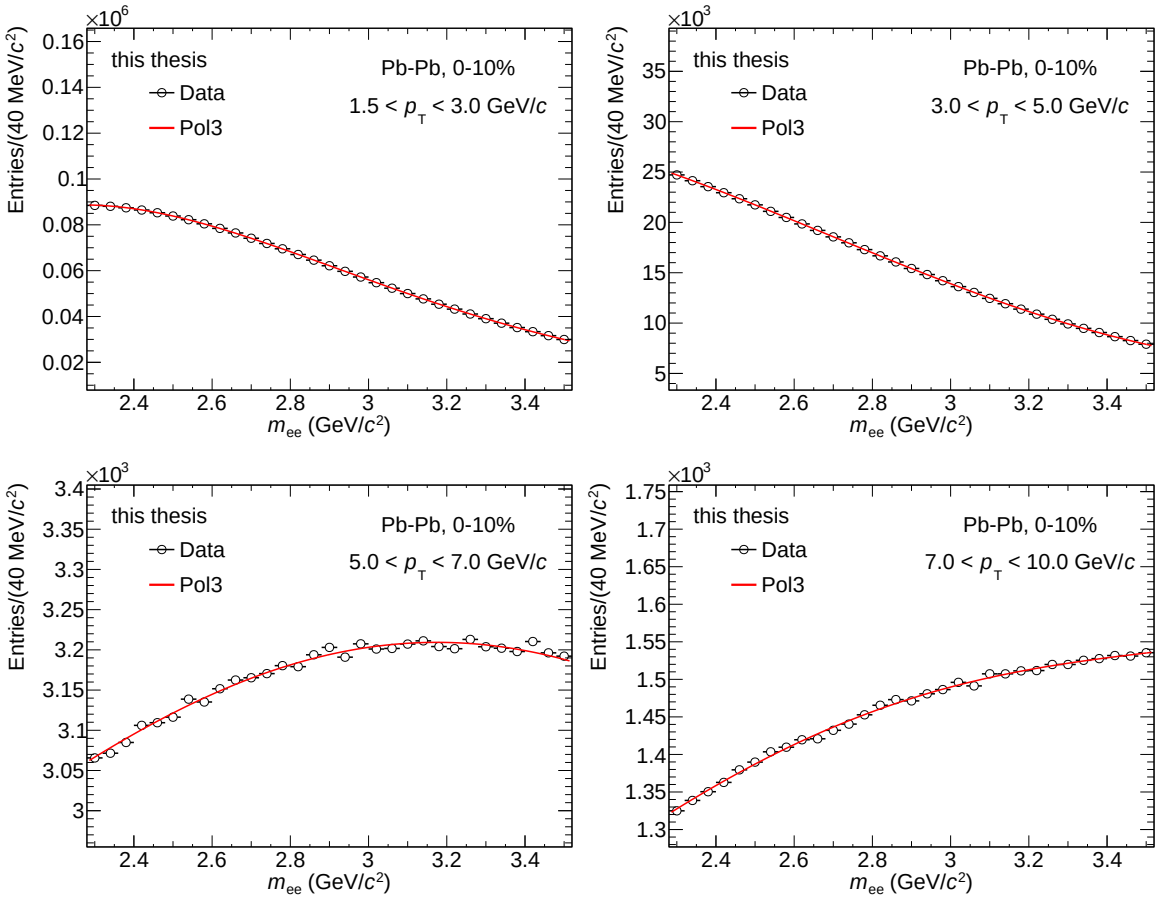

Figure 4.9 Parameterized mixed-event invariant mass distribution for different p_{T} intervals in the 0–10% centrality interval.

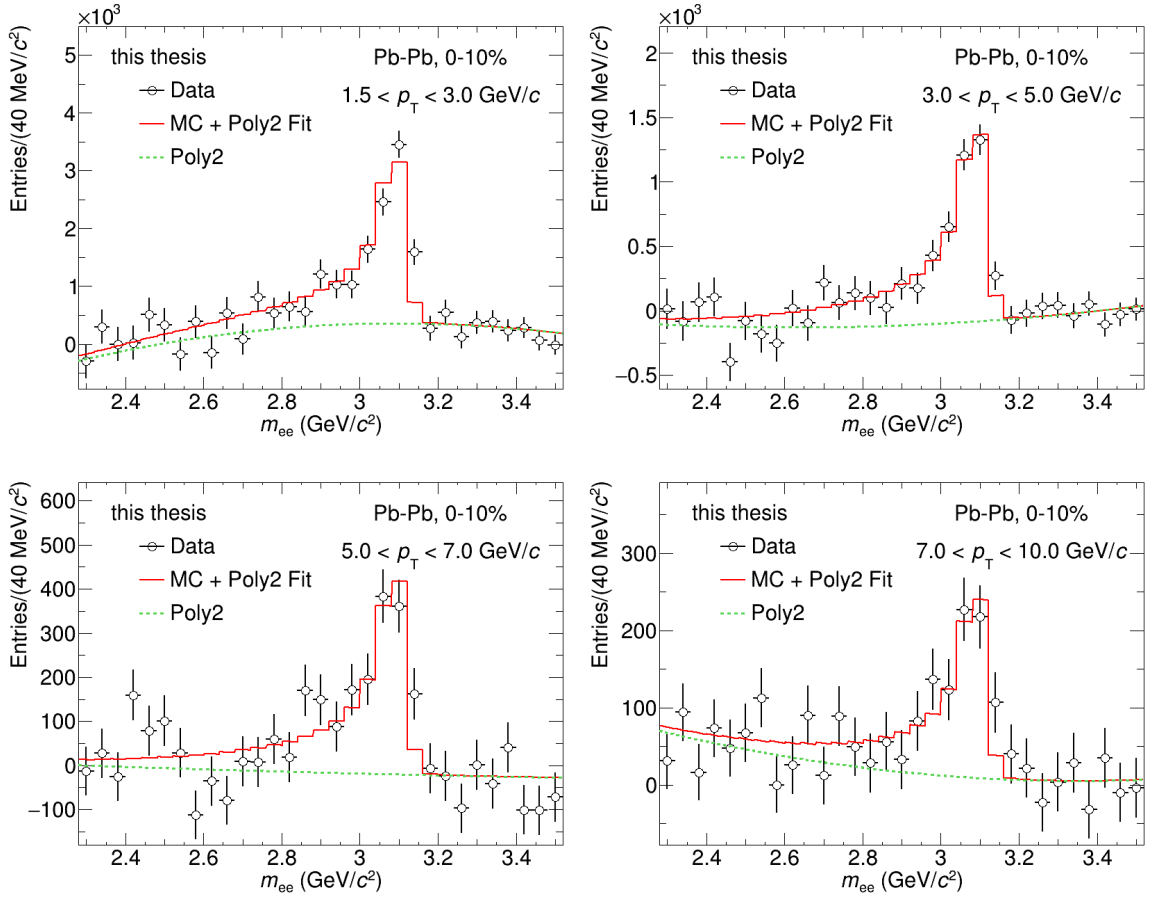

Figure 4.10 Parameterized invariant mass signal distribution for different p_{T} intervals in the 0–10% centrality interval.

Pseudoproper decay length for prompt J/ψ

The experimental resolution of pseudoproper decay length is given by $R(x)$ as described by the following expression, at first it was used by the CDF experiment [196],

$$R(x) = G_1(x;\mu_1,\sigma_1) + G_2(x;\mu_2,\sigma_2) + f(x;\alpha,\lambda), \tag{4.9}$$

where G_1 and G_2 are Gaussian functions and the power-law term is described by the following expression,

$$f(x;\alpha,\lambda) = \begin{cases} \frac{\lambda-1}{2\alpha\lambda}, & \text{if } |x| < \alpha, \\ \frac{\lambda-1}{2\alpha\lambda}\alpha|x|^{-\lambda}, & \text{if } |x| > \alpha, \end{cases}$$

where α and λ are free shape parameters. This PDF describes the pseudoproper decay length distribution for prompt J/ψ as well as experimental resolution for pseudoproper decay length. Resolution function PDFs are obtained by parameterizing the prompt J/ψ pseudoproper decay length distribution, extracted from the MC simulation sample. The pseudoproper

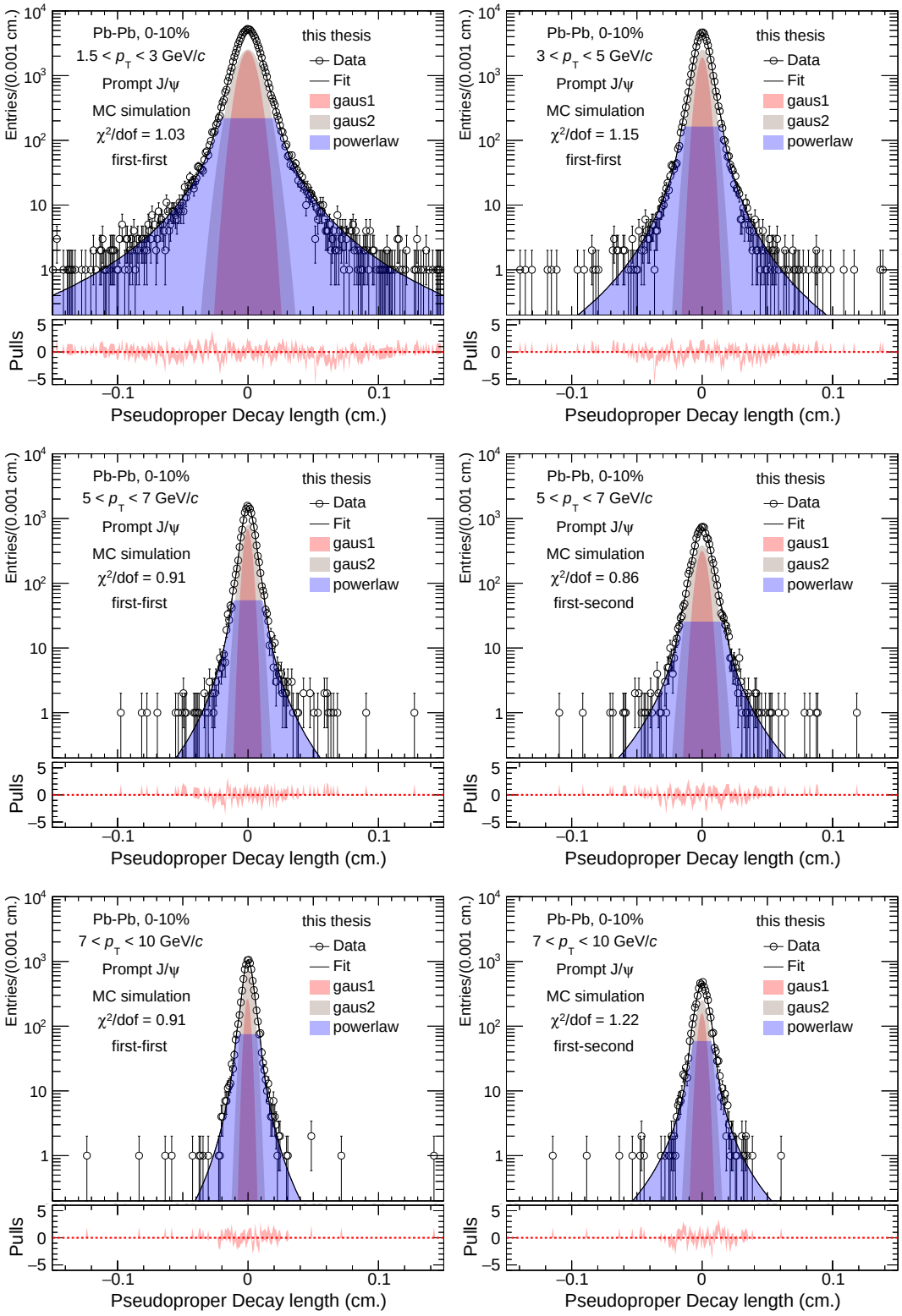

Figure 4.11 Parameterized prompt J/ψ x distribution in different p_{T} ranges for FF and FS J/ψ candidates in the 0–10% centrality interval.

decay length resolution is determined by the ITS spatial resolution and depends on the p_{T} of J/ψ. Therefore, separate resolution functions are used for J/ψ candidates based on their p_{T} and hits in the SPD layers. Pseudoproper decay length distribution gets narrower in higher p_{T} bins in comparison to lower p_{T} which implies that detector resolution is better at high p_{T}. Similarly, J/ψ candidates (FF) with both hits registered in the innermost SPD layer have better resolution in comparison to candidates (FS) having only a single hit. In each p_{T} interval, the parameterization accurately describes the MC distributions. At $p_{\mathrm{T}} < 5$ GeV/c, the background contributions are largest in 0–10% centrality interval. In this p_{T} range, only J/ψ candidates belonging to FF category are considered for the analysis and FS candidates are removed to enhance the f_{Sig} in the likelihood fits in 0–10% centrality interval. The Fig. 4.11 demonstrates parameterized x distribution for prompt J/ψ candidates in different p_{T} ranges in 0–10% centrality interval.

Pseudoproper decay length for non-prompt J/ψ

Non-prompt J/ψ pseudoproper decay length PDF is based on the x distribution of non-prompt J/ψ obtained from MC simulation. It is constructed by convolution of x-distribution of non-prompt J/ψ, $\chi_{\mathrm{B}}(x)$, and the resolution function $R(x)$ as shown by the following expression,

$$F_{\mathrm{B}}(x) = \chi_{\mathrm{B}}(x) \otimes R(x). \tag{4.10}$$

The Fig. 4.12 illustrates x distribution of non-prompt J/ψ obtained from MC simulation in different p_{T} bins in 0–10% centrality range. The $\chi_{\mathrm{B}}(x)$ distribution depends on the p_{T} distribution of non-prompt J/ψ. In the low p_{T} region, a large angle between J/ψ p_{T} and b-hadron direction yields in negative x values.

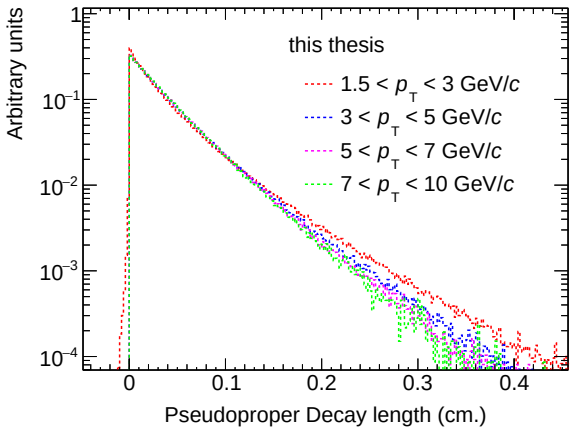

Figure 4.12 Non-prompt J/ψ pseudoproper decay length distribution, $\chi_{\mathrm{B}}(x)$, obtained from MC simulation for different p_{T} ranges.

Pseudoproper decay length background

In the invariant mass signal region, the pseudoproper decay length background is interpolated from x distribution in the invariant mass sidebands. There are two sidebands on each side of the signal region, as demonstrated in Fig. 4.13. Each x-distribution is parameterized by a function [196], described in the following way,

$$F^{i}_{\mathrm{Bkg}}(x) = (1 - f_1 - f_2 - f_+ - f_-) \cdot R(x - x') + \left(\frac{f_1}{2\mu_1} e^{\frac{-x'}{\mu_1}} \theta(x') + \frac{f_2}{2\mu_2} e^{\frac{-x'}{\mu_2}} \theta(x') + \frac{f_+}{\mu_+} e^{\frac{-x'}{\mu_+}} \theta(x') + \frac{f_-}{\mu_-} e^{\frac{-x'}{\mu_-}} \theta(x') \right) \otimes R(x - x'), \tag{4.11}$$

where i index runs from 1 to 4 representing each sideband with two SPD categories of candidates, $i.e.$, FF and FS. Therefore, there is a total of 4 $\times$ 2 parameterized templates in each p_{T} range. The parameters $f_{+,-,1,2}$ are the fractions corresponding to positive, negative, and both symmetrical distributions, while $\mu_{+,-,1,2}$ are the corresponding slopes of these distributions and $\theta(x)$ is a step function. The first term in Eq. 4.11 is a resolution term describes the residual combinatorics of prompt particles. The electrons originating from semileptonic decays of charm and beauty hadrons contribute to the pseudoproper decay length distribution of background candidates. Such contributions cause asymmetries in positive side of the x-distributions, therefore, it is described by an exponential function with a positive slope, $i.e.$, $\exp(f_+, \mu_+)$. It is similar to the non-prompt J/ψ component PDF, but the slope is different. Other sources contribute to positive and negative x values and are described by term with negative slope, $i.e.$, $\exp(f_-, \mu_-)$ and symmetric components, those are, $\exp(f_1, \mu_1)$ and $\exp(f_2, \mu_2)$.

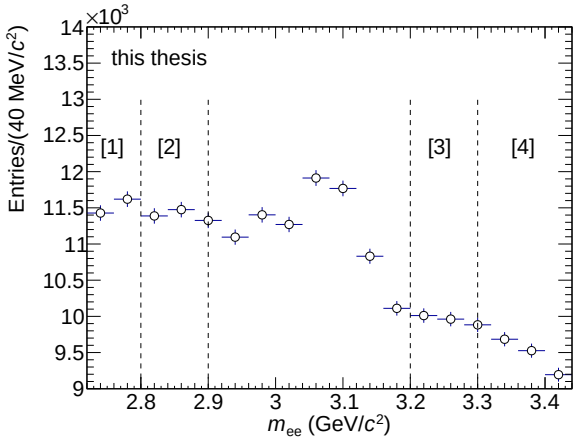

Figure 4.13 Classification of invariant mass sidebands (separated by dashed lines) for interpolation of pseudoproper decay length background template in signal region.

Centrality	Invariant mass bins (GeV/c^2)
0–10%	2.72–2.80, 2.80–2.90, 3.20–3.30, 3.30–3.40
10–30%, 30–50%	2.64–2.75, 2.75–2.85, 3.20–3.35, 3.35–3.52

Table 4.4 Invariant mass bins selection for sidebands in different centrality classes.

The pseudoproper decay length distributions, in different invariant mass sidebands are shown as an example in Fig. 4.14 for $5 < p_{\mathrm{T}} < 7$ GeV/c in 0–10% centrality interval. To proceed with the likelihood fits, we need two different x background templates for FF and FS candidates in the signal region. These templates are constructed according to following expression, where all parameterized sidebands are added with specific weights,

$$F_{\mathrm{Bkg}}(x) = \sum_{i=1}^{4} w_i F^i_{\mathrm{Bkg}}(x), \tag{4.12}$$

$$\text{where } w_i \propto \frac{1}{|\langle m\rangle^i - \langle m\rangle^{Sig}|^n},$$

where $n = 1$ or 2 for linear and quadratic weights, respectively. The interpolated template is determined by choosing weights (w_i) inversely proportional to the (square of) difference between the mean of the invariant mass distribution in the given mass interval and the signal region. Invariant mass sideband intervals are described in Table 4.4 for different centrality ranges. It differs for 0–10% centrality while the identical sidebands intervals are used for 10–30% and 30–50% centrality classes. The parameterized x projections are shown as an example in $5 < p_{\mathrm{T}} < 7$ GeV/c in 0–10% centrality interval in Fig. 4.15 and Fig. 4.16 for FF and FS candidates, respectively.

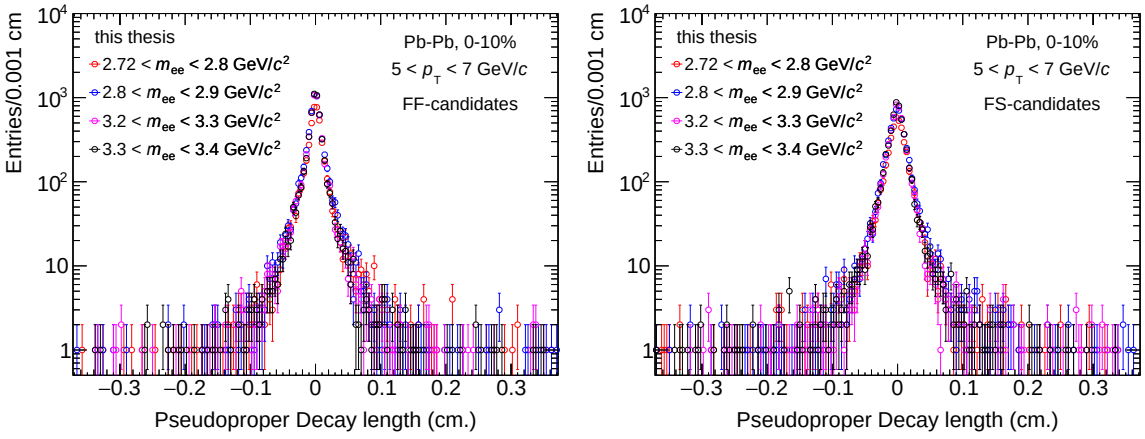

Figure 4.14 Projections of pseudoproper decay length distributions corresponding to different invariant mass sidebands for FF (left) and FS (right) candidates in $5 < p_{\mathrm{T}} < 7$ GeV/c in 0–10% centrality interval.

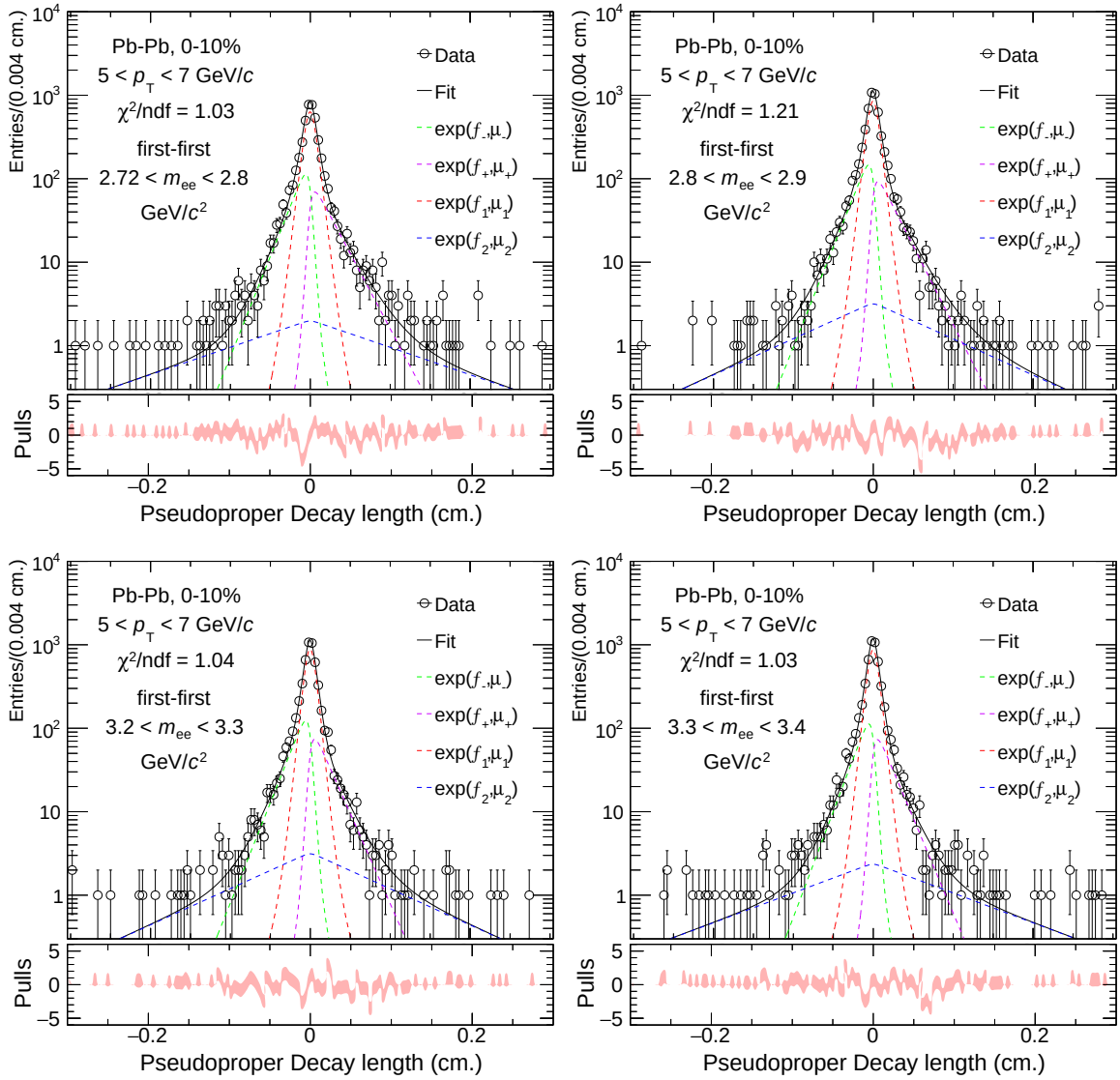

Figure 4.15 Parameterized pseudoproper decay length distributions corresponding to different invariant mass sidebands for FF candidates in $5 < p_{\mathrm{T}} < 7$ GeV/c in the 0–10% centrality.

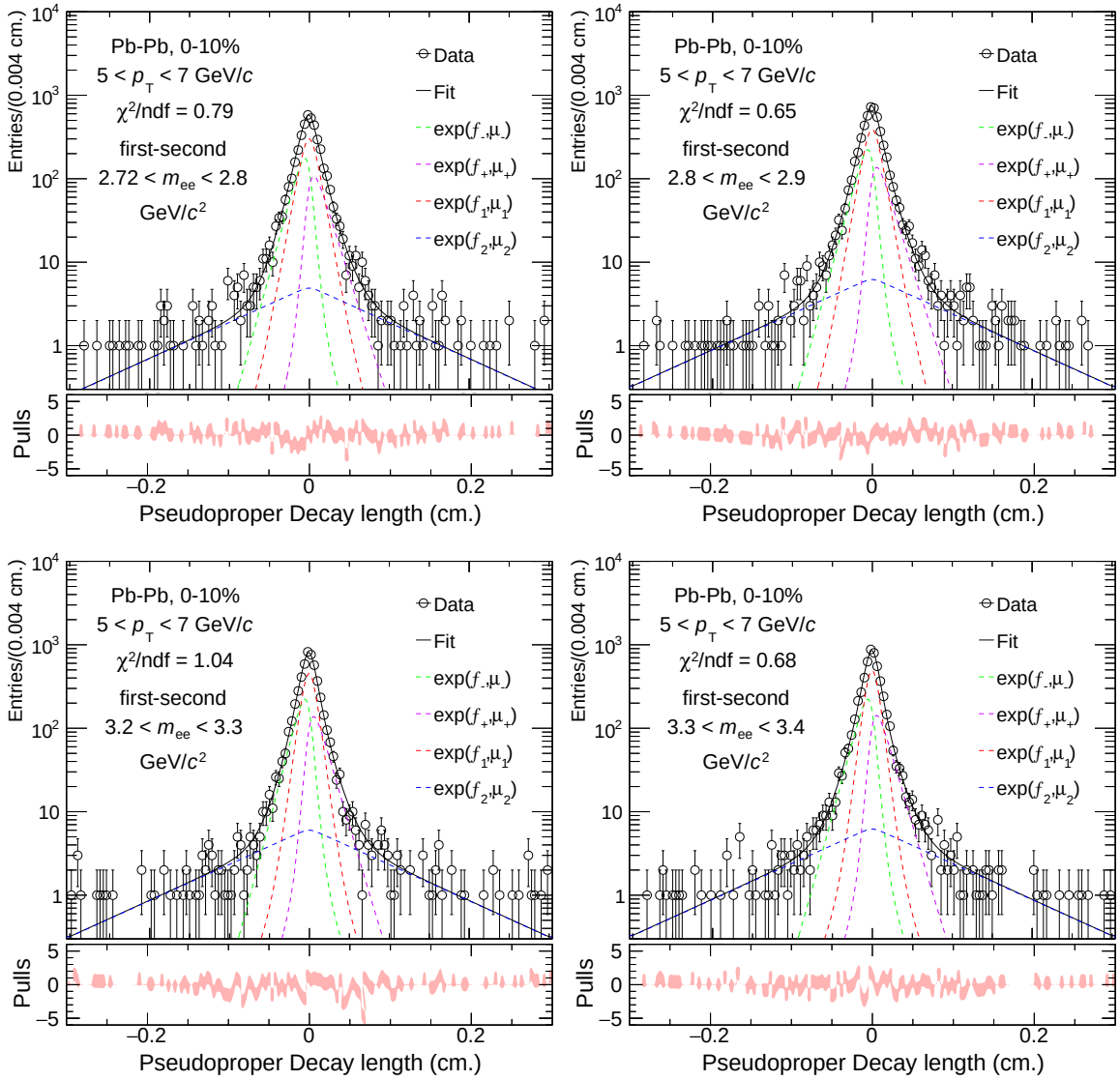

Figure 4.16 Parameterized pseudoproper decay length distributions corresponding to different invariant mass sidebands for FS candidates in $5 < p_{\mathrm{T}} < 7$ GeV/c in the 0–10% centrality.

4.2.3 Results

The invariant mass and pseudoproper decay length projections from the likelihood fits are demonstrated in all p_{T} and centrality intervals. In the 0–10% centrality interval, the invariant mass projections are demonstrated in Fig. 4.17 while pseudoproper decay length projections for FF and FS categories are shown in Fig. 4.18. In the 10–30% centrality interval, the invariant mass projections are demonstrated in Fig. 4.19 while pseudoproper decay length projections for FF and FS categories are shown in Fig. 4.20. In the 30–50% centrality interval, the invariant mass projections are demonstrated in Fig. 4.21 while pseudoproper decay length projections for FF and FS categories are shown in Fig. 4.22.

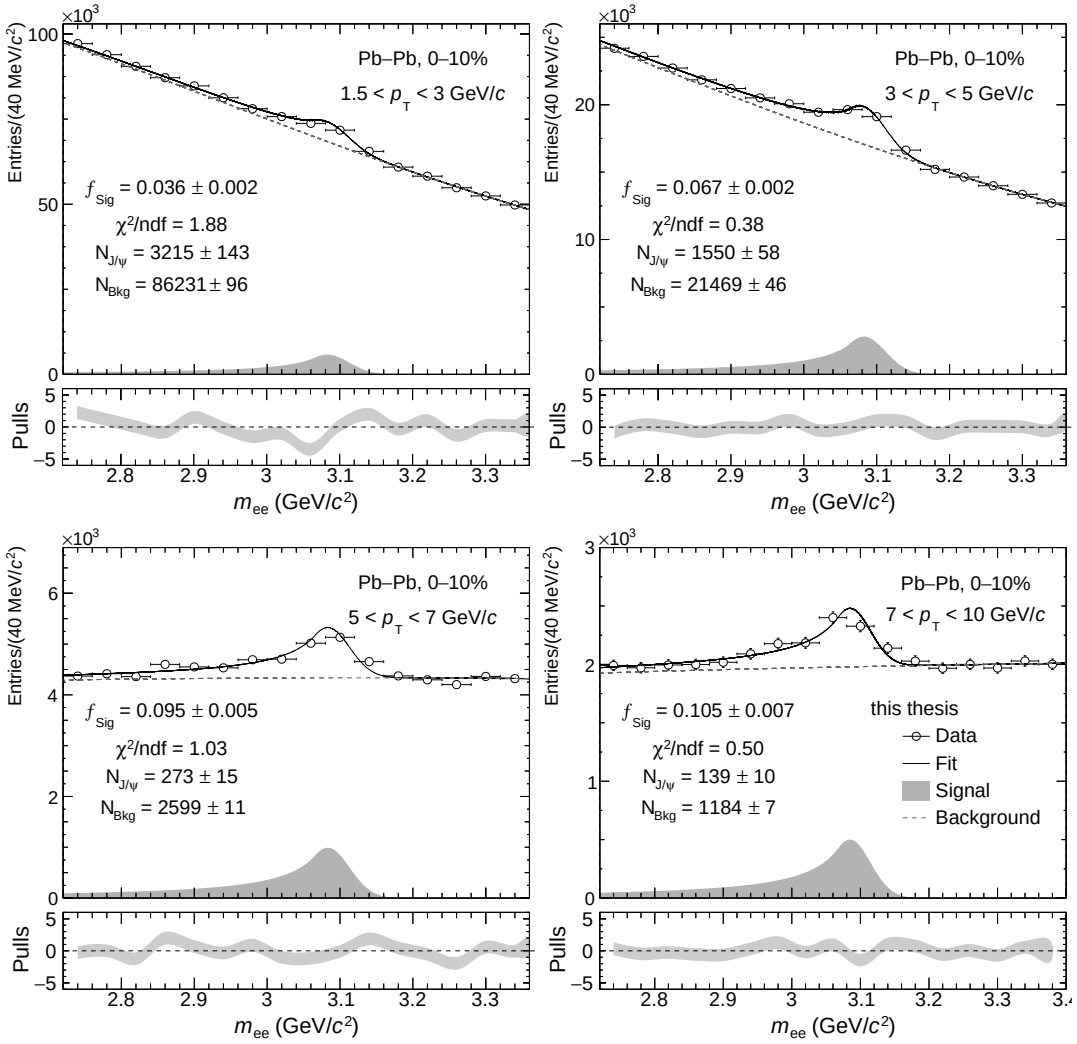

Figure 4.17 Unbinned likelihood fit projections of invariant mass distributions in different p_{T} intervals in 0–10% centrality range.

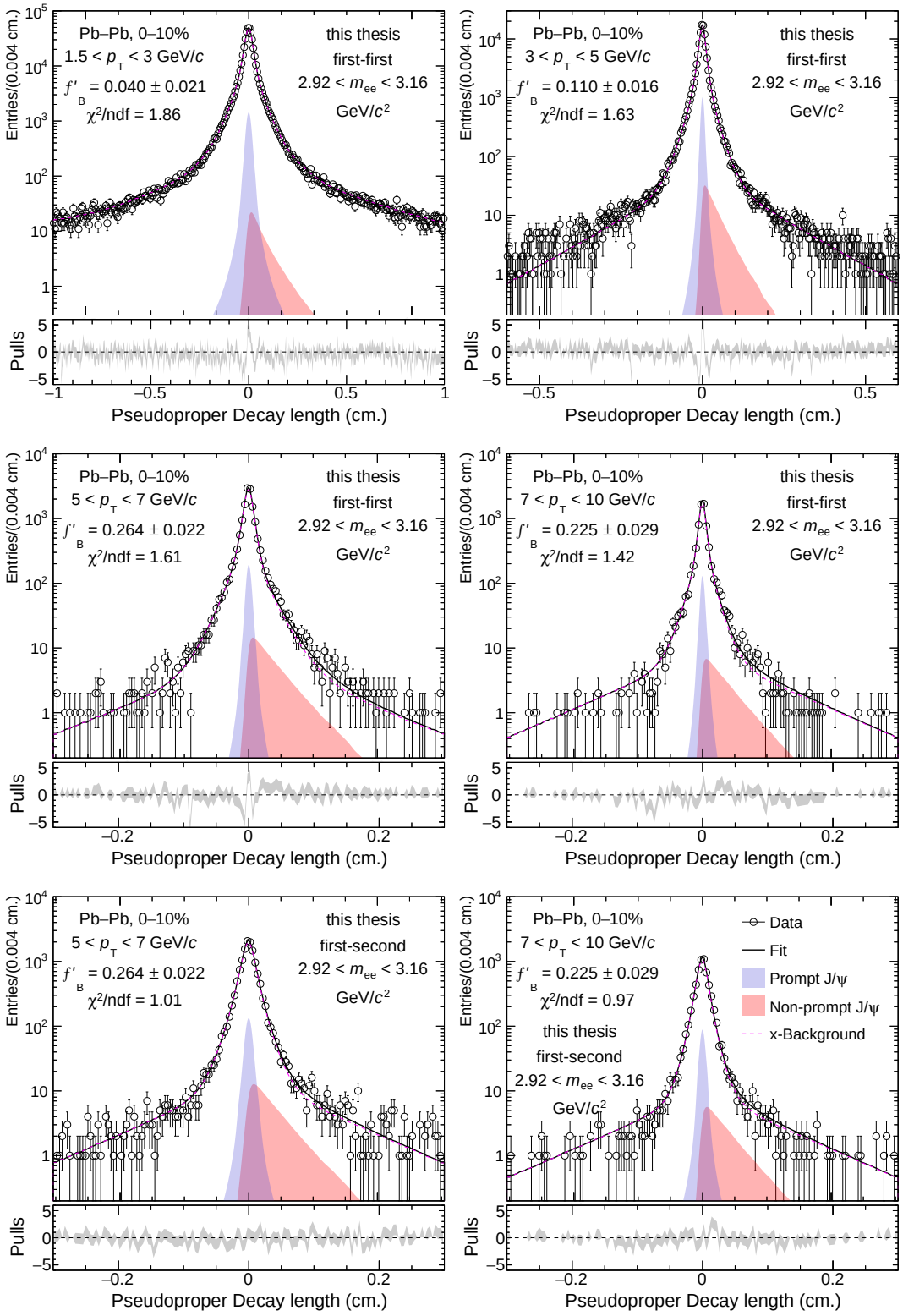

Figure 4.18 Unbinned likelihood fit projections of pseudoproper decay length distributions for FF candidates (top, middle) in different p_{T} intervals in 0–10% centrality range, projections for FS candidates in the bottom panels for $p_{\mathrm{T}} > 5$ GeV/c.

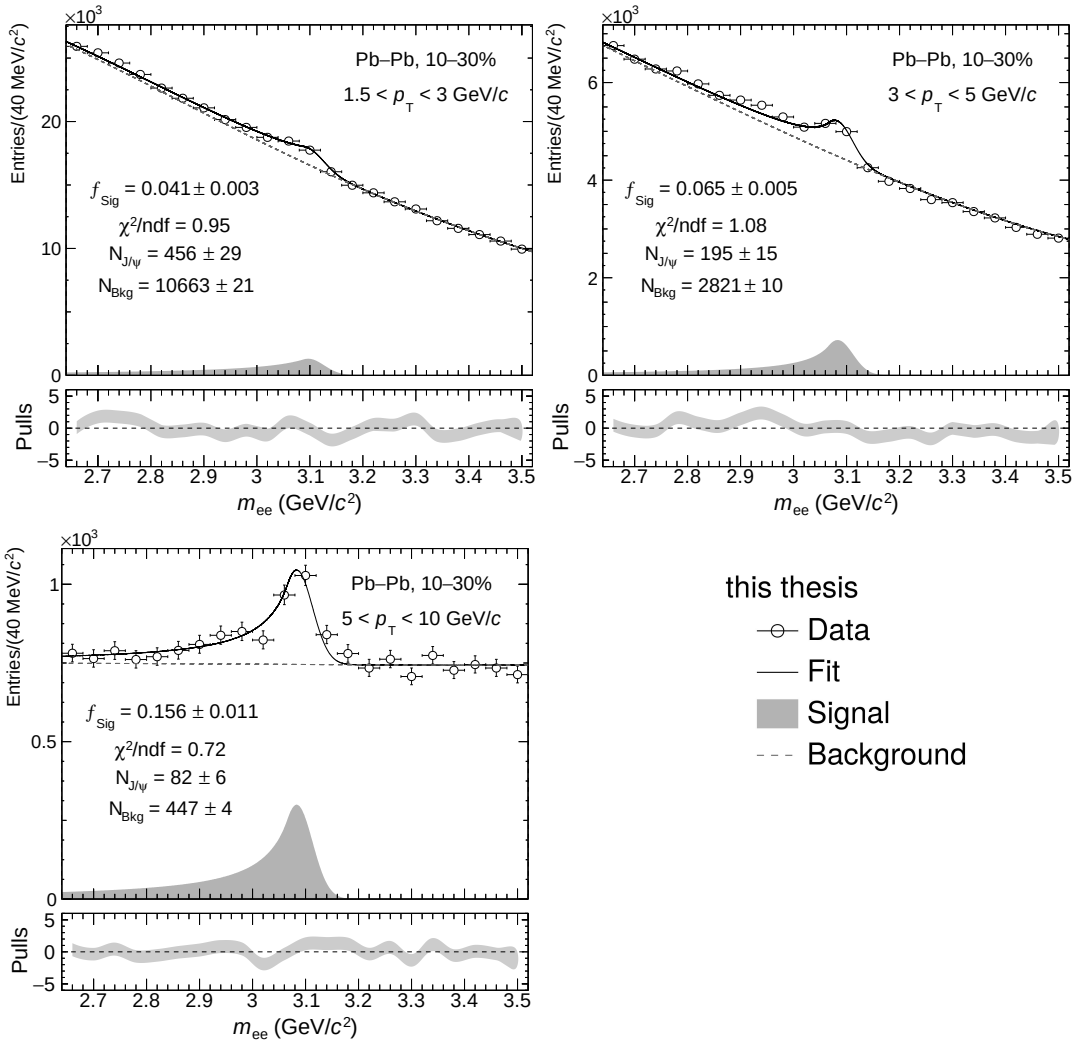

Figure 4.19 Unbinned likelihood fit projections of invariant mass distributions in different p_{T} intervals in 10–30% centrality range.

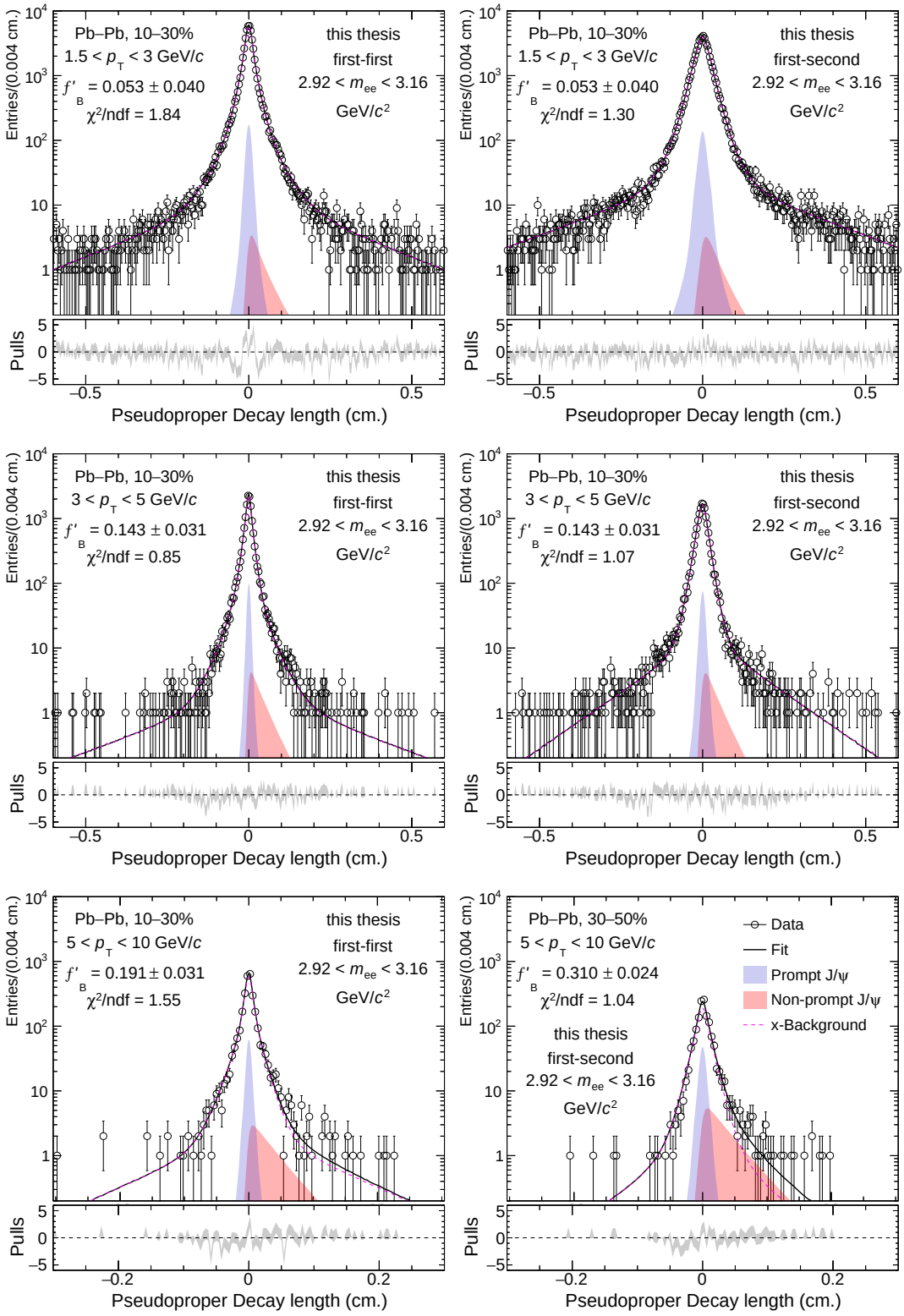

Figure 4.20 Unbinned likelihood fit projections of pseudoproper decay length distributions for FF (left column) and FS candidates (right column) in different p_{T} intervals in 10–30% centrality range.

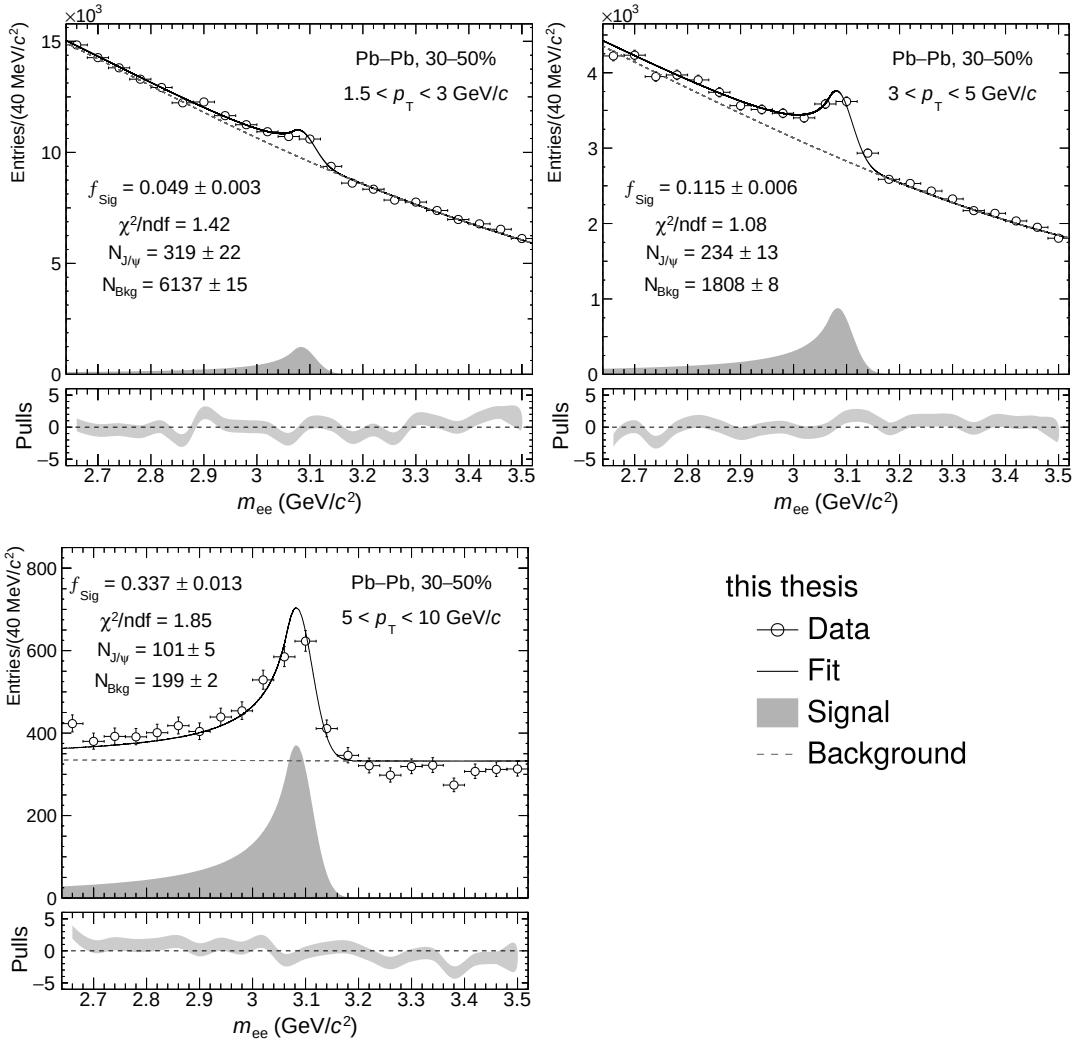

Figure 4.21 Unbinned likelihood fit projections of invariant mass distributions in different p_{T} intervals in 30–50% centrality range.

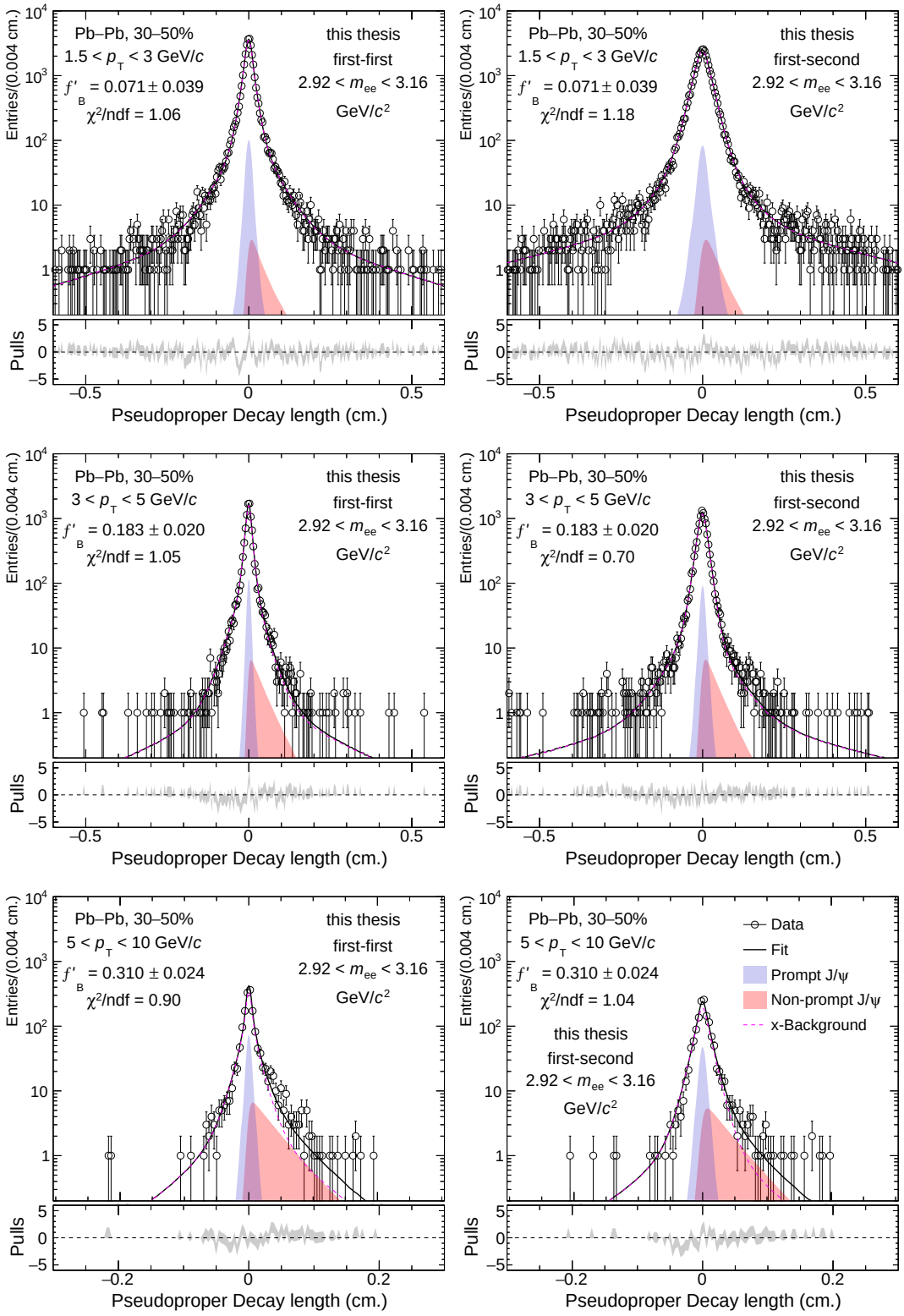

Figure 4.22 Unbinned likelihood fit projections of pseudoproper decay length distributions for FF (left column) and FS candidates (right column) in different p_{T} intervals in 30–50% centrality range.

The Fig. 4.23 demonstrates the obtained $f_{\mathrm{B}}^{'}$ (left) and f_{Sig} (right) as a function of p_{T} in all centrality intervals. The measured non-prompt J/ψ fraction shows an increasing trend with p_{T} suggesting a larger contribution of non-prompt J/ψ at higher p_{T} whereas no clear dependence on centrality has been observed. The f_{Sig} also increases as function of p_{T} which is due to less combinatorial background at higher p_{T}. There is a smaller background in the 30–50% as compared to 0–10% leading to larger signal to background ratio in 30–50%.

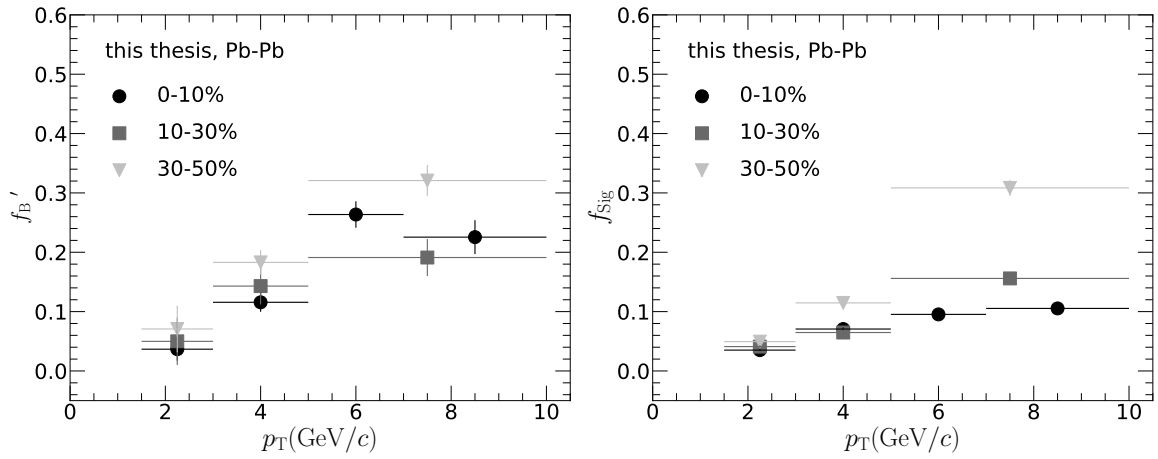

Figure 4.23 $f_{\mathrm{B}}^{'}$ (left) and f_{Sig} (right) obtained from likelihood fits as a function of p_{T} in different centrality ranges.

4.3 Efficiency corrections

Raw $f_{\mathrm{B}}^{'}$ obtained from likelihood fits is the fraction of non-prompt J/ψ in the reconstructed inclusive J/ψ sample. The prompt and non-prompt J/ψ exhibits a difference in the reconstruction efficiency (A $\times$ ϵ). Therefore, these fractions, $f_{\mathrm{B}}^{'}$, needs to be corrected in order to get the actual non-prompt J/ψ fraction (f_{B}). The corrections are applied to $f_{\mathrm{B}}^{'}$ according to the following expression,

$$f_{\mathrm{B}} = \left(1 + \frac{1 - f_{\mathrm{B}}^{'}}{f_{\mathrm{B}}^{'}} \cdot R\right)^{-1}, \tag{4.13}$$

where $R = \frac{\langle A \times \epsilon \rangle_{\mathrm{B}}}{\langle A \times \epsilon \rangle_{\mathrm{Prompt}}}$, ratio of mean efficiency of non-prompt J/ψ to that of prompt J/ψ. The mean efficiency is determined using the following equation for both non-prompt as well as prompt J/ψ,

$$\langle A \times \epsilon \rangle = \frac{\int_{p_{\mathrm{T}}^{\mathrm{min}}}^{p_{\mathrm{T}}^{\mathrm{max}}} (A \times \epsilon)(p_{\mathrm{T}}) \cdot (\frac{\mathrm{d}N}{\mathrm{d}p_{\mathrm{T}}})}{\int_{p_{\mathrm{T}}^{\mathrm{min}}}^{p_{\mathrm{T}}^{\mathrm{max}}} (\frac{\mathrm{d}N}{\mathrm{d}p_{\mathrm{T}}})}, \tag{4.14}$$

where $p_{\mathrm{T}}^{\mathrm{max}}$ and $p_{\mathrm{T}}^{\mathrm{min}}$ are the maximum and minimum values of a p_{T} bin considered in the analysis. The p_{T}-differential efficiency (A $\times$ ϵ) is defined in the following way,

$$A \times \epsilon = \frac{N_{\mathrm{acc}}(\Delta p_{\mathrm{T}}^{\mathrm{rec}})}{N_{\mathrm{gen}}(\Delta p_{\mathrm{T}}^{\mathrm{gen}})} \times \frac{N_{\mathrm{rec,\,sel}}(\Delta p_{\mathrm{T}}^{\mathrm{rec}})}{N_{\mathrm{acc}}(\Delta p_{\mathrm{T}}^{\mathrm{rec}})}, \tag{4.15}$$

where N_{gen} is number of total produced J/ψ, N_{acc} is the number of J/ψ seen or accepted by detector, and $N_{\mathrm{rec,sel}}$ is the number of J/ψ which are reconstructed in the experiment after passing all selection criteria. The $\Delta p_{\mathrm{T}}^{\mathrm{gen}}$ and $\Delta p_{\mathrm{T}}^{\mathrm{rec}}$ are p_{T} intervals of generated and reconstructed J/ψ, respectively. The p_{T}-differential efficiency is determined by dedicated Monte-Carlo production with injected J/ψ signal as demonstrated in Fig. 4.24. There is a smaller J/ψ efficiency observed for 0–10% centrality in comparison to 30–50% centrality. The reason for such an effect lies in the tight PID selection criteria for electrons in the central collisions.

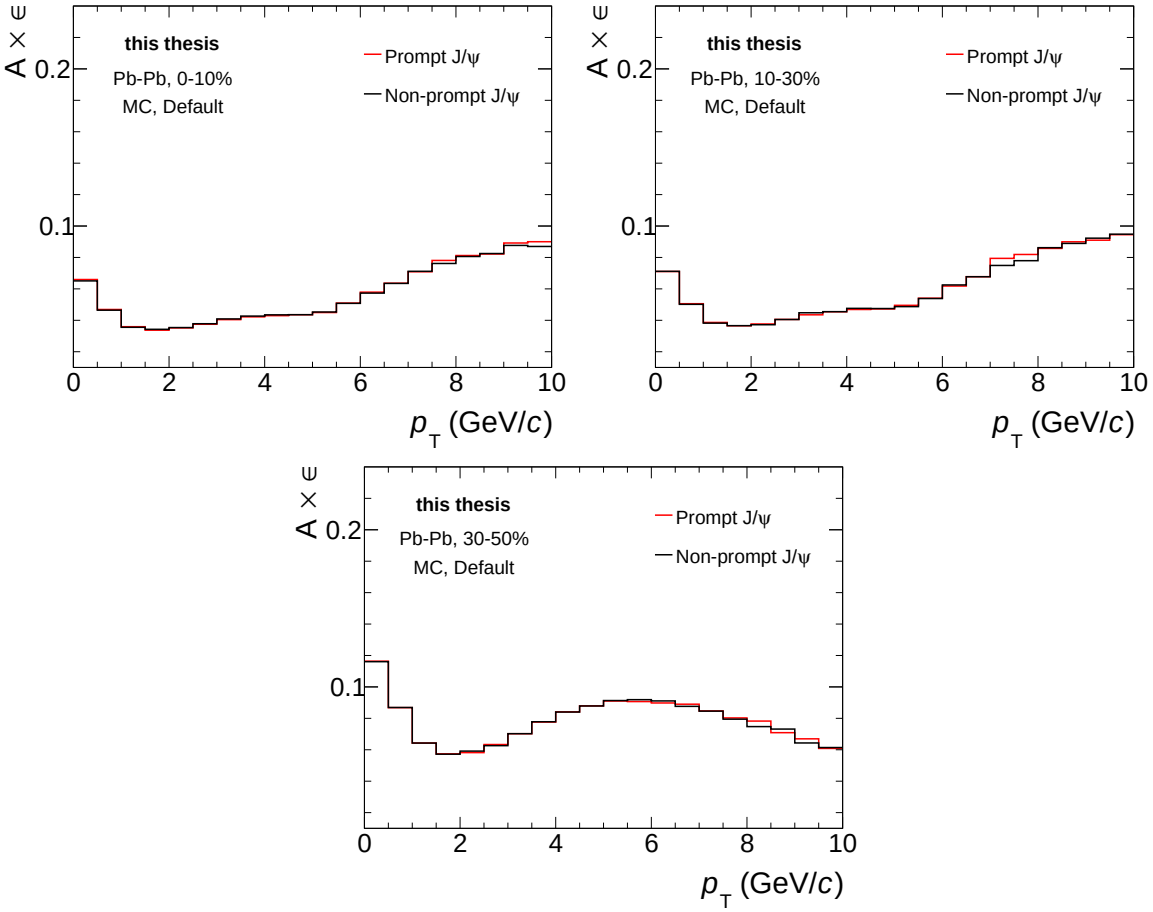

Figure 4.24 p_{T}-differential efficiency of prompt and non-prompt J/ψ in different centrality intervals.

A realistic p_{T} distribution for prompt J/ψ is obtained parameterizing p_{T} differential cross section of inclusive J/ψ in Pb–Pb collisions in different centrality intervals as demonstrated in Fig. 4.25 for 0–10% and 30–50% centrality intervals. The p_{T}-differential cross section of inclusive J/ψ is parameterized by the power-law function, described by the following

expression,

$$f(p_{\mathrm{T}}; C, n, p_0) = C \times \frac{p_{\mathrm{T}}}{(1 + (p_{\mathrm{T}}/p_0)^2)^n}, \tag{4.16}$$

where the free parameters p_0 and n are varied to get the largest and the smallest values of $\langle p_{\mathrm{T}} \rangle$. These p_{T} distributions with largest and smallest $\langle p_{\mathrm{T}} \rangle$ are chosen to determine systematic uncertainties arising from prompt J/ψ p_{T} spectrum. The example of such distributions are shown for 0–10% (left panel) and for 30–50% (right panel) centrality intervals in Fig. 4.26.

In the MC sample, the non-prompt J/ψ p_{T} spectrum is obtained from pp collisions, generated by Pythia simulations. It is reweighted by the R_{AA} of non-prompt J/ψ to obtain a realistic p_{T} spectrum in Pb–Pb collisions. Several models describe R_{AA} of non-prompt J/ψ as a function of p_{T} in Pb–Pb collisions at $\sqrt{s_{\mathrm{NN}}}$= 2.76 TeV [153] as shown in Fig. 4.27. These model predictions are based on different assumptions and used for reweighting the non-prompt J/ψ p_{T} distribution. In the BAMPS model [197], all partons interact through a partonic transport approach based on the Boltzmann equation, while heavy quarks do not undergo radiative energy loss. Using the relativistic Langevin equation, the Alberico model [198, 199] describes how heavy quarks propagate through a medium. The transport coefficients strongly influence p_{T} dependent behavior of R_{AA}. There are two kinds of values: those derived from perturbative calculations (hard thermal loop - HTL approach) and those derived from lattice-QCD simulations. The p_{T} spectrum and corresponding $A \times \epsilon(p_{\mathrm{T}})$ are reweighted by the R_{AA} predictions from aforementioned models as shown in Fig. 4.28 for 0–10% and 30–50% centrality intervals, respectively.

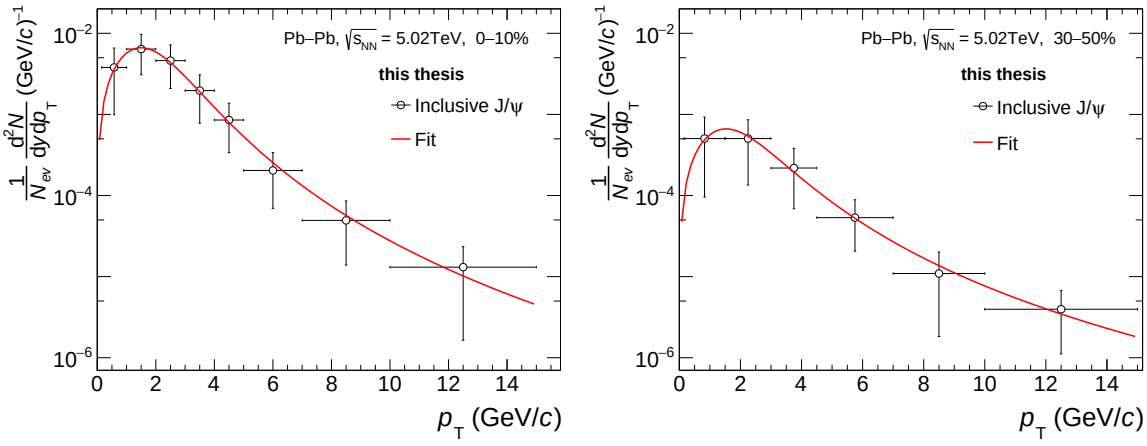

Figure 4.25 Inclusive J/ψ p_{T} spectra parameterized by power-law function in 0–10% (left) and 30–50% (right) centrality intervals at $\sqrt{s_{\mathrm{NN}}}$= 5.02 TeV.

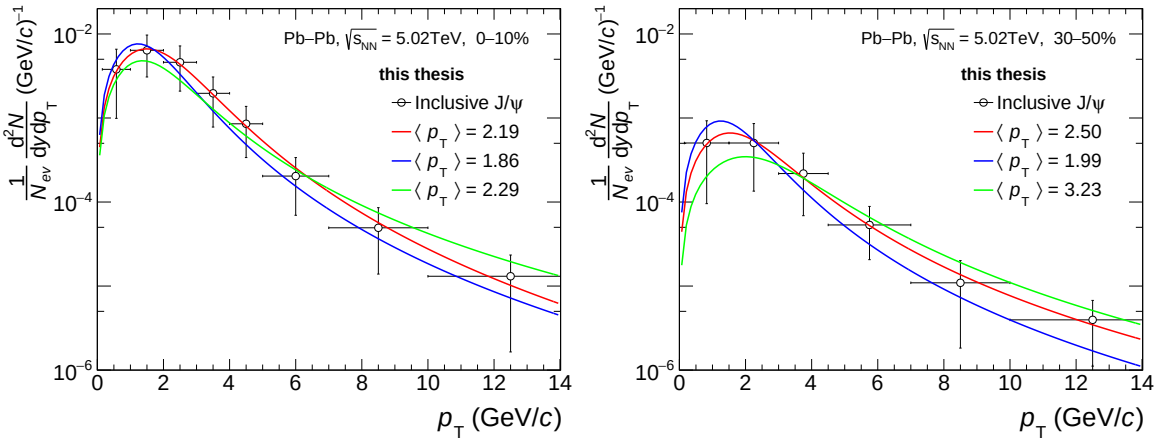

Figure 4.26 Inclusive J/ψ p_{T} spectrum parameterized by power-law function (red) and shape is varied to obtain extreme values of mean p_{T} (green and blue) 0-10% (left) and 30-50% (right).

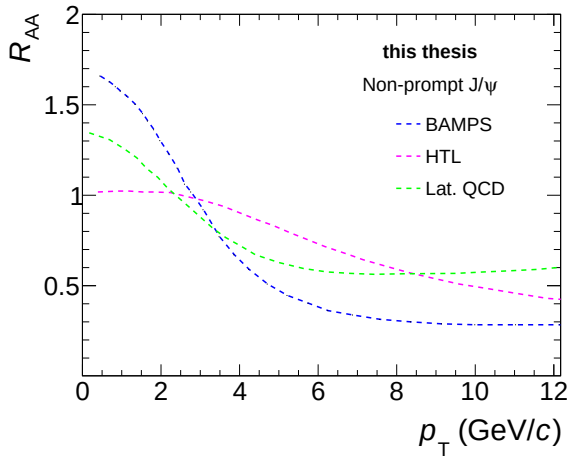

Figure 4.27 Predictions for non-prompt J/ψ R_{AA} as a function of p_{T} at midrapidity in Pb–Pb collisions, compared with measurements at $\sqrt{s_{\mathrm{NN}}}$= 2.76 TeV [153, 197–199].

The correction factor (R factor) is calculated for all the choices of prompt and non-prompt p_{T} spectra as demonstrated for all centrality classes in Fig. 4.29. The mean value of all evaluated R factors is considered as a final R factor to be used in f_{B} corrections as shown in the bottom-right panel of Fig. 4.29 in different centrality intervals. The corrected f_{B} and those obtained from fits, $f_{\mathrm{B}}{}'$, are shown as a function of p_{T} in Fig. 4.30 for 0–10%, 10–30%, and 30–50% centrality intervals.

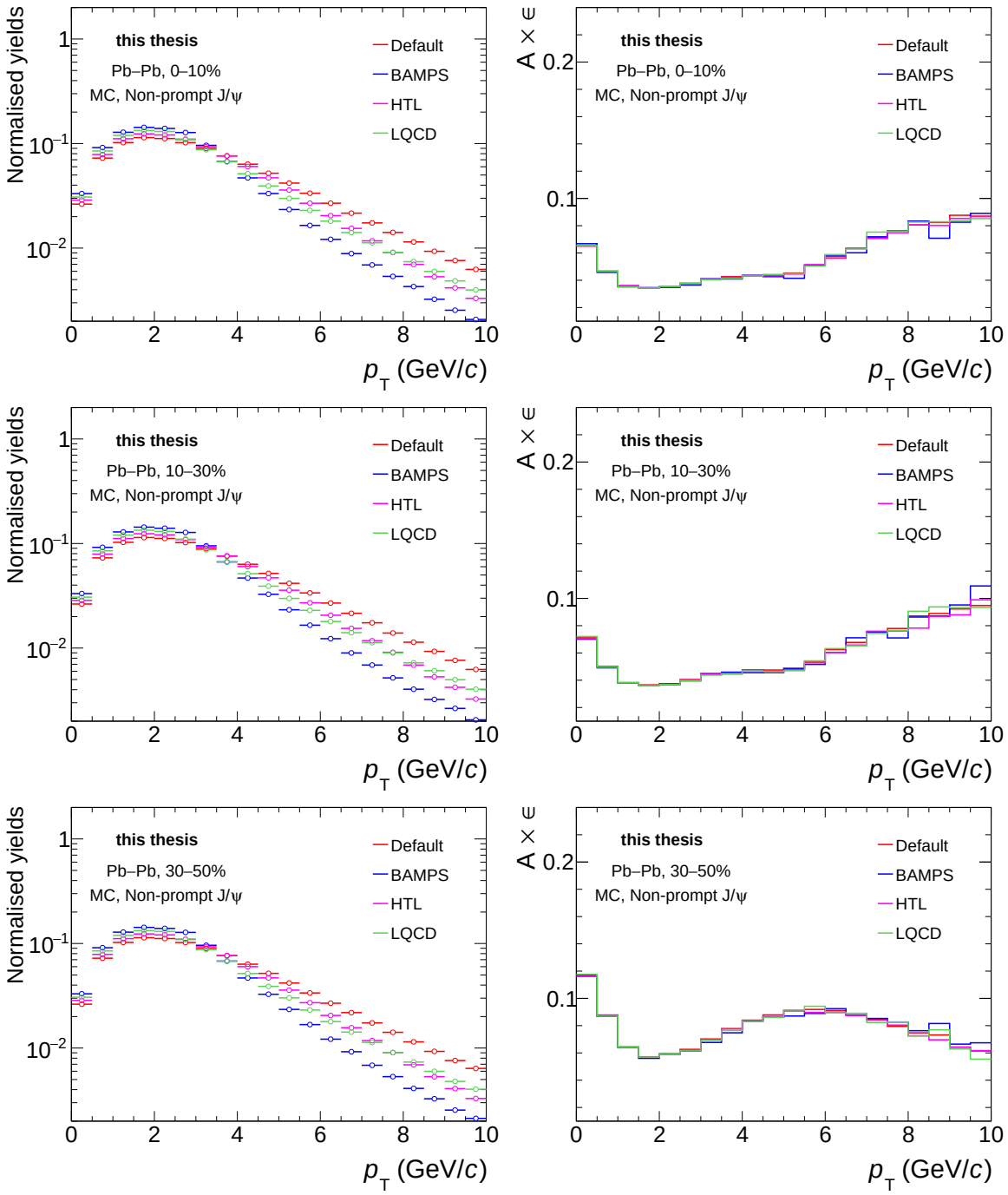

Figure 4.28 Reweighted p_{T} spectra (left column) and corresponding p_{T} differential efficiency (right column) for non-prompt J/ψ in 0–10%, 10–30%, and 30–50% centrality intervals.

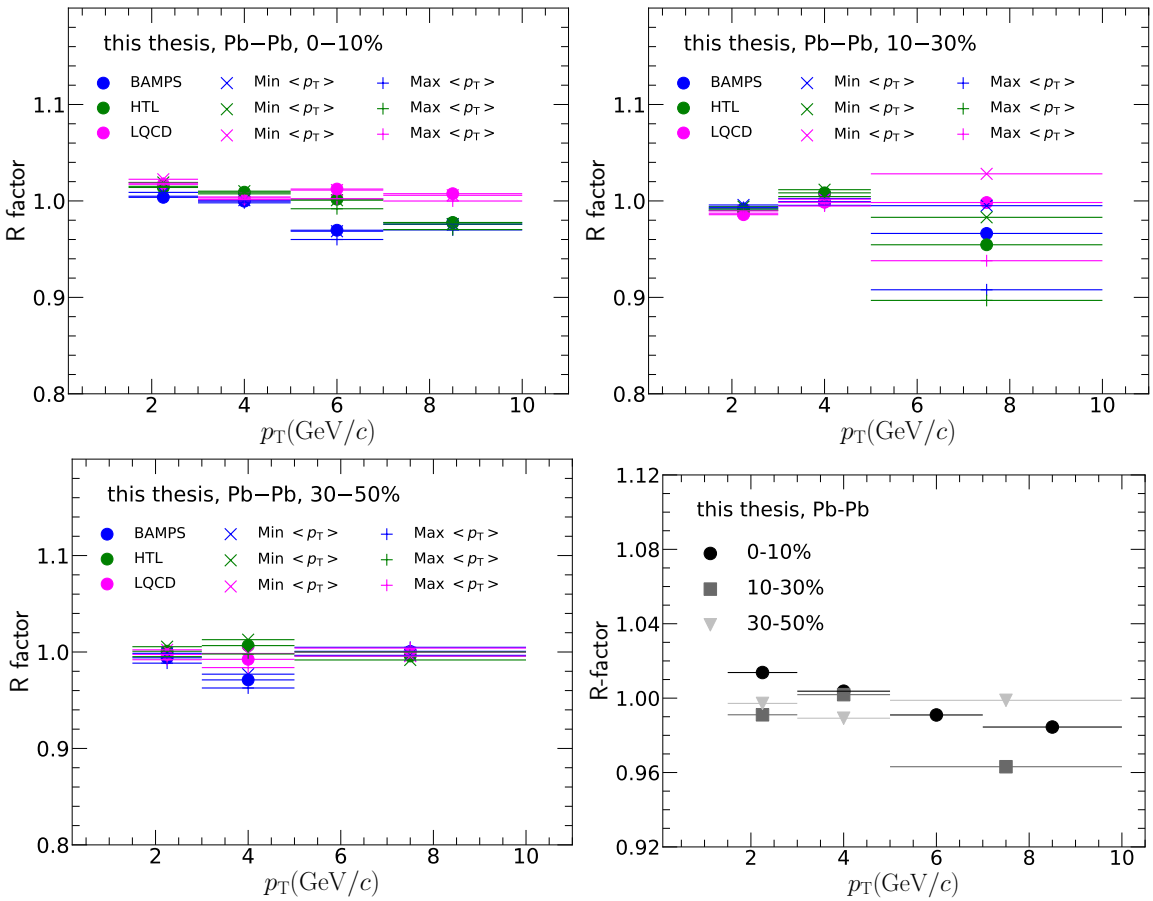

Figure 4.29 R factor as a function of J/ψ p_T considering the variations in prompt and non-prompt p_T spectra (MC) in 0–10% (top-left), 10–30% (top-right) and 30–50% (bottom-left) centrality classes. The mean R factor as a function of p_T in different centrality intervals (bottom-right).

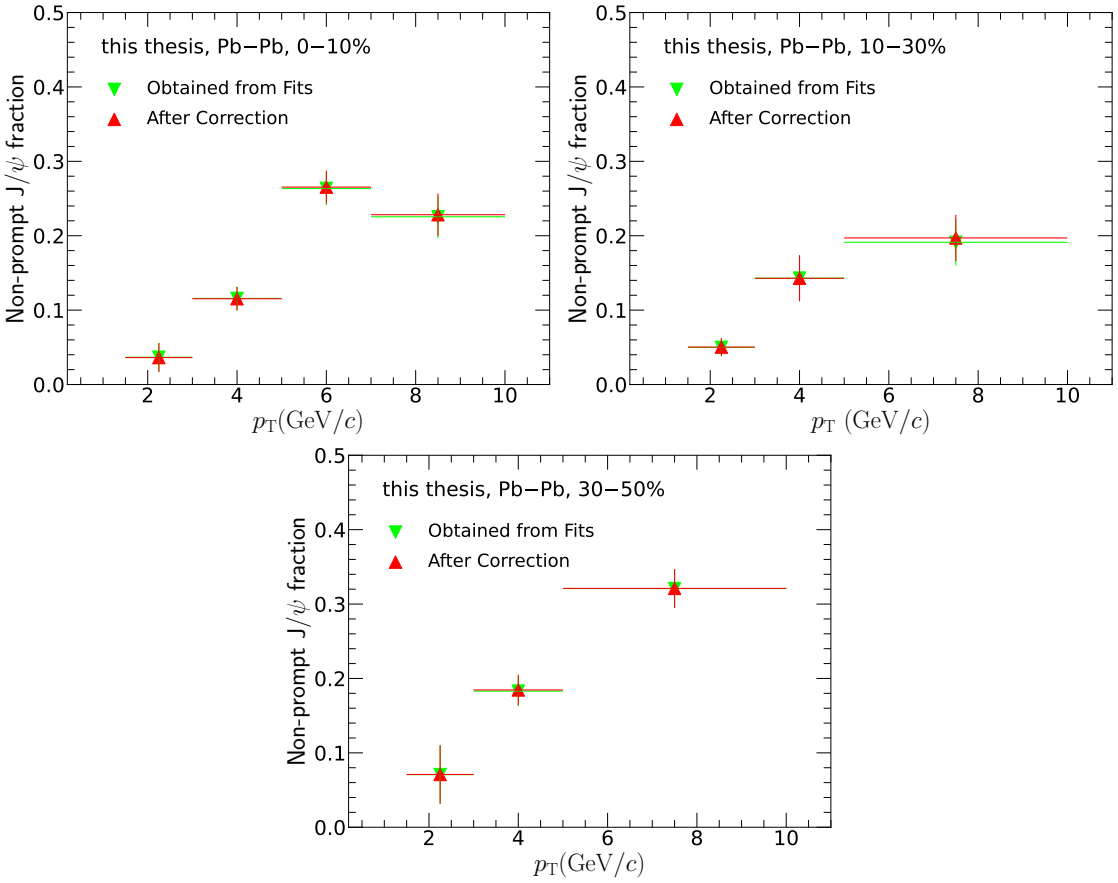

Figure 4.30 The non-prompt J/ψ fractions, obtained from fits (f'_{B}), and after efficiency corrections (f_{B}) as a function of p_{T} in different centrality intervals.

4.4 Systematic Uncertainties

Several sources contributing to the systematic uncertainties in f_{B} measurements, are described in this section. In this analysis, the main contributions come from the fitting templates used in the determination of the f_{B}. Systematic uncertainties in f_{B} measurement are summarized in the Tables 4.5, 4.6, and 4.7. All the contributions to systematic uncertainty smaller than 0.1% are neglected.

p_{T} (GeV/c)	$F_{\mathrm{Bkg}}(x)$	R(x)	$M_{\mathrm{Sig}}(m)$	$M_{\mathrm{Bkg}}(m)$	MC p_{T} spectra	Total
1.5 - 10	6%	3%	2%	Neg	5%	9%
1.5 - 3	27%	11%	3%	1%	1%	29%
3 - 5	11%	2%	0.4%	0.6%	0.5%	12%
5 - 7	3%	1%	0.2%	Neg	3%	4 %
7 - 10	4%	1%	1%	0.2%	2%	4 %

Table 4.5 Systematic uncertainties in f_{B} measurements in Pb–Pb collisions in the 0-10% centrality interval.

p_{T} (GeV/c)	$F_{\mathrm{Bkg}}(x)$	R(x)	$M_{\mathrm{Sig}}(m)$	$M_{\mathrm{Bkg}}(m)$	MC p_{T} spectra	Total
1.5 - 10	5%	4%	0.1%	0.4%	6%	9%
1.5 - 3	22%	10%	2%	4%	1%	25%
3 - 5	9%	3%	1%	0.3%	3%	10%
5 - 10	3%	2%	0.3%	0.1%	3%	5%

Table 4.6 Systematic uncertainties in f_{B} measurements in Pb–Pb collisions in the 10–30% centrality interval.

p_{T} (GeV/c)	$F_{\mathrm{Bkg}}(x)$	R(x)	$M_{\mathrm{Sig}}(m)$	$M_{\mathrm{Bkg}}(m)$	MC p_{T} spectra	Total
1.5 - 10	5%	3%	0.1%	0.2 %	6%	8%
1.5 - 3	10%	7%	0.4%	2 %	1%	12%
3 - 5	3%	2%	0.1%	0.1%	2%	4%
5 - 10	2%	2%	0.1%	0.5%	0.5%	3%

Table 4.7 Systematic uncertainties in f_{B} measurements in Pb–Pb collisions in the 30–50% centrality interval.

4.4.1 Pseudoproper decay length background

In the signal range ($2.92 < m_{\mathrm{ee}} < 3.16$ GeV/c^2), pseudoproper decay length background PDF, $F_{\mathrm{Bkg}}(x)$, is determined by interpolation of parameterized sidebands. The likelihood

fits are performed for different pseudoproper decay length background $F_{\mathrm{Bkg}}(x)$ templates, as discussed in Sec. 4.2.2. In these variations, limits of invariant mass sidebands, as listed in Table 4.4 are varied by $\pm$ 20 MeV/c^2, which produces 9 configurations for evaluation of systematic uncertainty due to $F_{\mathrm{Bkg}}(x)$ template in the each p_{T} and centrality range. The linear $(n = 1)$ and quadratic $(n = 2)$ weights are considered for the interpolation of $F_{\mathrm{Bkg}}(x)$ template, as described by Eq. 4.12. The assigned systematic uncertainty due to $F_{\mathrm{Bkg}}(x)$ template is equal to the standard deviation of extracted f_{B} values from all of these variations. Due to the smaller signal to background ratio, systematic uncertainties is the largest at low p_{T}. The values obtained from these variations are shown in Fig. 4.31 for 0–10%, Fig. 4.32 for 10–30%, and Fig. 4.33 for 30–50%.

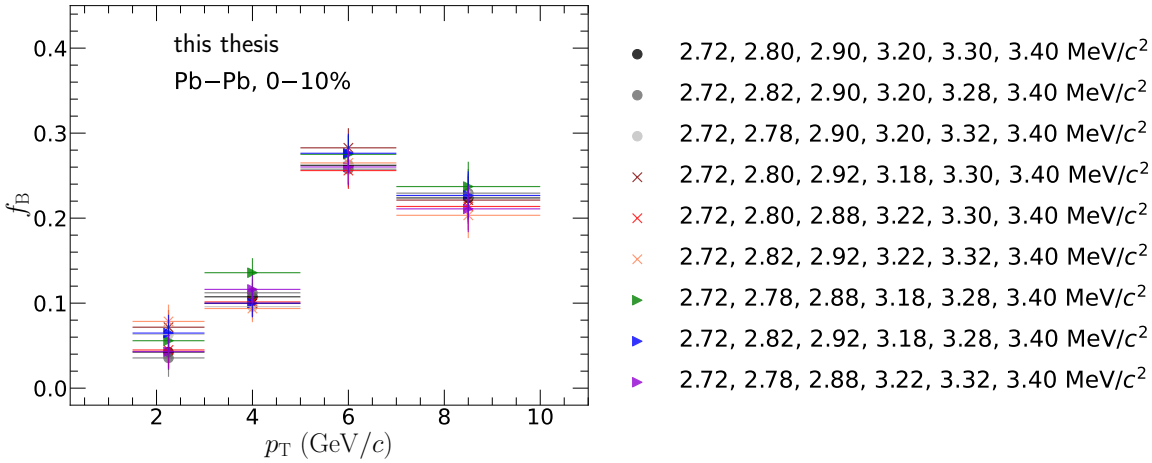

Figure 4.31 Systematic variations in f_{B} due to modifications in pseudoproper decay length background templates in case of linear weights $(n = 1)$ in 0–10% centrality interval (see text for details).

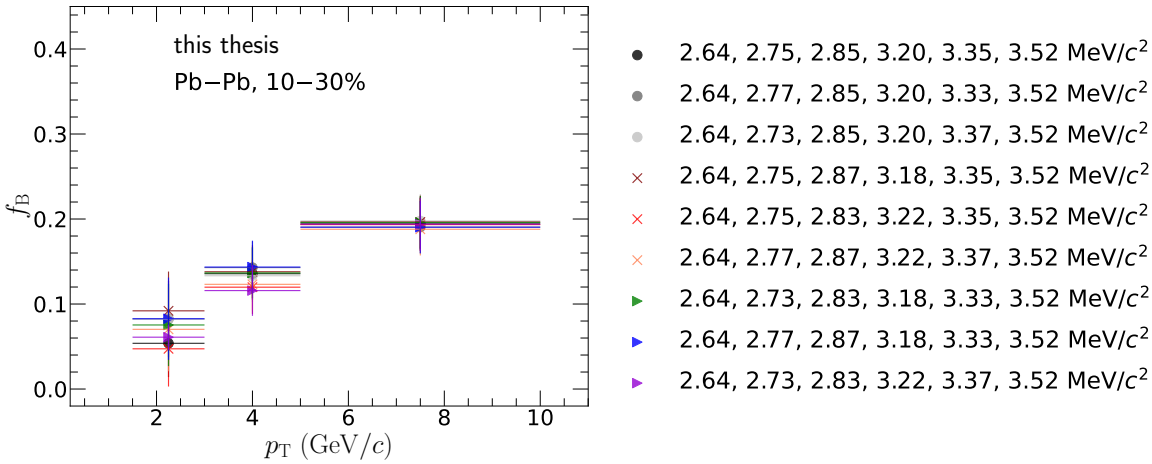

Figure 4.32 Systematic variations in f_{B} due to modifications in pseudoproper decay length background templates in case of linear weights $(n = 1)$ in 10–30% centrality interval (see text for details).

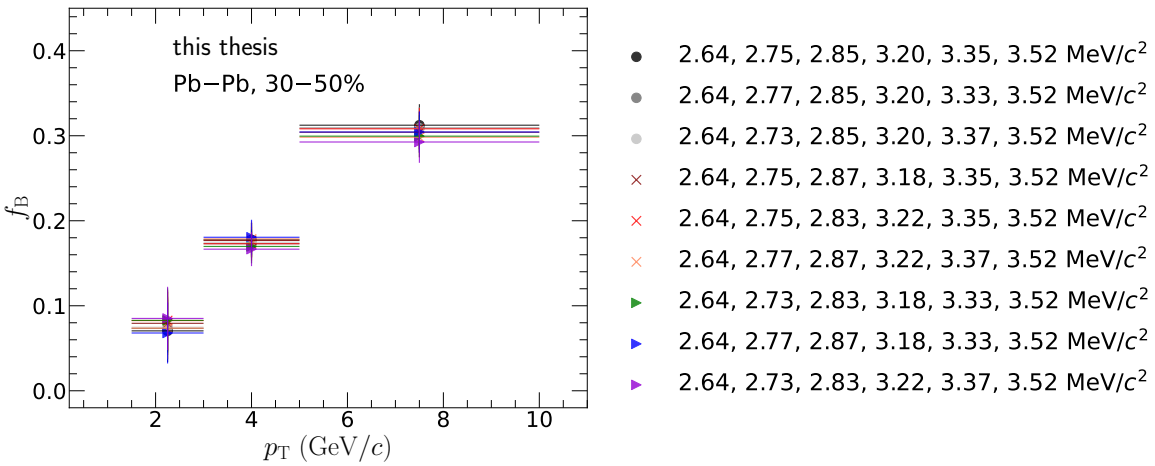

Figure 4.33 Systematic variations in f_{B} due to modifications in pseudoproper decay length background templates in case of linear weights ($n = 1$) in 30–50% centrality interval (see text for details).

4.4.2 Resolution function

The transverse impact parameter resolution ($d_0(r\phi)$) is worse in the data compared to the MC sample, as shown in Fig. 4.6. Therefore, a tuning procedure is applied to the MC sample which reduces the discrepancy in $d_0(r\phi)$ between data and MC simulation to approximately 3% (see Sec. 4.1.5). Hence, systematic uncertainty related to this difference is evaluated by modifying the resolution function according to following expression,

$$R^{'}(x) = \frac{1}{1+\delta} \cdot R\left(\frac{x}{1+\delta}\right), \tag{4.17}$$

where δ is $\pm$ 3%. For each p_{T} and centrality range, the likelihood fits are repeated with modified resolution functions by modifying δ by +3% and –3%, the largest deviation is considered as systematic uncertainty due to resolution function. In all centrality ranges, the largest systematic uncertainties are obtained in case of the lowest p_{T} ranges due to the lowest signal to background ratio in these p_{T} ranges. The relative difference in the f_{B}, after varying the resolution function, is shown in Fig. 4.34.

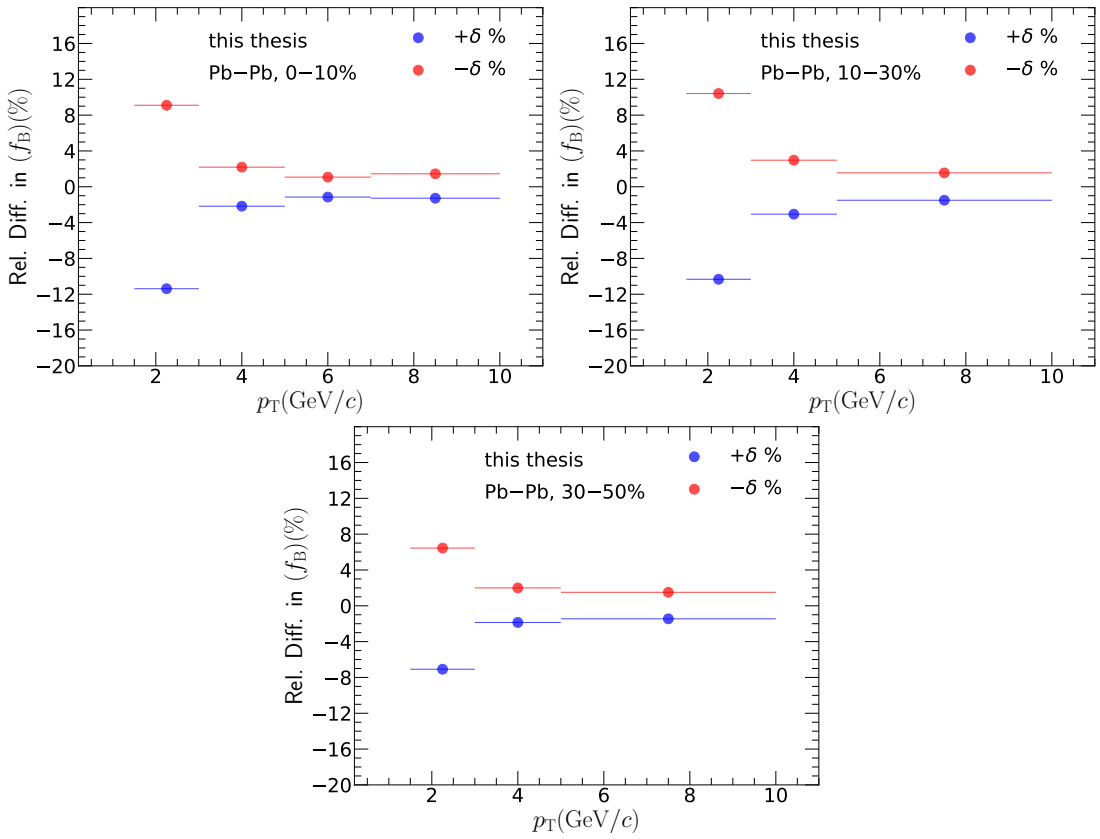

Figure 4.34 Systematic variations in f_B due to modifications in resolution function templates in 0–10%, 10–30% and 30–50% centrality classes; the value of δ is 3%.

4.4.3 Invariant mass signal

Invariant mass signal PDF, $M_{\mathrm{Sig}}(m)$, is determined from the dielectron invariant mass spectrum obtained from MC sample. In the MC simulation, EvtGen [190] and PHOTOS [191] packages produce radiative decay and detector resolution effects. The interactions of electrons with detector material are not completely described in the simulations. Therefore, a systematic uncertainty related to $M_{\mathrm{Sig}}(m)$ PDF is estimated by varying the $M_{\mathrm{Sig}}(m)$ PDF width such as signal fraction $\Delta f_{\mathrm{Sig}}/f_{\mathrm{Sig}}$ in the mass range, $2.92 < m_{\mathrm{ee}} < 3.16\ \mathrm{GeV}/c^2$, changes by δ = –3% and +3%. The variation is based on systematic uncertainties related to J/ψ signal shape in the inclusive J/ψ measurements in Pb–Pb collisions at $\sqrt{s_{\mathrm{NN}}}$= 5.02 TeV [152]. A modified $M_{\mathrm{Sig}}(m)$ PDF is shown in the top-left panel of Fig. 4.35. The likelihood fits are repeated by using modified $M_{\mathrm{Sig}}(m)$ PDFs, and maximum deviation is used as a systematic uncertainty due to $M_{\mathrm{Sig}}(m)$. The relative difference in the f_B, after varying the $M_{\mathrm{Sig}}(m)$, is shown in the top-right and bottom panels of Fig. 4.35. The systematic uncertainty contribution due to $M_{\mathrm{Sig}}(m)$ is smaller than 3% in all p_T and centrality ranges.

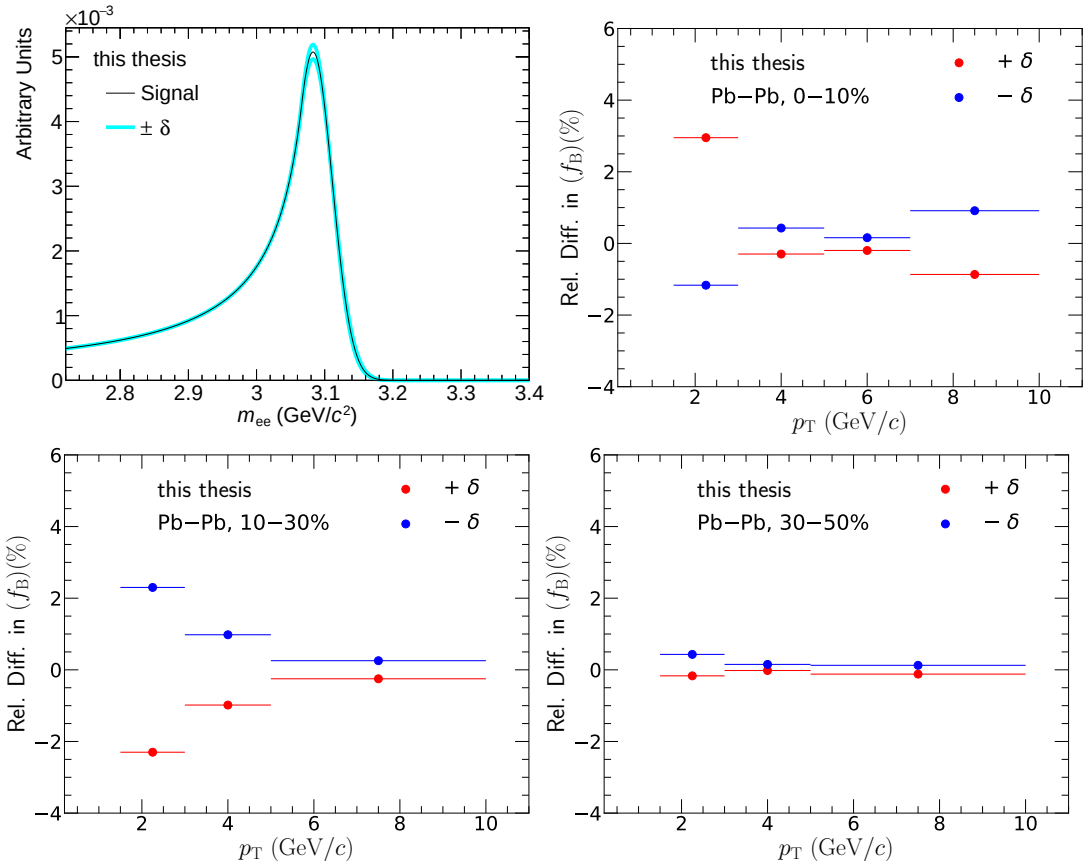

Figure 4.35 Modification in the invariant mass signal PDF by varying the relative signal fraction by $\delta = \pm 3\%$ (top, left), Systematic variations in f_B due to modifications in invariant mass background templates in 0–10% (top, right), 10–30% (bottom, left), and 30–50% (bottom, right) centrality intervals.

4.4.4 Invariant mass background

In the likelihood fits, the determination of invariant mass background is based on mixed event pairs and residual background as described in Sec. 4.2.2. The correlated background shape is described by the 2nd-order polynomial function. To account for the uncertainties in the correlated background shape, higher order polynomials (3rd and 4th order) are also considered. Different choices of polynomials are shown in the top-left panel of Fig. 4.36. The likelihood fits are repeated with modified $M_{\mathrm{Bkg}}(m)$ PDFs, and maximum deviation is used as a systematic uncertainty due to $M_{\mathrm{Bkg}}(m)$ PDF. The relative difference in the f_B, after varying the $M_{\mathrm{Bkg}}(m)$, is shown in the top-right and bottom panels of Fig. 4.36. The systematic uncertainty contribution due to $M_{\mathrm{Bkg}}(m)$ is smaller than 5% in all p_T and centrality ranges.

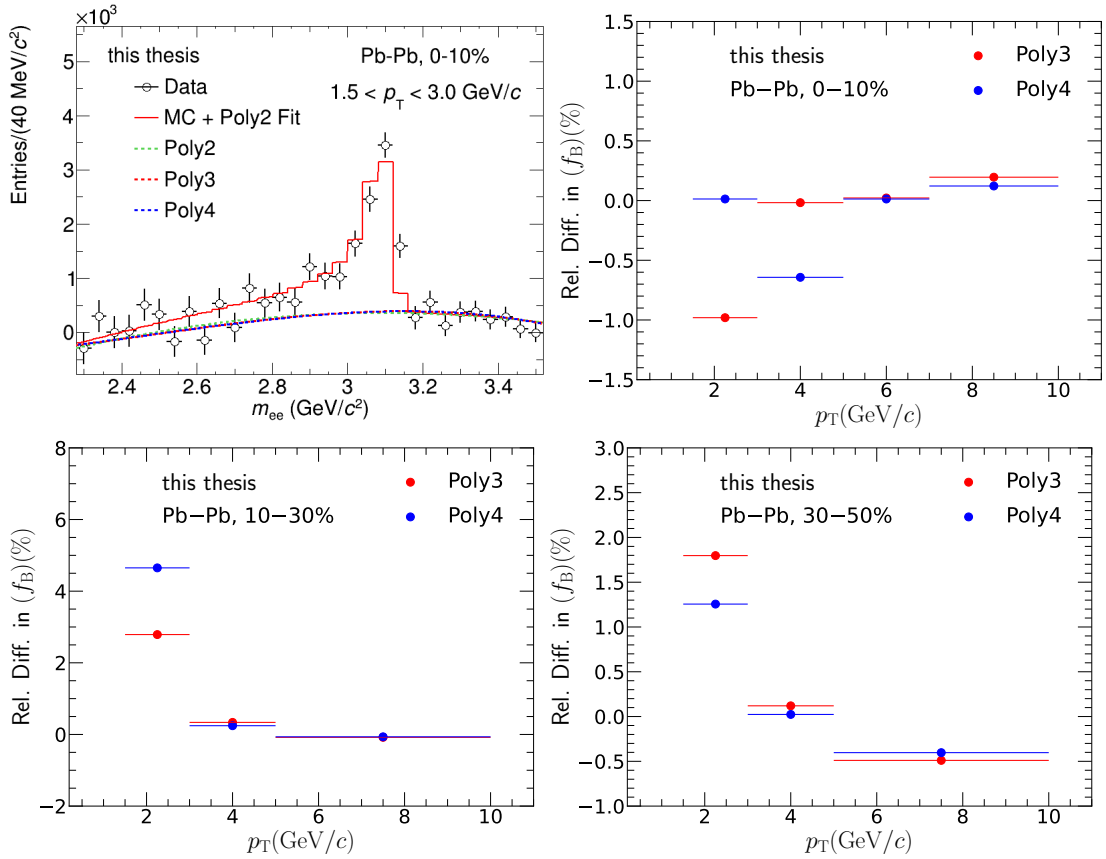

Figure 4.36 Invariant mass signal parametrization assuming different residual background shapes (top, left), Systematic variations in f_B due to modifications in invariant mass background templates in 0–10% (top, right), 10–30% (bottom, left), and 30–50% (bottom, right) centrality intervals.

4.4.5 MC p_T shape

For determining the systematic uncertainties due to MC p_T shapes, different choices of non-prompt J/ψ and prompt J/ψ p_T spectrum are used, as described in Sec. 4.3. It yields a set of $\langle A \times \epsilon \rangle$ for prompt and non-prompt J/ψ and corresponding R factors as demonstrated in Fig. 4.29 and a relative difference in f_B due to corresponding R factors are shown in Fig. 4.37. The maximum variation is considered as a systematic uncertainty due to the MC p_T shape in a given p_T range. The systematic uncertainty contribution due to MC p_T shape is smaller than 3% in all p_T and centrality ranges, as shown in Fig. 4.37 and in the Tables 4.5-4.7. In the integrated p_T range, the systematic uncertainties amounts to 5-6% which is one of the largest contribution in this range.

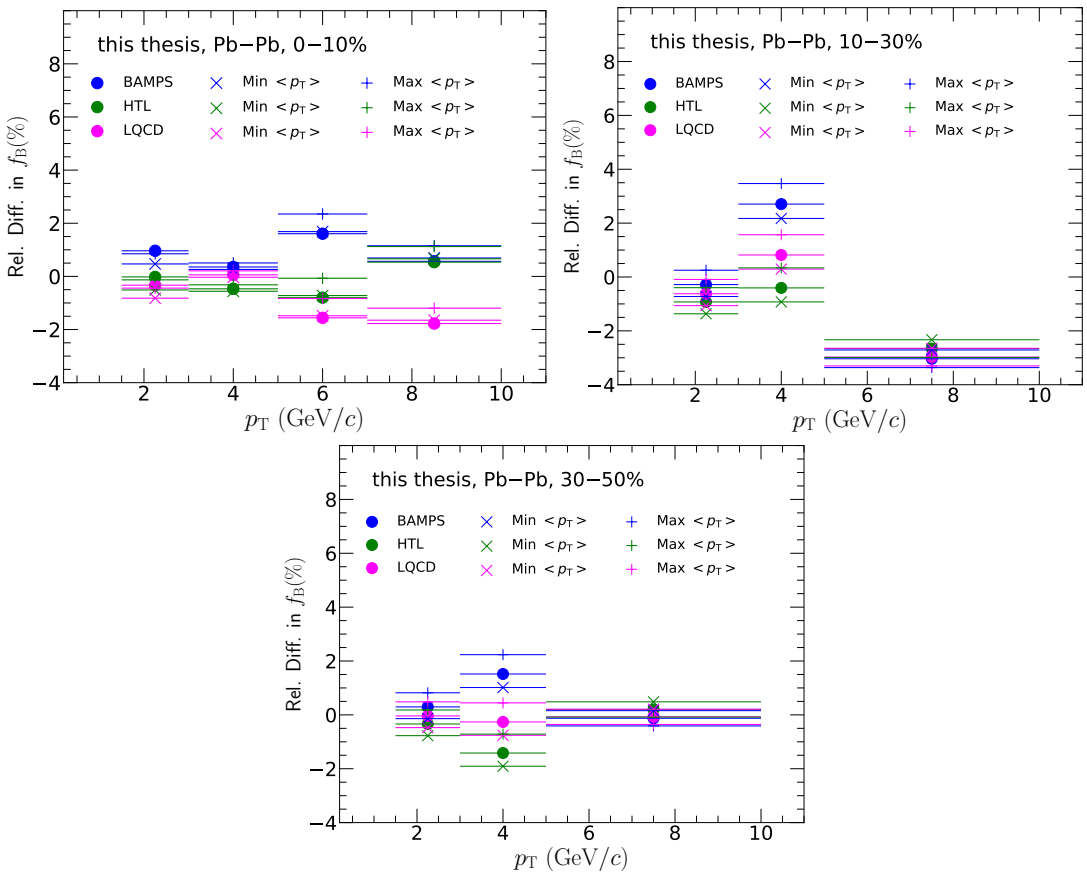

Figure 4.37 Systematic variations in f_B due to modifications in the MC p_T shapes of prompt and non-prompt J/ψ in 0–10%, 10–30%, and 30–50% centrality intervals.

4.5 Non-prompt J/ψ fraction

The non-prompt J/ψ fractions have been measured as a function of p_T in Pb–Pb collisions in 0–10%, 10–30%, and 30–50% centrality intervals. In addition, f_B is also measured in the integrated p_T range ($1.5 < p_T < 10$ GeV/c) in the aforementioned centrality intervals. The systematic uncertainties due to possible sources are also estimated. The Table 4.8, demonstrates the f_B mean values and statistical uncertainties obtained from unbinned likelihood fits along with the systematic uncertainties in each p_T and centrality range. In all centrality ranges, f_B exhibits an increasing trend with p_T, which demonstrates a large contribution of non-prompt J/ψ at high p_T. The fractions as a function of p_T are shown in the Fig. 4.38 in 0–10% (top-left), 10–30% (top-right) and 30–50% (bottom-left). The fractions as a function of $\langle N_{part} \rangle$, in $1.5 < p_T < 10$ GeV/c is also shown in the bottom-right panel of the Fig. 4.38. The statistical and systematic uncertainties are represented by bars and boxes, respectively.

Centrality	p_{T} (GeV/c)	$f_{\mathrm{B}}{}^{\mathrm{mean}} \pm f_{\mathrm{B}}{}^{\mathrm{stat}} \pm f_{\mathrm{B}}{}^{\mathrm{syst}}$
0–10%	1.5-10	0.130 $\pm$0.013 $\pm$ 0.011
	1.5-3	0.037 $\pm$0.020 $\pm$ 0.010
	3-5	0.105 $\pm$0.016 $\pm$ 0.012
	5-7	0.259 $\pm$0.022 $\pm$ 0.011
	7-10	0.221 $\pm$0.028 $\pm$ 0.010
10–30%	1.5-10	0.159 $\pm$0.027 $\pm$ 0.014
	1.5-3	0.059 $\pm$0.040 $\pm$ 0.014
	3-5	0.142 $\pm$0.031 $\pm$ 0.015
	5-10	0.191 $\pm$0.031 $\pm$ 0.008
30–50%	1.5-10	0.177 $\pm$0.020 $\pm$ 0.015
	1.5-3	0.070 $\pm$0.039 $\pm$ 0.008
	3-5	0.183 $\pm$0.020 $\pm$ 0.007
	5-10	0.310 $\pm$0.024 $\pm$ 0.008

Table 4.8 Measurements of non-prompt J/ψ fractions with statistical and systematic uncertainties as a function of p_{T} in different centrality intervals.

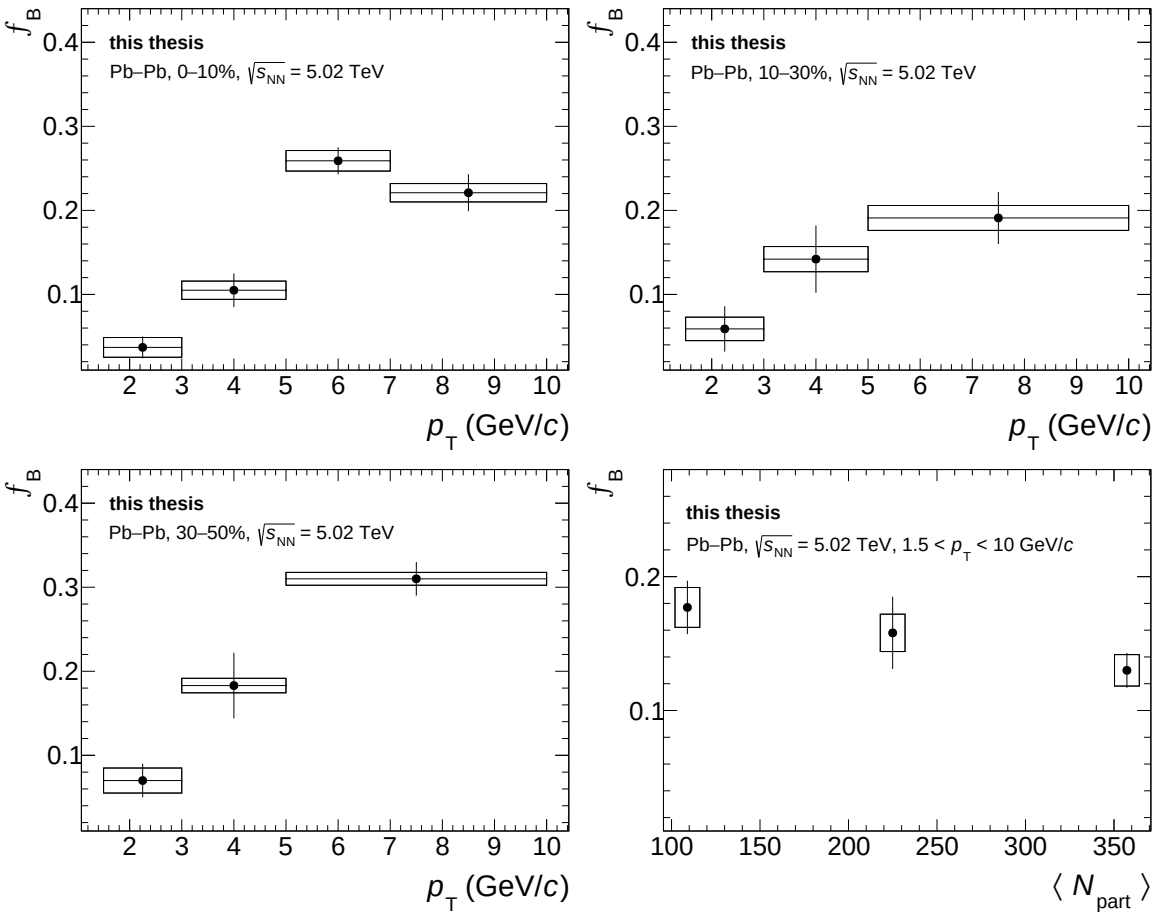

Figure 4.38 Non-prompt J/ψ fraction as a function of p_{T} in Pb–Pb collisions at $\sqrt{s_{\mathrm{NN}}}$= 5.02 TeV in 0–10% (top-left), 10–30% (top-right), 30–50% (bottom-left); f_{B} as function of $\langle N_{\mathrm{part}} \rangle$ is also shown in integrated p_{T} range in bottom-right panel; statistical and systematic uncertainties are shown as bars and boxes, respectively.

Chapter 5

Prompt and non-prompt J/ψ measurements

"The important thing in science is not so much to obtain new facts as to discover new ways of thinking about them."

W. L. Bragg

To evaluate the nuclear modification factors ($R_{\rm AA}$) of prompt and non-prompt J/ψ, the inclusive J/ψ $R_{\rm AA}$ is scaled by the ratio of prompt and non-prompt J/ψ fractions in Pb–Pb and pp collisions in a given $p_{\rm T}$ and centrality range. The non-prompt J/ψ fraction ($f_{\rm B}$) is obtained in the previous sections in Pb–Pb collisions at $\sqrt{s_{\rm NN}}$= 5.02 TeV at midrapidity. It is required to have $f_{\rm B}^{\rm pp}$ values in the same energy and $p_{\rm T}$-bins similar to Pb–Pb analysis.

The prompt and non-prompt production yields are determined according to the following expression,

$$\frac{{\rm d}^2N^{\text{ Prompt J}/\psi}}{{\rm d}y{\rm d}p_{\rm T}} = (1-f_{\rm B}) \times \frac{{\rm d}^2N^{\text{ Incl. J}/\psi}}{{\rm d}y{\rm d}p_{\rm T}}, \qquad \frac{{\rm d}^2N^{\text{ Non-prompt J}/\psi}}{{\rm d}y{\rm d}p_{\rm T}} = f_{\rm B} \times \frac{{\rm d}^2N^{\text{ Incl. J}/\psi}}{{\rm d}y{\rm d}p_{\rm T}}. \quad (5.1)$$

The $f_{\rm B}$ is non-prompt J/ψ fraction in Pb–Pb at $\sqrt{s_{\rm NN}}$= 5.02 TeV while $\frac{{\rm d}^2N^{\text{ Incl. J}/\psi}}{{\rm d}y{\rm d}p_{\rm T}}$ is inclusive J/ψ production yield in Pb–Pb collisions at the same $\sqrt{s_{\rm NN}}$.

Nuclear modification factors of prompt and non-prompt J/ψ in a given $p_{\rm T}$ range are determined by the following expression,

$$R_{\rm AA}^{\text{Prompt J}/\psi} = \frac{1-f_{\rm B}}{1-f_{\rm B}^{\rm pp}} R_{\rm AA}^{\text{Incl. J}/\psi}, \qquad R_{\rm AA}^{\text{Non-prompt J}/\psi} = \frac{f_{\rm B}}{f_{\rm B}^{\rm pp}} R_{\rm AA}^{\text{Incl. J}/\psi}, \quad (5.2)$$

where $f_{\rm B}$ and $f_{\rm B}^{\rm pp}$ are non-prompt J/ψ fractions in Pb–Pb and pp collisions, respectively, while $R_{\rm AA}^{\text{Incl. J}/\psi}$ is nuclear modification factor of inclusive J/ψ in Pb–Pb collisions.

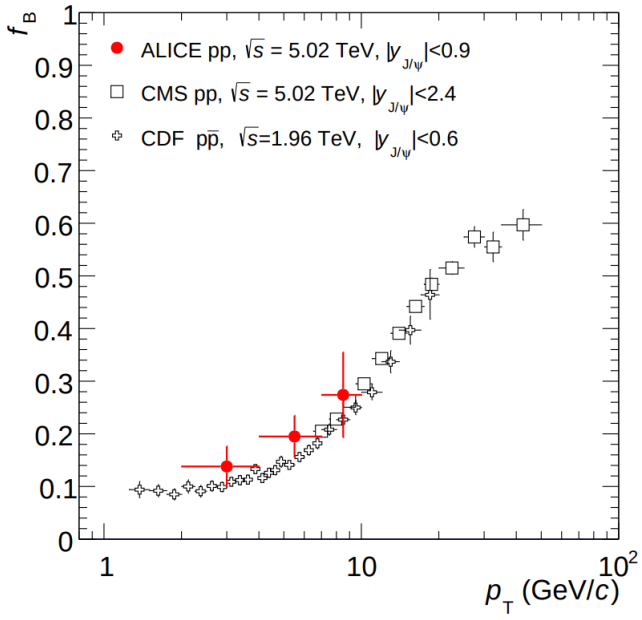

Figure 5.1 Non-prompt J/ψ fraction as a function of p_{T} in pp collisions at $\sqrt{s} = 5.02$ TeV by ALICE experiment [98].

5.1 f_{B} in pp collisions

ALICE has performed the non-prompt J/ψ measurements as a function of p_{T} in pp collisions at $\sqrt{s} = 5.02$ TeV [98], the non-prompt J/ψ fractions are shown in the Fig. 5.1. These measurements are performed in the different p_{T} ranges as compared to those measured in Pb–Pb collisions as described in the previous chapter. Therefore, f_{B} obtained in pp collisions cannot be used as a pp reference for the determination of prompt and non-prompt R_{AA}. The pp reference are therefore obtained in the same p_{T} ranges as in Pb–Pb collisions using a different method in which a phenomenological approach is adopted. This approach involves the results of previous non-prompt J/ψ measurements in pp collisions at different $\sqrt{s}$ at midrapidity. The available measurements at midrapidity, as mentioned in Table 5.1, are parameterized by the function described by the following expression,

$$f_{\mathrm{B}}^{\mathrm{model}}(p_{\mathrm{T}}, y) = \frac{\mathrm{d}^2\sigma_{(\mathrm{B}\to \mathrm{J}/\psi)}/\mathrm{d}y\mathrm{d}p_{\mathrm{T}}}{\mathrm{d}^2\sigma_{\mathrm{Incl.\,J}/\psi}/\mathrm{d}y\mathrm{d}p_{\mathrm{T}}}. \tag{5.3}$$

The Eq. 5.3 represents a ratio of p_{T}-differential production cross section of non-prompt J/ψ, obtained from the FONLL calculations [132] at midrapidity and p_{T}-differential cross section of inclusive J/ψ in pp collisions at $\sqrt{s} = 5.02$ TeV [200]. The inclusive J/ψ cross section is parameterized by the power-law function as described in Eq. 4.16.

The parameterized functional form is shown in Fig. 5.2 at $\sqrt{s} = 7$ TeV by ALICE [97], CMS [100] and ATLAS [101] measurements. The fit is performed for three cases: central, minimum and maximum values of non-prompt J/ψ cross section obtained from FONLL

calculation as shown in Fig 5.2. Similarly, the measurements at other $\sqrt{s}$ are parameterized to get $f_{\rm B}(p_{\rm T})$. In total, there are four $f_{\rm B}(p_{\rm T})$ spectra obtained from this parameterization at $\sqrt{s}$ = 1.96, 5.02, 7, and 8 TeV.

The $f_{\rm B}$ values are evaluated at the same $p_{\rm T}$ as a function of $\sqrt{s}$ and parameterized by three functional forms: linear, exponential and power-law function which results in three parametrizations $f_{\rm B}^{i}(\sqrt{s}\,)$ where i denotes linear, exponential and power-law functions. A weighted average of $f_{\rm B}^{i}(\sqrt{s}=5.02)$ from these functions is considered as $f_{\rm B}^{\rm pp}$ at given $p_{\rm T}$. To get $f_{\rm B}^{\rm pp}$, the non-prompt J/ψ measurements by CDF [196] at $\sqrt{s}$ = 1.96 TeV, CMS [99] and ALICE [98] at $\sqrt{s}$ = 5.02 TeV, CMS [100] and ATLAS [102] at $\sqrt{s}$ = 7 TeV and ATLAS [102] at $\sqrt{s}$ = 8 TeV are used. The measurements by CMS [99] and ALICE [98] at $\sqrt{s}$ = 5.02 TeV are crucial in the interpolation because they constrain the $f_{\rm B}^{\rm pp}$ values and help to reduce the systematic uncertainties on $f_{\rm B}^{\rm pp}$.

Systematic uncertainties are estimated for the interpolated values of $f_{\rm B}^{\rm pp}$ in each $p_{\rm T}$ interval. To obtain systematic uncertainties, the procedure is repeated several times, excluding each dataset one by one at each $\sqrt{s}$ = 1.96, 7, 8 TeV mentioned in Table 5.1. Systematic uncertainty on pp reference is the standard deviation of $f_{\rm B}^{\rm pp}$ mean values obtained from the mentioned variations. The final values of $f_{\rm B}^{\rm pp}$ with statistical and systematic uncertainties are shown in Table 5.2.

$\sqrt{s}$ (TeV)	Available measurements
1.96	CDF, $\|y\| < 0.6$ [196]
5	ALICE, $\|y\| < 0.9$ [98]
	CMS, $\|y\| < 2.4$ [99]
7	ALICE, $\|y\| < 0.9$ [97]
	ATLAS, $\|y\| < 0.25$ [102]
	ATLAS, $\|y\| < 0.75$ [101]
	CMS, $\|y\| < 0.9$ [100]
8	ATLAS, $\|y\| < 0.25$ [102]

Table 5.1 Available measurements of $f_{\rm B}$ $(p_{\rm T})$ in pp collisions at different $\sqrt{s}$ which are used for parameterization.

The obtained $f_{\rm B}^{\rm pp}$ values are shown as a function of $p_{\rm T}$ in Fig. 5.3 in comparison to previous ALICE measurements at $\sqrt{s}$ = 5.02 TeV [98]. It is clear from Fig. 5.3 that $f_{\rm B}^{\rm pp}$ values are determined with a better precision in comparison to the $f_{\rm B}$ measurements at $\sqrt{s}$ = 5.02 TeV [98] by the ALICE.

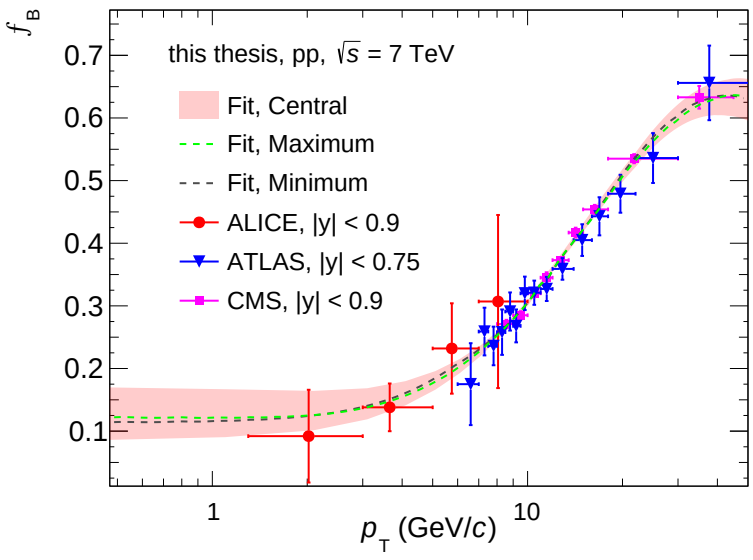

Figure 5.2 Parameterized non-prompt J/ψ fraction as a function of J/ψ p_{T} in pp collisions at $\sqrt{s}$ = 7 TeV; Central, maximum and minimum fits corresponds to the central, maximum and minimum values of FONLL predictions. Uncertainty band is shown for the central values FONLL of predictions.

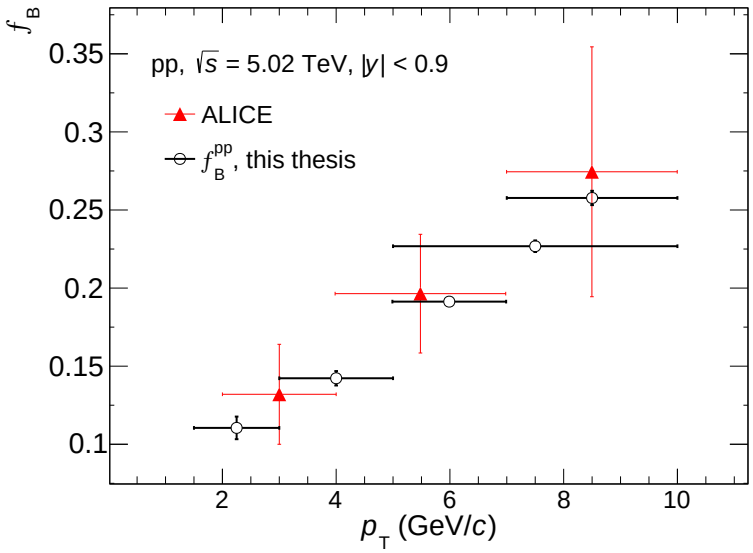

Figure 5.3 Non-prompt J/ψ fractions as a function of p_{T} extracted from interpolation at $\sqrt{s}$= 5.02 TeV compared with ALICE measurements at the same energies [98]; Demonstrated uncertainties in $f_{\mathrm{B}}^{\mathrm{pp}}$ represent quadrature sum of statistical and systematic uncertainties listed in Table 5.2.

p_{T} (GeV/c)	$f_{\mathrm{B}}^{\mathrm{pp}} \pm$ stat $\pm$ syst
1.5 - 10	$0.183 \pm 0.003 \pm 0.002$
1.5 - 3	$0.110 \pm 0.006 \pm 0.004$
3 - 5	$0.142 \pm 0.003 \pm 0.003$
5 - 7	$0.190 \pm 0.002 \pm 0.002$
7 - 10	$0.257 \pm 0.004 \pm 0.001$
5 - 10	$0.227 \pm 0.003 \pm 0.001$

Table 5.2 $f_{\mathrm{B}}^{\mathrm{pp}}$ at $\sqrt{s} = 5.02$ TeV obtained by interpolation in the different p_{T} intervals.

5.2 Production yields

The determination of prompt and non-prompt p_{T}-differential yields is based on inclusive J/ψ p_{T}-differential measurements [152] in Pb–Pb collisions at $\sqrt{s_{\mathrm{NN}}}$= 5.02 TeV, as described by Eq. 5.1. The prompt and non-prompt J/ψ p_{T}-differential yields are shown in Fig. 5.4 for p_{T} down to 1.5 GeV/c in 0–10%, 10–30% and 30–50% centrality intervals. These results follow a decreasing trend as a function of p_{T}. The productions yields are larger in the most central collision in comparison to semicentral collisions. Also, non-prompt J/ψ yields are less than prompt J/ψ in the corresponding centrality and p_{T} intervals.

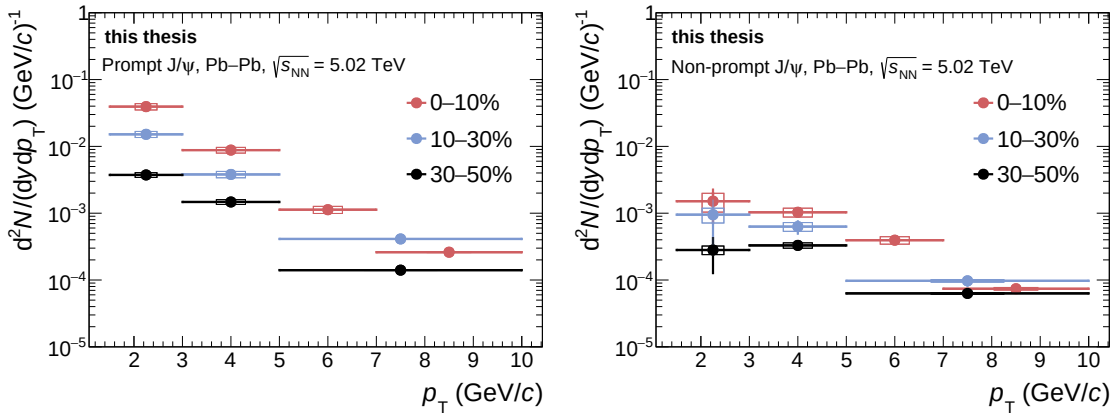

Figure 5.4 Prompt (left) and non-prompt (right) J/ψ p_{T} differential yield a function of p_{T} in 0–10%, 10–30%, and 30–50% centrality interval, statistical and systematic uncertainties are represented by vertical bars and boxes, respectively. In some cases, uncertainties are smaller than markers.

5.3 Nuclear modification factor

Prompt and non-prompt J/ψ nuclear modification factors are shown as a function of p_{T} in 0–10%, 10–30%, and 30–50% centrality classes in Fig. 5.5. The corresponding values are

listed in Table 5.3. The systematic uncertainties for the $R_{\rm AA}$ are determined by a quadrature sum of systematic uncertainties of $f_{\rm B}$ in Pb–Pb, $f_{\rm B}^{\rm pp}$ and the systematic uncertainties of inclusive J/ψ $R_{\rm AA}$ by considering uncorrelated from each other.

The measurements suggest that J/ψ production is largely suppressed at higher $p_{\rm T}$ while the degree of suppression reduces at low $p_{\rm T}$. For prompt J/ψ, $R_{\rm AA}$ increases up to a level where it is consistent with unity at low $p_{\rm T}$, especially in the most central collisions. Similarly, non-prompt J/ψ $R_{\rm AA}$ also increases at low $p_{\rm T}$, but no clear centrality dependence has been observed. Global uncertainties are shown in the boxes for all centrality intervals. They include uncertainties from the normalization of non-prompt J/ψ fraction in pp collisions as obtained in the previous section and $\langle T_{AA} \rangle$. The global uncertainties are 2.31%, 2.30%, and, 2.72% for 0–10%, 10–30%, and 30–50% centrality classes, respectively.

Centrality	$p_{\rm T}$ (GeV/c)	Prompt J/ψ	Non-prompt J/ψ
0–10%	1.5-3	1.405 $\pm 0.133 \pm 0.172$	0.436 $\pm 0.240 \pm 0.141$
	3-5	0.697 $\pm 0.070 \pm 0.078$	0.494 $\pm 0.090 \pm 0.080$
	5-7	0.289 $\pm 0.044 \pm 0.039$	0.431 $\pm 0.074 \pm 0.062$
	7-10	0.254 $\pm 0.052 \pm 0.017$	0.208 $\pm 0.049 \pm 0.016$
10–30%	1.5-3	1.087 $\pm 0.139 \pm 0.129$	0.551 $\pm 0.381 \pm 0.144$
	3-5	0.605 $\pm 0.081 \pm 0.074$	0.605 $\pm 0.154 \pm 0.097$
	5-10	0.429 $\pm 0.059 \pm 0.029$	0.345 $\pm 0.072 \pm 0.028$
30–50%	1.5-3	0.792 $\pm 0.099 \pm 0.078$	0.482 $\pm 0.276 \pm 0.080$
	3-5	0.692 $\pm 0.071 \pm 0.069$	0.937 $\pm 0.140 \pm 0.102$
	5-10	0.433 $\pm 0.052 \pm 0.029$	0.663 $\pm 0.093 \pm 0.049$

Table 5.3 Nuclear modification factors of prompt and non-prompt J/ψ with statistical and systematic uncertainties in different $p_{\rm T}$ and centrality intervals.

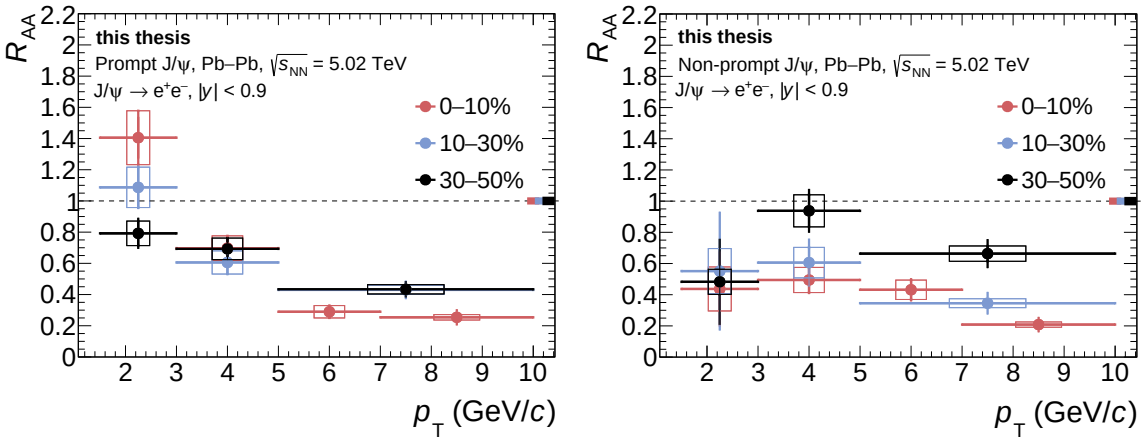

Figure 5.5 Prompt (left) and non-prompt (right) J/ψ nuclear modification factor (R_{AA}) as a function of p_{T} in different centrality intervals at $\sqrt{s_{\mathrm{NN}}}$= 5.02 TeV, statistical and systematic uncertainties are represented by vertical bars and boxes, respectively. The global uncertainties are shown on the right side on the line corresponding to $R_{\mathrm{AA}} = 1$.

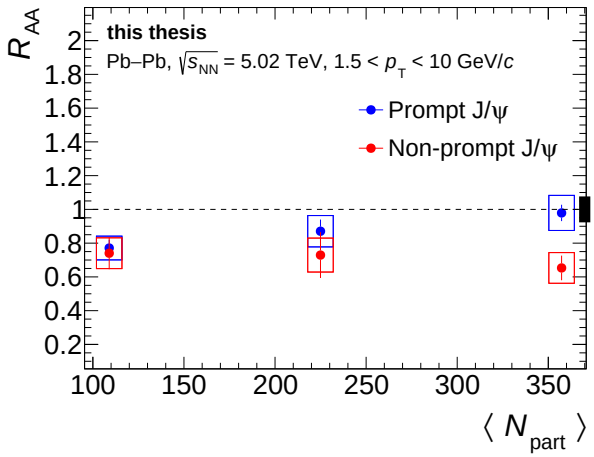

Figure 5.6 Prompt and non-prompt J/ψ nuclear modification factor as a function of $\langle N_{\mathrm{part}} \rangle$, statistical and systematic uncertainties are represented by vertical bars and boxes, respectively. The global uncertainty is shown on the right side on the line corresponding to $R_{\mathrm{AA}} = 1$.

The Fig. 5.6 illustrates the behavior of prompt and non-prompt J/ψ R_{AA} as a function of the average number of participants, $\langle N_{\mathrm{part}} \rangle$, in Pb–Pb collisions. It is observed that in semicentral collisions, both prompt and non-prompt productions exhibit a significant suppression. Furthermore, it has been quantitatively demonstrated that both productions are modified similarly, and their respective R_{AA} values are consistent within the uncertainties in the 10–30% and 30–50% centrality intervals. However, in the 0–10% centrality interval, non-prompt J/ψ production experiences a larger suppression compared to prompt J/ψ production, where the prompt J/ψ R_{AA} is consistent with unity. The difference between both measurements in this centrality range amounts to 1.7σ, considering both statistical and

systematic uncertainties. These observations suggest that prompt J/ψ production is less suppressed in most central collisions than in semicentral collisions.

Chapter 6

Results

"Science is a way of thinking much more than it is a body of knowledge."

Carl Sagan

In this chapter, the obtained non-prompt J/ψ fractions, prompt and non-prompt J/ψ production yields and $R_{\rm AA}$ are discussed. The discussion is extended to comparison of the results with similar measurements and theoretical models.

6.1 Comparison with similar measurements

The measurement of the non-prompt J/ψ fraction as a function of $p_{\rm T}$ has been conducted in Pb–Pb collisions at $\sqrt{s_{\rm NN}}$= 5.02 TeV at midrapidity in three different centrality intervals, namely 0–10%, 10–30%, and 30–50%, $p_{\rm T}$ down to 1.5 GeV/c as demonstrated in Fig. 4.38. The obtained results are compared with the results of similar measurements by ATLAS [155] in 0–10%, 20–40% and 40–80% centrality intervals and CMS [154] in 0–100% centrality interval at midrapidity. In the top-left, top-right, and bottom-left panels of Fig. 6.1, the obtained $f_{\rm B}$ values are compared with the measurements done by ATLAS in different centrality intervals for $p_{\rm T}$ larger than 9.5 GeV/c. The results demonstrate that the values of $f_{\rm B}$ increase as a function of $p_{\rm T}$ across all centrality intervals. These comparisons indicates that the obtained results are complementary to the ATLAS and CMS results, with a partial overlap observed in the highest $p_{\rm T}$ bin. Furthermore, in the bottom-right panel of Fig. 6.1, a comparison with CMS results is made for $p_{\rm T}$ above 6.5 GeV/c in 0–100% centrality, suggesting that the results are consistent in the high $p_{\rm T}$ region.

Additionally, the production yields of J/ψ as a function of $p_{\rm T}$ down to 1.5 GeV/c are compared with the corresponding results obtained by the ATLAS experiment [155]. The comparison is made in the 0–10% centrality intervals as shown in Fig. 6.2. The comparison reveals that the production yields of prompt and non-prompt J/ψ are in agreement with the yields observed at high $p_{\rm T}$ by the ATLAS.

Furthermore, the behavior of nuclear modification factors for prompt and non-prompt J/ψ production as a function of p_{T} is investigated down to 1.5 GeV/c. The results are presented in Fig. 5.5 for three centrality intervals: 0–10%, 10–30%, and 30–50%. The global uncertainties arise due to uncertainties in pp reference cross sections determination and $\langle T_{\mathrm{AA}} \rangle$ in the centrality determination. They are represented as bands on the right side of the dashed line at $R_{\mathrm{AA}} = 1$.

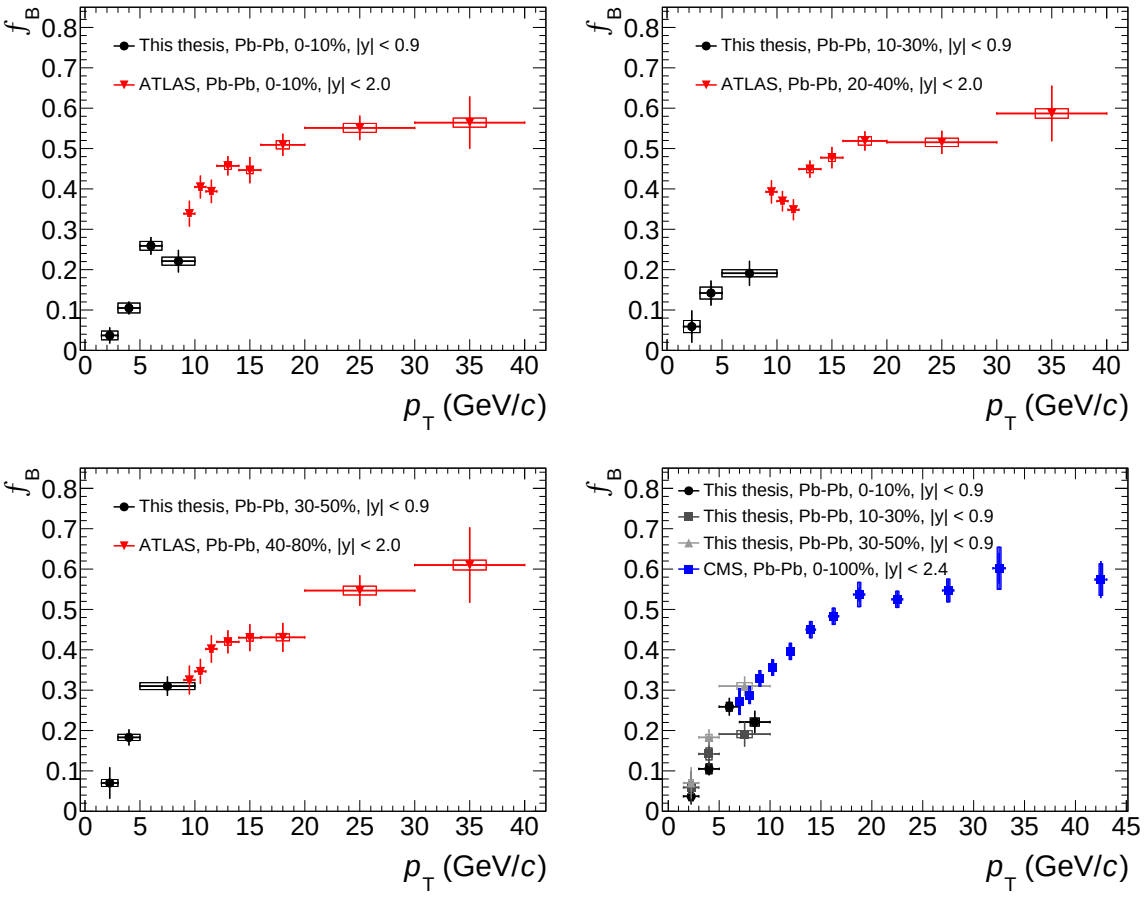

Figure 6.1 Non-prompt J/ψ fraction as a function of p_{T} in 0–10% (top, left), 10–30% (top, right), and 30–50% (bottom, left) centrality interval, in comparison with similar measurements by ATLAS [155]. Also, fractions in analyzed centrality intervals are compared with CMS [154] results (bottom, right). The statistical and systematic uncertainties are represented by vertical bars and boxes, respectively.

The observed behavior of R_{AA} suggests a strong suppression of J/ψ production due to dissociation effects and charm quark energy loss in the medium. For both prompt and non-prompt J/ψ, at p_{T} larger than 5 GeV/c, R_{AA} is lower than unity in all centrality intervals, indicating more suppression in most central collisions than in semicentral collisions. At p_{T} smaller than 5 GeV/c, prompt J/ψ R_{AA} tends towards higher values and approaches unity, which is most significant in the most central collisions. This observation is consistent with the regeneration of J/ψ at low p_{T}.

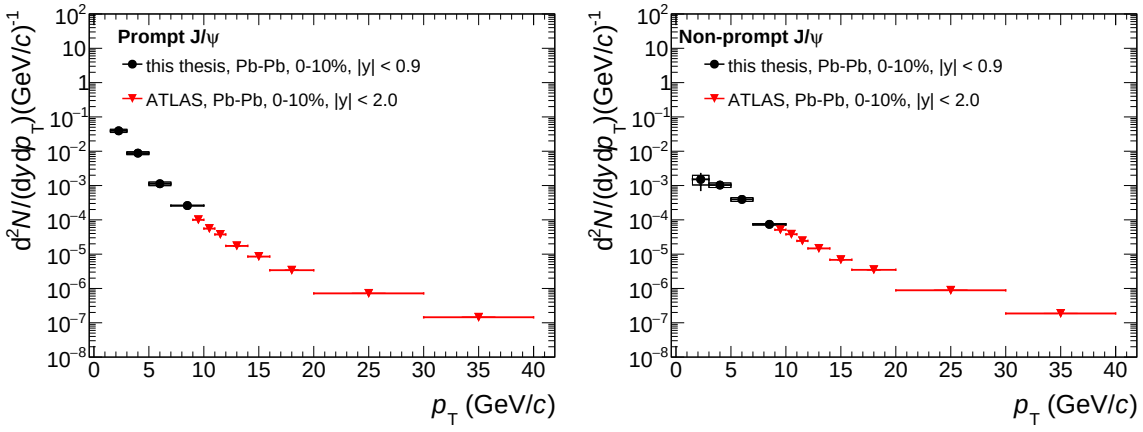

Figure 6.2 Prompt and non-prompt J/ψ p_{T} differential yield in 0–10% centrality interval, in comparison with similar measurements by ATLAS [155], statistical and systematic uncertainties are represented by vertical bars and boxes, respectively.

Nonetheless, at p_{T} smaller than 5 GeV/c, there is no clear centrality dependence for non-prompt J/ψ R_{AA}. However, the measurements hint towards a significant suppression of non-prompt J/ψ at low p_{T} in all considered centrality intervals, which suggests b-quark energy loss in the medium.

The nuclear modification factors of prompt and non-prompt J/ψ have been compared with similar measurements from ATLAS [155] and CMS [154] experiments at midrapidity. The comparisons are shown in Fig. 6.3 and Fig. 6.4 for prompt and non-prompt J/ψ, respectively. The figures show that prompt J/ψ R_{AA} values are consistent with those from ATLAS and CMS experiments in the overlapping p_{T} region within uncertainties in all centrality ranges. Apart from 0–10% centrality interval, the CMS and ATLAS results are obtained in different centrality intervals as compared to the centrality intervals presented in this work. However, the comparisons indicate that the degree of modification of prompt J/ψ production in Pb–Pb collisions within the specified p_{T} range is compatible across measurements.

Similarly, the non-prompt J/ψ R_{AA} values are also consistent with the CMS and ATLAS measurements within uncertainties, except for the 0–10% centrality interval, which shows a difference of 1.4σ and 2.5σ with the ATLAS and CMS results, respectively, in the overlapping p_{T} region. Nevertheless, the agreement of non-prompt J/ψ R_{AA} measurements from different experiments in most centrality ranges suggests a similar suppression of non-prompt J/ψ production due to b-quark energy loss in the medium. Overall, the comparisons with similar measurements from other experiments validate the findings of the current study on the suppression of prompt and non-prompt J/ψ production in heavy-ion collisions.

The Fig. 6.5 demonstrates the comparison of the p_{T}-differential R_{AA} of both prompt (left) and non-prompt (right) J/ψ obtained in the 0–10% centrality interval with the corresponding measurements made by the ALICE experiment [153] in the 0–50% centrality interval at $\sqrt{s_{\mathrm{NN}}}$= 2.76 TeV during LHC Run 1. The comparison shows that the measurements presented

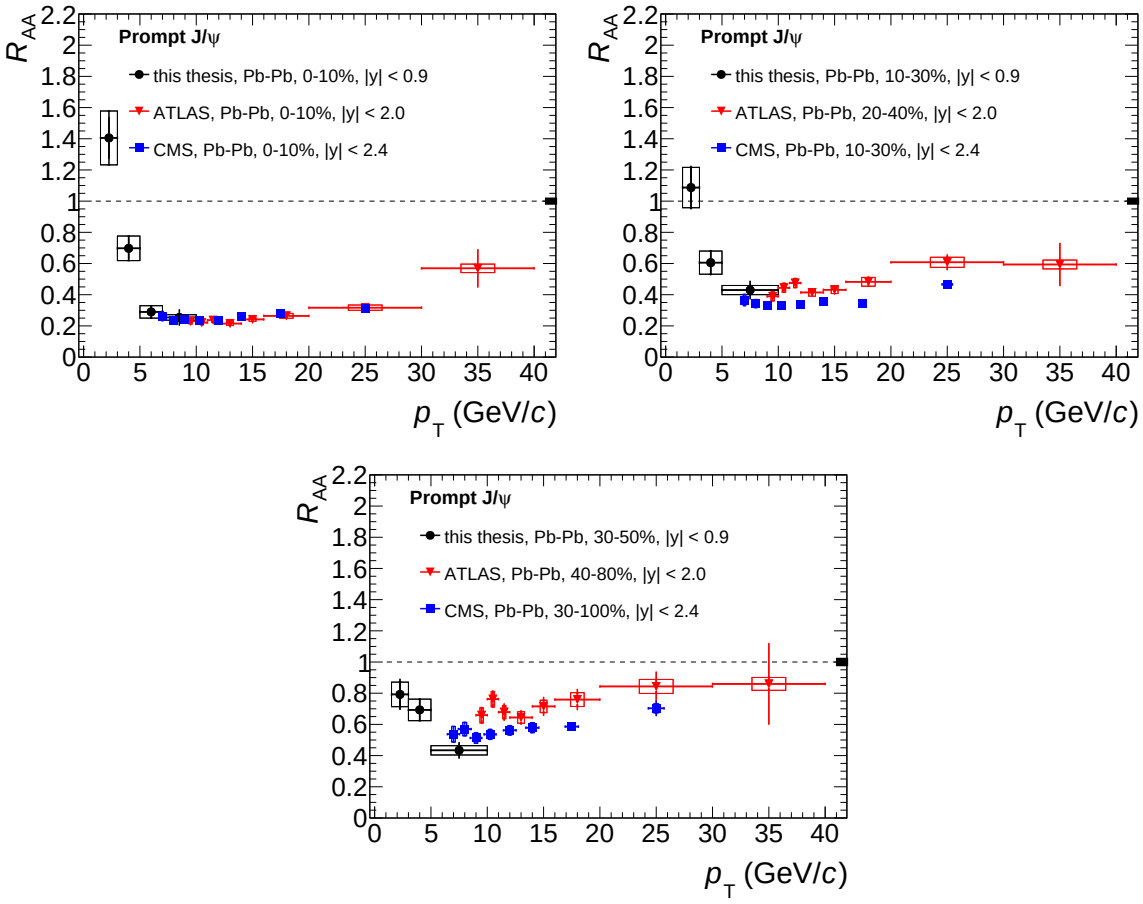

Figure 6.3 Nuclear modification factor of prompt J/ψ as a function of p_{T} in 0–10% (top, left), 10–30% (top, right), and 30–50% (bottom) at $\sqrt{s_{\mathrm{NN}}}$= 5.02 TeV, in comparison with similar measurements by ATLAS [155] and CMS [154], statistical and systematic uncertainties are represented by vertical bars and boxes, respectively. The global uncertainties are shown on the right side on the line corresponding to $R_{\mathrm{AA}} = 1$.

in this work are consistent with the previous measurements from LHC Run 1, taking into account the total uncertainties in each case for both prompt and non-prompt J/ψ.

It is important to note that the measurements based on the statistics from LHC Run 2 are more differential in both p_{T} and centrality compared to the measurements performed during LHC Run 1 by the ALICE experiment. This indicates that the present study provides a more precise and detailed picture of the production of prompt and non-prompt J/ψ in heavy-ion collisions at the LHC. The measurements are extended down to low p_{T} in central collision and semicentral collisions. These measurements are particularly important to understand the J/ψ production by regeneration mechanism which is dominant in the low p_{T} region.

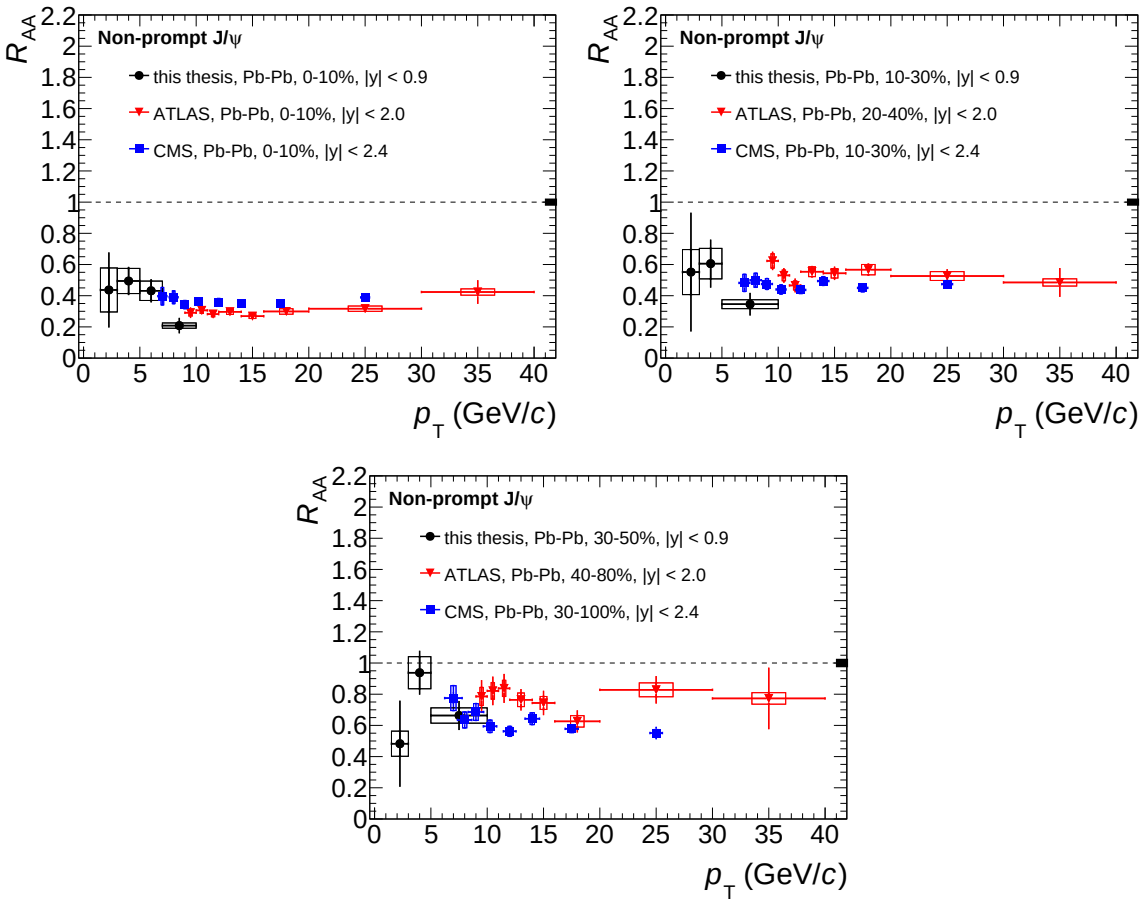

Figure 6.4 Nuclear modification factor of non-prompt J/ψ as a function of p_{T} in 0–10% (top, left), 10–30% (top, right), and 30–50% (bottom) at $\sqrt{s_{\mathrm{NN}}}$= 5.02 TeV, in comparison with similar measurements by ATLAS [155] and CMS [154], statistical and systematic uncertainties are represented by vertical bars and boxes, respectively. The global uncertainties are shown on the right side on the line corresponding to $R_{\mathrm{AA}} = 1$.

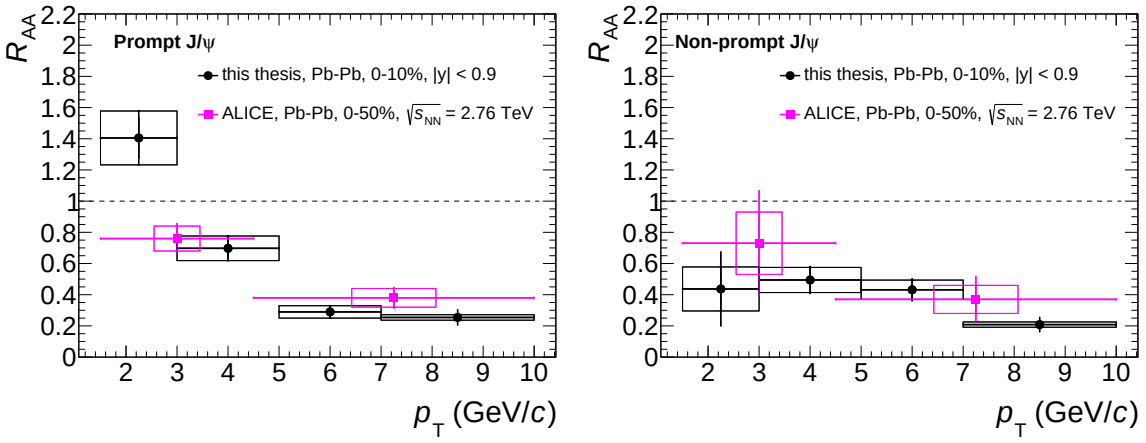

Figure 6.5 A comparison of p_{T} differential prompt J/ψ (left) and non-prompt J/ψ (right) R_{AA} in 0–10% centrality interval with similar measurements by ALICE [153] in 0–50% in Pb–Pb collisions at $\sqrt{s_{\mathrm{NN}}}$= 2.76 TeV, statistical and systematic uncertainties are represented by vertical bars and boxes, respectively.

6.2 Comparison with theoretical models

A comparison of prompt J/ψ R_{AA} to SHM for charm quarks (SHMc) [143] and Transport model [149, 201] is shown in Fig. 6.6 for 0–10% (left) and 30–50% (right) centrality intervals. Both models include dissociation and regeneration processes for charmonium states in the medium using different processes.

In the statistical hadronization model, it is assumed that all charm quark production takes place during the initial hard partonic interactions, and then they undergo thermalization in the medium. The relative yields of charm hadrons is determined exclusively at the chemical freeze-out stage, and hadrons are formed according to their thermal weights. The model inherits inclusive charm production cross section from open-charm measurements in Pb–Pb collisions [57] also, the model incorporated the CNM effects based on prompt D-meson measurement in p–Pb collisions at forward rapidity [202]. A more elaborated description of SHM for charm quarks can be found in Sec. 2.5.1.

The SHMc model is capable of describing the prompt J/ψ production with a reasonable degree of accuracy within the uncertainties in two centrality intervals, namely 0–10% and 30–50%. Specifically, for p_{T} values smaller than 5 GeV/c , the model is able to reproduce the experimental data within the limits of the uncertainties. However, it is worth noting that the model underestimates the prompt J/ψ production at higher p_{T} values, indicating a possible discrepancy between the model and the data.

The transport model is used to simulate the production and evolution of charmonium through a Boltzmann rate equation that includes dissociation and regeneration effects. In contrast to SHMc, the formation of charmonium states takes place during the evolution of the medium and chemical freeze-out, given that the medium temperature is lower than the

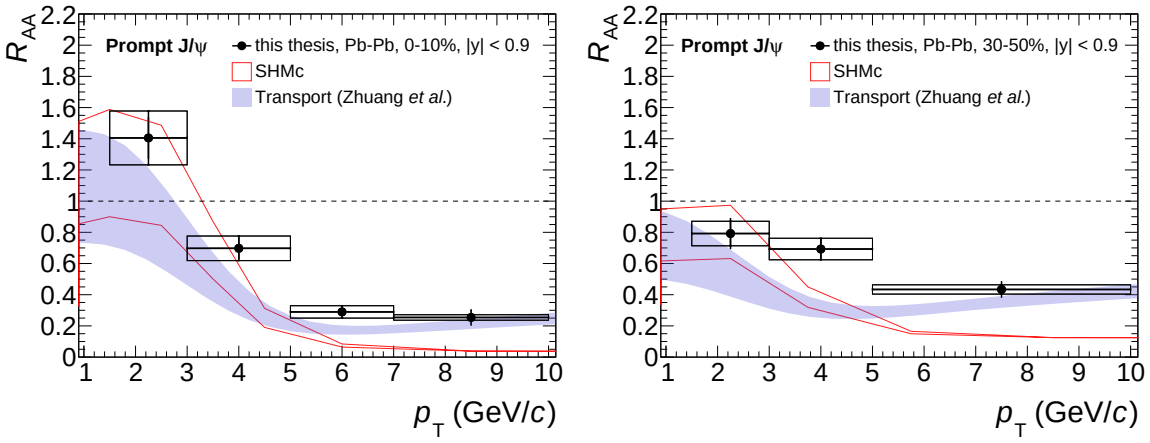

Figure 6.6 Prompt J/ψ nuclear modification factors as a function of p_{T} for 0–10% (left) and 30–50% (right) centrality intervals in comparison to theoretical predictions [143, 149], statistical and systematic uncertainties are represented by vertical bars and boxes, respectively.

dissociation temperature of the corresponding charmonium state. One of the requirements for the model is the total charm production cross section in Pb–Pb collisions evaluated by binary scaling of the total charm cross section measured in pp collisions [203]. The model utilizes the EPS09 gluon distributions [127] to account for the CNM effects. This model takes into consideration the temperature-dependent color screening effect and the scatterings that occur with thermal partons, particularly gluon dissociation, to account for the dissociation of charmonium states. In contrast, J/ψ regeneration process is reversed to the gluon dissociation process where a c and $\bar{\mathrm{c}}$ pair interacts with a parton to form a charmonium state. The model employs the equations for (2+1)D ideal hydrodynamics to depict the evolution of the fireball in space-time. These equations mathematically describe fluid dynamics in two spatial dimensions and one time dimension. Moreover, the model considers the production of non-prompt J/ψ through the Langevin equation, where their ancestor beauty quarks are propagated through the QGP and lose energy via radiation. The predictions of the models come with uncertainties that arise from two sources: the charm production cross-section and the assumptions made about CNM.

The Transport model predictions are compared p_{T}-differential nuclear modification factor of prompt J/ψ in Fig. 6.6. The model describes the production within uncertainties in the whole p_{T} range for 0–10% centrality interval. However, for the 30–50% centrality interval and particularly at intermediate p_{T}, the model underpredicts the production and shows a 3σ difference with the measurements. These findings suggest that the transport model may be a better description of the data for more central collisions than for peripheral ones.

In Fig. 6.7, the nuclear modification factors of non-prompt J/ψ are compared with theoretical predictions in 0–10% (left) and 30–50% (right) centrality intervals. The model predictions are significantly higher than the measurements, with an average 1.7σ, at p_{T} below 5 GeV/c in 0–10% centrality intervals and also at p_{T} larger than 7 GeV/c the predictions are larger by

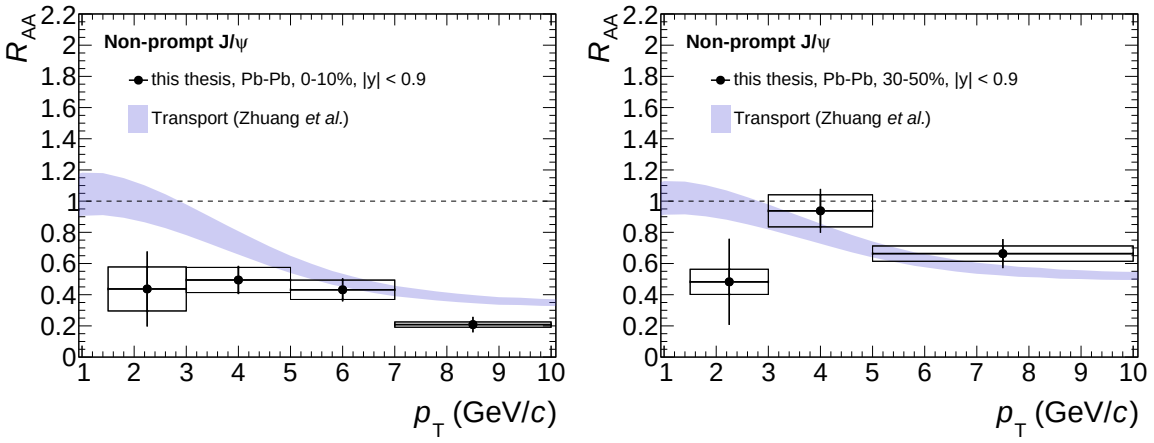

Figure 6.7 Non-prompt J/ψ nuclear modification factors as a function of p_{T} for 0–10% (left) and 30–50% (right) centrality intervals in comparison to theoretical predictions [149], statistical and systematic uncertainties are represented by vertical bars and boxes, respectively.

3σ with respect to measurements. A similar overestimation of non-prompt J/ψ R_{AA} has been observed in case of transport model with respect to measurements at p_{T} smaller than 3 GeV/c in 30–50% centrality interval. At low p_{T}, the predictions are larger with respect to measurements by a significance of 1.6σ while the model describes the measurements within uncertainties at high p_{T}. The model predictions are also compared with the prompt and non-prompt J/ψ production yields. These comparisons can be found in Appendix B.

The Fig. 6.8 presents a comparison between model predictions and the p_{T}-integrated R_{AA} of prompt (left) and non-prompt (right) J/ψ as a function of the average number of participating nucleons, $\langle N_{\mathrm{part}} \rangle$. In case of prompt J/$\psi$, both models show an increasing trend of R_{AA} with $\langle N_{\mathrm{part}} \rangle$. These predictions are in good agreement with the experimental measurements. On the other hand, for non-prompt J/ψ, the transport model predictions are almost constant with $\langle N_{\mathrm{part}} \rangle$, and they are consistent with the measurements. This indicates that the suppression of non-prompt J/ψ production in heavy-ion collisions is independent of the collision centrality.

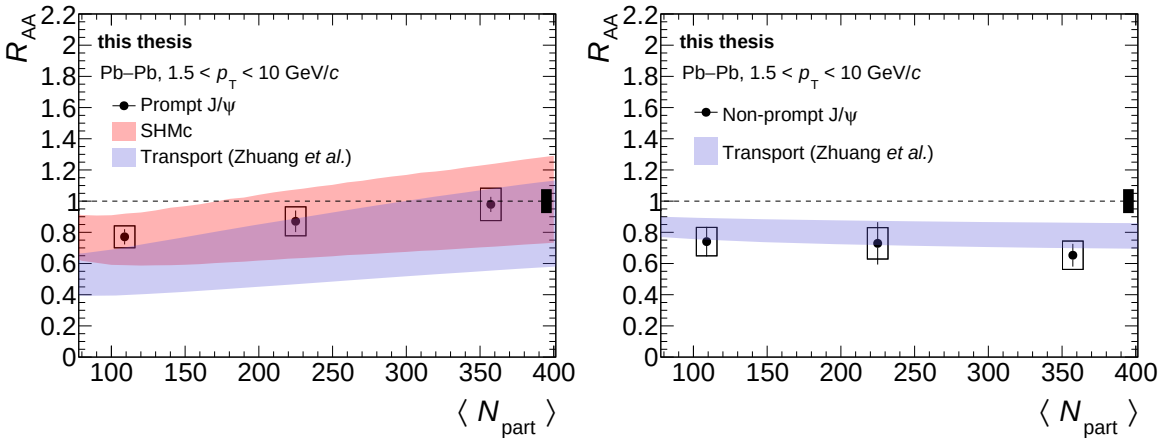

Figure 6.8 Prompt (left) J/ψ and non-prompt (right) nuclear modification factor as a function of $\langle N_{\mathrm{part}} \rangle$ in comparison to theoretical predictions [143, 149], statistical and systematic uncertainties are represented by vertical bars and boxes, respectively. The global uncertainties are shown on the right side on the line corresponding to $R_{\mathrm{AA}} = 1$.

Chapter 7

Summary and Conclusions

"Wonder is the seed of knowledge."

Francis Bacon

This study presents the prompt and non-prompt J/ψ measurements in Pb–Pb collisions at $\sqrt{s_{\rm NN}}$= 5.02 TeV at very low $p_{\rm T}$ down to 1.5 GeV/c at midrapidity ($|y| < 0.9$). The analysis is conducted to investigate the prompt and non-prompt J/ψ production as a function of $p_{\rm T}$ and in 0–10%, 10–30%, and 30–50% centrality intervals.

The measurements are performed in more differential centrality intervals compared to the previous measurements with the data collected from Pb–Pb collisions at $\sqrt{s_{\rm NN}}$ = 2.76 TeV during LHC Run 1 [153]. The measurements presented in this thesis enable a more detailed investigation of the centrality dependence of prompt and non-prompt J/ψ $R_{\rm AA}$. This study demonstrates an increasing trend in the prompt J/ψ $R_{\rm AA}$ as we approach the most central collisions. Conversely, the non-prompt J/ψ $R_{\rm AA}$ exhibits no significant variation with respect to collision centrality. The $R_{\rm AA}$ measurements provide clear evidence of a significant difference between prompt and non-prompt J/ψ production in the most central collisions.

The prompt J/ψ $R_{\rm AA}$ exhibits larger values in the 0–10% centrality interval compared to the 30–50% centrality interval for $p_{\rm T}$ below 3 GeV/c. The observation implies that in most central collisions, there is a more pronounced involvement of regeneration mechanism in prompt J/ψ production at low $p_{\rm T}$ in contrast to semi-central collisions. In the corresponding $p_{\rm T}$ range, there is a subtle indication of an ordering pattern in the prompt J/ψ $R_{\rm AA}$ across different centrality intervals. Conversely, no similar observations are made in the case of non-prompt J/ψ production at low $p_{\rm T}$. Interestingly, for $p_{\rm T}$ greater than 5 GeV/c, it is observed that non-prompt J/ψ production experiences a larger suppression in the 0-10% centrality interval compared to the 30-50% centrality interval. Moreover, the presented measurements are consistent with similar measurements at the high $p_{\rm T}$ [154, 155]. The comparisons, as a function of $p_{\rm T}$ and centrality, provide substantial evidence in favor of mass-dependent parton energy loss at high $p_{\rm T}$.

The model predictions are compared with the obtained production yields and $R_{\rm AA}$ as a function of $p_{\rm T}$ and collisions centrality. The SHM describes the prompt J/ψ $R_{\rm AA}$ as a function of centrality. The SHM describes the prompt J/ψ production yields and $R_{\rm AA}$ up to $p_{\rm T}$ around 3-4 GeV/c, but it tends to underestimate the production at higher $p_{\rm T}$ values in 0–10% and 30–50% centrality intervals. Additionally, the Transport Model predictions are consistent for both the prompt and non-prompt J/ψ $R_{\rm AA}$ within the considered centrality range. The transport model provides a better description for prompt J/ψ production at higher $p_{\rm T}$ compared to SHM. The non-prompt J/ψ production is overestimated by the transport model, especially at low $p_{\rm T}$ in both 0–10% and 30–50% centrality classes.

This study advances our understanding of J/ψ production in Pb–Pb collisions, particularly at low $p_{\rm T}$. By successfully distinguishing between prompt and non-prompt J/ψ components at low $p_{\rm T}$, this study allows us to investigate prompt J/ψ production specifically through the regeneration mechanism. The non-prompt J/ψ production reflects the interactions of b-quark within the nuclear medium. At high $p_{\rm T}$, larger suppression in prompt and non-prompt J/ψ $R_{\rm AA}$ indicates energy loss effects of charm and beauty quarks within the medium, respectively. These effects are most prominent in the most central collisions. It is challenging to arrive at conclusive findings regarding b-quark energy loss at low $p_{\rm T}$ across different centrality intervals due to large uncertainties associated with the non-prompt J/ψ measurements.

Chapter 8

Outlook

"An expert is a man who has made all the mistakes which can be made, in a narrow field."

Niels Bohr

For several decades, charmonium production in ultrarelativistic nuclear collisions has been a highly debated and extensively explored topic. Despite considerable efforts and progress in the field, our understanding of charmonium production remains incomplete. The ALICE experiment has provided a unique opportunity to investigate the charmonium production mechanism in Pb–Pb collisions, reaching the lowest p_{T} ever achieved to date. Continued improvements in the precision of such measurements have the potential to enhance our knowledge and understanding of charmonium production. The forthcoming LHC Run programs will continue to provide valuable opportunities to study charmonium production. The Fig. 8.1 illustrates the Long-term LHC Run schedule up to Run 6.

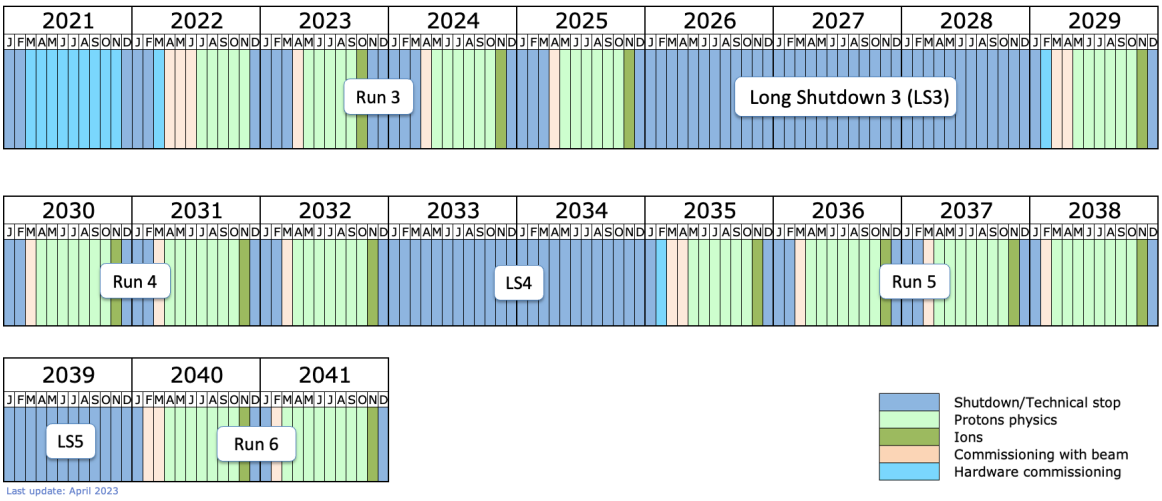

Figure 8.1 The Long-term LHC schedule extending to Run 6.

In the upcoming LHC Run 3 program (2022-25) [204], the integrated luminosity for Pb–Pb collisions is 10 nb^{-1}, representing an increase by a factor of 10-100 compared to Run 2. The ALICE detector has gone through a major upgrade where its central barrel detectors have been upgraded to achieve a significant improvement in the precision of collision vertex and track reconstruction [205]. Notably, there has been a substantial improvement in the resolution of the track impact parameter by a factor of 3 in the transverse direction and a factor of 6 in the beam direction. These improvements hold vital importance for the precise measurements of prompt and non-prompt J/ψ nuclear modification factors. In addition, v_2 and v_3 coefficients for both prompt and non-prompt J/ψ can be precisely determined by utilizing the ALICE central barrel during Run 3. These measurements have the potential to enhance our understanding of the thermalization of charm and beauty quarks within the nuclear medium.

Until now, prompt and non-prompt J/ψ production has not been explored within the ALICE experiment at forward rapidity. In the upgraded ALICE, the newly installed Muon Forward Tracker (MFT) introduces the capability to distinguish prompt and non-prompt J/ψ precisely at forward rapidity ($-3.6 < \eta < -2.5$) at p_{T} down to ~ 0 [206].

During the Run 3 program, the measurements are not limited only to J/ψ, but other charmonium states will also be explored to achieve remarkable precision. At forward rapidity, the MFT will be vital in improving the precision of $\psi(2\mathrm{s})$ measurements, allowing for p_{T}-differential studies for the first time. It will enable the extraction of the $\psi(2\mathrm{s})$ signal with unprecedented precision, reducing uncertainties to as low as approximately 10% even at $p_{\mathrm{T}} = 0$ [206]. Furthermore, there will be measurements conducted to determine the polarization providing an additional understanding of the different production mechanisms present in Pb–Pb collisions compared to pp collisions. According to the SHM predictions, prompt J/ψ production is not likely to exhibit any polarization. Although the measurement of other states, such as χ_c, is possible, it is challenging to obtain a significant precision at low p_{T} for such measurements.

A study for the measurement of B_c mesons is possible in $\mathrm{B}_c \to \mathrm{J}/\psi\, \pi$ or $\mathrm{B}_c \to \mathrm{J}/\psi\, \mu\nu_\mu$ decay channel. This will allow us to understand the regeneration mechanism within the beauty sector.

Bibliography

[1] J.J Sakurai. "Theory of strong interactions". In: *Annals of Physics* 11.1 (1960), pp. 1–48. ISSN: 0003-4916. DOI: https://doi.org/10.1016/0003-4916(60)90126-3. URL: https://www.sciencedirect.com/science/article/pii/0003491660901263.

[2] Franz Gross et al. "50 Years of Quantum Chromodynamics". In: (Dec. 2022). arXiv: 2212.11107 [hep-ph].

[3] K.A. Olive. "Review of Particle Physics". In: *Chinese Physics C* 38.9 (Aug. 2014), p. 090001. DOI: 10.1088/1674-1137/38/9/090001. URL: https://dx.doi.org/10.1088/1674-1137/38/9/090001.

[4] D. J. Gross. "The discovery of asymptotic freedom and the emergence of QCD". In: *Proc. Nat. Acad. Sci.* 102 (2005), pp. 9099–9108. DOI: 10.1073/pnas.0503831102.

[5] H. David Politzer. "Reliable Perturbative Results for Strong Interactions?" In: *Phys. Rev. Lett.* 30 (26 June 1973), pp. 1346–1349. DOI: 10.1103/PhysRevLett.30.1346. URL: https://link.aps.org/doi/10.1103/PhysRevLett.30.1346.

[6] B. L. Ioffe. *Quantum chromodynamics: Perturbative and nonperturbative aspects*. Cambridge University Press, 2010.

[7] J. Greensite. *An Introduction to the Confinement Problem*. Vol. 821. Springer, 2011.

[8] N. Cabibbo and G. Parisi. "Exponential hadronic spectrum and quark liberation". In: *Physics Letters B* 59.1 (1975), pp. 67–69. ISSN: 0370-2693. DOI: https://doi.org/10.1016/0370-2693(75)90158-6. URL: https://www.sciencedirect.com/science/article/pii/0370269375901586.

[9] J. C. Collins and M. J. Perry. "Superdense Matter: Neutrons or Asymptotically Free Quarks?" In: *Phys. Rev. Lett.* 34 (21 May 1975), pp. 1353–1356. DOI: 10.1103/PhysRevLett.34.1353. URL: https://link.aps.org/doi/10.1103/PhysRevLett.34.1353.

[10] Edward V. Shuryak. "Theory of Hadronic Plasma". In: *Sov. Phys. JETP* 47 (1978), pp. 212–219.

[11] A. Bazavov et al. "Up-, down-, strange-, charm-, and bottom-quark masses from four-flavor lattice QCD". In: *Phys. Rev. D* 98.5 (2018), p. 054517. DOI: 10.1103/PhysRevD.98.054517. arXiv: 1802.04248 [hep-lat].

[12] Szabocls Borsanyi et al. "Full result for the QCD equation of state with 2+1 flavors". In: *Phys. Lett. B* 730 (2014), pp. 99–104. DOI: 10.1016/j.physletb.2014.01.007. arXiv: 1309.5258 [hep-lat].

[13] A. Bazavov et al. "Equation of state in (2+1)-flavor QCD". In: *Phys. Rev. D* 90 (2014), p. 094503. DOI: 10.1103/PhysRevD.90.094503. arXiv: 1407.6387 [hep-lat].

[14] A. Adare et al. "Energy Loss and Flow of Heavy Quarks in Au+Au Collisions at s(NN)**(1/2) = 200-GeV". In: *Phys. Rev. Lett.* 98 (2007), p. 172301. DOI: 10.1103/PhysRevLett.98.172301. arXiv: nucl-ex/0611018.

[15] Peter F. Kolb and Ulrich W. Heinz. "Hydrodynamic description of ultrarelativistic heavy ion collisions". In: (May 2003). Ed. by Rudolph C. Hwa and Xin-Nian Wang, pp. 634–714. arXiv: nucl-th/0305084.

[16] Eemeli Annala et al. "Evidence for quark-matter cores in massive neutron stars". In: *Nature Phys.* 16.9 (2020), pp. 907–910. DOI: 10.1038/s41567-020-0914-9. arXiv: 1903.09121 [astro-ph.HE].

[17] Jeffrey Goldstone, Abdus Salam, and Steven Weinberg. "Broken Symmetries". In: *Phys. Rev.* 127 (1962), pp. 965–970. DOI: 10.1103/PhysRev.127.965.

[18] Volker Koch. "Aspects of chiral symmetry". In: *Int. J. Mod. Phys. E* 6 (1997), pp. 203–250. DOI: 10.1142/S0218301397000147. arXiv: nucl-th/9706075.

[19] Rajan Gupta. "Introduction to lattice QCD: Course". In: *Les Houches Summer School in Theoretical Physics, Session 68: Probing the Standard Model of Particle Interactions*. July 1997, pp. 83–219. arXiv: hep-lat/9807028.

[20] Claudia Ratti. "Lattice QCD and heavy ion collisions: a review of recent progress". In: *Rept. Prog. Phys.* 81.8 (2018), p. 084301. DOI: 10.1088/1361-6633/aabb97. arXiv: 1804.07810 [hep-lat].

[21] C. P. Burgess. "Introduction to Effective Field Theory". In: *Ann. Rev. Nucl. Part. Sci.* 57 (2007), pp. 329–362. DOI: 10.1146/annurev.nucl.56.080805.140508. arXiv: hep-th/0701053.

[22] Nora Brambilla et al. "Potential NRQCD: An Effective theory for heavy quarkonium". In: *Nucl. Phys. B* 566 (2000), p. 275. DOI: 10.1016/S0550-3213(99)00693-8. arXiv: hep-ph/9907240.

[23] N. Cabibbo and G. Parisi. "Exponential Hadronic Spectrum and Quark Liberation". In: *Phys. Lett. B* 59 (1975), pp. 67–69. DOI: 10.1016/0370-2693(75)90158-6.

[24] Rajeev S. Bhalerao. "Relativistic heavy-ion collisions". In: *1st Asia-Europe-Pacific School of High-Energy Physics*. 2014, pp. 219–239. DOI: 10.5170/CERN-2014-001.219. arXiv: 1404.3294 [nucl-th].

[25] A. Pandav, D. Mallick, and B. Mohanty. "Search for the QCD critical point in high energy nuclear collisions". In: *Prog. Part. Nucl. Phys.* 125 (2022), p. 103960. DOI: 10.1016/j.ppnp.2022.103960. arXiv: 2203.07817 [nucl-ex].

[26] Ulrich W. Heinz. "Concepts of heavy ion physics". In: *2nd CERN-CLAF School of High Energy Physics*. July 2004, pp. 165–238. arXiv: hep-ph/0407360.

[27] Wit Busza, Krishna Rajagopal, and Wilke van der Schee. "Heavy Ion Collisions: The Big Picture and the Big Questions". In: *Annual Review of Nuclear and Particle Science* 68.1 (2018), pp. 339–376. DOI: 10.1146/annurev-nucl-101917-020852. eprint: https://doi.org/10.1146/annurev-nucl-101917-020852. URL: https://doi.org/10.1146/annurev-nucl-101917-020852.

[28] Francois Gelis et al. "The Color Glass Condensate". In: *Annual Review of Nuclear and Particle Science* 60.1 (2010), pp. 463–489. DOI: 10.1146/annurev.nucl.010909.083629. eprint: https://doi.org/10.1146/annurev.nucl.010909.083629. URL: https://doi.org/10.1146/annurev.nucl.010909.083629.

[29] Francesco Becattini. "The Quark Gluon Plasma and relativistic heavy ion collisions in the LHC era". In: *Journal of Physics: Conference Series* 527.1 (July 2014), p. 012012. DOI: 10.1088/1742-6596/527/1/012012. URL: https://dx.doi.org/10.1088/1742-6596/527/1/012012.

[30] Michael L. Miller et al. "Glauber modeling in high energy nuclear collisions". In: *Ann. Rev. Nucl. Part. Sci.* 57 (2007), pp. 205–243. DOI: 10.1146/annurev.nucl.57.090506.123020. arXiv: nucl-ex/0701025.

[31] Jaroslav Adam et al. "Measurement of transverse energy at midrapidity in Pb-Pb collisions at $\sqrt{s_{\mathrm{NN}}} = 2.76$ TeV". In: *Phys. Rev. C* 94.3 (2016), p. 034903. DOI: 10.1103/PhysRevC.94.034903. arXiv: 1603.04775 [nucl-ex].

[32] J. Adams et al. "Measurements of transverse energy distributions in Au + Au collisions at s(NN)**(1/2) = 200-GeV". In: *Phys. Rev. C* 70 (2004), p. 054907. DOI: 10.1103/PhysRevC.70.054907. arXiv: nucl-ex/0407003.

[33] Jaroslav Adam et al. "Centrality Dependence of the Charged-Particle Multiplicity Density at Midrapidity in Pb-Pb Collisions at $\sqrt{s_{\mathrm{NN}}} = 5.02$ TeV". In: *Phys. Rev. Lett.* 116.22 (2016), p. 222302. DOI: 10.1103/PhysRevLett.116.222302. arXiv: 1512.06104 [nucl-ex].

[34] I. Arsene et al. "Quark gluon plasma and color glass condensate at RHIC? The Perspective from the BRAHMS experiment". In: *Nucl. Phys. A* 757 (2005), pp. 1–27. DOI: 10.1016/j.nuclphysa.2005.02.130. arXiv: nucl-ex/0410020.

[35] B. B. Back et al. "The PHOBOS perspective on discoveries at RHIC". In: *Nucl. Phys. A* 757 (2005), pp. 28–101. DOI: 10.1016/j.nuclphysa.2005.03.084. arXiv: nucl-ex/0410022.

[36] John Adams et al. "Experimental and theoretical challenges in the search for the quark gluon plasma: The STAR Collaboration's critical assessment of the evidence from RHIC collisions". In: *Nucl. Phys. A* 757 (2005), pp. 102–183. DOI: 10.1016/j.nuclphysa.2005.03.085. arXiv: nucl-ex/0501009.

[37] K. Adcox et al. "Formation of dense partonic matter in relativistic nucleus-nucleus collisions at RHIC: Experimental evaluation by the PHENIX collaboration". In: *Nucl. Phys. A* 757 (2005), pp. 184–283. DOI: 10.1016/j.nuclphysa.2005.03.086. arXiv: nucl-ex/0410003.

[38] Ulrich Heinz and Raimond Snellings. "Collective Flow and Viscosity in Relativistic Heavy-Ion Collisions". In: *Annual Review of Nuclear and Particle Science* 63.1 (2013), pp. 123–151. DOI: 10.1146/annurev-nucl-102212-170540. URL: https://doi.org/10.1146/annurev-nucl-102212-170540.

[39] Charles Gale et al. "Event-by-Event Anisotropic Flow in Heavy-ion Collisions from Combined Yang-Mills and Viscous Fluid Dynamics". In: *Phys. Rev. Lett.* 110 (1 Jan. 2013), p. 012302. DOI: 10.1103/PhysRevLett.110.012302. URL: https://link.aps.org/doi/10.1103/PhysRevLett.110.012302.

[40] P. Kovtun, Dan T. Son, and Andrei O. Starinets. "Viscosity in strongly interacting quantum field theories from black hole physics". In: *Phys. Rev. Lett.* 94 (2005), p. 111601. DOI: 10.1103/PhysRevLett.94.111601. arXiv: hep-th/0405231.

[41] S. Acharya et al. "Anisotropic flow of identified particles in Pb-Pb collisions at $\sqrt{s_{\mathrm{NN}}} = 5.02$ TeV". In: *JHEP* 09 (2018), p. 006. DOI: 10.1007/JHEP09(2018)006. arXiv: 1805.04390 [nucl-ex].

[42] Derek A. Teaney. "Viscous Hydrodynamics and the Quark Gluon Plasma". In: *Quark-gluon plasma 4*. Ed. by Rudolph C. Hwa and Xin-Nian Wang. 2010, pp. 207–266. DOI: 10.1142/9789814293297_0004. arXiv: 0905.2433 [nucl-th].

[43] V. Greco, C. M. Ko, and P. Lévai. "Partonic coalescence in relativistic heavy ion collisions". In: *Phys. Rev. C* 68 (3 Sept. 2003), p. 034904. DOI: 10.1103/PhysRevC.68.034904. URL: https://link.aps.org/doi/10.1103/PhysRevC.68.034904.

[44] R. J. Fries et al. "Hadron production in heavy ion collisions: Fragmentation and recombination from a dense parton phase". In: *Phys. Rev. C* 68 (4 Oct. 2003), p. 044902. DOI: 10.1103/PhysRevC.68.044902. URL: https://link.aps.org/doi/10.1103/PhysRevC.68.044902.

[45] Rudolph C. Hwa and C. B. Yang. "Recombination of shower partons in fragmentation processes". In: *Phys. Rev. C* 70 (2 Aug. 2004), p. 024904. DOI: 10.1103/PhysRevC.70.024904. URL: https://link.aps.org/doi/10.1103/PhysRevC.70.024904.

[46] Berndt Müller. "Hadronic signals of deconfinement at RHIC". In: *Nuclear Physics A* 750.1 (2005). Quark-Gluon Plasma. New Discoveries at RHIC: Case for the Strongly Interacting Quark-Gluon Plasma. Contributions from the RBRC Workshop held May 14-15, 2004, pp. 84–97. ISSN: 0375-9474. DOI: https://doi.org/10.1016/j.nuclphysa.2004.12.067. URL: https://www.sciencedirect.com/science/article/pii/S0375947404012850.

[47] Miklos Gyulassy, Ivan Vitev, and Xin-Nian Wang. "High p_T Azimuthal Asymmetry in Noncentral $A+A$ at RHIC". In: *Phys. Rev. Lett.* 86 (12 Mar. 2001), pp. 2537–2540. DOI: 10.1103/PhysRevLett.86.2537. URL: https://link.aps.org/doi/10.1103/PhysRevLett.86.2537.

[48] S. Afanasiev et al. "High-$p_T\pi^0$ production with respect to the reaction plane in Au + Au collisions at $\sqrt{s_{NN}} = 200$ GeV". In: *Phys. Rev. C* 80 (5 Nov. 2009), p. 054907. DOI: 10.1103/PhysRevC.80.054907. URL: https://link.aps.org/doi/10.1103/PhysRevC.80.054907.

[49] Steffen A. Bass et al. "Systematic comparison of jet energy-loss schemes in a realistic hydrodynamic medium". In: *Phys. Rev. C* 79 (2 Feb. 2009), p. 024901. DOI: 10.1103/PhysRevC.79.024901. URL: https://link.aps.org/doi/10.1103/PhysRevC.79.024901.

[50] Matteo Cacciari, Paolo Nason, and Ramona Vogt. "QCD Predictions for Charm and Bottom Quark Production at RHIC". In: *Phys. Rev. Lett.* 95 (12 Sept. 2005), p. 122001. DOI: 10.1103/PhysRevLett.95.122001. URL: https://link.aps.org/doi/10.1103/PhysRevLett.95.122001.

[51] Benjamin Svetitsky. "Diffusion of charmed quarks in the quark-gluon plasma". In: *Phys. Rev. D* 37 (9 May 1988), pp. 2484–2491. DOI: 10.1103/PhysRevD.37.2484. URL: https://link.aps.org/doi/10.1103/PhysRevD.37.2484.

[52] Ralf Rapp and Hendrik van Hees. "Heavy Quarks in the Quark-Gluon Plasma". In: 2010, pp. 111–206. DOI: 10.1142/9789814293297_0003. arXiv: 0903.1096 [hep-ph].

[53] Shreyasi Acharya et al. "Transverse-momentum and event-shape dependence of D-meson flow harmonics in Pb–Pb collisions at $\sqrt{s_{NN}} = 5.02$ TeV". In: *Phys. Lett. B* 813 (2021), p. 136054. DOI: 10.1016/j.physletb.2020.136054. arXiv: 2005.11131 [nucl-ex].

[54] Denes Molnar. "Charm elliptic flow from quark coalescence dynamics". In: *J. Phys. G* 31 (2005). Ed. by F. Antinori et al., S421–S428. DOI: 10.1088/0954-3899/31/4/052. arXiv: nucl-th/0410041.

[55] V. Greco, C. M. Ko, and R. Rapp. "Quark coalescence for charmed mesons in ultrarelativistic heavy ion collisions". In: *Phys. Lett. B* 595 (2004), pp. 202–208. DOI: 10.1016/j.physletb.2004.06.064. arXiv: nucl-th/0312100.

[56] Xin Dong, Yen-Jie Lee, and Ralf Rapp. "Open Heavy-Flavor Production in Heavy-Ion Collisions". In: *Annual Review of Nuclear and Particle Science* 69.1 (2019), pp. 417–445. DOI: 10.1146/annurev-nucl-101918-023806. eprint: https://doi.org/10.1146/annurev-nucl-101918-023806. URL: https://doi.org/10.1146/annurev-nucl-101918-023806.

[57] Shreyasi Acharya et al. "Prompt D^0, D^+, and D^{*+} production in Pb–Pb collisions at $\sqrt{s_{NN}} = 5.02$ TeV". In: *JHEP* 01 (2022), p. 174. DOI: 10.1007/JHEP01(2022)174. arXiv: 2110.09420 [nucl-ex].

[58] J. P. Blaizot and Larry D. McLerran. "Jets in expanding quark-gluon plasmas". In: *Phys. Rev. D* 34 (9 Nov. 1986), pp. 2739–2745. DOI: 10.1103/PhysRevD.34.2739. URL: https://link.aps.org/doi/10.1103/PhysRevD.34.2739.

[59] A. Majumder and M. van Leeuwen. "The theory and phenomenology of perturbative QCD based jet quenching". In: *Progress in Particle and Nuclear Physics* 66.1 (2011), pp. 41–92. ISSN: 0146-6410. DOI: https://doi.org/10.1016/j.ppnp.2010.09.001. URL: https://www.sciencedirect.com/science/article/pii/S0146641010000542.

[60] Megan Connors et al. "Jet measurements in heavy ion physics". In: *Rev. Mod. Phys.* 90 (2018), p. 025005. DOI: 10.1103/RevModPhys.90.025005. arXiv: 1705.01974 [nucl-ex].

[61] Shanshan Cao and Xin-Nian Wang. "Jet quenching and medium response in high-energy heavy-ion collisions: a review". In: *Rept. Prog. Phys.* 84.2 (2021), p. 024301. DOI: 10.1088/1361-6633/abc22b. arXiv: 2002.04028 [hep-ph].

[62] "The ALICE experiment – A journey through QCD". In: (Nov. 2022). arXiv: 2211.04384 [nucl-ex].

[63] Charles Gale. "Photon Production in Hot and Dense Strongly Interacting Matter". In: *Landolt-Bornstein* 23 (2010). Ed. by R. Stock, p. 445. DOI: 10.1007/978-3-642-01539-7_15. arXiv: 0904.2184 [hep-ph].

[64] Joseph Kapusta, Peter Lichard, and David Seibert. "High-energy photons from quark-gluon plasma versus hot hadronic gas". In: *Phys. Rev. D* 44 (9 Nov. 1991), pp. 2774–2788. DOI: 10.1103/PhysRevD.44.2774. URL: https://link.aps.org/doi/10.1103/PhysRevD.44.2774.

[65] Simon Turbide, Ralf Rapp, and Charles Gale. "Hadronic production of thermal photons". In: *Phys. Rev. C* 69 (2004), p. 014903. DOI: 10.1103/PhysRevC.69.014903. arXiv: hep-ph/0308085.

[66] Jaroslav Adam et al. "Direct photon production in Pb-Pb collisions at $\sqrt{s_{NN}} = 2.76$ TeV". In: *Phys. Lett. B* 754 (2016), pp. 235–248. DOI: 10.1016/j.physletb.2016.01.020. arXiv: 1509.07324 [nucl-ex].

[67] J. H. Christenson et al. "Observation of Massive Muon Pairs in Hadron Collisions". In: *Phys. Rev. Lett.* 25 (21 Nov. 1970), pp. 1523–1526. DOI: 10.1103/PhysRevLett.25.1523. URL: https://link.aps.org/doi/10.1103/PhysRevLett.25.1523.

[68] J. J. Aubert et al. "Experimental Observation of a Heavy Particle J". In: *Phys. Rev. Lett.* 33 (23 Dec. 1974), pp. 1404–1406. DOI: 10.1103/PhysRevLett.33.1404. URL: https://link.aps.org/doi/10.1103/PhysRevLett.33.1404.

[69] J. -E. Augustin et al. "Discovery of a Narrow Resonance in e^+e^- Annihilation". In: *Phys. Rev. Lett.* 33 (23 Dec. 1974), pp. 1406–1408. DOI: 10.1103/PhysRevLett.33.1406. URL: https://link.aps.org/doi/10.1103/PhysRevLett.33.1406.

[70] J. D. Bjorken and S. L. Glashow. "Elementary Particles and SU(4)". In: *Phys. Lett.* 11 (1964), pp. 255–257. DOI: 10.1016/0031-9163(64)90433-0.

[71] S. L. Glashow, J. Iliopoulos, and L. Maiani. "Weak Interactions with Lepton-Hadron Symmetry". In: *Phys. Rev. D* 2 (7 Oct. 1970), pp. 1285–1292. DOI: 10.1103/PhysRevD.2.1285. URL: https://link.aps.org/doi/10.1103/PhysRevD.2.1285.

[72] E. Eichten et al. "Charmonium: The Model". In: *Phys. Rev. D* 17 (1978). [Erratum: Phys.Rev.D 21, 313 (1980)], p. 3090. DOI: 10.1103/PhysRevD.17.3090.

[73] J. P. Lansberg. "J/ψ, ψ ' and Υ production at hadron colliders: A Review". In: *Int. J. Mod. Phys. A* 21 (2006), pp. 3857–3916. DOI: 10.1142/S0217751X06033180. arXiv: hep-ph/0602091.

[74] Ramona Vogt. *Ultrarelativistic Heavy-Ion Collisions*. Elsevier Science, 2007.

[75] S. Okubo. "-meson and unitary symmetry model". In: *Physics Letters* 5.2 (1963), pp. 165–168. ISSN: 0031-9163. DOI: https://doi.org/10.1016/S0375-9601(63)92548-9. URL: https://www.sciencedirect.com/science/article/pii/S0375960163925489.

[76] G. Zweig. "An SU(3) model for strong interaction symmetry and its breaking. Version 2". In: *DEVELOPMENTS IN THE QUARK THEORY OF HADRONS. VOL. 1. 1964 - 1978*. Ed. by D. B. Lichtenberg and Simon Peter Rosen. Feb. 1964, pp. 22–101.

[77] Jugoro Iizuka. "A Systematics and Phenomenology of Meson Family*". In: *Progress of Theoretical Physics Supplement* 37-38 (Mar. 1966), pp. 21–34. ISSN: 0375-9687. DOI: 10.1143/PTPS.37.21. eprint: https://academic.oup.com/ptps/article-pdf/doi/10.1143/PTPS.37.21/5215468/37-38-21.pdf. URL: https://doi.org/10.1143/PTPS.37.21.

[78] S. Eidelman et al. "Review of Particle Physics". In: *Physics Letters B* 592.1 (2004). Review of Particle Physics, pp. 1–5. ISSN: 0370-2693. DOI: https://doi.org/10.1016/j.physletb.2004.06.001. URL: https://www.sciencedirect.com/science/article/pii/S0370269304007579.

[79] F. Abe et al. "Production of J/ψ mesons from χ_c meson decays in $p\bar{p}$ collisions at $\sqrt{s} = 1.8$ TeV". In: *Phys. Rev. Lett.* 79 (1997), pp. 578–583. DOI: 10.1103/PhysRevLett.79.578.

[80] P. Faccioli et al. "Study of ψ' and χ_c decays as feed-down sources of J/ψ hadroproduction". In: *JHEP* 10 (2008), p. 004. DOI: 10.1088/1126-6708/2008/10/004. arXiv: 0809.2153 [hep-ph].

[81] T. Aaltonen et al. "Production of psi(2S) Mesons in p anti-p Collisions at 1.96-TeV". In: *Phys. Rev. D* 80 (2009), p. 031103. DOI: 10.1103/PhysRevD.80.031103. arXiv: 0905.1982 [hep-ex].

[82] Matteo Cacciari, Mario Greco, and Paolo Nason. "The P(T) spectrum in heavy flavor hadroproduction". In: *JHEP* 05 (1998), p. 007. DOI: 10.1088/1126-6708/1998/05/007. arXiv: hep-ph/9803400.

[83] V. G. Kartvelishvili, A. K. Likhoded, and V. A. Petrov. "On the Fragmentation Functions of Heavy Quarks Into Hadrons". In: *Phys. Lett. B* 78 (1978), pp. 615–617. DOI: 10.1016/0370-2693(78)90653-6.

[84] Matteo Cacciari and Paolo Nason. "Is there a significant excess in bottom hadroproduction at the Tevatron?" In: *Phys. Rev. Lett.* 89 (2002), p. 122003. DOI: 10.1103/PhysRevLett.89.122003. arXiv: hep-ph/0204025.

[85] Matteo Cacciari and Paolo Nason. "Charm cross-sections for the Tevatron Run II". In: *JHEP* 09 (2003), p. 006. DOI: 10.1088/1126-6708/2003/09/006. arXiv: hep-ph/0306212.

[86] M. Cacciari et al. "QCD analysis of first b cross-section data at 1.96-TeV". In: *JHEP* 07 (2004), p. 033. DOI: 10.1088/1126-6708/2004/07/033. arXiv: hep-ph/0312132.

[87] N. Brambilla et al. "Heavy quarkonium physics". In: (Dec. 2004). DOI: 10.5170/CERN-2005-005. arXiv: hep-ph/0412158.

[88] Chao-Hsi Chang. "Hadronic Production of J/ψ Associated With a Gluon". In: *Nucl. Phys. B* 172 (1980), pp. 425–434. DOI: 10.1016/0550-3213(80)90175-3.

[89] F. Abe et al. "J/ψ and $\psi(2S)$ production in $p\bar{p}$ collisions at $\sqrt{s} = 1.8$ TeV". In: *Phys. Rev. Lett.* 79 (1997), pp. 572–577. DOI: 10.1103/PhysRevLett.79.572.

[90] Harald Fritzsch. "Producing Heavy Quark Flavors in Hadronic Collisions: A Test of Quantum Chromodynamics". In: *Phys. Lett. B* 67 (1977), pp. 217–221. DOI: 10.1016/0370-2693(77)90108-3.

[91] F. Halzen. "CVC for gluons and hadroproduction of quark flavours". In: *Physics Letters B* 69.1 (1977), pp. 105–108. ISSN: 0370-2693. DOI: https://doi.org/10.1016/0370-2693(77)90144-7. URL: https://www.sciencedirect.com/science/article/pii/0370269377901447.

[92] R. Vogt, C. Lourenço, and H.K. Wöhri. "J/ production and absorption in p + A and d+Au collisions". In: *Nuclear Physics A* 855.1 (2011). Proceedings of the 4th International Conference on Hard and Electromagnetic Probes of High-Energy Nuclear Collisions – HP2010, pp. 453–456. ISSN: 0375-9474. DOI: https://doi.org/10.1016/j.nuclphysa.2011.02.104. URL: https://www.sciencedirect.com/science/article/pii/S0375947411001916.

[93] Shreyasi Acharya et al. "Energy dependence of forward-rapidity J/ψ and ψ(2S) production in pp collisions at the LHC". In: *Eur. Phys. J. C* 77.6 (2017), p. 392. DOI: 10.1140/epjc/s10052-017-4940-4. arXiv: 1702.00557 [hep-ex].

[94] Yan-Qing Ma and Ramona Vogt. "Quarkonium Production in an Improved Color Evaporation Model". In: *Phys. Rev. D* 94.11 (2016), p. 114029. DOI: 10.1103/PhysRevD.94.114029. arXiv: 1609.06042 [hep-ph].

[95] Geoffrey T. Bodwin, Eric Braaten, and G. Peter Lepage. "Rigorous QCD analysis of inclusive annihilation and production of heavy quarkonium". In: *Phys. Rev. D* 51 (1995). [Erratum: Phys.Rev.D 55, 5853 (1997)], pp. 1125–1171. DOI: 10.1103/PhysRevD.55.5853. arXiv: hep-ph/9407339.

[96] Pietro Faccioli et al. "Towards the experimental clarification of quarkonium polarization". In: *Eur. Phys. J. C* 69 (2010), pp. 657–673. DOI: 10.1140/epjc/s10052-010-1420-5. arXiv: 1006.2738 [hep-ph].

[97] Betty Abelev et al. "Measurement of prompt J/ψ and beauty hadron production cross sections at mid-rapidity in pp collisions at $\sqrt{s} = 7$ TeV". In: *JHEP* 11 (2012), p. 065. DOI: 10.1007/JHEP11(2012)065. arXiv: 1205.5880 [hep-ex].

[98] Shreyasi Acharya et al. "Prompt and non-prompt J/ψ production cross sections at midrapidity in proton-proton collisions at $\sqrt{s}$ = 5.02 and 13 TeV". In: *JHEP* 03 (2022), p. 190. DOI: 10.1007/JHEP03(2022)190. arXiv: 2108.02523 [nucl-ex].

[99] Albert M Sirunyan et al. "Measurement of prompt and nonprompt J/ψ production in pp and pPb collisions at $\sqrt{s_{\mathrm{NN}}} = 5.02$ TeV". In: *Eur. Phys. J. C* 77.4 (2017), p. 269. DOI: 10.1140/epjc/s10052-017-4828-3. arXiv: 1702.01462 [nucl-ex].

[100] Vardan Khachatryan et al. "Prompt and Non-Prompt J/ψ Production in pp Collisions at $\sqrt{s} = 7$ TeV". In: *Eur. Phys. J. C* 71 (2011), p. 1575. DOI: 10.1140/epjc/s10052-011-1575-8. arXiv: 1011.4193 [hep-ex].

[101] Georges Aad et al. "Measurement of the differential cross-sections of inclusive, prompt and non-prompt J/ψ production in proton-proton collisions at $\sqrt{s} = 7$ TeV". In: *Nucl. Phys. B* 850 (2011), pp. 387–444. DOI: 10.1016/j.nuclphysb.2011.05.015. arXiv: 1104.3038 [hep-ex].

[102] Georges Aad et al. "Measurement of the differential cross-sections of prompt and non-prompt production of J/ψ and ψ(2S) in pp collisions at $\sqrt{s} = 7$ and 8 TeV with the ATLAS detector". In: *Eur. Phys. J. C* 76.5 (2016), p. 283. DOI: 10.1140/epjc/s10052-016-4050-8. arXiv: 1512.03657 [hep-ex].

[103] R. Aaij et al. "Measurement of J/ψ production cross-sections in pp collisions at $\sqrt{s} = 5$ TeV". In: *JHEP* 11 (2021), p. 181. DOI: 10.1007/JHEP11(2021)181. arXiv: 2109.00220 [hep-ex].

[104] R. Aaij et al. "Measurement of J/ψ production in pp collisions at $\sqrt{s} = 7$ TeV". In: *Eur. Phys. J. C* 71 (2011), p. 1645. DOI: 10.1140/epjc/s10052-011-1645-y. arXiv: 1103.0423 [hep-ex].

[105] R Aaij et al. "Measurement of J/ψ polarization in pp collisions at $\sqrt{s} = 7$ TeV". In: *Eur. Phys. J. C* 73.11 (2013), p. 2631. DOI: 10.1140/epjc/s10052-013-2631-3. arXiv: 1307.6379 [hep-ex].

[106] Serguei Chatrchyan et al. "Measurement of the Prompt J/ψ and ψ(2S) Polarizations in pp Collisions at $\sqrt{s}$ = 7 TeV". In: *Phys. Lett. B* 727 (2013), pp. 381–402. DOI: 10.1016/j.physletb.2013.10.055. arXiv: 1307.6070 [hep-ex].

[107] A. Abulencia et al. "Polarization of J/ψ and ψ_{2S} Mesons Produced in $p\bar{p}$ Collisions at $\sqrt{s}$ = 1.96-TeV". In: *Phys. Rev. Lett.* 99 (2007), p. 132001. DOI: 10.1103/PhysRevLett.99.132001. arXiv: 0704.0638 [hep-ex].

[108] A. Adare et al. "Transverse momentum dependence of J/psi polarization at midrapidity in p+p collisions at s**(1/2) = 200-GeV". In: *Phys. Rev. D* 82 (2010), p. 012001. DOI: 10.1103/PhysRevD.82.012001. arXiv: 0912.2082 [hep-ex].

[109] I. Abt et al. "Angular distributions of leptons from J/ψ ' s produced in 920 GeV fixed-target proton-nucleus collisions". In: *Eur. Phys. J. C* 60 (2009), pp. 517–524. DOI: 10.1140/epjc/s10052-009-0957-7. arXiv: 0901.1015 [hep-ex].

[110] Betty Abelev et al. "J/ψ polarization in pp collisions at $\sqrt{s} = 7$ TeV". In: *Phys. Rev. Lett.* 108 (2012), p. 082001. DOI: 10.1103/PhysRevLett.108.082001. arXiv: 1111.1630 [hep-ex].

[111] S. Acharya et al. "Measurement of the inclusive J/ ψ polarization at forward rapidity in pp collisions at $\sqrt{s} = 8$ TeV". In: *Eur. Phys. J. C* 78.7 (2018), p. 562. DOI: 10.1140/epjc/s10052-018-6027-2. arXiv: 1805.04374 [hep-ex].

[112] Mathias Butenschoen and Bernd A. Kniehl. "J/psi polarization at Tevatron and LHC: Nonrelativistic-QCD factorization at the crossroads". In: *Phys. Rev. Lett.* 108 (2012), p. 172002. DOI: 10.1103/PhysRevLett.108.172002. arXiv: 1201.1872 [hep-ph].

[113] Michele Arneodo. "Nuclear effects in structure functions". In: *Physics Reports* 240.5 (1994), pp. 301–393. ISSN: 0370-1573. DOI: https://doi.org/10.1016/0370-1573(94)90048-5. URL: https://www.sciencedirect.com/science/article/pii/0370157394900485.

[114] Edmond Iancu and Raju Venugopalan. "The Color glass condensate and high-energy scattering in QCD". In: *Quark-gluon plasma 4*. Ed. by Rudolph C. Hwa and Xin-Nian Wang. Mar. 2003, pp. 249–3363. DOI: 10.1142/9789812795533_0005. arXiv: hep-ph/0303204.

[115] K. J. Eskola, V. J. Kolhinen, and R. Vogt. "Obtaining the nuclear gluon distribution from heavy quark decays to lepton pairs in pA collisions". In: *Nucl. Phys. A* 696 (2001), pp. 729–746. DOI: 10.1016/S0375-9474(01)01221-0. arXiv: hep-ph/0104124.

[116] Kari J. Eskola et al. "EPPS16: Nuclear parton distributions with LHC data". In: *Eur. Phys. J. C* 77.3 (2017), p. 163. DOI: 10.1140/epjc/s10052-017-4725-9. arXiv: 1612.05741 [hep-ph].

[117] Ivan Vitev. "Non-Abelian energy loss in cold nuclear matter". In: *Phys. Rev. C* 75 (6 June 2007), p. 064906. DOI: 10.1103/PhysRevC.75.064906. URL: https://link.aps.org/doi/10.1103/PhysRevC.75.064906.

[118] Javier L. Albacete et al. "Predictions for Cold Nuclear Matter Effects in p+Pb Collisions at $\sqrt{s_{NN}} = 8.16$ TeV". In: *Nucl. Phys. A* 972 (2018), pp. 18–85. DOI: 10.1016/j.nuclphysa.2017.11.015. arXiv: 1707.09973 [hep-ph].

[119] B Alessandro et al. "Charmonia and Drell–Yan production in proton–nucleus collisions at the CERN SPS". In: *Physics Letters B* 553.3 (2003), pp. 167–178. ISSN: 0370-2693. DOI: https://doi.org/10.1016/S0370-2693(02)03265-3. URL: https://www.sciencedirect.com/science/article/pii/S0370269302032653.

[120] A. Adare et al. "Transverse-Momentum Dependence of the J/ψ Nuclear Modification in d+Au Collisions at $\sqrt{s_{NN}} = 200$ GeV". In: *Phys. Rev. C* 87.3 (2013), p. 034904. DOI: 10.1103/PhysRevC.87.034904. arXiv: 1204.0777 [nucl-ex].

[121] D. Kharzeev and R. L. Thews. "Quarkonium formation time in a model independent approach". In: *Phys. Rev. C* 60 (1999), p. 041901. DOI: 10.1103/PhysRevC.60.041901. arXiv: nucl-th/9907021.

[122] Shreyasi Acharya et al. "Inclusive J/ψ production at forward and backward rapidity in p-Pb collisions at $\sqrt{s_{\rm NN}}$ = 8.16 TeV". In: *JHEP* 07 (2018), p. 160. DOI: 10.1007/JHEP07(2018)160. arXiv: 1805.04381 [nucl-ex].

[123] François Arleo and Stéphane Peigné. "Quarkonium suppression in heavy-ion collisions from coherent energy loss in cold nuclear matter". In: *JHEP* 10 (2014), p. 073. DOI: 10.1007/JHEP10(2014)073. arXiv: 1407.5054 [hep-ph].

[124] Aleksander Kusina et al. "Gluon Shadowing in Heavy-Flavor Production at the LHC". In: *Phys. Rev. Lett.* 121.5 (2018), p. 052004. DOI: 10.1103/PhysRevLett.121.052004. arXiv: 1712.07024 [hep-ph].

[125] Jean-Philippe Lansberg and Hua-Sheng Shao. "Towards an automated tool to evaluate the impact of the nuclear modification of the gluon density on quarkonium, D and B meson production in proton–nucleus collisions". In: *Eur. Phys. J. C* 77.1 (2017), p. 1. DOI: 10.1140/epjc/s10052-016-4575-x. arXiv: 1610.05382 [hep-ph].

[126] K. Kovarik et al. "nCTEQ15 - Global analysis of nuclear parton distributions with uncertainties in the CTEQ framework". In: *Phys. Rev. D* 93.8 (2016), p. 085037. DOI: 10.1103/PhysRevD.93.085037. arXiv: 1509.00792 [hep-ph].

[127] K. J. Eskola, H. Paukkunen, and C. A. Salgado. "EPS09: A New Generation of NLO and LO Nuclear Parton Distribution Functions". In: *JHEP* 04 (2009), p. 065. DOI: 10.1088/1126-6708/2009/04/065. arXiv: 0902.4154 [hep-ph].

[128] Yan-Qing Ma et al. "$\psi(2S)$ versus J/ψ suppression in proton-nucleus collisions from factorization violating soft color exchanges". In: *Phys. Rev. C* 97.1 (2018), p. 014909. DOI: 10.1103/PhysRevC.97.014909. arXiv: 1707.07266 [hep-ph].

[129] B. Ducloué, T. Lappi, and H. Mäntysaari. "Forward J/ψ production at high energy: centrality dependence and mean transverse momentum". In: *Phys. Rev. D* 94.7 (2016), p. 074031. DOI: 10.1103/PhysRevD.94.074031. arXiv: 1605.05680 [hep-ph].

[130] "Inclusive, prompt and non-prompt J/ψ production at midrapidity in p-Pb collisions at $\sqrt{s_{\rm NN}} = 5.02$ TeV". In: *JHEP* 06 (2022), p. 011. DOI: 10.1007/JHEP06(2022)011. arXiv: 2105.04957 [nucl-ex].

[131] François Arleo et al. "Centrality and pT dependence of J/psi suppression in proton-nucleus collisions from parton energy loss". In: *JHEP* 05 (2013), p. 155. DOI: 10.1007/JHEP05(2013)155. arXiv: 1304.0901 [hep-ph].

[132] Matteo Cacciari et al. "Theoretical predictions for charm and bottom production at the LHC". In: *JHEP* 10 (2012), p. 137. DOI: 10.1007/JHEP10(2012)137. arXiv: 1205.6344 [hep-ph].

[133] Albert M Sirunyan et al. "Observation of prompt J/ψ meson elliptic flow in high-multiplicity pPb collisions at $\sqrt{s_{\rm NN}} = 8.16$ TeV". In: *Phys. Lett. B* 791 (2019), pp. 172–194. DOI: 10.1016/j.physletb.2019.02.018. arXiv: 1810.01473 [hep-ex].

[134] A. M. Sirunyan et al. "Elliptic flow of charm and strange hadrons in high-multiplicity pPb collisions at $\sqrt{s_{\rm NN}} = 8.16$ TeV". In: *Phys. Rev. Lett.* 121.8 (2018), p. 082301. DOI: 10.1103/PhysRevLett.121.082301. arXiv: 1804.09767 [hep-ex].

[135] A. K. Chaudhuri. *A short course on Relativistic Heavy Ion Collisions*. IOPP, Sept. 2014. ISBN: 978-0-7503-1061-1, 978-0-7503-1060-4. DOI: 10.1088/978-0-750-31060-4. arXiv: 1207.7028 [nucl-th].

[136] N. Brambilla et al. "Heavy Quarkonium: Progress, Puzzles, and Opportunities". In: *Eur. Phys. J. C* 71 (2011), p. 1534. DOI: 10.1140/epjc/s10052-010-1534-9. arXiv: 1010.5827 [hep-ph].

[137] T. Matsui and H. Satz. "J/ψ Suppression by Quark-Gluon Plasma Formation". In: *Phys. Lett. B* 178 (1986), pp. 416–422. DOI: 10.1016/0370-2693(86)91404-8.

[138] P. Braun-Munzinger and J. Stachel. "(Non)thermal aspects of charmonium production and a new look at J / psi suppression". In: *Phys. Lett. B* 490 (2000), pp. 196–202. DOI: 10.1016/S0370-2693(00)00991-6. arXiv: nucl-th/0007059.

[139] Robert L. Thews, Martin Schroedter, and Johann Rafelski. "Enhanced J/ψ production in deconfined quark matter". In: *Phys. Rev. C* 63 (5 Apr. 2001), p. 054905. DOI: 10.1103/PhysRevC.63.054905. URL: https://link.aps.org/doi/10.1103/PhysRevC.63.054905.

[140] Shreyasi Acharya et al. "Studies of J/ψ production at forward rapidity in Pb-Pb collisions at $\sqrt{s_{\mathrm{NN}}}$ = 5.02 TeV". In: *JHEP* 02 (2020), p. 041. DOI: 10.1007/JHEP02(2020)041. arXiv: 1909.03158 [nucl-ex].

[141] Z. Conesa del Valle et al. "Quarkonium production in high energy proton-proton and proton-nucleus collisions". In: *Nuclear Physics B - Proceedings Supplements* 214.1 (2011), pp. 3–36. ISSN: 0920-5632. DOI: https://doi.org/10.1016/j.nuclphysbps.2011.03.053. URL: https://www.sciencedirect.com/science/article/pii/S0920563211000867.

[142] Anton Andronic et al. "Decoding the phase structure of QCD via particle production at high energy". In: *Nature* 561.7723 (2018), pp. 321–330. DOI: 10.1038/s41586-018-0491-6. arXiv: 1710.09425 [nucl-th].

[143] Anton Andronic et al. "Transverse momentum distributions of charmonium states with the statistical hadronization model". In: *Phys. Lett. B* 797 (2019), p. 134836. DOI: 10.1016/j.physletb.2019.134836. arXiv: 1901.09200 [nucl-th].

[144] Anton Andronic et al. "The multiple-charm hierarchy in the statistical hadronization model". In: *JHEP* 07 (2021), p. 035. DOI: 10.1007/JHEP07(2021)035. arXiv: 2104.12754 [hep-ph].

[145] Jaroslav Adam et al. "J/ψ suppression at forward rapidity in Pb-Pb collisions at $\sqrt{\mathrm{s_{NN}}} = \mathbf{5.02}$ TeV". In: *Phys. Lett. B* 766 (2017), pp. 212–224. DOI: 10.1016/j.physletb.2016.12.064. arXiv: 1606.08197 [nucl-ex].

[146] Xingbo Zhao and Ralf Rapp. "Transverse Momentum Spectra of J/ψ in Heavy-Ion Collisions". In: *Phys. Lett. B* 664 (2008), pp. 253–257. DOI: 10.1016/j.physletb.2008.03.068. arXiv: 0712.2407 [hep-ph].

[147] Xingbo Zhao and Ralf Rapp. "Medium Modifications and Production of Charmonia at LHC". In: *Nucl. Phys. A* 859 (2011), pp. 114–125. DOI: 10.1016/j.nuclphysa.2011.05.001. arXiv: 1102.2194 [hep-ph].

[148] Xiaojian Du and Ralf Rapp. "Sequential Regeneration of Charmonia in Heavy-Ion Collisions". In: *Nucl. Phys. A* 943 (2015), pp. 147–158. DOI: 10.1016/j.nuclphysa.2015.09.006. arXiv: 1504.00670 [hep-ph].

[149] Kai Zhou et al. "Medium effects on charmonium production at ultrarelativistic energies available at the CERN Large Hadron Collider". In: *Phys. Rev. C* 89.5 (2014), p. 054911. DOI: 10.1103/PhysRevC.89.054911. arXiv: 1401.5845 [nucl-th].

[150] Zebo Tang et al. "Charmonium Transverse Momentum Distribution in High Energy Nuclear Collisions". In: *J. Phys. G* 41.12 (2014), p. 124006. DOI: 10.1088/0954-3899/41/12/124006. arXiv: 1409.5559 [nucl-th].

[151] Shreyasi Acharya et al. "Centrality and transverse momentum dependence of inclusive J/ψ production at midrapidity in Pb–Pb collisions at sNN=5.02 TeV". In: *Phys. Lett. B* 805 (2020), p. 135434. DOI: 10.1016/j.physletb.2020.135434. arXiv: 1910.14404 [nucl-ex].

[152] Shreyasi Acharya et al. "Measurements of inclusive J/ψ production at midrapidity and forward rapidity in Pb$-$Pb collisions at $\sqrt{s_{\mathrm{NN}}}$ = 5.02 TeV". In: (Mar. 2023). arXiv: 2303.13361 [nucl-ex].

[153] Jaroslav Adam et al. "Inclusive, prompt and non-prompt J/ψ production at midrapidity in Pb-Pb collisions at $\sqrt{s_{\mathrm{NN}}}$ = 2.76 TeV". In: *JHEP* 07 (2015), p. 051. DOI: 10.1007/JHEP07(2015)051. arXiv: 1504.07151 [nucl-ex].

[154] Albert M Sirunyan et al. "Measurement of prompt and nonprompt charmonium suppression in PbPb collisions at 5.02 TeV". In: *Eur. Phys. J. C* 78.6 (2018), p. 509. DOI: 10.1140/epjc/s10052-018-5950-6. arXiv: 1712.08959 [nucl-ex].

[155] Morad Aaboud et al. "Prompt and non-prompt J/ψ and $\psi(2S)$ suppression at high transverse momentum in 5.02 TeV Pb+Pb collisions with the ATLAS experiment". In: *Eur. Phys. J. C* 78.9 (2018), p. 762. DOI: 10.1140/epjc/s10052-018-6219-9. arXiv: 1805.04077 [nucl-ex].

[156] Catherine Silvestre. "PHENIX first measurement of the J/psi elliptic flow parameter v(2) in Au + Au collisions at s(NN)**(1/2) = 200-GeV". In: *J. Phys. G* 35 (2008). Ed. by Jan-e Alam et al., p. 104136. DOI: 10.1088/0954-3899/35/10/104136. arXiv: 0806.0475 [nucl-ex].

[157] L. Adamczyk et al. "Measurement of J/ψ Azimuthal Anisotropy in Au+Au Collisions at $\sqrt{s_{NN}} = 200$ GeV". In: *Phys. Rev. Lett.* 111.5 (2013), p. 052301. DOI: 10.1103/PhysRevLett.111.052301. arXiv: 1212.3304 [nucl-ex].

[158] Shreyasi Acharya et al. "J/ψ elliptic and triangular flow in Pb-Pb collisions at $\sqrt{s_{\rm NN}}$ = 5.02 TeV". In: *JHEP* 10 (2020), p. 141. DOI: 10.1007/JHEP10(2020)141. arXiv: 2005.14518 [nucl-ex].

[159] Min He, Biaogang Wu, and Ralf Rapp. "Collectivity of J/ψ Mesons in Heavy-Ion Collisions". In: *Phys. Rev. Lett.* 128.16 (2022), p. 162301. DOI: 10.1103/PhysRevLett.128.162301. arXiv: 2111.13528 [nucl-th].

[160] Shreyasi Acharya et al. "First measurement of quarkonium polarization in nuclear collisions at the LHC". In: *Phys. Lett. B* 815 (2021), p. 136146. DOI: 10.1016/j.physletb.2021.136146. arXiv: 2005.11128 [nucl-ex].

[161] Betty Abelev et al. "Coherent J/ψ photoproduction in ultra-peripheral Pb-Pb collisions at $\sqrt{s_{NN}} = 2.76$ TeV". In: *Phys. Lett. B* 718 (2013), pp. 1273–1283. DOI: 10.1016/j.physletb.2012.11.059. arXiv: 1209.3715 [nucl-ex].

[162] E. Abbas et al. "Charmonium and e^+e^- pair photoproduction at mid-rapidity in ultra-peripheral Pb-Pb collisions at $\sqrt{s_{\rm NN}}$=2.76 TeV". In: *Eur. Phys. J. C* 73.11 (2013), p. 2617. DOI: 10.1140/epjc/s10052-013-2617-1. arXiv: 1305.1467 [nucl-ex].

[163] Jaroslav Adam et al. "Coherent $\psi(2S)$ photo-production in ultra-peripheral Pb Pb collisions at $\sqrt{s}_{\rm NN}$ = 2.76 TeV". In: *Phys. Lett. B* 751 (2015), pp. 358–370. DOI: 10.1016/j.physletb.2015.10.040. arXiv: 1508.05076 [nucl-ex].

[164] V. Guzey et al. "Nuclear suppression from coherent J/ photoproduction at the Large Hadron Collider". In: *Physics Letters B* 816 (2021), p. 136202. ISSN: 0370-2693. DOI: https://doi.org/10.1016/j.physletb.2021.136202. URL: https://www.sciencedirect.com/science/article/pii/S0370269321001428.

[165] Shreyasi Acharya et al. "Coherent J/ψ photoproduction at forward rapidity in ultra-peripheral Pb-Pb collisions at $\sqrt{s_{\rm NN}} = 5.02$ TeV". In: *Phys. Lett. B* 798 (2019), p. 134926. DOI: 10.1016/j.physletb.2019.134926. arXiv: 1904.06272 [nucl-ex].

[166] Lyndon Evans and Philip Bryant. "LHC Machine". In: *JINST* 3 (2008), S08001. DOI: 10.1088/1748-0221/3/08/S08001.

[167] "The ALICE experiment at the CERN LHC". In: *JINST* 3 (2008), S08002. DOI: 10.1088/1748-0221/3/08/S08002.

[168] G. Aad et al. "The ATLAS Experiment at the CERN Large Hadron Collider". In: *JINST* 3 (2008), S08003. DOI: 10.1088/1748-0221/3/08/S08003.

[169] S. Chatrchyan et al. "The CMS Experiment at the CERN LHC". In: *JINST* 3 (2008), S08004. DOI: 10.1088/1748-0221/3/08/S08004.

[170] A. Augusto Alves Jr. et al. "The LHCb Detector at the LHC". In: *JINST* 3 (2008), S08005. DOI: 10.1088/1748-0221/3/08/S08005.

[171] Georges Aad et al. "Observation of a new particle in the search for the Standard Model Higgs boson with the ATLAS detector at the LHC". In: *Phys. Lett. B* 716 (2012), pp. 1–29. DOI: 10.1016/j.physletb.2012.08.020. arXiv: 1207.7214 [hep-ex].

[172] Serguei Chatrchyan et al. "Observation of a New Boson at a Mass of 125 GeV with the CMS Experiment at the LHC". In: *Phys. Lett. B* 716 (2012), pp. 30–61. DOI: 10.1016/j.physletb.2012.08.021. arXiv: 1207.7235 [hep-ex].

[173] K Aamodt et al. "First proton-proton collisions at the LHC as observed with the ALICE detector: Measurement of the charged particle pseudorapidity density at s**(1/2) = 900-GeV". In: *Eur. Phys. J. C* 65 (2010), pp. 111–125. DOI: 10.1140/epjc/s10052-009-1227-4. arXiv: 0911.5430 [hep-ex].

[174] Andrea Dainese. "First ALICE results from heavy-ion collisions at the LHC". In: *Nuovo Cim. C* 035N1 (2012). Ed. by Etienne Augé, Jacques Dumarchez, and Jean Trân Thanh Vân, pp. 197–205. DOI: 10.1393/ncc/i2012-11150-8. arXiv: 1106.1341 [nucl-ex].

[175] Jens Wiechula. "Inbetriebnahme und Kalibrierung der ALICE-TPC". 2008. URL: https://cds.cern.ch/record/1295506.

[176] "Performance of the ALICE Electromagnetic Calorimeter". In: (Sept. 2022). arXiv: 2209.04216 [physics.ins-det].

[177] P. Kuijer. "The inner tracking system of the Alice experiment". In: *Nuclear Instruments and Methods in Physics Research Section A: Accelerators, Spectrometers, Detectors and Associated Equipment* 530.1 (2004), pp. 28–32. DOI: https://doi.org/10.1016/j.nima.2004.05.042.

[178] P Cortese et al. *ALICE forward detectors: FMD, TO and VO: Technical Design Report*. Technical design report. ALICE. Submitted on 10 Sep 2004. Geneva: CERN, 2004. URL: https://cds.cern.ch/record/781854.

[179] M Gallio et al. *ALICE Zero-Degree Calorimeter (ZDC): Technical Design Report*. Technical design report. ALICE. Geneva: CERN, 1999. URL: https://cds.cern.ch/record/381433.

[180] ALICE Collaboration. *ALICE Central Trigger Processor*. URL: https://alicetrigger.web.cern.ch/.

[181] R. E. Kalman. "A New Approach to Linear Filtering and Prediction Problems". In: *Journal of Basic Engineering* 82.1 (Mar. 1960), pp. 35–45. ISSN: 0021-9223. DOI: 10.1115/1.3662552. URL: https://doi.org/10.1115/1.3662552.

[182] Antonin Maire. "Track reconstruction principle in ALICE for LHC run I and run II. Principes de reconstruction de traces dans ALICE pour les runs I et II du LHC". General Photo. 2011. URL: https://cds.cern.ch/record/1984041.

[183] Betty Bezverkhny Abelev et al. "Performance of the ALICE Experiment at the CERN LHC". In: *Int. J. Mod. Phys. A* 29 (2014), p. 1430044. DOI: 10.1142/S0217751X14300440. arXiv: 1402.4476 [nucl-ex].

[184] Luigi Rolandi, Werner Riegler, and Walter Blum. *Particle Detection with Drift Chambers*. Springer Berlin Heidelberg, 2008. DOI: 10.1007/978-3-540-76684-1. URL: https://doi.org/10.1007%2F978-3-540-76684-1.

[185] B. Zagreev. "Algorithms and methods for particle identification with ALICE TOF detector at a very high particle multiplicity". In: *Nucl. Instrum. Meth. A* 502 (2003). Ed. by V. A. Ilyin, V. V. Korenkov, and D. Perret-Gallix, pp. 716–718. DOI: 10.1016/S0168-9002(03)00554-0.

[186] M. Bondila et al. "ALICE T0 detector". In: *IEEE Trans. Nucl. Sci.* 52 (2005), pp. 1705–1711. DOI: 10.1109/TNS.2005.856900.

[187] "Centrality determination in heavy ion collisions". In: (Aug. 2018). URL: https://cds.cern.ch/record/2636623.

[188] Wei-Tian Deng, Xin-Nian Wang, and Rong Xu. "Hadron production in p+p, p+Pb, and Pb+Pb collisions with the HIJING 2.0 model at energies available at the CERN Large Hadron Collider". In: *Phys. Rev. C* 83 (2011), p. 014915. DOI: 10.1103/PhysRevC.83.014915. arXiv: 1008.1841 [hep-ph].

[189] Torbjorn Sjostrand, Stephen Mrenna, and Peter Z. Skands. "PYTHIA 6.4 Physics and Manual". In: *JHEP* 05 (2006), p. 026. DOI: 10.1088/1126-6708/2006/05/026. arXiv: hep-ph/0603175.

[190] D. J. Lange. "The EvtGen particle decay simulation package". In: *Nucl. Instrum. Meth. A* 462 (2001). Ed. by S. Erhan, P. Schlein, and Y. Rozen, pp. 152–155. DOI: 10.1016/S0168-9002(01)00089-4.

[191] Elisabetta Barberio and Zbigniew Was. "PHOTOS: A Universal Monte Carlo for QED radiative corrections. Version 2.0". In: *Comput. Phys. Commun.* 79 (1994), pp. 291–308. DOI: 10.1016/0010-4655(94)90074-4.

[192] René Brun et al. "GEANT Detector Description and Simulation Tool". In: (Oct. 1994). DOI: 10.17181/CERN.MUHF.DMJ1.

[193] B Abelev et al. *Technical Design Report for the Upgrade of the ALICE Inner Tracking System*. Tech. rep. 2014. DOI: 10.1088/0954-3899/41/8/087002. URL: https://cds.cern.ch/record/1625842.

[194] John Erthal Gaiser. "Charmonium Spectroscopy From Radiative Decays of the J/ψ and ψ'". Other thesis. Aug. 1982.

[195] D. Drijard, H. G. Fischer, and T. Nakada. "Study of Event Mixing and Its Application to the Extraction of Resonance Signals". In: *Nucl. Instrum. Meth. A* 225 (1984), p. 367. DOI: 10.1016/0167-5087(84)90275-8.

[196] D. Acosta et al. "Measurement of the J/ψ meson and $b-$hadron production cross sections in $p\bar{p}$ collisions at $\sqrt{s} = 1960$ GeV". In: *Phys. Rev. D* 71 (2005), p. 032001. DOI: 10.1103/PhysRevD.71.032001. arXiv: hep-ex/0412071.

[197] Jan Uphoff et al. "Open Heavy Flavor in Pb+Pb Collisions at $\sqrt{s} = 2.76$ TeV within a Transport Model". In: *Phys. Lett. B* 717 (2012), pp. 430–435. DOI: 10.1016/j.physletb.2012.09.069. arXiv: 1205.4945 [hep-ph].

[198] W. M. Alberico et al. "Heavy-flavour spectra in high energy nucleus-nucleus collisions". In: *Eur. Phys. J. C* 71 (2011), p. 1666. DOI: 10.1140/epjc/s10052-011-1666-6. arXiv: 1101.6008 [hep-ph].

[199] W. M. Alberico et al. "Heavy flavors in AA collisions: production, transport and final spectra". In: *Eur. Phys. J. C* 73 (2013), p. 2481. DOI: 10.1140/epjc/s10052-013-2481-z. arXiv: 1305.7421 [hep-ph].

[200] Shreyasi Acharya et al. "Inclusive J/ψ production at mid-rapidity in pp collisions at $\sqrt{s} = 5.02$ TeV". In: *JHEP* 10 (2019), p. 084. DOI: 10.1007/JHEP10(2019)084. arXiv: 1905.07211 [nucl-ex].

[201] Baoyi Chen. "Thermal production of charmonia in Pb-Pb collisions at $\sqrt{s_{NN}} = 5.02$ TeV". In: *Chin. Phys. C* 43.12 (2019), p. 124101. DOI: 10.1088/1674-1137/43/12/124101. arXiv: 1811.11393 [nucl-th].

[202] Roel Aaij et al. "Study of prompt D^0 meson production in pPb collisions at $\sqrt{s_{\rm NN}} = 5$ TeV". In: *JHEP* 10 (2017), p. 090. DOI: 10.1007/JHEP10(2017)090. arXiv: 1707.02750 [hep-ex].

[203] Shreyasi Acharya et al. "Charm-quark fragmentation fractions and production cross section at midrapidity in pp collisions at the LHC". In: *Phys. Rev. D* 105.1 (2022), p. L011103. DOI: 10.1103/PhysRevD.105.L011103. arXiv: 2105.06335 [nucl-ex].

[204] "High-Luminosity Large Hadron Collider (HL-LHC): Technical Design Report V. 0.1". In: 4/2017 (2017). Ed. by G. Apollinari et al. DOI: 10.23731/CYRM-2017-004.

[205] "ALICE upgrades during the LHC Long Shutdown 2". In: (Feb. 2023). arXiv: 2302.01238 [physics.ins-det].

[206] *Addendum of the Letter of Intent for the upgrade of the ALICE experiment : The Muon Forward Tracker*. Tech. rep. Final submission of the presetn LoI addendum is scheduled for September 7th. Geneva: CERN, 2013. URL: https://cds.cern.ch/record/1592659.

Appendix A

The PID responses of the TPC can be changed by many of the detector effects during data taking. Therefore, a PID postcalibration has been performed to overcome such effects. When $n\sigma$ distributions of different particle species, such as electron, pion, and proton, are parameterized by a Gaussian, the extracted parameters mean and sigma is not exactly 0 and 1, respectively. Also, the parameters show a dependence on event and track properties. The PID postcalibration procedure minimizes such dependence of fit parameters by constraining the Gaussian mean and width at 0 and 1, respectively. For this purpose, a pure electron sample is used from photon conversions which are selected using the same track selection criteria as electrons from J/ψ. Such a condition allows having a sample similar to J/ψ dielectrons sample. Similarly, pion and proton samples are taken from K0s decays and Λ decays, respectively. The $n\sigma$ distributions from these pure samples are fitted by Gaussian to obtain the postcalibration parameters, *i.e.* , mean and width of Gaussian. For the electron sample, a double Gaussian is used because of the pion signal adjacent to the electron signal in its $n\sigma$ distribution. Such fits are performed in four dimensions: track properties such as pseudorapidity η, particle's momentum in inner TPC wall p_{IN} and event properties such as the number of SSD+SDD clusters and z position of pileup vertex. The fit parameters exhibit a dependence on these observables, for e.g., η dependence of mean and width of electron distribution for LHC18q and LHC18r periods has been shown in Fig. A.1. These four-dimensional maps apply PID corrections to TPC $n\sigma$ distribution of electron, protons, and pions according to Eq. A.1.

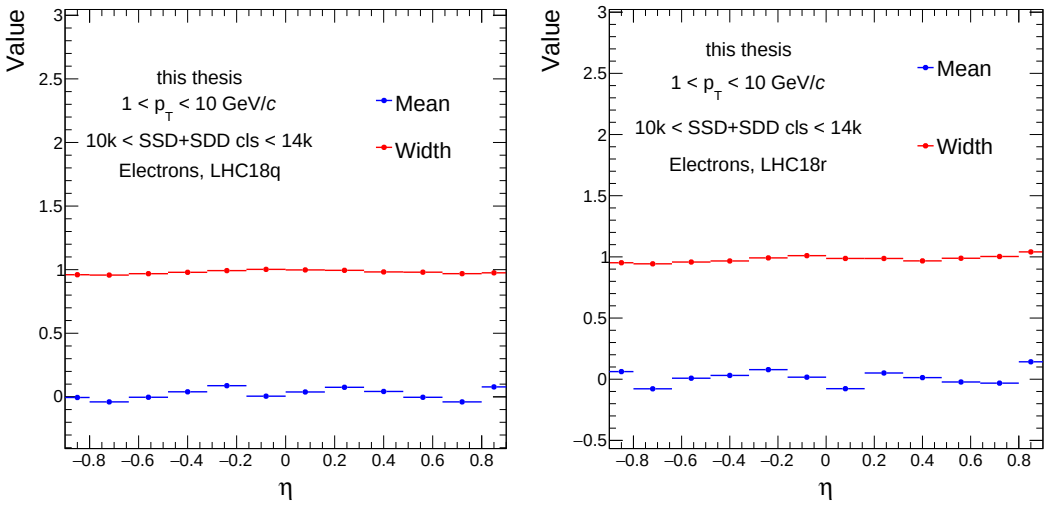

Figure A.1 Variation of mean and sigma of Gaussian with respect to η of the tracks in LHC18q and LHC18r.

$$n\sigma_i^{cal}(P) = \frac{n\sigma_i(P) - \mu(P)}{\sigma(P)}, \tag{A.1}$$

where P is permutation of event and track properties (V_z^{Pileup}, $N_{cls}^{SSD+SDD}$, η, p_{IN}) used in postcalibration, μ and σ are mean and width of gaussian fit for particular i^{th} particle specie. The postcalibration maps of LHC15o have a dependence on pileup vertex, while it is not considered for LHC18 datasets.

Appendix B

The prompt J/ψ p_{T} -differential yields in the 0–10% and 30–50% centrality intervals are depicted with the model predictions in Fig. B.1. In the left panel, the model predictions and data are compared for the 0–10% centrality interval, while the right panel shows the comparison for the 30–50% centrality interval. It is observed that the prompt J/ψ yields are consistent with the models within the uncertainties for p_{T} values below 5 GeV/c in both centrality intervals. However, at higher p_{T} values, the transport model predictions are closer to the data in comparison to the SHMc model. The SHMc model underestimates the prompt J/ψ production at high p_{T} , regardless of the centrality interval.

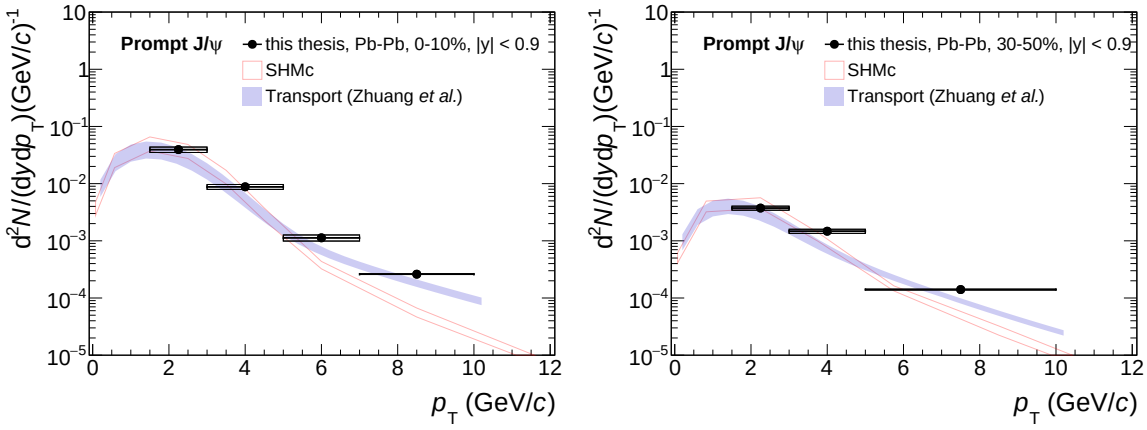

Figure B.1 Prompt J/ψ p_{T} -differential yields for 0–10% (left) and 30–50% (right) centrality intervals in comparison to theoretical predictions [143, 149], statistical and systematic uncertainties are represented by vertical bars and boxes, respectively.

In Fig. B.2, the Transport model predictions are compared with non-prompt J/ψ yields in 0–10% and 30–50% centrality intervals. In both centrality intervals at p_{T} below 5 GeV/c, the model predicts larger values of the non-prompt J/ψ yields than the measurements. The discrepancy between the data and the model is around 2 σ at low p_{T} in both centrality intervals. However, the model predictions are consistent with the measurements within the level of uncertainties.

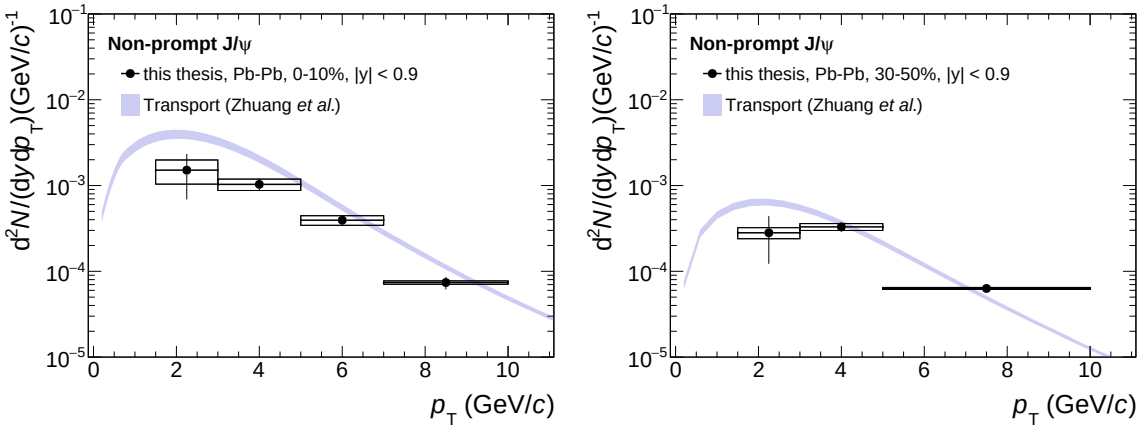

Figure B.2 Non-prompt J/ψ p_{T} -differential yields for 0–10% (left) and 30–50% (right) centrality intervals in comparison to theoretical predictions [149], statistical and systematic uncertainties are represented by vertical bars and boxes, respectively.